Three-Dimensionally Ordered Macroporous Materials For Use as Color Pigments, Ultraviolet Reflectors, And Modified Thermal Emission Devices

A DISSERTATION SUBMITTED TO THE FACULTY OF THE GRADUATE SCHOOL OF THE UNIVERSITY OF MINNESOTA BY

David Peter Josephson

IN PARTIAL FULFILLMENT OF THE REQUIREMENTS FOR THE DEGREE OF DOCTOR OF PHILOSOPHY

Andreas Stein

January 2014

Acknowledgments

I would like to thank the following individuals for their help and support:

Professor Andreas Stein, for his insights, ideas, and passion for chemistry. His enthusiasm for new discoveries fostered a great atmosphere of creativity and collaboration in which all of his group members could thrive.

All current and former Stein group members for their continued support and cooperative discussions. Their ready supply of suggestions and ideas were always appreciated.

Professor David J. Norris, Dr. Sang Eon Han, Dr. Prashant Nagpal, Emmanuel Dimotakis, Laurent Vidal, and Jeanne Chang for their collaboration and insight.

My family, who have been vital in shaping who I am as a person and have always been there with their support, love, and understanding.

My wife and best friend, Emily, who was always there to listen to my latest advancement in the field of *science*.

Abstract

Photonic crystals are periodic optical nanostructures that can selectively disallow the propagation of specific ranges of electromagnetic radiation. Among photonic crystals, three-dimensionally ordered macroporous (3DOM) materials are of interest for a new class of colored pigments, UV reflectors, and modified thermal emission devices synthesized from a wide range of materials.

For color pigment applications of 3DOM materials, this dissertation explores the important role of light-absorbing species within the 3DOM structure through the variation of processing parameters in the synthesis of 3DOM zirconia. It was found that intense coloration strongly depended on the concentration of in-situ carbon generated within the structure, which was controlled by processing temperature and atmosphere. The tunability of color in 3DOM silica through variations in maximum processing temperature is also discussed as well as the discovery of a unique additive color-mixing mechanism found in 3DOM pigments.

3DOM materials with stop bands outside of the visible spectrum were also investigated. 3DOM TiO_2/SiO_2 was synthesized with UV stop bands that, coupled with strong TiO_2 absorbance, decreased overall UV transmittance. Thermally-stable metallic photonic crystals with stop bands in the IR range were also synthesized for thermophotovoltaic applications where tailored emission could be potentially coupled with specific diode materials.

Table of Contents

List of Tables

List of Figures

List of Abbreviations

3D	Three-dimensional
3DO	Three-dimensionallt ordered
3DOM	Three-dimensionally ordered macroporous
°C	Degrees Celsius
AIBN	2,2-azobisisobutyronitrile
ALD	Atomic Layer Deposition
APTA	Acetylated peroxotungstic acid
CMY	Cyan-magenta-yellow
CIE	Commission Internationale de l'Eclairage
CTAB	Cetyl trimethylammonium bromide
CVD	Chemical Vapor Deposition
ΔD	Diameter chance from pore shrinkage
d_{hkl}	spacing of diffraction layers
D_{pore}	Pore diameter
d-spacing	Spacing between adjacent lattice planes
D_{sphere}	Sphere diameter
EDS	Energy-Dispersive X-ray spectroscopy
η	Viscosity of solvent
n_{avg}	Average refractive index
n_{wall}	Refractive index of wall
f	Scattering factor
fcc	Face-centered cubic
FD&C	Food, Drug, and Cosmetic Act
FF	Fill fraction
g	gram
g	Gravitational force
h	hour
hcp	Hexagonally close-packed
HWHM	Half-width half-max
I_0	Intensity of incident light
I_H	Diffraction intensity
IR	Infrared
$K_{\sigma, \pi}$	Polarizations with respect to diffraction plane
L	Liter
λ	Stop band position
m	Order of diffraction
min	Minute
M	Molarity
mL	Milliliter
MMA	Methyl methacrylate
NMR	Nuclear magnetic resonance
v	Velocity
φ	Fill fraction
PS	Poly(styrene)

Ψ_0''	Scattering losses in intensity
PMMA	Poly(methyl methacrylate)
PVP	Poly(vinyl pyrrolidone)
R%	Reflectance %
R(∞)	Kubelka-Munk adjusted reflectance
RGB	Red-green-blue
rhcp	Random hexagonally close-packed
RF	Resorcinol-Formaldehyde
ρ_1	Density of sphere
ρ_2	Density of solvent
RPM	Revolutions per minute
r_s	Radius of sphere
SEM	Scanning electron microscopy
T%	Transmittance %
TEM	Transmission electron microscope
TEOS	Tetraethyl orthosilicate
TGA	Thermogravimetric analysis
TPV	Thermophotovoltaic
TTIP	Titanium tetraisopropoxide
UV	Ultraviolet
UV-vis	Ultraviolet-visible
w%	Weight %
XRD	X-ray diffraction

Chapter 1
Introduction

1.1 Overview

As living organisms, humans perceive and interact with the world around us through the use of the senses available to us. Our intricate bodies can detect changes in texture or temperature, smell and taste chemical compounds, and sense vibrations through the air by audition. But as humans, our greatest tool in perceiving our environment comes from our ability to detect and differentiate wavelengths of electromagnetic radiation. Using this sense we are able to visualize the world around us as a cascade of photonic absorptions, reflections, and emissions that our brains interpret as color.

Due to the importance of color to our human perceptions, it has long been used by humanity, both functionally and aesthetically. As we have learned to use color to suit our needs, we have also begun to understand the mechanisms of color generation and how our eyes are able to sense it. We began by learning how the mixing of two colors could generate a new color.[3] We then progressed into discovering less obvious phenomena such as the ability of gold nanoparticles in water to possess multiple colorations.[4] With the discovery and understanding of these numerous color mechanisms, we began to understand the nature of photons themselves and how their interactions with the objects around us shape our polychromatic world.

Further advances in the understanding of color have been made within the past few decades. A new form of coloration has begun to be understood that arises due to structural morphology rather than molecular properties. By imbuing a material with periodic diffraction planes that reflect specific wavelengths of light based on Bragg diffraction, brilliant colors can be imparted onto objects that would otherwise possess no color. The colors that result from this mechanism can be selected solely by alterations to the structure of a chosen material, allowing one material to exhibit various colors throughout the spectrum with no change to the chemical nature of the material itself.

The creation of these structurally-colored materials through a colloidal crystal templating procedure and their optimization for color pigments is discussed herein. Discoveries regarding the role of light-absorbing species within these materials as well as the effects of various process conditions on the coloration of these pigments are discussed. Further studies on materials that possess photonic reflections outside of the visible range (ultra-violet and infrared) for non-color applications are also discussed.

1.2. Color

1.2.1. Traditional Color Mechanisms

The portion of the electromagnetic spectrum that we refer to as color (400-700 nm) constitutes a very small series of wavelengths between short wave gamma rays (10^{-11} m) and long wave radio waves (10^{3} m). These wavelengths can be perceived by humans due to the specific energy levels of the photons associated with this range. At this range of energy, electromagnetic radiation can interact with electrons within molecules to initiate

conformational changes. This interaction allows receptors in our eyes to be photoisomerized by photons. Conformational changes in these receptors initiate electrochemical responses that are sent to the brain for interpretation through a complex neurological pathway. Higher energy radiation (UV) is too ionizing for this task and lower energy radiation (IR) only imparts a small amount of molecular motion that we perceive as heat.[5]

Approximately 45% of our sun's radiation is emitted in the visible spectrum.[6] The white glow of the sun is a combination of all spectral colors. Only when this light has reached matter does it begin to separate into specific colors through the selective absorption, scattering, transmission, and reflection of light. Numerous mechanisms for the generation of color have been identified. In Nassau's *The Physics and Chemistry of Color: The Fifteen Causes of Color*,[7] these mechanisms are categorized according to Nassau in Table 1.1.

Table 1.1: Recreation of a table from Nassau's *The Physics and Chemistry of Color: The Fifteen Causes of Color*[7] describing the fifteen causes of color, as categorized by the author.

Vibrations and Simple Excitations
1. *Incandescence*: Flames, lamps, carbon arc, limelight
2. *Gas excitations*: Vapor lamps, lightning, auroras, some lasers
3. *Vibrations and Rotations:* Water, ice, iodine, blue gas flame
Transitions Involving Ligand Field Effects
4. *Transition Metal Compounds*: Turquoise, many pigments, some fluorescence, lasers, phosphors
5. *Transition Metal Impurities*: Ruby, emerald, red iron ore, some fluorescence, and lasers
Transitions Between Molecular Orbitals
6. *Organic Compounds*: Most dyes, most biological colorations, some fluorescence, and lasers
7. *Charge Transfer*: Blue sapphire, magnetite, lapis lazuli, many pigments
Transitions Involving Energy Bands
8. *Metals*: Copper, silver, gold, iron, brass, "ruby" glass
9. *Pure Semiconductors*: Silicon, galena, cinnabar, diamond
10. *Doped or Activated Semiconductors*: Blue and yellow diamond, light emitting diodes, some lasers, and phosphors
11. *Color Centers*: Amethyst, smoky quartz, desert "amethyst" glass, some fluorescence, and lasers
Geometrical and Physical Optics
12. *Dispersive Refraction*, Polarization, etc.: Rainbows, halos, sun dogs, green flash of sun, "fire" in gemstones
13. *Scattering*: Blue sky, red sunset, blue moon, moonstone, Raman scattering, blue eyes, and some other biological colors
14. *Interference:* Oil slick on water, soap bubbles, coating on camera lenses, some biological colors
15. *Diffraction:* Aureole, glory, diffraction gratings, opal, some biological colors, most liquid crystals.

Table 1.1 separates color mechanisms into those that are caused by atomic excitations, ligand field effects, molecular orbital transitions, band transitions, or phenomena occurring due to geometric or physical causes. Of all the mechanisms listed in Table 1.1, the use of color by humans has traditionally been dominated by materials that harness the effects of electronic transitions. Almost all traditional dyes and pigments

use color mechanisms that selectively subtract specific parts of the visible spectrum through electronic transitions and reflect or transmit the remaining visible wavelengths. This phenomenon is referred to as ‘subtractive color’ and allows the mixing of various colors in order to partially or completely subtract portions of the spectrum to change the perceived color that arises from an illuminated surface. The primary colors in a subtractive system that can be combined to form all other colors are cyan, magenta, and yellow. When these primary colors are mixed together in equal ratios, they form black due to the complete subtraction of the entire visible spectrum. A majority of the objects in our world follow this mechanism, where color is dictated by the selective absorbance of light.

This subtractive color mechanism is distinct from colors that arise from the mixing of colored light, called ‘additive color’. Additive coloration is used in display systems such as monitors and televisions in which numerous colored pixels are selectively activated in order to combine specific colored emissions into a desired final color. In this case, photons are not being selectively absorbed but, rather, narrow band emissions of specific wavelengths of photons are responsible for the perceived color. The emitted color wavelengths from each individual source add together to form the final color. The primary colors within the additive color system are distinct from the subtractive primaries. Blue, green, and red are the primary colors in the additive system and when mixed together form white instead of black, approximating the white light of the sun, which includes emissions of all spectral colors. The use of blue, green, and red as primary colors caters to the physiology of the human eye, which contains three separate classifications of cone cells that detect varying amounts of blue, green, and red light, and

send that sensory information to the brain, which then interprets the response as color.[5] Thus, by manipulating the intensity of each level of blue, green, and red, all spectral colors that can be observed with the human eye are possible.

1.2.2. Structural Color

One such additive color mechanism was not well-understood until a little more than 25 years ago. In 1987, Yablonovitch[8] and John[9] independently brought forward the concept that a material could possess a photonic band gap that would disallow the propagation of certain wavelengths of light. The disallowed photons would be, instead, reflected away from the material. This introduced a new mechanism of controlling the movement of photons and ushered in a new understanding of the presence of structural color in our world. These materials were labeled as 'photonic crystals' and are described in the following section.

The term 'structural color' implies that the coloration of a material arises from its morphology rather than its inherent molecular properties. In a structurally-colored material, photons are diffracted or interfered with, resulting in the preferential reflection of certain wavelengths. Since this coloration does not depend on electronic transitions within a material, but is primarily governed by the morphology of the material, it is referred to as structural color. The narrow region of spectral reflectance from these materials approximates an emission of light and, therefore, follows the same additive color mechanism used in display technologies.

Several examples of structural color can be found in nature. Certain species of butterflies and invertebrates as well as multiple types of flora possess color resulting from the periodic arrangement of features on their surfaces.[10-12] Natural examples can also be found in minerals such as labradorite.[13] The most well-known mineral example is probably the natural opal which, despite being composed of optically transparent silica spheres, expresses a wide range of colors caused by the reflection of light due to its periodic structure.[14-15]

1.2.2.1. Photonic Crystals

Natural gem opals are structurally-colored because they are a type of photonic crystal, as described by Yablonovitch[8] and John[9]. Photonic crystals are materials with a periodic arrangement of high and low dielectric zones that act as Bragg diffraction planes. Materials with a high dielectric contrast can form complete photonic band gaps that prevent the propagation of a range of wavelengths from passing through the material in all directions.[9] Materials with a lower dielectric contrast form an incomplete band gap, also called a stop band, where propagation is only partially inhibited. These materials, however, can still exhibit unique optical properties, such as structural color, if their stop bands fall within the visible spectrum, as in the case of natural opals. The close-packed, periodic arrangement of silica spheres that make up natural opals creates the regular diffraction planes necessary for photonic reflection (Figure 1.1).

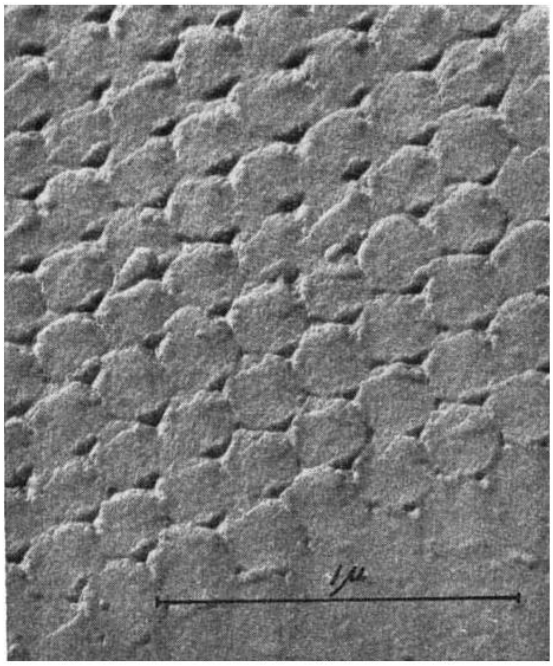

Figure 1.4. Scanning electron micrograph of precious natural opal. A periodic arrangement of spheres can be observed. Image reproduced from Sanders *et al*.[15]

These diffraction events disallow a range of wavelengths of electromagnetic radiation from propagating through the material depending on the spacing between adjacent lattice planes of the periodic structure. In the case of natural opals, the observed lie within the visible range of the electromagnetic spectrum and are perceived as color. The disallowance of these spectral ranges is similar to the behavior of electrons in a semiconductor.[9] Semiconductors have electronic bandgaps that disallow the propagation of electrons of specific energies. Photonic crystals have similar bandgaps called photonic bandgaps that disallow the propagation of photons with energies associated with specific bands. Figure 1.2 illustrates the similarity between electronic and photonic bandgap diagrams.

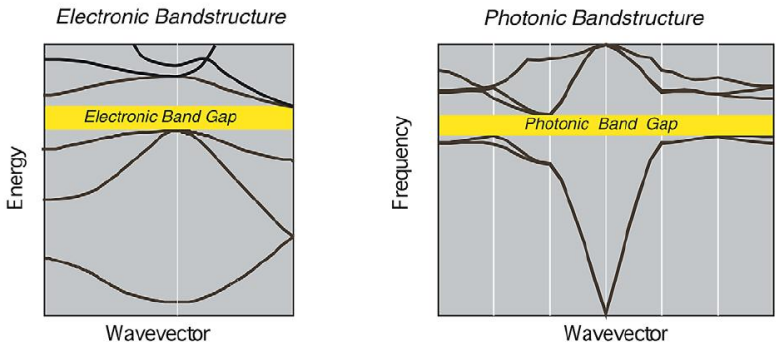

Figure 1.2. Band diagrams for a semiconductor (left) and a photonic crystal (right). Reproduced from John *et al*.[9]

While many examples of photonic crystals exist in nature, they can also be synthesized using several different synthetic techniques such as layer-by-layer stacking,[16-17] lithography,[18-19] and laser-induced direct-write deposition.[20-21] These techniques, however, are laborious and require expensive equipment with limited scalability. Due to these considerations, one of the most promising methods for producing well-ordered synthetic photonic crystals is the self-assembly of colloidal particles, which naturally assemble into face-centered cubic (fcc) structures similar to natural opals (Figure 1.3).[22-23] This technique does not require specialized equipment and can produce photonic crystals with sufficient long-range order to possess intense stop bands in the visible region.

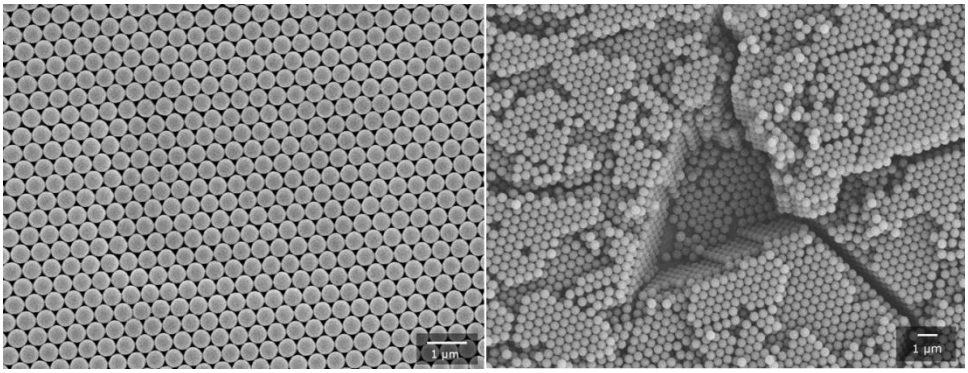

Figure 1.3. Scanning electron micrographs of a synthetic opal composed of uniformly sized polymer spheres. Left: The (111) plane of the opal. Note the highly periodic array of spheres that create Bragg diffraction planes within the material. Right: An incomplete opal showing the 3D structure of the material.

1.3. Colloidal Crystallization

1.3.1. Self-Assembly of Monodisperse, Charged Nanospheres

In cases where interparticle forces are sufficiently balanced in a colloidal system, self-assembly of particles into regular, periodic arrays can occur. For example, monodisperse nanometer and micrometer sized spheres in a suspension can spontaneously form close-packed colloidal crystal arrays if their free volume is restricted below a certain value.[24] In order to form periodic crystalline arrays, the surface charge of the particles must be sufficiently repulsive to discourage random aggregation but not large enough to prevent close packing.[25] The slight repulsive interactions between particles also allow the particles to reorder into lower energy conformations without aggregation as the free volume around the particles is decreased.[26] Monodisperse, spherical colloids typically pack into face-centered cubic (fcc), hexagonal close-packed (hcp), or random hexagonally close-packed (rhcp) arrays, with fcc being entropically favored over hcp.[27]

Several techniques including vertical deposition,[28-30] float packing,[31] gravity sedimentation,[32] filtration,[33] electrophoretically controlled sedimentation,[34] and accelerated sedimentation by centrifugation[35] have been used to form colloidal crystals with few defects. Several additional strategies to control long-range cracking defects in dried colloidal crystals have also been investigated in order maintain large crystalline domains outside of a liquid suspension.[36-39]

For the gravity sedimentation technique used to create most of the colloidal crystals in this dissertation, polymer nanospheres were synthesized and allowed to sediment and self-assemble into an ordered fcc close packed array to produce a colloidal crystal.[40] This sedimentation was done slowly over many weeks, depending on the diameter of the colloidal spheres. Equation 1.1 shows the dependence of sedimentation velocity on sphere radii:[41]

Equation 1.1

$$v = \frac{2}{9}\frac{r_s^2(\rho_2 - \rho_1)g}{\eta}$$

where v is the sedimentation velocity, r_s is the radius of the sphere, ρ_2 is the density of the solvent, ρ_1 is the density of the sphere, g is the force of gravity, and η is the viscosity of the solvent. As sphere radius increases, an exponential rise in sedimentation velocity occurs. At high velocities, colloidal particles do not self-assemble into ordered arrays as they are not able to re-order into lower-energy conformations before other sedimenting particles pin the spheres into place, often in an undesirable conformation. This increases the disorder of the crystal and introduces defects in the lattice. For this reason, gravity

sedimentation works best for particles that take more than several weeks to sediment fully in order to create a crystal with very long-range order. After the spheres have sedimented, the solvent is allowed to evaporate over time. The resulting solid is a periodic array of spheres with ABCABC layered stacking.[42] This method produces well-ordered colloidal crystal templates at the expense of long sedimentation times.

Centrifugal sedimentation has also been used to accelerate sedimentation times of colloidal spheres.[35] The degree of angular acceleration replaces the term for gravitational acceleration in Equation 1.1 for this case. Larger values for angular acceleration correspond to higher sedimentation velocities. However, the faster sedimentation times increase crystal disorder and care must be taken not to introduce too much disorder for the intended application.

Despite the facile approach described above for the formation of colloidal crystals in this dissertation, an understanding of the interparticle forces involved in colloidal self-assembly is vital in order to produce well-ordered colloidal crystals in response to potential changes in particle composition or environment. Several studies have been performed on the self-assembly of particles with various characteristics and the strategies involved in obtaining well-ordered crystalline arrays from these particles. All of these strategies beg the consideration of specific characteristics of the colloidal particles involved.

1.3.2. Influencing Self-Assembly by Modifying Particle Characteristics

While the fcc close-packed arrangement is thermodynamically favored for techniques using monodisperse, similarly charged spheres in suspension, other self-assembly methods can also be used to produce both close-packed and non-close-packed arrays by altering particle characteristics, such as size disparity, surface charge, geometry, or a combination of these factors.

1.3.2.1. Adjusting Radius Ratios in Binary Systems

Natural Brazilian opals contain a binary superlattice of two sizes of non-close packed silica spheres that are self-assembled into an ordered array.[43] Similar binary superlattices have also been synthetically fabricated using two sphere types with carefully controlled size ratios.[44-48] A relatively fast and simple method for preparing large-area, multilayered binary colloidal assemblies involves a horizontal deposition process.[49] By varying both number and size ratios between large and small polystyrene (PS) spheres, different packing configurations have been achieved. All configurations consisted of an fcc lattice of large spheres containing small spheres in the interstitial spaces. The small spheres were ordered into regular patterns on the surface of the colloidal crystal but exhibited reduced order further into the crystal.

By using a sequential self-assembly method, non-close-packed silica arrays could be obtained.[50] Silica spheres were deposited onto close-packed arrays of the PS spheres and became trapped in the void spaces between the larger PS spheres. The silica spheres had size ratios from 0.28–0.68:1 compared to the PS spheres. Removal of the PS spheres by

calcination exposed the silica packing structure at the PS sphere–silica sphere interface. The packing structure depended on the size ratio between the spheres, a ratio of 0.28:1 producing a disordered structure, 0.40:1 and 0.48:1 an LS_2 structure, and 0.68:1 an LS structure, where L represents large spheres and S small spheres (Figure 1.4). These structures were only observed at or near the interface with PS because, as multilayers of silica spheres were added, the spheres self-adjusted into close-packed arrays as if they had been grown on a flat substrate.

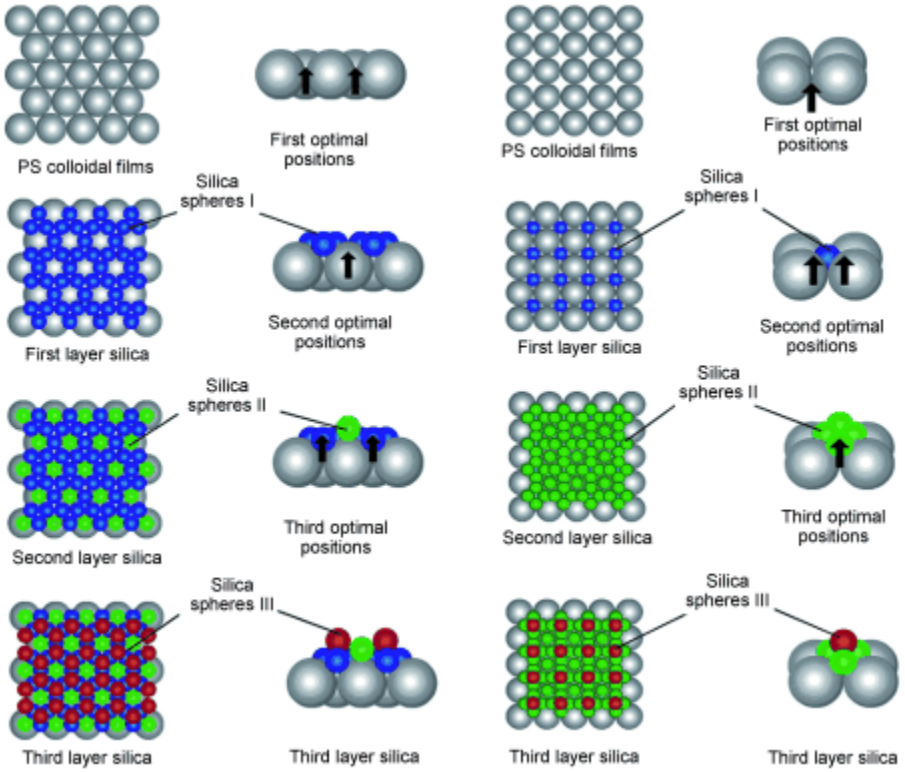

Figure 1.4. The packing mechanisms for small and large spheres into non-close-packed hexagonal (left) and rectangular structures (right). Reproduced from Zhou *et al*.[50]

1.3.2.2. Control through Electrostatic Interactions

Electrostatic interactions play a large role in the self-assembly of particles into crystalline and non-crystalline arrays. Electrostatic interactions between particles may be altered to direct the formation of these arrays. For example, surface charges can be introduced on nanocrystals by the addition of a variety of capping groups. The charge on polymer spheres can be altered by the choice of polymerization initiators or added surface functionalization. Unique structures can also be prepared by invoking attractive interactions between spheres. However, these interactions must not be too strong or random aggregation may occur as a result of irreversible binding. If a crystalline, self-assembled structure of oppositely charged colloids is targeted, a delicate balance must be maintained between the entropically favored close-packed arrangements and the electrostatically driven non-close-packed structures.

While the ordering of close-packed spheres requires a sufficiently repulsive interaction between particles, the extent of that repulsion can be controlled through the use of amphoteric groups on the surface of the particles. Such groups introduce a pH-value-dependent surface charge, which allows both the sign and magnitude of the charge to be tuned. In the case of amphoteric PS spheres, colloidal crystals formed from a drop-cast suspension during solvent evaporation were more highly ordered when the surface charge on the particles was increased through adjustment of the pH value.[51] By adding an equal amount of oppositely charged silica spheres, it was possible to force weakly charged PS into a crystalline lattice.

Ionic colloidal crystals of oppositely charged particles have also been fabricated by taking advantage of the inherent surface charge of colloidal spheres.[52] Colloidal particles were dispersed in a density- and refractive-index-matched organic solvent to eliminate the influence of van der Waals forces. By varying the salt concentration of the colloidal suspension, it was possible to reverse the small charges on the particles. Utilizing the fact that different batches of poly(methyl methacrylate) (PMMA) and silica spheres had different charge reversal points, suspensions could be created that contained oppositely charged particles at a specific salt concentration. These particles spontaneously assembled into a CsCl-type lattice (Figure 1.5). At higher volume fractions, a randomly packed array was obtained. When particles of differing diameters were used, different structures were assembled based on the size ratios. Arrays with LS_6 and LS_8 stoichiometry, as well as NaCl (Figure 1.5) and NiAs structures were obtained under separate conditions. The assembly of high-quality ionic colloidal crystals with long-range order, could be further facilitated by using a dielectrophoretic field to avoid gravitational separation of the binary colloids.[53]

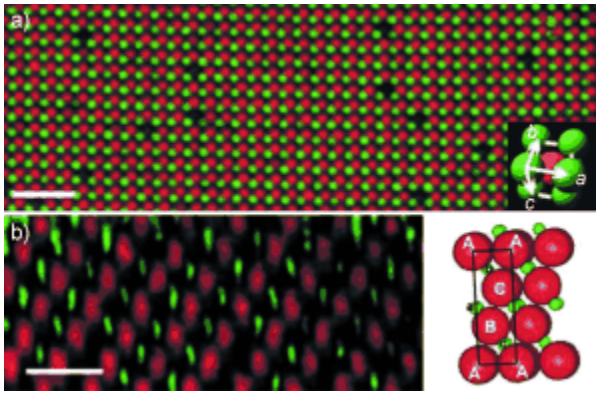

Figure 1.5. Confocal micrographs and models of a) a CsCl-type unit cell (scale bar=10 μm) and b) an NaCl-type unit cell (scale bar=8 μm). Reproduced from Leunissen *et al*.[52]

The charge on colloidal particles can be further controlled by taking advantage of the polarity of added fluorescent dyes.[54] A binary mixture of nearly identical PMMA spheres was prepared with a nonpolar solvent that was both density and refractive-index matched. The two types of spheres were distinguished from one another by the presence of one of two types of cationic fluorescent dyes. The sphere charges were tuned by the addition of free bromide generated through the catalytic decomposition of cycloheptyl bromide by a length of ferromagnetic wire. Because the point of zero charge for each type of particle was different, given the separate polarities of the two dyes, the particle charge could be tuned near the zero charge point, where one type of particle underwent a charge inversion. The now attractive particles then self-assembled into ordered arrays. Using particles of similar size but opposite charge, rhcp, CsCl, and NaCl structures were obtained with successively increasing differences in particle charge.

Although this thesis work involves the use of colloidal particles that have diameters between ca. 200 nm and 4 μm, lessons may be learned from the assembly of small nanoparticles. For self-assembled arrays of larger colloidal particles of differing charges,

interparticle interactions tend to be short range with respect to the dimensions of the particle. This feature allows them to self-assemble more easily without aggregation. However, when very small nanoparticles are considered, the overall interaction forces are much more long range with respect to the particle sizes. This property leads to aggregation in systems with oppositely charged particles. Greater control over the extent of these forces is required to stabilize these smaller nanoparticle arrays.

If ordered, self-assembled structures of small, less than 10 nm, oppositely charged nanoparticles are targeted, more attention must be given to the degree of electrostatic interactions in the suspension. Thus, a reduction of the screening layer is necessary to avoid aggregation of the particles. This decrease may be achieved by using smaller nanoparticles to stabilize the larger ones in a process similar to Debye screening. A diamond-like structure was created when gold and silver nanoparticles (4–6 nm) were coated with functionalized alkane thiols to endow them with opposite charges.[55] When these particles were mixed, they assembled into ordered sphalerite arrays in which each nanoparticle was surrounded by four nanoparticles of opposite charge. The arrays spanned distances of a few microns.

Multiple binary superlattices have been assembled from small nanoparticles using a combination of sterically stabilized semiconducting, metallic, and magnetic nanoparticles.[56-57] It was demonstrated that the stoichiometry of the resulting self-assembled structures was established by the electrical charges on the sterically stabilized particles and that entropic, van der Waals, steric, and dipolar forces served to stabilize the arrays. Crystals of types AB, AB_2, AB_3, AB_4, AB_5, AB_6, and AB_{13} resembling NaCl,

CuAu, AlB_2, $MgZn_2$, $MgNi_2$, Cu_3Au, Fe_4C, $CaCu_5$, CaB_6, and $NaZn_{13}$ structures self-assembled upon evaporation of solvent in a vertical assembly method. These self-assembled arrays were formed by tuning crystallite sizes and compositions (using combinations of oxides or other chalcogenides with metals) and modifying the surface charges of the nanoparticles with capping ligands.

1.3.2.3. Long-Range Self-Assembly of Non-spherical Particles

The shapes of colloidal particles also influence the packing patterns obtained through self-assembly. Different geometries of gold nanoparticles were assembled by solvent drop evaporation using concentrated aqueous dispersions of particles (Figure 1.6).[58] The particles were stabilized by cetyltrimethylammonium bromide (CTAB) to balance the attractive depletion forces and the repulsive electrostatic forces and thus induce formation of ordered arrays during solvent evaporation without random aggregation. When gold nanorods were used, smectic and nematic liquid-crystal-like assemblies were obtained; gold polyhedra produced hexagonally packed structures; nanocubes produced tetragonal arrays; and bipyramidal shapes were found to form either nematic arrays or a 3D superlattice that had positional ordering in multiple directions (Figure 1.6). By combining nanorods with polyhedra in a binary mixture under precisely adjusted CTAB concentrations, the system organized into a non-close-packed rectangular lattice of polyhedra with nanorod arrays filling the interstitial spaces. Pentagonal silver nanoparticle rods have also been observed to self-assemble into densely packed arrays upon drying.[59] For rods with a length:diameter ratio of less than 4:1, the particles had a hexagonal packing structure over a long range despite their pentagonal geometry. The

self-assembled layers of silver nanorods combined into a structure similar to a smectic mesophase.

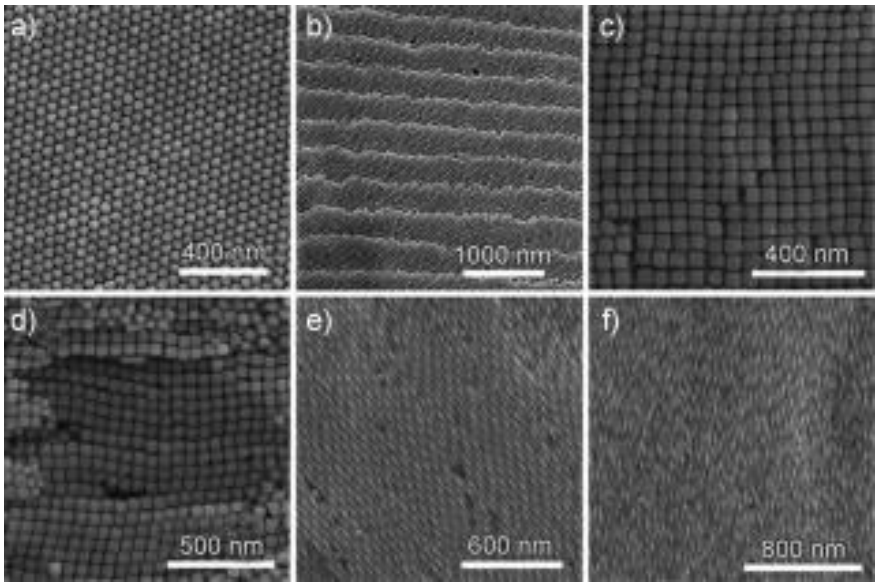

Figure 1.6. SEM images of ordered arrays of gold nanoparticles, including a) hexagonally packed Au polyhedra, b) hexagonally packed gold polyhedra with nearly periodic monosteps, c) tetragonally packed gold nanocubes, d) steps showing nanocubes in different layers, e) a superstructure formed from gold bipyramids and f) a nematic superstructure. Reproduced from Ming *et al.*[58]

A separate approach to direct the assembly of oxide nanocubes to construct 3D simple cubic arrays was discovered. This unique route was based on using colloidal crystals as molds to control particle shapes and organization.[60] High quality colloidal crystals composed of PMMA spheres approximately 400 nm in diameter were infiltrated with a precursor solution for a mixed titania/phosphate glass phase. After removal of the polymer spheres, an ordered porous structure formed initially, which, through controlled heating, spontaneously disassembled and evolved into individual particles with well-defined shapes.[61] Mediated by evaporation of the volatile phosphate phase, which possibly induced anisotropic capillary interactions,[62] the resulting nanocubes self-

reassembled into simple cubic arrays (Figure 1.7). Such self-reassembly represents a simple and low-cost approach to realize long-range, non-fcc packing for large colloids, and has been successfully applied to several different metal oxide/phosphate systems.[63]

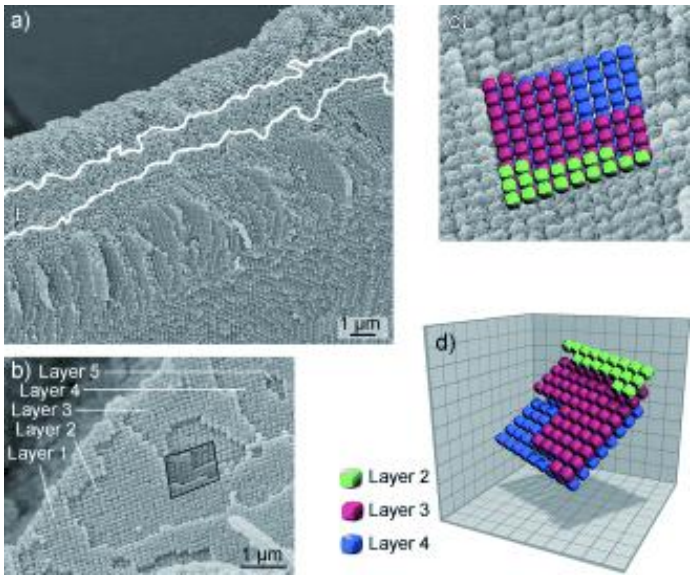

Figure 1.7. a) SEM image of a TiO_2/P_2O_5 sample (Ti:H_2O molar ratio=1:1.8) prepared by self-reassembly. The image shows the transition from connected nanocubes (A), disconnected, randomly distributed nanocubes (B), to the largest region with simple cubic packing of nanocubes (C). b) SEM image of an ordered nanocube array with five discrete layers of square packing. c) An expanded view of the outlined region from (b) overlaid by colored cubes to illustrate the simple cubic packing. d) A three-dimensional plot of the three colored layers from (c). Reproduced from Li *et al.*[61]

The various self-assembly techniques highlighted in this section illustrate the complex interparticle relationships that must be managed at the colloidal level. While fine control over colloidal crystallization is an important consideration for future applications, the work included in this dissertation deals with particles size ranges where facile self-assembly is achievable with the simple sedimentation of electrostatically charged, monodisperse, colloidal spheres. However, despite the ease of that technique,

the same considerations must be taken into account in order to understand the forces involved in producing high-quality templates.

1.4. Three Dimensionally-Ordered Macroporous (3DOM) Materials

1.4.1. Synthesis of 3DOM Materials

The synthesis of artificial opals through colloidal self-assembly results in brilliantly opalescent photonic crystals that contain stop bands in the visible region for a certain range of sphere sizes. However, the selection of materials that form monodisperse spherical particles is limited, thus restricting the potential applications of any self-assembled crystal. In order to circumvent this limitation, these synthetic opals can also be used as sacrificial templates to create the inverse of the opal structures. The inverse opals retain the photonic properties of the opal template but can be fabricated using various inorganic oxides,[33, 35, 64-72] metals,[73-79] polymers,[80-83] and hydrogels.[84-85] This facile process generally involves filling the interstitial spaces between the sphere array with a precursor material and then processing the composite to convert the precursor into the target material. Removal of the template via thermal treatment or dissolution then produces the inverse structure of the opal, which is referred to as a three-dimensionally ordered macroporous (3DOM) material. 3DOM materials retain the periodic arrangement of high and low dielectric zones and so also act as photonic crystals.

3DOM materials were first reported in the late 1990's.[33, 35, 72, 80] These materials are characteristically high in surface area and consist of an extended network of interconnected pores that have applications in several areas, such as catalysis,[86-94] optical

and electronic sensing,[64, 95-99] energy storage,[100-105] and other photonic applications.[40, 65, 106] The continuous porosity of the material is owed to the templating procedure used to create them. 3DOM structures are produced through the use of an ordered colloidal crystal array of monodisperse spheres as a template. These colloidal crystals are typically composed of polymer or silica spheres[66, 79, 107-108] A main requirement of a template material is that it is easily removed from the structure without harming the framework of the final product. Polymer spheres are typically removed by thermal treatment or solvent removal while silica spheres require the use of hydrofluoric acid (HF) or strong base to remove the template from the structure.

Most 3DOM materials in this dissertation were templated from colloidal crystals that were formed through gravity sedimentation or centrifugation of a colloidal suspension. A typical colloidal crystal formed in this manner exhibited domain sizes larger than tens of microns with scattered point and line defects. A representative example of a typical colloidal crystal can be seen in Figure 1.8.

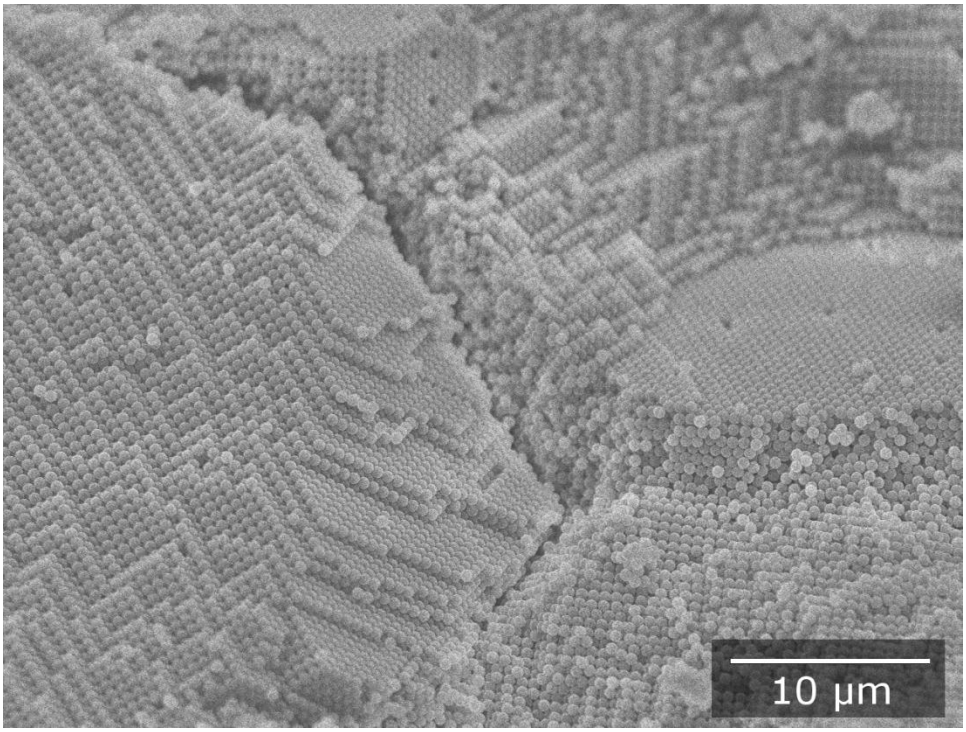

Figure 1.8. An SEM micrograph of an fcc close-packed array of PMMA spheres used in colloidal crystal templating to create 3DOM materials.

After a colloidal crystal template is fabricated, it is then infiltrated with an appropriate precursor material through either liquid or vapor phase infiltration. Depending on the desired final product, the precursor is chosen based on the ease of infiltration into the void spaces of the template and the quality and stability of the final structure. Common materials include titania,[35, 65, 72] zirconia,[72, 107-108] silica,[33, 72, 109-110] carbon,[111-113] and tungsten.[72, 114]

After infiltration of the colloidal crystal, the precursor is converted into the desired product by processes such as calcination, pyrolysis, chemical etching, solvent extraction, or reduction.[40, 114-116] Conversion to the final 3DOM product and sphere removal is most commonly done in one thermal step in which the polymer is combusted in air or

depolymerized under N_2. This thermal process also converts the infiltrated precursor material into a solid form. In cases where silica spheres are used, a two-step etching and thermal treatment process is common.[5,40] The process of templating a 3DOM material from colloidal crystal to completed 3DOM structure can be seen in Figure 1.9.

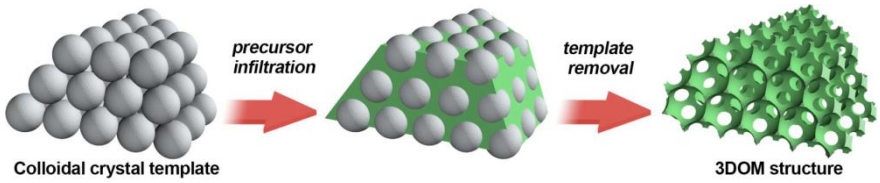

Figure 1.9. Figure depicting 3DOM synthesis. A colloidal crystal is infiltrated with a precursor material. The precursor is converted into the final product and the sphere template is removed to give a completed 3DOM structure. Reproduced from Stein *et al.*[40]

The resulting material is a periodic array of air spheres with walls made of the precursor component material (Figure 1.10). The walls are typically on the order of tens of nanometers in thickness, while the air sphere voids usually range from a few hundred nanometers to 2–3 microns in diameter, depending on the original template size and the thermal shrinkage properties of the solid portion. In a well-ordered 3DOM material formed from a low-defect colloidal crystal, the void spaces are all interconnected due to pore windows throughout the structure where the colloidal crystal particles were previously in contact.

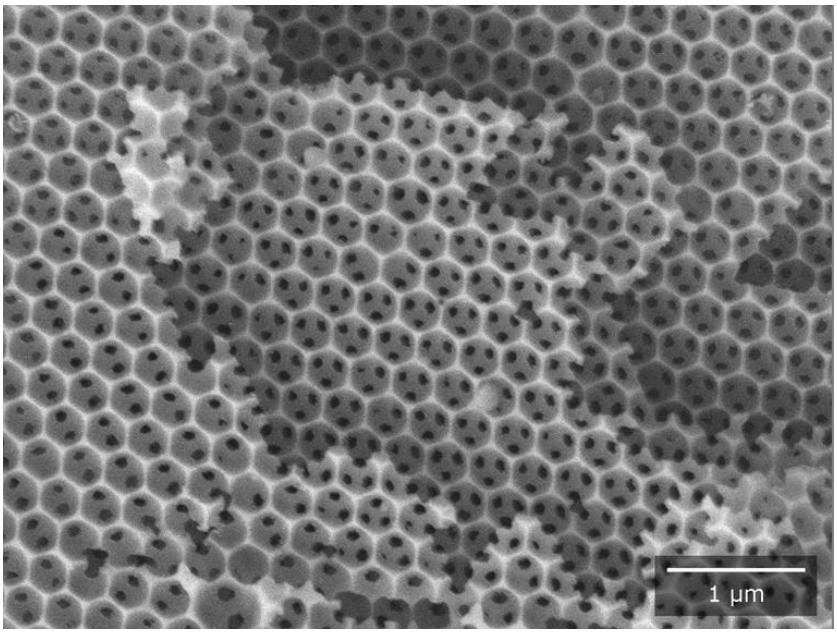

Figure 1.10. Scanning electron micrograph of 3DOM zirconia.

1.4.2. 3DOM Material Stop Bands

The spectral position of photonic crystal stop bands that arise based on Bragg diffraction from specific photonic diffraction planes within a 3DOM material can be approximated by a combination of Bragg's law and Snell's law[117-119] (Equation 1.2) with the d_{hkl} termed defined in Equation 1.3 for an fcc lattice:

Equation 1.2

$$\lambda = \frac{2d_{hkl}}{m}\sqrt{{n_{avg}}^2 - sin^2\theta}$$

Equation 1.3

$$d_{hkl} = \frac{D\sqrt{2}}{\sqrt{h^2 + k^2 + l^2}}$$

where λ is the stop band peak wavelength, d_{hkl} is the spacing of diffraction layers, n_{avg} is the average refractive index of the material, θ is the angle of incident light with respect to the surface normal, m is an integer representing the order of diffraction, D is the distance between adjacent pore layers, and h, k, and l correspond to the Miller indices of a given diffraction plane. In the case of the randomly oriented bulk powders obtained for colored materials in this dissertation, the value for θ averages to $\theta = 0°$ for normal incidence, and Equation 1.2 simplifies to produce Equation 1.4.

Equation 1.4

$$\lambda = \frac{2d_{hkl}}{m} n_{avg}$$

Stop bands can be observed in 3DOM materials by performing UV-vis spectroscopy if the bands lie within the instrumental range. The stop bands present in a given spectrum appear as areas of high reflectance consisting of an approximately Gaussian peak. A stop band is present for multiple sets of diffraction planes throughout the material. For most fcc photonic crystals with stop bands in the visible region, the only diffraction peaks that are observed in the visible spectrum according to UV-vis spectra are the (111) and (200) planes. Based on multiplicity rules, the main reflection comes from the (111) diffraction planes. The (200) stop band is weak and is often encompassed by the (111) reflection. However, for materials with a (111) stop band that is sufficiently red-shifted into the longer-wave visible region, it should be noted that other diffraction peaks, such as the (220) peak, can enter the visible region and influence color properties (Figure 1.11).

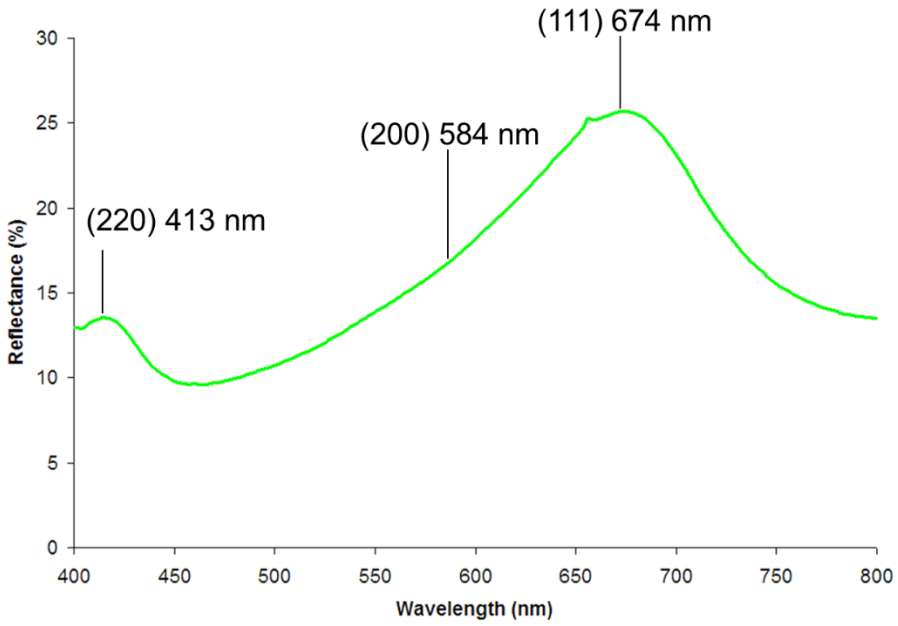

Figure 1.11. UV-vis spectrum of inverse opal silica with a (111) stop band in the red region. A strong second reflection (220) can be seen at shorter wavelengths. A weak shoulder on the (111) can be identified as the (200) diffraction peak. The positions of the (200) and (220) peaks were calculated using the (111) position and an established fill fraction value for the solid component.

The ability to template 3DOM materials with polymer spheres enables a high degree of tunability for photonic properties. The polymer spheres are typically synthesized using an emulsion polymerization technique, which allows for variability in the size of the spheres that are produced. Since the size of the template spheres determines the final size of the 3DOM structure pores, the stop band positions of the material can vary greatly.[120] Figure 1.12 shows the wide range of visible bandgaps in 3DOM ZrO_2 that can be achieved using various diameters of monodisperse colloidal spheres. Using a solvent to infiltrate the pores is also a way to increase the wavelength that is reflected because the addition of a solvent will affect the n_{avg} term in Equation 1.2. When the pores are filled with solvent instead of air, the average refractive index of the material increases, red-shifting the stop band position.[64]

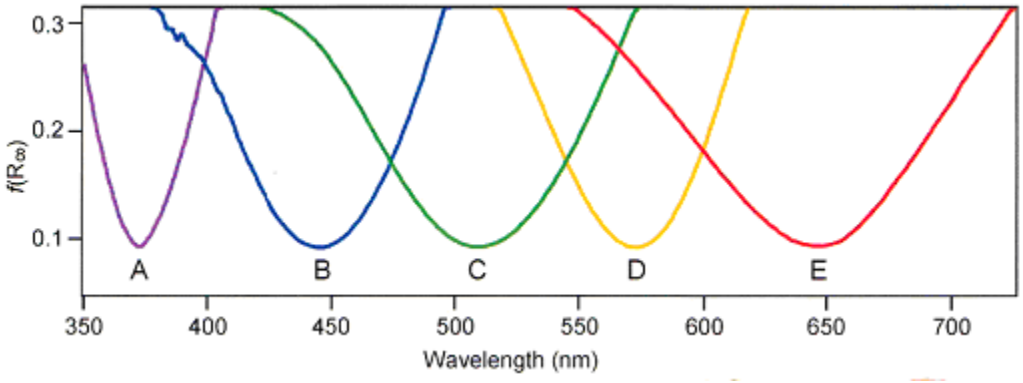

Figure 1.12. 3DOM zirconia powders. Diffuse-reflectance UV-vis. A) ZrO_2 (200), B) ZrO_2 (250), C) ZrO_2 (285), D) ZrO_2 (250) filled with methanol, E) ZrO_2 (285) filled with methanol. Numbers in parentheses represent pore sizes. Reproduced from Schroden *et al.*[64]

While the primary (111) stop band position of a photonic crystal dictates the color expressed by the material, the shape of the stop band (as observed in UV-vis spectra of photonic crystals) governs the purity and intensity of that color. The shape of the peak can be broken down into two vital characteristics, the bandwidth, and the reflection intensity.

The bandwidth of the stop band in a photonic crystal affects the color expression of the crystal by including or excluding the wavelengths around the stop band position. If the bandwidth is small, few wavelengths are included within the stop band and the color expression will be limited to a small portion of the visible spectrum. The structural contribution to the perceived color of the material is limited to those few, grouped wavelengths, allowing the manifestation of specific colors found in the electromagnetic spectrum. If the stop band is broad, however, the perceived color is more influenced by the wavelengths around the stop band position, leading to color-mixing as the stop band extends out from the center. Kanai at al.[121] have proposed that increases in the width of

the stop band in a photonic crystal are likely the result of inhomogeneities in *d*-spacing or refractive index within the crystal layers, with the values for these properties fluctuating around a value that represents a perfectly homogeneous crystal. This fluctuation produces an effect that can be approximated as several overlapping stop bands with small changes in n_{avg} and d_{hkl} giving rise to small shifts up or down in the spectrum, but always centered about the homogeneous crystal stop band.

The shape of the stop band is also dictated by the diffraction intensity,[118] which determines the relative magnitude of the stop band. The ratio of diffraction intensity (I_H) and incident intensity (I_0) for a set of planes *H* can be expressed as

Equation 1.5 $$\frac{I_H}{I_0} = L - (L^2 - 1)^2$$

where

Equation 1.6 $$L = y^2 + g^2 + \sqrt{(y^2 - g^2 - 1)^2 + 4g^2y^2}$$

with the components *y* and *g* described as

Equation 1.7 $$y = \frac{\psi_0' + 2\left(\frac{\lambda}{\lambda_B} - 1\right)sin^2\theta}{K_{\sigma,\pi}\psi_0' f}$$

and

Equation 1.8 $$g = \frac{\psi_0''}{K_{\sigma,\pi}\psi_0' f}$$

In these expressions, λ is the wavelength of the incident light, ψ_0'' is a term that accounts for losses in intensity caused by scattering, and, for polarizations normal or

parallel to the diffraction plane, K_σ = 1 and K_π = cos2θ can be used, respectively. The scattering factor (*f*) for spherical particles of radius *a* is provided by

Equation 1.9
$$f = \frac{3}{u^3}(\sin u - u\cos u)$$

with

Equation 1.10
$$u = \frac{4\pi a}{\lambda}\sin\theta$$

These equations show that the intensity of the stop band is largely dependent on refractive index contrast of the dielectric materials, with high contrast increasing the intensity of the reflection.

1.4.3. 3DOM Materials for Color Applications

1.4.3.1. 3DOM Materials as Pigments

The structural color of 3DOM materials is an important advantage of photonic crystal-based pigments over traditional pigments that are based on light absorption through electronic effects. For conventional pigments, each color requires the use of one or more specific compounds. Photonic crystals, however, employ a structural color mechanism that enables the use of a single material in order to achieve all spectral colors through the tailoring of the periodic spacing in the structure. The use of light-stable materials in photonic crystals also prevents photo-bleaching, which is a common cause for the degradation of color in conventional colorants.

For structurally-colored pigments, 3DOM materials also offer some advantages over other photonic pigments. Currently used photonic pigments made from layered clays or

other types of Bragg stacks are often fabricated using top-down, layer by layer techniques.[122-124] The facile, bottom-up approach to synthesizing 3DOM materials allows for a high degree of control over long-range periodicity and does not require multiple synthesis steps to construct each layer. In finely powdered materials and with diffuse light sources, the multi-dimensionality of 3DOM materials also helps to mitigate the high angle dependence seen in one-dimensional Bragg stack photonic crystals by presenting diffraction planes from multiple crystal orientations and averaging the photonic angle-dependent colors.

1.4.3.2. 3DOM Materials as Dynamic Optical Sensors

3DOM colored materials also possess another advantage over traditional pigments in that they can function as dynamic and reversible optical sensors under certain conditions using specialized materials. Such optical sensors have been realized by employing opaline materials in the past.[125-126, 127-128, 129-130]

While 3DOM materials can be used in many of the same ways as opaline photonic crystals for temperature and infiltration-induced lattice changes in hydrogel and polymer compositions,[131-139] 3DOM materials have the greatest advantage over opaline materials in their response to refractive index changes. To illustrate this, Equation 1.4 can be used to estimate the difference in stop band shifts for a dry silica opal and a dry silica inverse opal after infiltration with ethanol (refractive index of silica=1.455, ethanol=1.333). Using the values for perfect packing and a d_{hkl} of 250 nm for both structures, the stop band for the opal shifts by 43 nm while the inverse opal experiences a shift of 123 nm to

longer wavelengths, resulting in a sensor that is more sensitive to slight changes in refractive index.

In addition to the morphological advantage of having at least three times the void space as photonic crystal opals, 3DOM materials also offer much greater variety in potential structural compositions. The ability to choose from a larger pool of potential materials enables researchers to increase the refractive index contrast in a photonic crystal by employing materials with a higher value of *n*. This allows for much higher stop band intensities and increased coloration, opening up opportunities for color-changing pigment applications.

The use of higher refractive index materials beyond polymers and hydrogels for opaline photonic crystals enables syntheses of high refractive index photonic crystals that do not undergo lattice changes, allowing for purely refractive index-induced solvochromic changes of a much greater magnitude than those seen in opaline photonic crystals. Also, the greater thermal stability and, often, good chemical stability of metal or metal oxide-based inverse opals allow for dynamic color changes in a wider array of conditions and environments.

The first example of a solvent-induced color change in 3DOM materials was put forth by Schroden et al.[64] Colored 3DOM powders of various metal oxides were synthesized with stop bands in the visible spectrum. The powders were then infiltrated with various solvents while the stop band position was monitored by UV-vis spectroscopy (Figure 1.13). The 3DOM metal oxides exhibited a much larger shift in position than similar studies by Bogolomov et al. on opals of similar composition.[140-141] Such a large shift in

color is a product of having a larger void space capable of accommodating solvent. With >74% of the structure being composed of air with a refractive index of 1, replacing that fraction of space with solvents of various refractive indices (all larger than 1) raises the n_{avg} of the photonic crystal beyond what would be possible with an opal structure. This increases the potential optical signal shift.

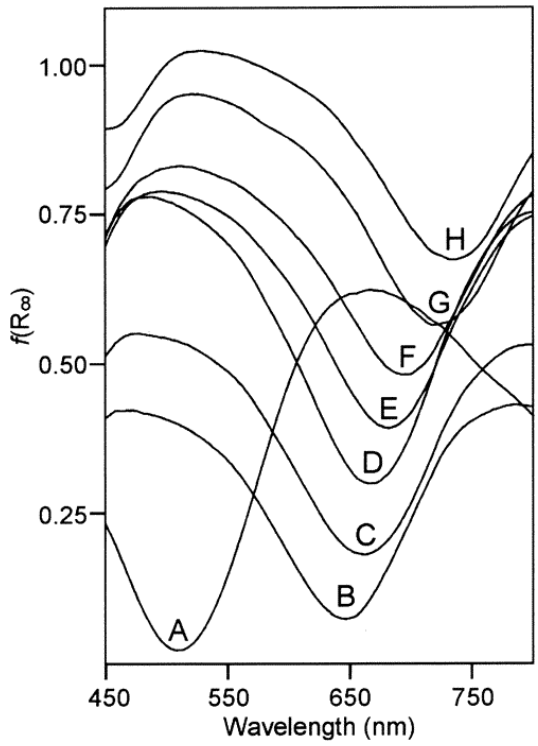

Figure 1.13. Diffuse reflectance UV-vis spectra of 3DOM zirconia with different infilling material. (A) Air n = 1 , (B) methanol n = 1.329, (C) ethanol n = 1.360, (D) 2-propanol n = 1.377, (E) tetrahydrofuran n = 1.407, (F) DMF n = 1.431, (G) toluene n = 1.496, and (H) 1,2-dibromoethane n = 1.538. Reproduced from Schroden *et al.*[64]

The response of a colored 3DOM material to infiltration can be further tuned, as in the case of silica inverse opals modified to create regions of different wettability within the crystal (Figure 1.14).[142-143] Upon infiltration with a solvent, only regions that are wettable above a certain threshold allow for the infiltration of the solvent. The wetted

areas are revealed by their stop band shift from the refractive index change in the pores of the material. Using this technique, it is possible to create patterned photonic crystals with regioselective optical switching that can function as selectively exposable pigmentation. This sort of discriminatory stop band shifting has numerous applications for sensing of liquids with a specific surface tension.

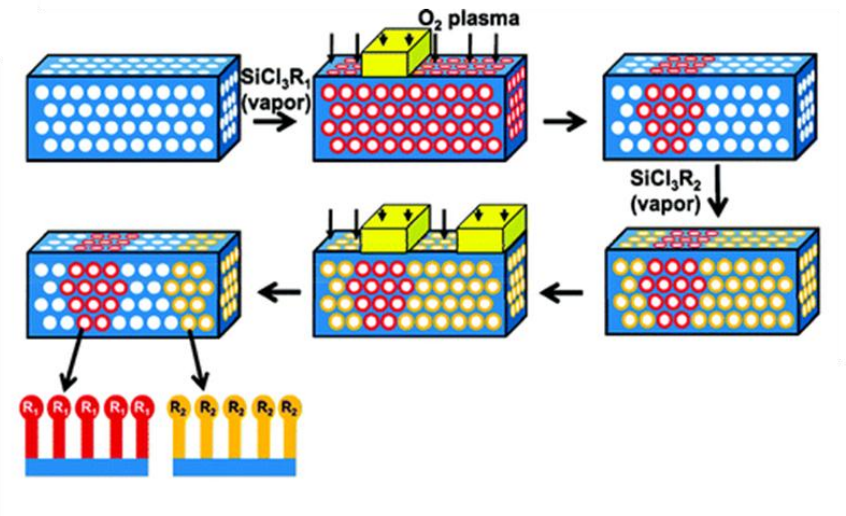

Figure 1.14. Schematic of the procedure for introducing variations in wettability within a photonic crystal. Repeated exposure to alkylchlorosilane vapors followed by oxygen plasma etching while using poly(dimethylsiloxane) masks allows for the creation of different areas of wettability. Reproduced from Burgess *et al.*[142]

This selective, solvochromic tunability of 3DOM materials over wide wavelength ranges provides an advantage in optical sensing over opaline photonic crystals. Sensors that can detect analytes in liquids or gases, or even phase detection sensors have been realized by harnessing the sensitivity and functionalizability of these inverse opal structures. Numerous examples of these sensors that detect shifts in stop band position with changing refractive index have been published.[96, 144-145]

More sophisticated materials that tailor these optical sensors for detection of specific analyte compounds or selection of specific solvents from a mixture have also been realized. A 3DOM optical sensor based on a phenolic resin exhibited both superoleophilic and superhydrophobic properties, allowing it to act as a hydrocarbon sensor that does not suffer from the interference of water or other polar solvents. The sensor exhibited a linear response in stop band position with increases in refractive index when exposed to several different petroleum components such as octane, tetradecane, hexadecane, diesel oil, wax oil, and isopropylbenzene. The uptake of solvents into the 3DOM structure was reversible by washing with octane and drying.[146]

Inverse opal optical sensors can be further specialized for certain analytes by attaching specific functional groups to the surface of the material. For example, by attaching specific probe antibodies, it is possible to create functionalized inverse opal photonic beads that exhibit average refractive index changes upon the binding of analyte proteins. The large void space present in the inverse opal increases the throughput of potential analyte throughout the structure and improves the response times of such devices.[147]

The large void space present in 3DOM structures is also ideal for infiltration with liquids whose own refractive index can be dynamically tuned. Optically birefringent nematic liquid crystals infiltrated into an inverse opal can provide instantaneous dynamic tunability through both electrooptical switching and a thermally-driven phase transition of the liquid crystal.[148] An electro-optic shutter effect was realized by switching the

orientation of nematic molecules inside an inverse opal structure using an external electric field.

Rapid photo-induced switching has been realized using liquid crystal infiltration into an inverse opal lattice. Photochromic liquid crystal azo dyes were incorporated into a silica inverse opal and irradiatiated with UV light. A *cis-trans* isomerism induced by the irradiation caused a nematic-to-isotropic phase transition in the liquid crystal. The reverse was accomplished upon irradiation with visible light. In the nematic phase, the dielectric constant of the liquid crystal was not uniform throughout each inverse opal pore due to random orientations of the liquid crystal. This interrupted the periodicity of the Bragg diffraction planes, and a strong stop band was not observed. Upon irradiation and a phase change to the isotropic phase, anisotropy was lost, the dielectric constant became uniform throughout the material, and a stop band was produced. This same experiment was attempted with a silica opal structure, however, the small void space limited the effects that could be observed with the photo-induced switching.[149]

1.4.4. Color Optimization in 3DOM Materials

In order to increase the magnitude of the optical signal in photonic sensors or increase the coloration of photonic pigments, structural color optimization in 3DOM photonic crystals is an important step toward achieving the full potential of these materials. A simple strategy towards improving the optical signal from a material standpoint is to increase the refractive index contrast between the high and low dielectric portions of the crystal. This serves to increase the intensity of the stop band, improving response intensity. In sensor applications, little can be done about the refractive indices of the

chosen analytes. Therefore, higher *n* materials must be used in order to increase the magnitude of contrast between diffraction planes. By increasing the reflective response of these photonic crystals, it is also possible to retain a higher stop band intensity after the decrease in reflectance associated with the infiltration of liquids. These infiltrations reduce the refractive index contrast between the high and low dielectric portions of the crystal and decrease the intensity of the photonic reflection. However, care must be taken to avoid strong optical absorption by the material itself in the stop band region, lest electronic transitions affect the intended color properties.

In the case of 3DOM materials, the enhancement of the stop band can be achieved by increasing the refractive index contrast of the wall material. With a highly periodic structure, complete band gaps are possible for 3DOM materials with an index of refraction contrast of 2.8 or greater.[150] Towards this end, high refractive index inverse opals have been prepared using materials such as tantalum nitride,[151] silicon,[152] and germanium[153] in order to achieve a complete band gap.

Structural modification can also be used to improve the optical properties of inverse opals. Most high *n* inverse opals have very limited penetration of light into the structure due to visible light absorbance from the structure walls and limited window sizes between pores. By enlarging the windows and opening up the structure for penetration of photons, truly 3-dimensional optical effects start to appear rather than just surface effects commonly seen in structures with small window sizes (Figure 1.15).[154]

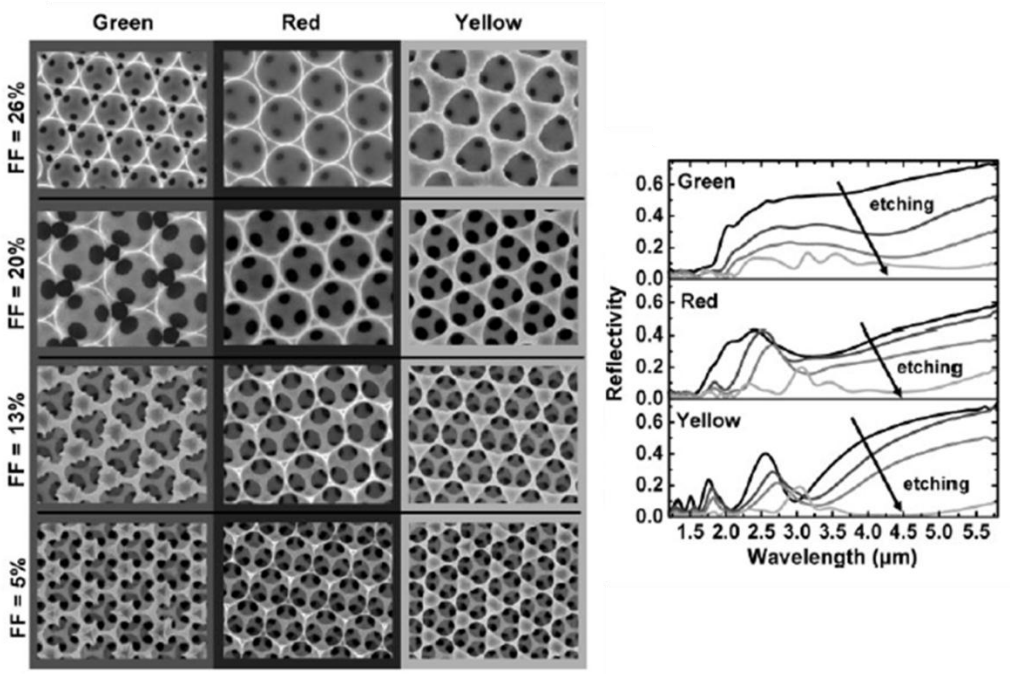

Figure 1.15. Left: SEM images of Ni inverse opals with varying fill fraction (FF). Right: Reflectivity as Ni FF reduces for each color presented. Spectra with black lines represent 26% FF with lighter lines representing decreasing FF. Reproduced from Yu *et al.*[154]

For applications such as pigmentation, where intense and vibrant colors are desired, increasing the reflectance of the photonic crystal through refractive index contrast is not the only strategy to use in order to increase the coloration of the material. Some potential materials for 3DOM photonic crystals may not be suitable for pigmentation due to their low or high absorbance, with low absorbers appearing mostly white and high absorbers appearing mostly black. Both still manifest opalescent color, but the effect is largely trumped by the materials' absorbance properties. It has been shown that predominantly white, opalescent, polymer colloidal crystals can become more intensely colored by the controlled incorporation of an absorbing material with the structure.[155] The absorbing material acts to decrease the number of photons that are scattered out of the crystal that

are not part of a diffraction event, lowering the reflectance spectrum of the material at all wavelengths, allowing easier visual perception of the stop band wavelengths. Several functional materials employing this concept have been recently synthesized. They exhibit a dramatic enhancement of color intensities as a result of the addition of an absorbing substance, usually carbon black or carbon nanoparticles.[156-161]

The effects of the amount of carbon black incorporated into a polymer opal structure were also studied, showing an increase in maximum stop band reflectance above the background reflectance with the addition of a small amount (0.05 %wt) of carbon black. A maximum in stop band peak height was reached at 0.15 %wt, with subsequent additions of carbon black reducing the intensity of the reflectance at the stop band by absorbing photons even at the stop band (Figure 1.16). The reduction in scattering due to the added absorber can be seen clearly in Figure 1.16 by the reduction in background reflectance relative to the stop band peak.[156] This effect can also be seen in colloidal sphere arrays using magnetite particles that provide a dark background without the addition of an absorber.[162] The incorporation of an in-situ carbon absorber into 3DOM materials and the optical effects that results from the incorporation are discussed in Chapter 2 of this dissertation.

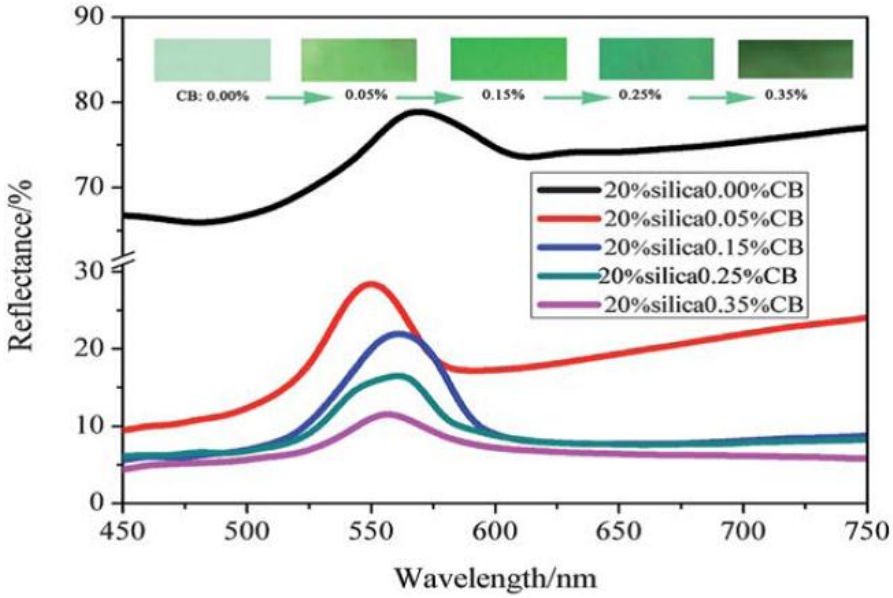

Figure 1.16. Reflectance spectra of colloidal crystal films consisting of 241 nm polymer spheres with differing %wt. composition of carbon black. Reproduced from Shen *et al*.[156]

1.4.5. 3DOM Photonic Crystals For Non-Color Applications

3DOM photonic materials with stop bands outside of the visible spectrum are also of interest for various applications. By coupling the semiconductor band edge absorbance properties of certain 3DOM compositions with the reflectance properties of a photonic stop band, a material could potentially be synthesized that has UV-blocking properties beyond the material properties of commercially available, physical UV blockers. To date, no research has been published on this topic.

While dielectric materials are often used for photonic crystals, metallic materials can also be used with interesting results. Most of the focus in the field of periodic photonic crystals has dealt with dielectric materials because their absorption in the optical range is low, which is desirable for optical applications such as photonic circuits and waveguides. Metallic photonic crystals have been considered inferior for these applications because

they can exhibit significant absorbance as optical frequencies are increased.[163] However, for thermal emission applications, metallic photonic crystals have other properties that can be very useful. It has been shown that if the metallic photonic crystal is part of a network such as a 3DOM structure, a different type of photonic band gap arises. If a networked metallic structure is considered, the photonic band gap theoretically can broaden and extend to the zero frequency level, effectively forbidding all included frequencies from propagating through the crystal (Figure 1.17). Because of the wide range of affected wavelengths, the precise symmetry of the crystal is no longer as vital as it is in the case of dielectric crystals.[163]

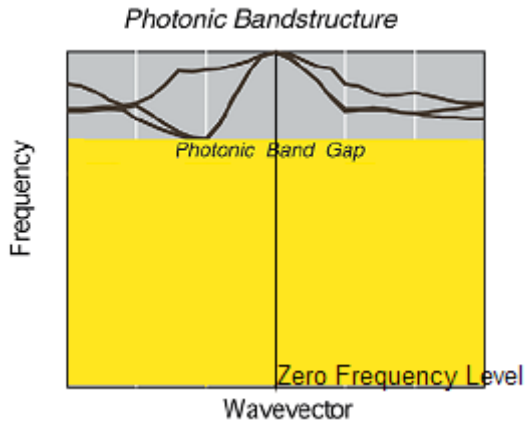

Figure 1.17. Cartoon of a metallic photonic crystal band diagram. The band gap extends down to the zero frequency level. All frequencies in the band gap are forbidden from propagating inside of the structure. Modified from John *et al.*.[9]

The stop band responsible for reflection of electromagnetic radiation in a photonic crystal can also modify the emission of radiation from the material.[115, 164-165] Therefore, if a photonic material possesses a stop band at a certain spectral position, any emission from that material at the stop band position will be reduced. This phenomenon can

potentially be harnessed in order to create specialized thermophotovoltaic emitter/absorber materials. By tailoring the emission of these materials in the IR range of wavelengths, these metallic photonic crystals can be made to emit in specific ranges of IR radiation upon heating through renewable sources such as solar and waste heat from existing energy conversion pathways. The emission spectrum can be matched with specific diode materials in order to maximize the energy conversion while avoiding emission in unusable wavelengths. These thermophotovoltaic materials can be used as renewable energy sources if they are heated through solar mirrors or use waste heat from existing energy pathways.

1.5. Thesis Organization

The subsequent chapters in this dissertation outline the synthesis and characterization of several 3DOM compositions for various optical and photonic applications. The following two chapters involve the synthesis, characterization, and optimization of colored 3DOM pigment powders. Chapter 2 will address the important role of light-absorbing carbon as a contrast agent within 3DOM structures. Investigations into various synthesis parameters that can provide in-situ control over the presence and magnitude of this contrast are described along with a method of incorporating carbon species within 3DOM structures through an ex-situ process. Chapter 3 then describes the synthesis of 3DOM SiO_2 for colored pigment applications. An emphasis is placed on the influence of heating temperatures on the final unit-cell parameters of the photonic structure which allows for fine-tuning of the structural color. Also demonstrated is the unique additive color-mixing mechanism of 3DOM colored pigments.

Chapter 4 discusses the use of 3DOM TiO_2/SiO_2 composites for UV blocking applications. The main goal of these studies is to extend the UV blocking properties of materials used for UV protection by placing photonic stop bands at specific wavelengths in order to improve UV coverage. In addition to this, methods of eliminating solvent infiltration into 3DOM pores are discussed.

The synthesis of metallic photonic thermophotovoltaic emitter materials is investigated in Chapter 5. Several issues in the production of these materials are addressed, such as the challenges of creating colloidal crystal-templated materials with stop bands in the IR and concerns about the thermal stability of metallic photonic crystals at high temperatures.

Chapter 2

The Effects of Integrated Carbon as a Light Absorber on the Coloration of Photonic Crystal-based Pigments

Parts of this chapter are reproduced with permission from ref.[166]

2.1 Introduction

Color is an important means of visual expression and impacts much of our lives. Colored materials are used for decoration, communication, guidance, organization, a means of warning, and other applications.[7] Most dyes and pigments used to impart a material with color are based on light absorption via electronic transitions between energy levels that are separated by an amount of energy corresponding to the visible portion of the spectrum. The resulting colors are therefore a function of the composition of the dyes and pigments and their structures at an atomic and molecular level. In the case of pigments, which are insoluble colorants in the medium of consideration, light scattering plays an additional role in their appearance.

Still less ubiquitous in technological applications are materials that display structural color. Here, the coloration arises not from electronic transitions but from structural features on a length scale that is on the order of wavelengths in the visible range. Interaction of light with these structures results in interference and diffraction effects that can produce a colored appearance, often with a strong dependence on the viewing angle. Technologically, these effects are exploited, for example in color-shifting interference pigments or pearlescent pigments.[167] Several examples of structural color can also be found in nature. Certain species of butterflies and invertebrates as well as multiple types of flora possess color resulting from the periodic arrangement of features on their surfaces.[10-12] Natural examples can also be found in minerals such as labradorite.[13] The most well-known mineral example is probably the natural opal which, despite being

composed of optically transparent silica spheres, is able to express a wide range of colors caused by the reflection of light due to its periodic structure.[14]

One such photonic crystal structure, a 3DOM material, is described in Chapter 1. The color properties of 3DOM photonic crystals allow for their use as photonic pigments. For applications targeting 3DOM pigments with specific structural colors, the position of the stop band is approximated by a combination of Bragg's law and Snell's law (Equations 1.2-1.4).

This relationship points out an important advantage of photonic crystal-based pigments over traditional pigments that are based on light absorption through electronic effects. For conventional pigments, each color requires the use of one or more specific compounds. Photonic crystals, however, employ a structural color mechanism that enables the use of a single material, in order to achieve all spectral colors through the tailoring of the periodic spacing in the structure. The use of light-stable materials in photonic crystals also prevents photo-bleaching, which is a common cause for the degradation of color in conventional colorants.

In order to create vividly colored 3DOM pigments, it is necessary to optimize their color characteristics. Long-range structural order, as well as regular periodicity of pore walls, is important in order to produce intense stop bands. Stop band intensities can also be enhanced by employing materials with high indices of refraction such as TiO_2 or ZrO_2. In previous studies by Schroden *et al*., brilliantly colored 3DOM ZrO_2 powders were synthesized using an acetate precursor and heating the colloidal crystal template/precursor composite to 450 °C in an air/nitrogen mixture.[64] However, when

3DOM ZrO_2 was prepared using an alkoxide precursor with heating to 575 °C in air, a white powder was obtained. Both structures were highly periodic at the length scale of macropores, and in both materials the periodic ZrO_2 skeleton was composed of interconnected crystalline grains. After analyzing the grain sizes of each sample (1–2 nm and 28 nm, respectively), it was concluded that the difference in microstructure was responsible for the different visual appearances of the samples. Random light scattering from the rougher wall surfaces was considered to be a cause for the reduced coloration of the second sample. However, later observations have provided evidence that the wall roughness in 3DOM materials may not be the major factor influencing color intensity. For example, 3DOM ZrO_2 coated with Ru-loaded zeolite nanoparticles exhibited a high degree of surface roughness,[168] yet the material was strongly opalescent with green structural color (Figure 2.1). Therefore another cause may be responsible for the variation in color intensities.

Figure 2.1. Photographs of (A) 3DOM sulfated ZrO_2, (B) the same sample in which the surface was coated with a polyelectrolyte, (C) the material, surface coated with NaY zeolite nanoparticles, (D) the zeolite-coated sample after partial ion exchange with Ru^{3+} and reduction of Ru. As illustrated in Figure 1A–D of Wang *et al.*,[168] samples A and B have smooth macropore surfaces, C and D have highly textured. In these samples, the sample color and color intensities are therefore not correlated with surface roughness of the 3DOM skeletal walls. The samples exhibit reversible color shifts when infiltrated with isopropanol, confirming that the colors are photonic. Reproduced from Wang *et al.*[168]

Considering the polymer-sphere templated synthesis of 3DOM ZrO_2 using precursors containing carbon, incomplete combustion of the organic components may leave carbon in the heated 3DOM material. Such carbon inclusions would provide a light-absorbing background that can contribute to increased coloration of the material. In the case of opal-type structures, it has recently been shown that addition of carbon nanoparticles can enhance the photonic coloration of the materials.[155-161, 169] For example, Aguirre *et al.* found that white opalescent polymer colloidal crystals became uniformly and strongly colored after the addition of carbon black that acted as an absorber within the structure.[155]

The color could be tuned by the size of the polymer spheres, and its intensity depended on the carbon loading up to a few wt% of carbon, above which the materials became black. The inclusion of this absorber species served to prevent the scattering of stray light and limited the reflected light to coherent light generated by the stop band alone. Interestingly, carbon nanoparticles were not uniformly distributed throughout the opaline material and were in direct contact with the photonic crystal particles only in a few regions.

Given their brilliant colors, 3DOM ZrO_2 particles are potential candidates as novel pigments with excellent thermal stability and chemical resistance. Because of the large difference in optical properties of these materials, depending on processing conditions, a proper understanding of the source of the different color intensities is important. In the current work we will test the hypothesis that in-situ generated carbon is responsible for enhancing color intensities of 3DOM ZrO_2 materials. Multiple syntheses are discussed in this chapter, in which the intrinsic carbon content of the products is controlled by employing different heating temperatures and atmospheres and correlated with color and color intensities. Grain size effects will also be considered. These studies are then followed by a controlled, systematic re-addition of carbon to colorless 3DOM ZrO_2 in order to provide further information about the effect of absorber content on the coloration of 3DOM materials. It was found that the light absorber plays a key role in imbuing these materials with intense structural color. The ability to fine-tune photonic color characteristics through modulation of the absorber content will be an important consideration in future developments of 3DOM pigments and related pigments with structural color.

2.2. Experimental

2.2.1. Materials

Reagents were obtained from the following sources: zirconium acetate (in dilute acetic acid) and methyl methacrylate (99%) from Aldrich; methanol and potassium persulfate from Fisher; sucrose from Mallinckrodt. Water was obtained from an in-house system and was distilled and deionized to 18.3 MΩ·cm.

2.2.2. Synthesis of the PMMA Colloidal Crystal Template

Monodisperse PMMA colloidal spheres (diameter: 410±7 nm) were synthesized by emulsifier-free emulsion polymerization adapted from established syntheses.[170-171] Negatively charged spheres in a water suspension (~18 wt%) were obtained by using potassium persulfate as a radical initiator. The sphere suspension was then placed in a crystallization dish and allowed to sediment into face-centered cubic arrays. After drying at room temperature for approximately one week, white opalescent monoliths of the colloidal crystal template were obtained with dimensions ranging from 1 mm to 1 cm. The sphere size of 410 nm was chosen in order to ensure that the stop band positions of all materials herein would lie within the visible spectrum.

2.2.3. Synthesis of 3DOM ZrO_2

A mixture of 3 g of zirconium acetate and 3 g of methanol was stirred in a glass vial for 5 min. PMMA colloidal crystal template pieces (6 g) were placed on filter paper in a Büchner funnel, and the zirconia precursor solution was added dropwise over the top of the colloidal crystal template while suction was applied to pull excess precursor solution

through the funnel. The infiltrated template was allowed to dry for 24 h. The composite was then placed in an alumina crucible inside a quartz tube and heated in a tube furnace under either air or N_2 flowing at 0.6 L/min to convert the infiltrated precursor into solid macroporous ZrO_2 and remove the template. Samples were heated at 2 °C/min to either 450 °C or 700 °C. Identical procedures without sphere templates were also used to synthesize non-templated materials. This synthesis produced powdered samples that were further ground using a mortar and pestle to minimize the color contribution of randomly-oriented large crystal faces. Final particle sizes varied widely, with typical ranges from 10 to 200 μm and periodically ordered domains of ca. 10 to 50 μm within particles.

2.2.4. Addition of Carbon to 3DOM ZrO_2

Multiple samples of 3DOM ZrO_2 (0.15 g each) that had previously been heated to 700 °C in air were infiltrated with 0.5 g of aqueous sucrose solutions with various concentrations (0.1, 1, 5, 10, 15, and 20 wt% sucrose). The wet materials were then quickly heated to 100 °C in a drying oven for 30 min to prevent large sucrose crystals from forming and to ensure the formation of a homogeneous coating throughout the porous structure. The dried 3DOM ZrO_2 powders were then heated at 15 °C/min to 500 °C under nitrogen and immediately cooled.

2.2.5. Characterization

Diffuse reflectance UV-vis spectra were obtained using a Hewlett Packard 8452A diode array spectrophotometer with a Labsphere RSA-HP-84 reflectance attachment and a barium sulfate disc as a reference. Scanning electron microscopy (SEM) images were

obtained using a JEOL 6700 scanning electron microscope. Samples were prepared for the SEM by lightly dusting them onto adhesive carbon tape and affixing them to aluminum mounts. All samples were coated with 50 Å of platinum. Transmission electron microscopy (TEM) images and electron diffraction patterns were obtained using an FEI Technai T121 microscope (LaB_6 filament) operated at 120 kV. Samples for TEM were prepared by sonicating the 3DOM ZrO_2 powders in ethanol for 10 min and dispersing the resulting material on a carbon-coated Cu grid. Thermogravimetric analyses (TGA) were carried out using a Netzsch STA 409 PC thermal analyzer. All samples were heated in alumina crucibles. XRD was performed on a Panalytical X'pert Pro diffractometer with a cobalt source (Kα, λ = 1.789 Å) operated at 45 kV, 40 mA. Elemental analysis for carbon and hydrogen was performed by combustion analysis by Atlantic Microlab, Inc. (Norcross, GA).

2.3. Results and Discussion

2.3.1. Synthesis of 3DOM ZrO_2

Potential sources for carbon in the 3DOM ZrO_2 samples are the acetate ions in the precursor and the polymeric colloidal crystal template. To investigate the roles of carbon and zirconia grain size in 3DOM ZrO_2 pigments, materials were synthesized at either 450 °C or 700 °C under either an oxidizing atmosphere (air) or a non-oxidizing atmosphere (N_2). The same ZrO_2 precursor and the same PMMA colloidal crystal template were used for all materials. All 3DOM ZrO_2 samples exhibited structural color that varied in intensity and hue as the heating atmosphere or temperature were changed (Figure 2.2). For comparison, the corresponding samples prepared without a colloidal crystal template

did not show structural color but appeared either white when heated to 700 ˚C in air or exhibited various shades of gray and black. The gray/black appearance of the nontemplated materials indicates that acetate ions must be a significant source of carbon and PMMA is not needed to produce the darkening effect.

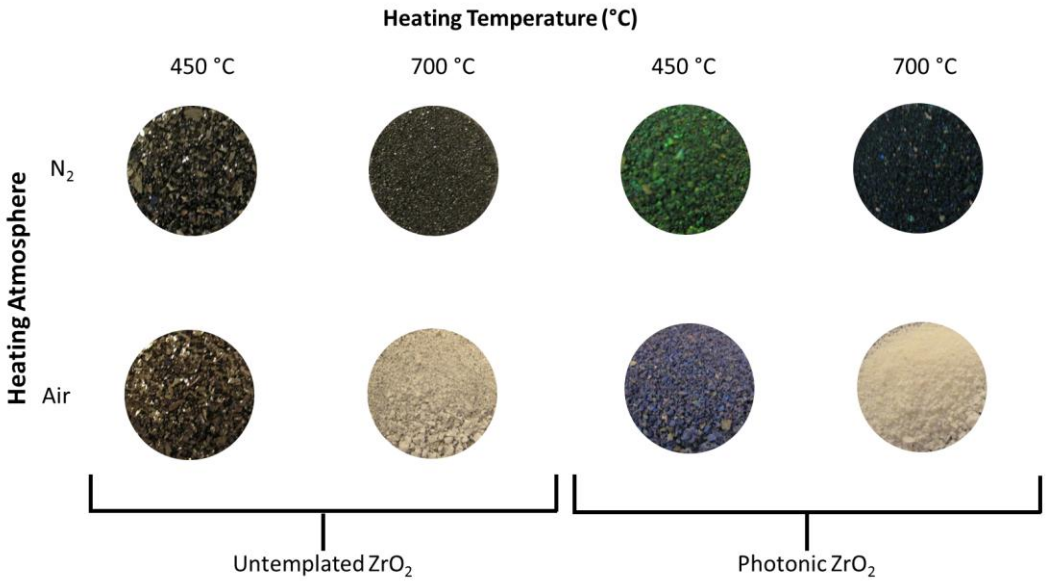

Figure 2.2. Photographs of untemplated ZrO_2 and 3DOM ZrO_2 samples heated under various conditions. Because the sample appearance depends strongly on the type and position of the light source, multiple photos of each sample were taken, and the most representative images were chosen for this figure. Untemplated ZrO_2, shown here for comparison, was synthesized using identical procedures but without a sphere template.

2.3.2. UV-vis Characterization of 3DOM ZrO_2

Optical reflectance spectra of all 3DOM ZrO_2 samples showed a single stop band in the visible region of the spectrum assigned to the (111) diffraction peak (Figure 2.3). The width of the stop band is typical for 3DOM materials produced by the methods used in this study, in which boundaries between ordered domains and surface defects on each

photonic crystal particle contribute to broadening of stop bands. The differences in hue of each material were due to shifts in the stop band position as a result of the reduction in pore spacing as 3DOM ZrO_2 underwent densification at higher temperatures. For 3DOM ZrO_2 synthesized at 450 °C in air (designated as 3DOM ZrO_2(450/air)), higher temperatures were experienced than for 3DOM ZrO_2(450/N_2) due to the exothermic combustion of carbonized precursor and polymer template constituents that caused increased local temperatures within the structure. As a result, the macropore size in 3DOM ZrO_2(450/air) was smaller, which was manifested as a strong blue-shift of 74 nm in the stop band position (Table 2.1). Therefore, the 3DOM ZrO_2(450/air) sample appeared purple, whereas the 3DOM ZrO_2(450/N_2) sample was green. For the 3DOM ZrO_2(700/air) and 3DOM ZrO_2(700/N_2) samples, there was also a stop band shift of 50 nm. However, neither material was vividly colored, with 3DOM ZrO_2(700/air) being nearly white and 3DOM ZrO_2(700/N_2) exhibiting a very dark blue coloration.

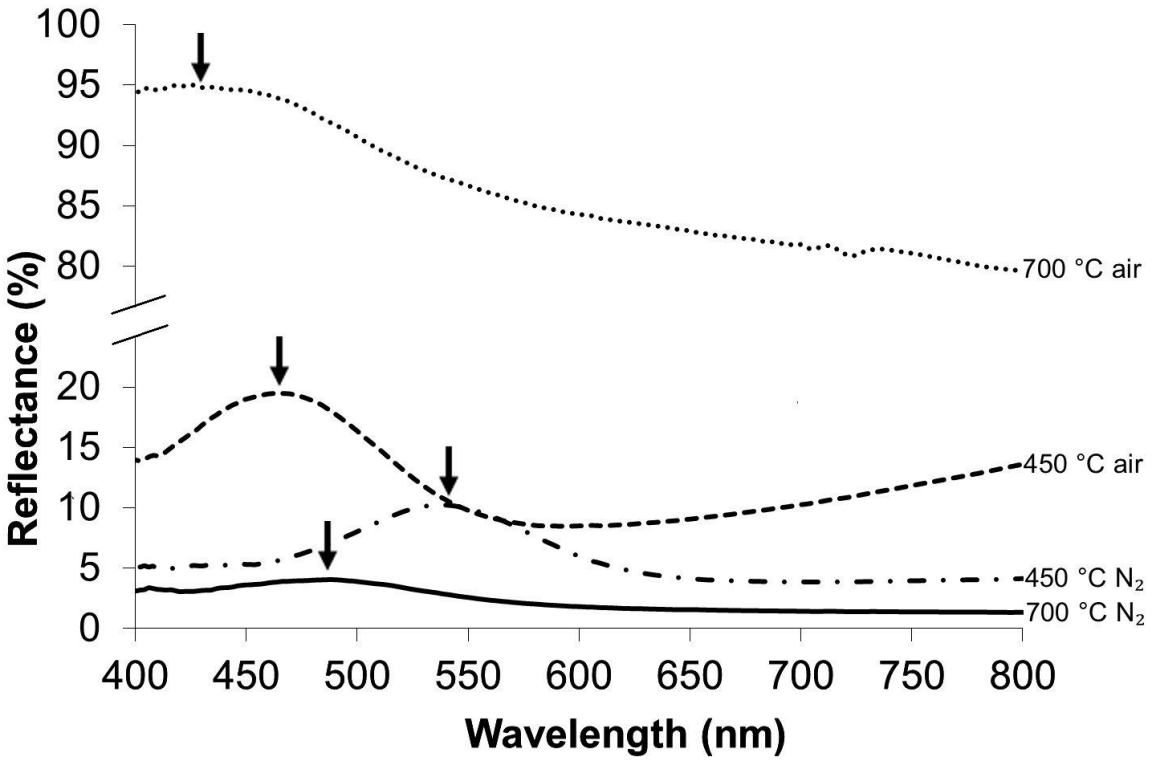

Figure 2.3. UV-vis spectra of 3DOM ZrO_2 samples synthesized at varying heating temperatures in air or N_2 atmospheres. The (111) peak positions are marked with arrows.

The UV-vis reflectance spectra showed significant differences in the stop band intensities (Table 2.1), which were calculated as the differences in absolute peak intensities and background reflectance (here defined as the lowest intensity in the spectral range from 400 to 800 nm for each sample). When comparing Figures 2.2 and 2.3, it can be seen that the most vividly colored samples were those heated to 450 ˚C, which exhibited background reflectance values between around 3 and 10% with clearly defined photonic stop bands. Although 3DOM ZrO_2(700/air) was opalescent and exhibited a comparatively intense stop band, its high reflectance across the whole visible spectrum led to the white appearance. The darkest sample, 3DOM ZrO_2(700/N_2), on the other

hand, reflected very little light across the whole spectrum and the (111) stop band projected only slightly above the background.

Table 2.2. Structural, optical, and compositional data of 3DOM ZrO_2 samples heated under various conditions

	450 °C air	450 °C N_2	700 °C air	700 °C N_2
pore size[a] (nm)	269	319	252	278
stop band position (nm)	462	536	436	486
stop band intensity[b] (%)	11.0	5.2	15.2	2.7
background[b] (%)	8.5	3.9	79.9	1.4
grain size[c] (nm)	11	<1	12	6
wt% loss (TGA)	4.8	20.0	0.6	15.7
% carbon (EA)	2.48	14.93	0.33	12.36
% hydrogen (EA)	0.13	1.44	0.15	0.43

[a]Pore sizes were estimated from SEM images.
[b]Intensity and background values are the highest and lowest reflectance values in the UV-vis spectra, respectively, in the spectral range from 400 to 800 nm.
[c]Grain sizes were determined by line broadening in XRD patterns, using the Scherrer equation.

2.3.3. Powder XRD of 3DOM ZrO_2

Because the surface texture of the zirconia skeleton had previously been considered to be a factor in determining the coloration of 3DOM ZrO_2 materials, it was investigated by powder XRD and electron microscopy. Powder XRD patterns of all samples showed peaks associated with the tetragonal zirconia phase (Figure 2.4). The 3DOM ZrO_2(700/air) sample also contained a monoclinic component. This phase change indicated that 3DOM ZrO_2(700/air) was exposed to higher local temperatures than 700 ˚C during calcination,[172] which was consistent with the UV-vis spectrum showing a stop band at lower wavelength than for the other samples (i.e., increased shrinkage). Grain

sizes for all samples were estimated from X-ray line broadening by the Scherrer equation and can be found in Table 2.1. As expected, all samples exposed to temperatures higher than 450 ˚C, either through an increased synthesis temperature or the combustion of carbon in an oxidizing atmosphere, produced measurable grain sizes while the grain size for 3DOM ZrO_2(450/N_2) was too small to be estimated by the Scherrer equation. Interestingly, 3DOM ZrO_2(700/N_2), which possessed the lowest stop band intensity, also had the lowest measurable grain size, making this another counter-example to the idea that weak structural color results from larger skeletal grains. Furthermore, 3DOM ZrO_2(700/air), which appeared almost pure white, had similar grain sizes when compared to 3DOM ZrO_2(450/air), which was intensely colored. SEM and TEM images of each sample show relatively little difference between the skeletal texture of the different samples, regardless of coloration Figures 2.5 and 2.6). Therefore, no direct correlation could be found between grain size and color intensities of these 3DOM ZrO_2 materials.

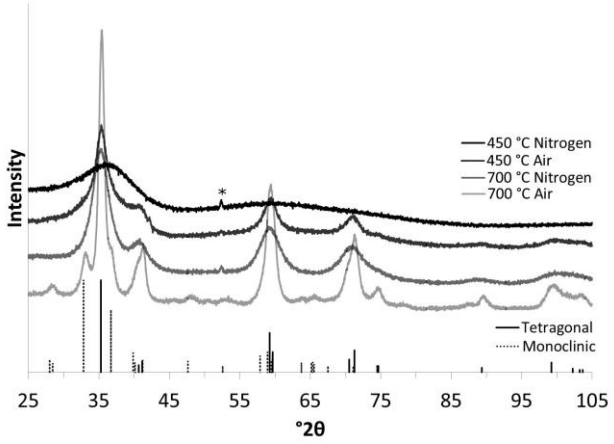

Figure 2.4. Powder XRD patterns of 3DOM ZrO_2 heated under the conditions indicated. The diffraction peak located at 52° 2θ corresponds to the aluminum sample holder.

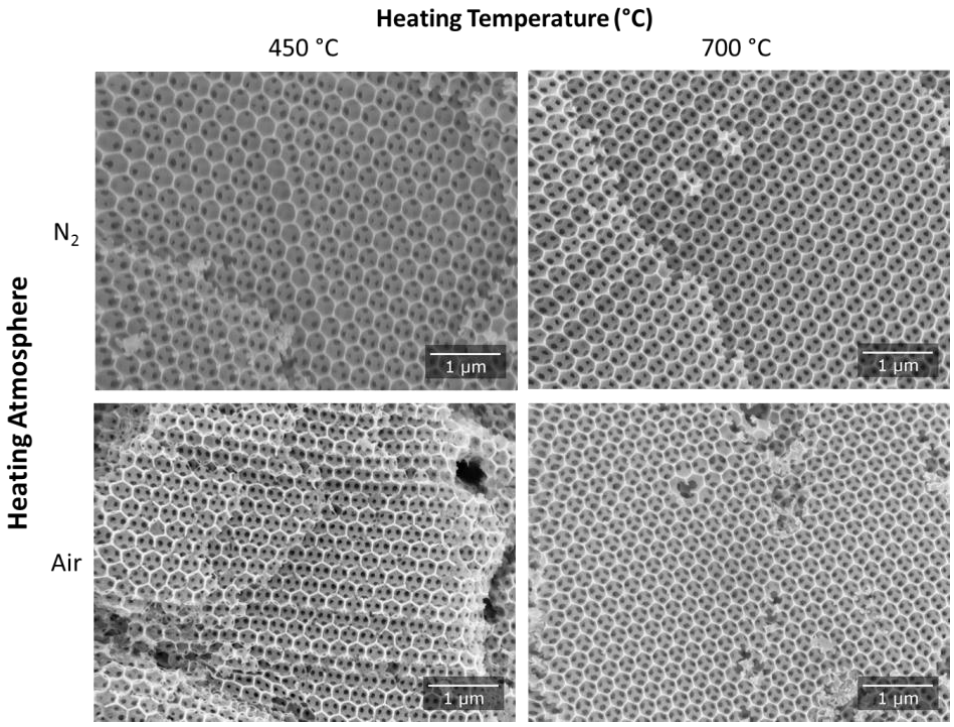

Figure 2.5. SEM images of 3DOM ZrO_2 heated under various conditions. The atmospheres during heating and maximum heating temperatures are indicated. All samples exhibit highly ordered porosity.

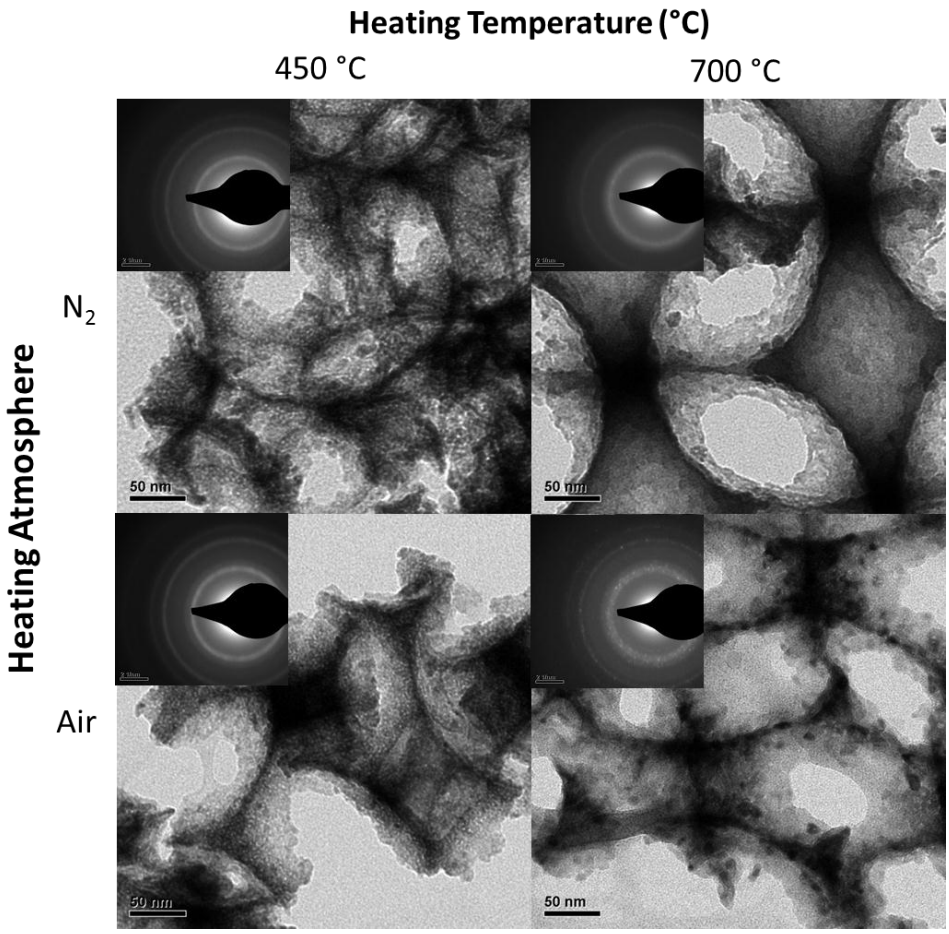

Figure 2.6. TEM images of 3DOM ZrO_2 heated under various conditions. The atmospheres during heating and maximum heating temperatures are indicated. Insets show electron diffraction patterns for each sample.

2.3.4. Carbon Content in 3DOM ZrO_2

To examine the role of carbon on coloration, the carbon and hydrogen content of each of the four samples was determined by elemental analysis (Table 2.1). Results showed that 3DOM $ZrO_2(450/N_2)$ and 3DOM $ZrO_2(700/N_2)$ contained the most residual carbon with 14.9 wt% and 12.4 wt%, respectively. However, the hydrogen content of 3DOM $ZrO_2(700/N_2)$ was much lower, indicating less-functionalized, more graphitic carbon, which would act as a better light absorber and produce the observed darker coloration of this sample. As expected, both samples calcined in air contained less carbon than the

samples heated under N_2, with 2.5 wt% and 0.6 wt% carbon for 3DOM ZrO_2(450/air) and 3DOM ZrO_2(700/air), respectively. As both of these samples possessed similar grain sizes, the much stronger coloration of 3DOM ZrO_2(450/air) was likely due to the presence of small amounts of carbon.

TGA carried out in air up to a temperature of 1000 °C provided information about the temperatures at which mass losses occurred (Figure 2.7). Two separate mass loss events could be found, one above ~300 °C and one between ~600 and 700 °C. Similar mass loss events were also observed in the case of sulfonated zirconia that included small amounts of coke.[173] These mass loss events correspond to different moieties of carbon, the nature of which has proven difficult to determine. It is possible that the lower temperature mass loss is due to surface carbon and the higher temperature loss due to carbon trapped within the zirconia walls. In support of this explanation, the higher temperature event was much less pronounced for corresponding 3DOM ZrO_2 samples prepared from 325 nm PMMA spheres, i.e., materials which would have thinner walls (data not shown). Furthermore, when carbon was added to 3DOM ZrO_2 after the synthesis (see below), the higher temperature mass loss was also absent (Figure 2.11, see below). 3DOM ZrO_2(700/air) had lost most carbon during the original synthesis heating step, accounting for its lower carbon content vs. 3DOM ZrO_2(450/N_2). Some carbon was retained in 3DOM ZrO_2(450/air) after the synthesis, because this sample had not undergone the ~600–700 °C mass loss event during calcination.

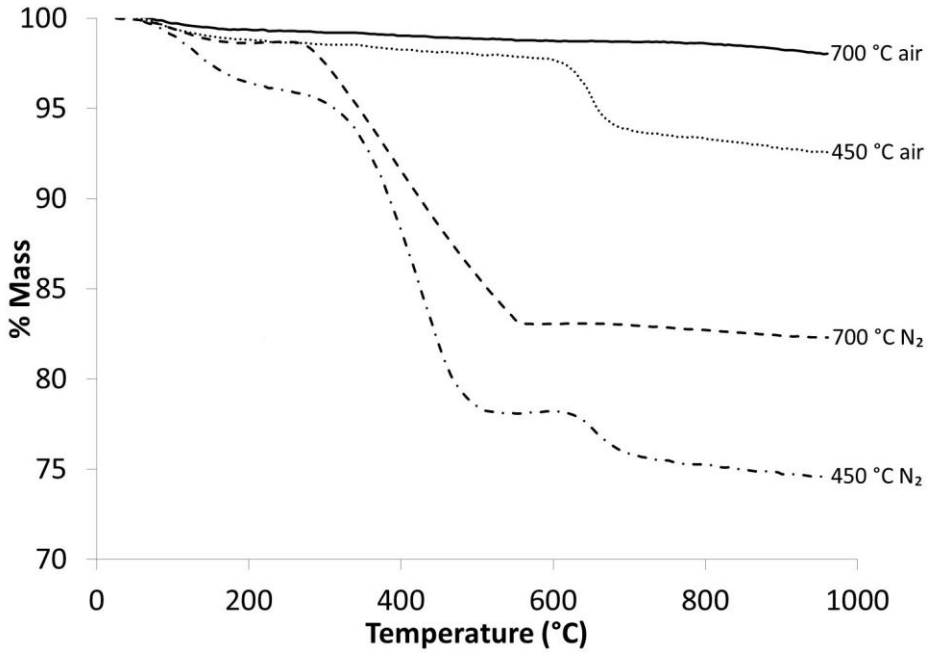

Figure 2.7. TG plots of 3DOM ZrO_2 samples prepared by the indicated conditions analyzed under flowing air. Mass losses after 300 °C is related to combustion of carbon in the samples.

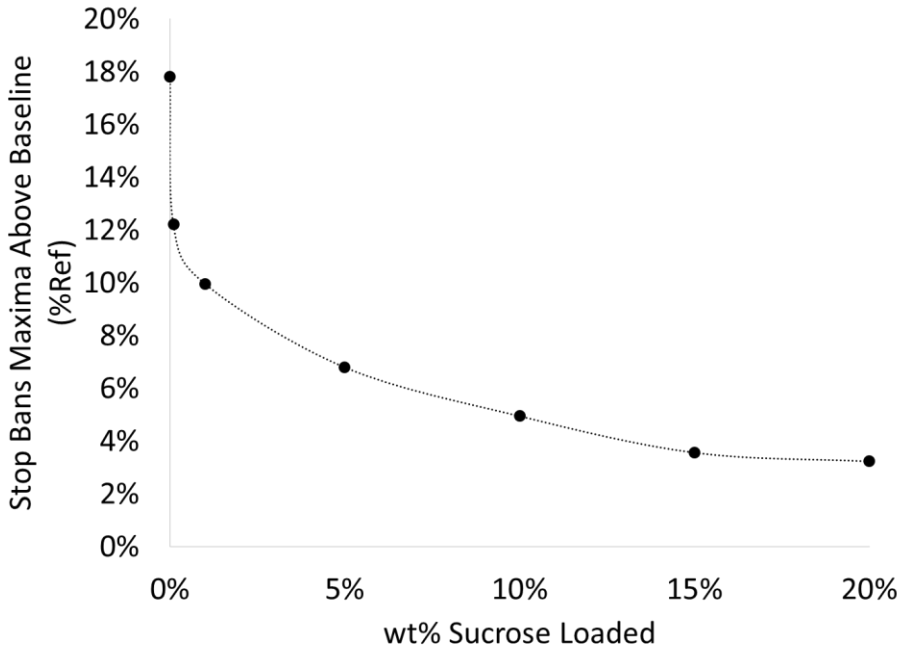

Figure 2.8. Plot of stop band maxima above baseline reflectance for originally white 3DOM ZrO_2 samples after addition of carbon through infiltration with various loadings of sucrose and carbonization. The values in this plot were calculated from the difference between peak intensity and background intensity at the peak wavelength of the stop band. Note that this is different from Tables 2.1 and 2.2, where stop band intensities are based on the difference in highest and lowest reflectance values in the UV-vis spectra in the spectral range from 400 to 800 nm.

These findings regarding both grain size and carbon content of 3DOM ZrO_2 lead us to an alternate explanation for the different color intensities observed in 3DOM ZrO_2 materials. A difference in zirconia grain sizes is likely not the decisive factor for the absence or presence of color. Rather, the extent of coloration relates to the carbon content of the material, which depends on the chemical nature of the precursor and template, as well as the heating temperature and atmosphere. In contrast to the PMMA opal/carbon black composites described by Aguirre *et al.*, no discrete carbon particles were observed by electron microscopy (Figures 2.5 and 2.6). The carbon appears to be spread evenly through the sample, providing a uniform light absorber throughout the structure of the 3DOM ZrO_2. It should be noted that white 3DOM ZrO_2(700/air), which contained almost no residual carbon appeared light-violet-colored when a thin layer of the powder was spread on a black background. This indicated that its photonic stop band was still intact, but the sample lacked an intense coloration due to the influence of randomly scattered light throughout the structure.

2.3.5. Reintroduction of Carbon into White 3DOM ZrO_2

As a further verification that the color intensity of 3DOM ZrO_2 is related to carbon content rather than grain size, we reintroduced color in the white 3DOM ZrO_2(700/air) material. This was accomplished by infiltrating already-synthesized 3DOM ZrO_2(700/air) with sucrose solutions containing different amounts of sucrose. Sucrose is a commonly used source for the preparation of nanoporous carbon materials by nanocasting processes.[174] The infiltrated and dried samples were then reheated to 500 °C under nitrogen to carbonize the sucrose. The resulting powders exhibited gradual shifts in

optical properties, displaying visual changes in brightness and color intensity as the carbon content was altered (Figure 2.9). UV-vis reflectance spectra of the re-carbonized 3DOM ZrO_2 materials showed an evident decrease in both background reflectance and stop band intensity with increased carbon content (Figure 2.10 and Table 2.2). However, for samples with 10 wt% sucrose or greater, the change in the magnitude of background reflectance lessened, indicating a minimum value for background reflectance after which any extra absorbing material only served to reduce the stop band intensity through strong absorption of light (Figures 2.9 and 2.10). Because carbon is a broad spectral absorber in the visible range, the baselines decreased across the whole spectrum with increasing carbon loading. The stop band position stayed relatively constant with varying carbon content.

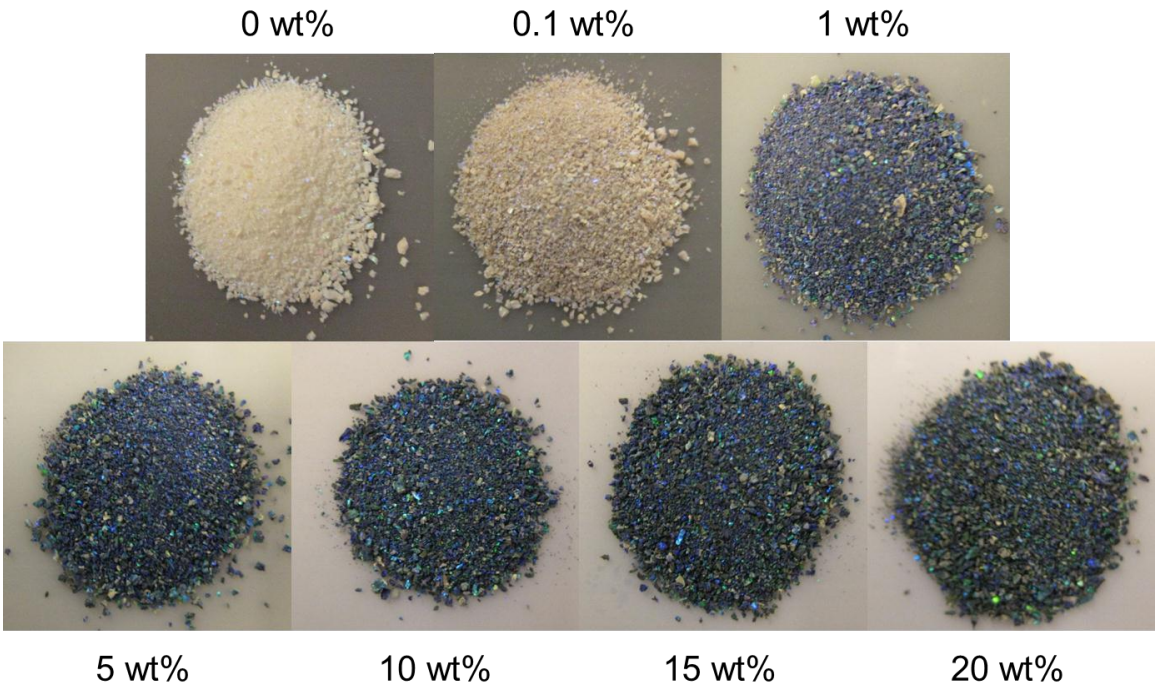

Figure 2.9. Photos of 3DOM ZrO_2 with various loadings of carbon. Wt% values correspond to the concentration of the sucrose solution used to deposit carbon into the 3DOM material.

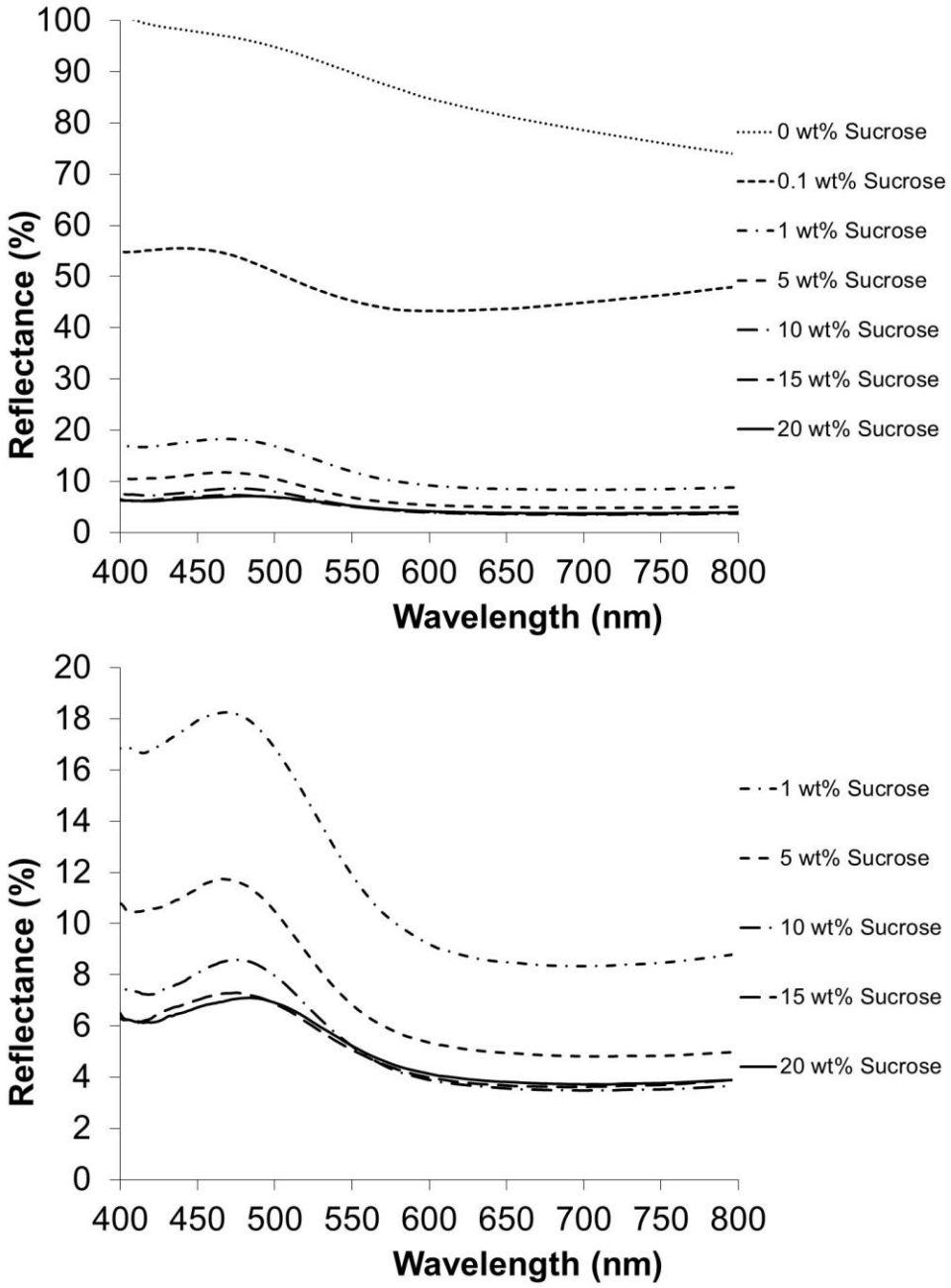

Figure 2.10. UV-vis spectra of white 3DOM ZrO_2 samples with carbon added though sucrose infiltration. Upper: Spectra of all re-colored samples. Lower: Expanded view of the 0–20% reflectance region magnified to resolve lower reflectance spectra.

Table 2.2. Values for Mass Loss (TGA), Stop Band Intensities (UV-vis), and Background Reflectance (UV-vis) for Re-colored 3DOM ZrO_2 (700/air) Using Various Concentrations of Sucrose

	0 wt%	0.1 wt%	1 wt%	5 wt%	10 wt%	15 wt%	20 wt%
wt% loss (TGA)	0.2	0.1	1.1	3.7	6.4	10.2	13.1
stop band intensity %	27.0	12.4	10.0	7.0	5.2	3.9	3.4
background %	73.8	43.2	8.3	4.8	3.5	3.4	3.7

TGA measurements of re-colored 3DOM ZrO_2(700/air) were performed in air to determine the carbon content added during re-carbonization (Figure 2.11 and Table 2.2). As expected, the amount of carbon present in the structure varied linearly with the concentration of the sucrose solution administered to 3DOM ZrO_2(700/air) (Figure 2.12). This showed that direct control of the carbon content of 3DOM ZrO_2 was achievable for specific tuning of the structural color brightness. The sample prepared by infiltration with 5 wt% sucrose solution was most similar in spectral and visual appearance to 3DOM ZrO_2(450/air), both of which contained similar amounts of carbon (3.7 and 4.8 wt%, respectively).

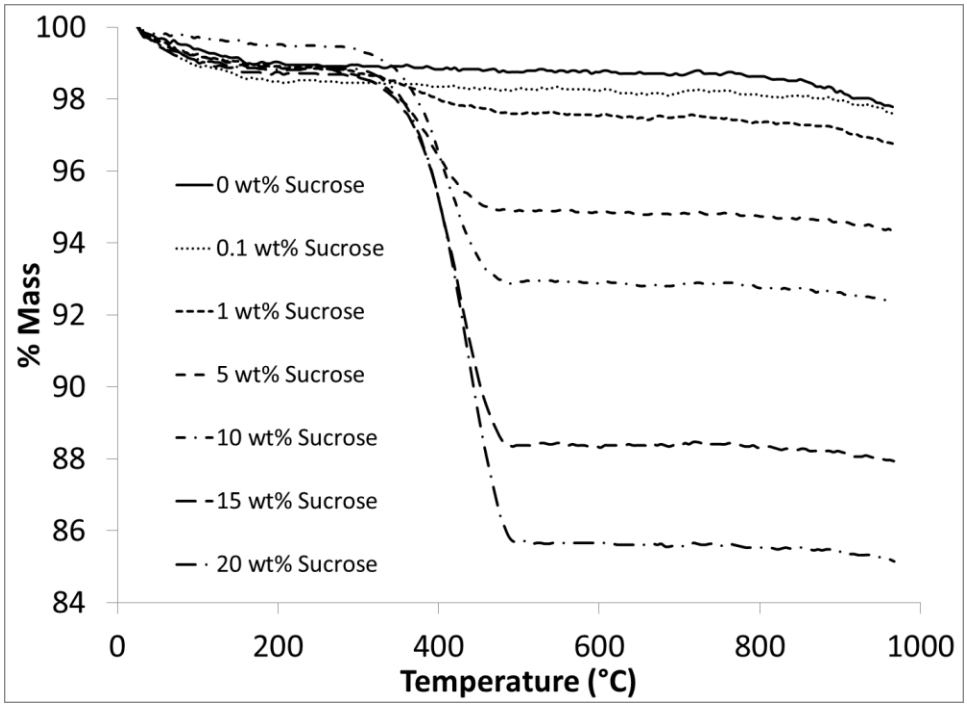

Figure 2.11. TG plots for 3DOM ZrO_2 samples that were infiltrated with different concentrations of sucrose solution and then heated to 500 ˚C to carbonize the sucrose.

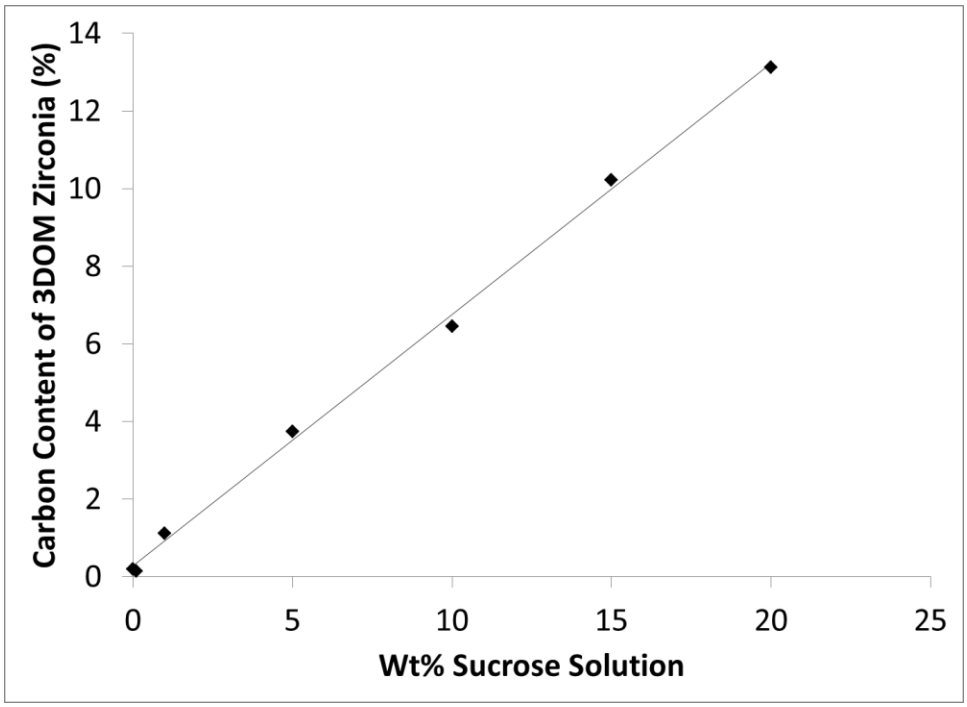

Figure 2.12. Plot of carbon content vs. wt% of sucrose solution used. The plot shows a linear relationship between these parameters.

2.4. Conclusions

This study confirmed our hypothesis that the content of light-absorber (here carbon) in 3DOM ZrO_2 photonic pigments strongly influences the color intensity of these materials, more so than any grain size effects under the conditions studied. The mechanism for the color enhancement by carbon is similar to that described for opal/carbon black mixtures.[155, 48] In these 3DOM materials, diffracted wavelengths that coincide with the stop band are reflected at the (111) and higher order lattice planes of the photonic crystal while other wavelengths pass through the material. Without carbon, multiple incoherent scattering events can occur with the transmitted wavelengths, resulting in non-photonic reflections from the material, which raise the background reflectance across the whole spectrum. In the presence of carbon, however, the transmitted wavelengths are absorbed, preventing non-photonic reflections and allowing those wavelengths reflected through Bragg diffraction to dominate. The material therefore maintains a specific color that is controlled by its structural periodicity. However, if the carbon content is too high, even the stop band wavelengths are absorbed, so that the material appears black.

The carbon absorber can be produced within the material directly during the synthesis by in situ carbonization of the precursor and/or template. If the synthesis conditions are well controlled, no external light absorbing material is necessary to produce strong coloration. Further fine-tuning is possible by the post-synthesis addition of carbon materials, as illustrated by the conversion of white 3DOM ZrO_2 to a material with structural color after carbonization of infiltrated sucrose solutions. The 3DOM ZrO_2

materials could be prepared as white, lightly colored, or darkly colored products by adjusting the amount of absorber within the structure. It is believed that these procedures are also applicable to 3DOM materials with other compositions. Fine-tuning of the carbon content can potentially be realized with other carbon sources added to the precursor material to ensure precise values of the absorber content in the final products. Although carbon is one of the most convenient additives to produce the observed optical effects, non-carbon based light absorbers incorporated into 3DOM materials or intrinsic absorption by the material are expected to produce similar effects. Combined with the ability to tune the stop band position through the pore size, the capability of controlled variation in color intensity makes 3DOM materials promising candidates for novel pigments based on structural color.

Chapter 3

Inverse Opal SiO_2 Photonic Crystals as Structurally-Colored Pigments with Additive Primary Colors

3.1. Introduction

Porous silica is widely employed in commercial applications as a catalyst support, chromatographic material, sorbent, and for many other uses.[175-178] Although silica is also a common component of pigments, e.g., for inkjet printing, it is not normally the source of color in such pigments.[177] Here it is demonstrated that porous silica materials with a 3DOM morphology (see Chapter 1) can be effective pigments with structural color that can be controlled precisely through synthesis conditions and mixing of additive primary colors.

These materials are of interest as specialty pigments because they do not rely on organic dyes or metal complexes to achieve their color. Oxide-based 3DOM materials do not undergo photobleaching, commonly observed in conventional dyes, and a single material can be templated using various template sphere sizes in order to achieve many spectral colors without the need for multiple compounds.

For colored 3DOM materials, it has been shown that a light–absorbing substance within the structure greatly enhances the color intensity through the absorption of incoherently scattered light.[166] A similar enhancement of color intensities through the use of carbon nanoparticles infiltrated into opaline materials has also been observed.[155-161] For 3DOM materials, however, this absorber species can be created *in situ* during thermal processing and does not require additional integration steps (see Chapter 2). Carbon as an absorber species is produced by incomplete combustion of decomposition products from

the polymer template and/or precursor material, especially if heated in an inert atmosphere, or it can be added after the synthesis of the 3DOM materials.[166]

As described in this chapter, 3DOM SiO_2 was synthesized in various colors for use as photonic pigments. SiO_2 was chosen because of its non-toxicity, relative abundance, high chemical stability, ease of synthesis, and ability to be functionalized with other surface groups if needed. Another important consideration is that the amount of carbon absorber species produced from the template and precursor decomposition during the synthesis of 3DOM SiO_2 falls within an ideal range that enhances coloration without over-darkening. The creation of structurally-colored 3DOM SiO_2 pigments with primary colors is also described, pigments that exhibit a unique additive color mixing mechanism with red-green-blue (RGB) primaries instead of the cyan-magenta-yellow (CMY) primaries found in conventional pigments. Also addressed are important processing considerations in the synthesis of these materials with an emphasis on the effects of heating temperature to control unit cell parameters and hence, stop band positions and colors. This technique can be used to fine-tune the color of the structural pigments.

3.2. Experimental

3.2.1. Materials

Reagents were obtained from the following sources: tetraethyl orthosilicate and methyl methacrylate (99%) from Aldrich; HCl, methanol, and potassium persulfate from Fisher; nitrogen was obtained from an in-house system; water was distilled and deionized to 18.3 MΩ·cm.

3.2.2. Synthesis of PMMA Colloidal Crystal Templates

PMMA nanospheres were synthesized using an established literature method.[64] All PMMA spheres used in this study possessed less than 4% dispersity in sphere size. In order to achieve specific sizes of polymer spheres, the concentrations of methyl methacrylate, water, and initiator, as well as the synthesis temperature were all altered to varying degrees until the desired sphere size was obtained, similar to a previous report.[179] Typical conditions can be found in Table 3.1.

Table 3.1. Synthesis conditions for achieving various PMMA polymer sphere sizes. Other sphere sizes can be obtained by altering methyl methacrylate (MMA), water, and/or potassium persulfate initiator concentrations.

Size	MMA	Water	Initiator	Temp.
350 nm	0.3 L	1.6 L	1.5 g	70 °C
409 nm	0.3 L	1.6 L	1.75 g	70 °C
475 nm	0.3 L	1.3 L	1.0 g	70 °C

Colloidal crystal templates were formed from the PMMA sphere suspension using either centrifugation or sedimentation techniques. For centrifugation, the sphere suspension was placed into two balanced glass centrifugation cups with 1 inch diameter and spun at 1000 RPM until a majority of spheres were settled out of the suspension, and an opalescent colloidal crystal could be observed (typically 72 h). The water was then decanted by pipette until the water level within the centrifugation cup was ~1 cm above the settled spheres. The remaining water was left open to the air and allowed to dry. Drying was complete when the templates had fully cracked apart and the remaining dried colloidal crystal was easily broken apart.

For the sedimentation method, the PMMA sphere suspension was poured into a covered glass crystallization dish and allowed to sediment for several weeks until an opalescent colloidal crystal was observed. The cover was then removed and the water was allowed to evaporate until dry.

3.2.3. Synthesis of SiO_2 Precursor Composite

A precursor for silica was prepared by adding 6 g tetraethyl orthosilicate (TEOS), 4 g methanol, and 3 g deionized water to a 20 mL scintillation vial and stirring for 5 seconds. A mass of 1 g of concentrated hydrochloric acid was then added, and the mixture was stirred for 5 min.

A mass of 15 g of colloidal crystal template was broken into pieces with edge-lengths of ~0.5 cm. These pieces were then placed on a sheet of filter paper in a Buchner funnel that was fitted onto a suction filtration flask. The precursor solution was added dropwise to the colloidal crystal templates, ensuring that all colloidal crystal template pieces were wetted. Once all of the precursor solution was added, suction was applied to the funnel, and excess liquid precursor was slowly removed. The infiltrated template pieces were then allowed to gel and dry for 24 h.

After drying, the template/precursor composite pieces were placed in a 10 cm × 1.9 cm alumina combustion boat. The boat was inserted into a 60 cm long quartz heating tube with an internal diameter of 2.54 cm and placed in a Lindberg/Blue M 800W tube furnace. Rubber stoppers fitted with glass pipettes were placed on each end of the tube and N_2 was flowed through the tube at 0.6 L/min. The material was heated at 5 °C/min to

a desired maximum temperature between 475 °C and 900 °C and maintained at that temperature for 2 h. The primary color samples (blue, 480 nm stop band; green, 554 nm stop band; red, 620 nm stop band) were all prepared by pyrolysis at 700 °C for 2 h. After pyrolysis, the materials emerged as powders with particle sizes between 10 to 200 μm and periodically ordered domains of ca. 10–50 μm within particles. Before UV-vis characterization, all samples were lightly ground using a mortar and pestle to homogenize the particle size and avoid preferred orientation of crystalline domains.

3.2.4. Grinding of 3DOM SiO_2 Pigments

3DOM SiO_2 powders were placed on a 38-μm stainless steel mesh sieve. The 3DOM powder and mesh were wetted with ethanol. The 3DOM powder was then gently rubbed into the mesh using a gloved finger with frequent washings of the mesh with ethanol into a collection pan. The ethanol/3DOM suspension was poured into a 0.75 L polyethylene bottle and allowed to sediment for 24 h. After this time, the ethanol was carefully removed by pipette until ~10 mL of ethanol and the sedimented 3DOM powder were left. This mixture was then washed out of the bottle with ~10 mL ethanol into a 20 mL scintillation vial. The suspension was again allowed to sediment for 24 h, after which time the ethanol was removed by pipette. The remaining wet powder was then placed in an oven at 100 °C until dry.

3.2.5. Characterization

Diffuse reflectance UV-vis spectra were obtained using a Hewlett Packard 8452A diode array spectrophotometer with a Labsphere RSA-HP-84 reflectance spectroscopy

attachment. Absorbance values were converted to %-reflectance using the relationship reflectance = $10^{(2 - \text{absorbance})}$. All spectra were smoothed using an exponential smoothing algorithm. Background reflectance values were obtained by analyzing the lowest continual value to the right of the stop band peak. Scanning electron microscopy (SEM) images were obtained using a JEOL 6700 scanning electron microscope operating at 5 keV. Samples were prepared for the SEM by lightly dusting them onto adhesive carbon and affixing them to aluminum mounts. All samples were then coated with 50 Å of platinum. Transmission electron microscopy (TEM) images were obtained using an FEI Technai T121 microscope (LaB_6 filament) operated at 120 kV. Samples for TEM were prepared by sonication of 3DOM powders in ethanol for 10 min and dispersing the resulting material on a carbon-coated Cu grid. Thermogravimetric analysis coupled with differential scanning calorimetry was carried out using a Netzsch STA 409 PC simultaneous thermal analyzer.

3.3. Results and Discussion

3.3.1. 3DOM SiO_2 Structure and Composition

3DOM SiO_2 powders were synthesized under various processing conditions in order to produce materials spanning multiple spectral colors and intensities and to identify the best synthetic approaches to control the coloration. All products had well-ordered, periodic macroporous structures that extended over domains of ca. 10–50 μm (Figure 3.1). Structural defects were also present but at an acceptable level for pigment applications. TEM images showed relatively smooth amorphous silica walls that replicated the curvature of the templating spheres. Due to shrinkage of the walls during

pyrolysis, the spherical void sizes were ca. 18–24% smaller than the dimensions of the templating spheres (see also Table 3.2).

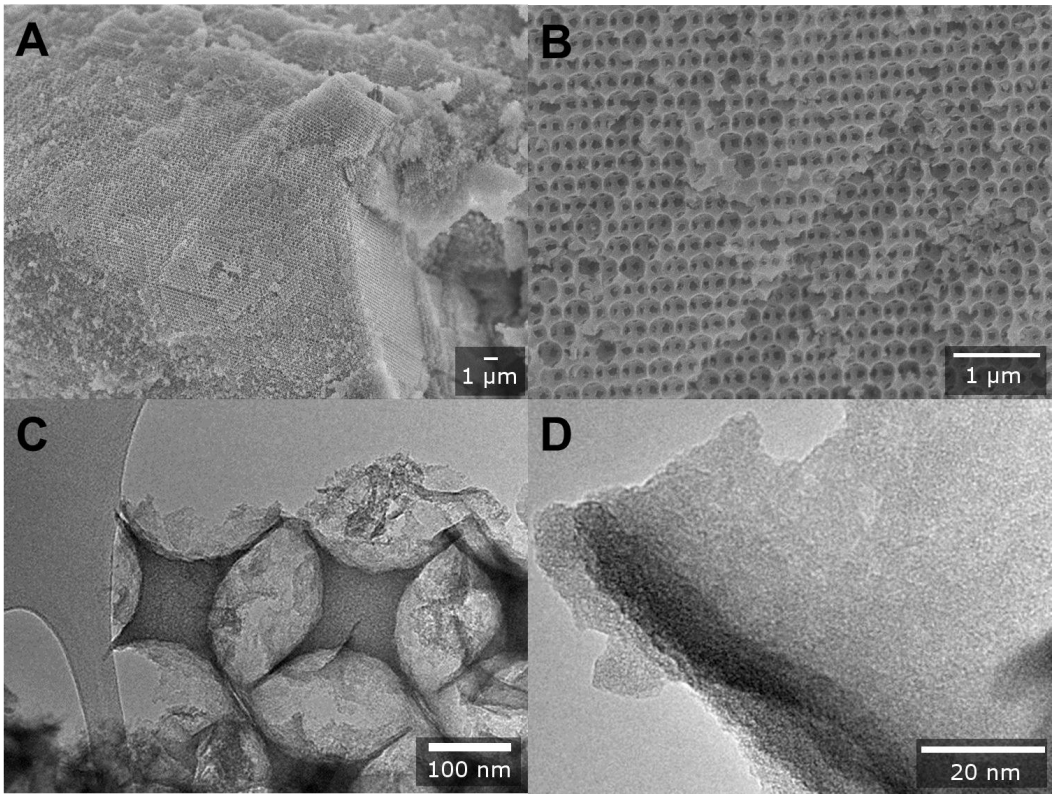

Figure 3.5. (A,B) SEM images of representative 3DOM SiO_2 powders. Long-range structural order and clearly defined periodic macropores are observed. (C,D) TEM images of 3DOM SiO_2, showing the texture of the amorphous silica walls, without any aggregated carbon particles.

The synthesis of opalescent 3DOM SiO_2 materials was previously reported.[64] However, these materials were only weakly colored, because they lacked carbon as a broad-spectrum absorber. Building on recent advances that demonstrated the benefit of including carbon within the 3DOM oxide structure,[166] we employed pyrolysis under an inert gas atmosphere to maintain small levels of carbon that originated from

decomposition products of the alkoxide precursor and the polymeric template. On the basis of thermogravimetric analyses, all 3DOM SiO_2 samples contained 5–8 wt% carbon (Figure 3.2). Although the TEM images did not show any carbon agglomerates, the incorporated carbon absorbs randomly scattered light, so that the corresponding stop band is emphasized in the appearance of the product.

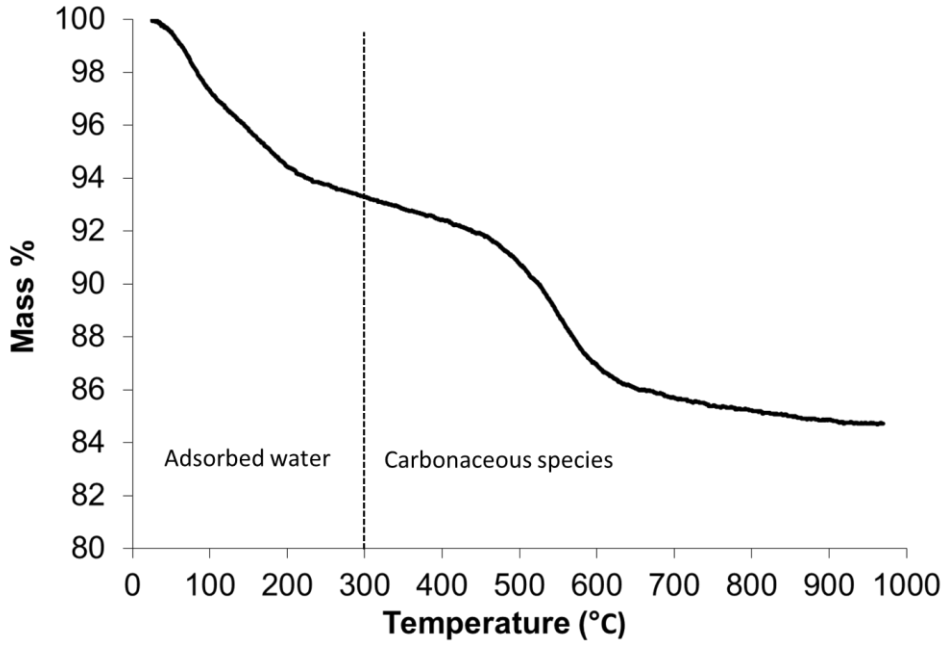

Figure 3.2. Typical TGA plot of a 3DOM SiO_2 sample heated to 1000 °C under flowing air. The mass loss before 300 °C corresponds mostly to adsorbed water. The mass loss after 300 °C is attributed to the combustion of carbonaceous species contained within the 3DOM structure and corresponds to ca. 8%.

3.3.2. Structural Color of 3DOM SiO_2

For 3DOM SiO_2 to exhibit structural coloration, the photonic stop band of the material must lie within the visible spectrum. To a first approximation that works well for these structural pigments, the spectral location of the stop band is governed by a combination of Bragg's law and Snell's laws (Equations 1.2-1.4).

Analyzing Equation 1.4, it becomes apparent that the *d*-spacing and average index of refraction are the properties that control the position of the stop bands in 3DOM materials. Since 3DOM materials are comprised of an *fcc* array of pores, stop bands are expected when the indices of the lattice planes are all odd or all even. Therefore, photonic reflections occur for d_{111}, d_{200}, d_{220}, d_{311}, etc. with the most prominent reflection originating from the (111) plane due to multiplicity rules. Even though the (111) reflection peak is the most intense and most visible, other reflection peaks can be observed in the UV-vis spectra of select 3DOM materials. The (200) peak is often present as a shoulder on the shorter wavelength side of the (111) peak, and the (220) peak is observed in the visible spectrum in samples with (111) stop bands larger than ca. 650 nm (see, for example, the spectrum of the red sample in Figure 3.8). All of these reflections within the visible spectrum contribute to the color of the 3DOM powders, but the perceived color is dominated by the (111) peak. For this reason, the discussion of the photonic stop band position within this publication will refer to the major (111) reflection, and the reported location of this reflection will correspond to the position of maximum reflectance.

3.3.3. Tuning Color via Thermal Processing

To select a specific color for a 3DOM material with a given index of refraction, it is necessary to effect changes in the *d*-spacing of that material. The most obvious method to control pore sizes, and, consequently, d_{hkl} values, in 3DOM SiO_2 is by using template spheres with different sizes. It was possible to synthesize PMMA spheres of various sizes by altering the polymer sphere synthesis parameters to tune the colloidal sphere sizes and

synthesize materials with photonic stop bands in the full range of the visible spectrum. Table 3.2 shows a selection of samples synthesized using various template sphere sizes and their respective UV-vis characteristics after heating under N_2 to a temperature between 475 °Cand 900 °C. For a given synthesis temperature, the initial template sphere size was the main factor determining the final stop band position. Figure 3.3 displays the relationship between the template sphere size and the final stop band position for samples heated to three different temperatures (550 °C, 600 °C, and 700 °C). The relationship between these values was approximately linear according to the equations found in the caption of Figure 3.3. These equations became important for choosing sphere sizes that produce materials with specific stop band positions and colors for a given synthesis temperature.

Table 3.2. Values of λ_{max},[a] maximum reflectance (R% at λ_{max}, determined by UV-vis spectroscopy),[a] baseline reflectance (Base R%, determined by UV-vis), stop band height above baseline (R% at λ_{max} – Base R%, determined by UV-vis), template sphere size, maximum pyrolysis temperature, and the half-width at half-maximum intensity of the (111) diffraction peak (HWHM, determined by UV-vis) for select 3DOM SiO_2 samples. Half-widths were measured using the right side of the (111) peak in order to avoid influence from the (200) shoulder. All samples included in this table were heated under N_2 to preserve carbonaceous species within the 3DOM structure.

Sample	λ_{max}	R% at	Base R%	Peak	Sphere size	Pyrolysis	HWHM
182[c]	564	38.9	22.5	16.4	384	475.0	36
181[c]	564	34.1	18.7	15.4	384	500.0	37
103	442	10.2	2.3	7.9	300	550.0	33
106	494	9.8	3.3	6.5	345	550.0	38
108	494	14.0	5.4	8.6	345	550.0	33
110	492	10.6	3.9	6.7	345	550.0	40
113	486	11.1	3.9	7.2	332	550.0	38
115	488	9.4	2.8	6.6	332	550.0	40
116	490	11.2	3.0	8.2	332	550.0	39
133	672	25.7	13.5	12.2	425	550.0	47
136	472	6.7	2.4	4.3	332	550.0	34
145	474	10.3	3.5	6.8	332	550.0	34
153	462	6.1	0.9	5.2	332	550.0	32
160	472	12.0	3.2	8.8	332	550.0	32
161	470	12.1	3.3	8.8	332	550.0	33
165	480	9.3	4.5	4.8	332	550.0	36
166	482	11.7	3.9	7.8	332	550.0	35
167	482	15.3	4.8	10.5	332	550.0	36
168	478	12.6	3.5	9.1	332	550.0	36
170	554	12.0	4.5	7.5	384	550.0	37
172	574	11.2	3.8	7.4	384	550.0	47

Sample	λ_{max}	R% at	Base R%	Peak	Sphere size	Pyrolysis	HWHM
180[c]	558	25.6	10.8	14.8	384	550.0	38
201	568	26.0	11.0	15.0	384	550.0	41
232	644	9.9	2.1	7.8	425	550.0	42
233	636	9.4	1.9	7.5	425	550.0	44
137	466	5.8	1.6	4.2	332	600.0	35
150	464	4.9	1.4	3.5	332	600.0	32
179	550	18.4	6.1	12.3	384	600.0	38
189	446	9.0	1.8	7.2	319	600.0	32
190	442	14.1	4.1	10.0	319	600.0	33
178[c]	545	16.2	4.7	11.5	384	650.0	36
130	470	7.3	1.2	6.1	345	700.0	38
134	454	4.5	1.0	3.5	332	700.0	38
173	552	7.0	1.6	5.4	384	700.0	44
177[c]	536	15.1	4.2	10.9	384	700.0	38
193	424	10.0	1.5	8.5	319	700.0	36
195	404	7.2	2.0	5.2	298	700.0	34
198	404	7.1	1.2	5.9	298	700.0	34
199	412	12.3	1.9	10.4	298	700.0	34
200	414	11.0	2.3	8.7	298	700.0	33
203	582	14.8	3.3	11.5	440	700.0	43
205	586	15.3	3.0	12.3	440	700.0	41
207	590	15.6	3.1	12.5	440	700.0	44
209	582	15.8	3.7	12.1	440	700.0	43
223	648	17.7	6.3	11.4	475	700.0	38
224	554	12.4	2.7	9.7	409	700.0	34
225[b,d]	558	13.4	2.5	10.9	409	700.0	40
226	560	14.7	2.9	11.8	409	700.0	44
227	556	18.1	7.9	10.2	409	700.0	42

Sample	λ_{max}	R% at	Base R%	Peak	Sphere Size	Pyrolysis	HWHM
	560	19.2	8.0	11.2	409	700.0	42
229	478	9.2	1.6	7.6	350	700.0	36
230[b]	486	9.1	1.6	7.5	350	700.0	32
233[b]	622	9.1	1.9	7.2	475	700.0	46
235	546	17.3	7.7	9.6	409	700.0	40
236	548	13.6	4.2	9.4	409	700.0	43
237	552	16.0	7.0	9.0	409	700.0	38
238	548	22.2	8.9	13.3	409	700.0	42
239	552	9.0	5.2	3.8	409	700.0	50
240	556	15.4	7.6	7.8	409	700.0	40
241	550	13.7	6.4	7.3	409	700.0	42
242	550	20.8	8.1	12.7	409	700.0	42
243	550	18.3	6.3	12.0	409	700.0	42
244	550	16.6	7.7	8.9	409	700.0	42
245	482	18.1	7.7	10.4	350	700.0	38
246	486	12.3	5.9	6.4	350	700.0	42
247	484	15.3	7.1	8.2	350	700.0	42
248	486	16.9	7.5	9.4	350	700.0	34
249	484	10.2	5.0	5.2	350	700.0	48
250	482	11.3	5.7	5.7	350	700.0	45
251	484	15.0	5.4	9.6	350	700.0	39
252	480	18.4	9.9	8.5	350	700.0	40
253	484	17.2	7.9	9.3	350	700.0	38
254	640	17.9	6.9	11.0	475	700.0	43
255	642	19.1	7.9	11.2	475	700.0	52
256	652	17.3	6.8	10.5	475	700.0	52
257	642	14.6	4.1	10.5	475	700.0	52

Sample	λ_{max}	R% at	Base R%	Peak	Sphere size	Pyrolysis	HWHM
258	656	18.1	8.9	9.2	475	700.0	50
259	634	17.3	7.4	9.9	475	700.0	52
260	662	29.7	14.0	15.7	475	700.0	50
261	636	17.7	8.4	9.3	475	700.0	50
262	654	18.0	8.2	9.8	475	700.0	44
263	668	19.4	8.9	10.5	475	700.0	46
264	666	18.6	7.3	11.3	475	700.0	52
265	662	17.6	8.4	9.2	475	700.0	46
266	660	17.4	7.6	9.8	475	700.0	46
267	638	13.5	3.5	10.0	475	700.0	52
268	660	17.0	6.2	10.8	475	700.0	50
269	608	14.1	6.1	8.0	475	700.0	50
270	632	16.4	7.5	8.9	475	700.0	53
220[d]	554	6.0	1.1	4.9	425	900.0	42

[a] Values of λ_{max} and R% at λ_{max} within this table are taken from the raw data. These values may differ slightly from those in the main paper, for which an exponential smoothing function was applied as noted in the Experimental Section.
[b] Samples used for 3DOM SiO_2 primary colors.
[c] Samples used for Figure 3.8.
[d] Samples used for Figure 3.12.

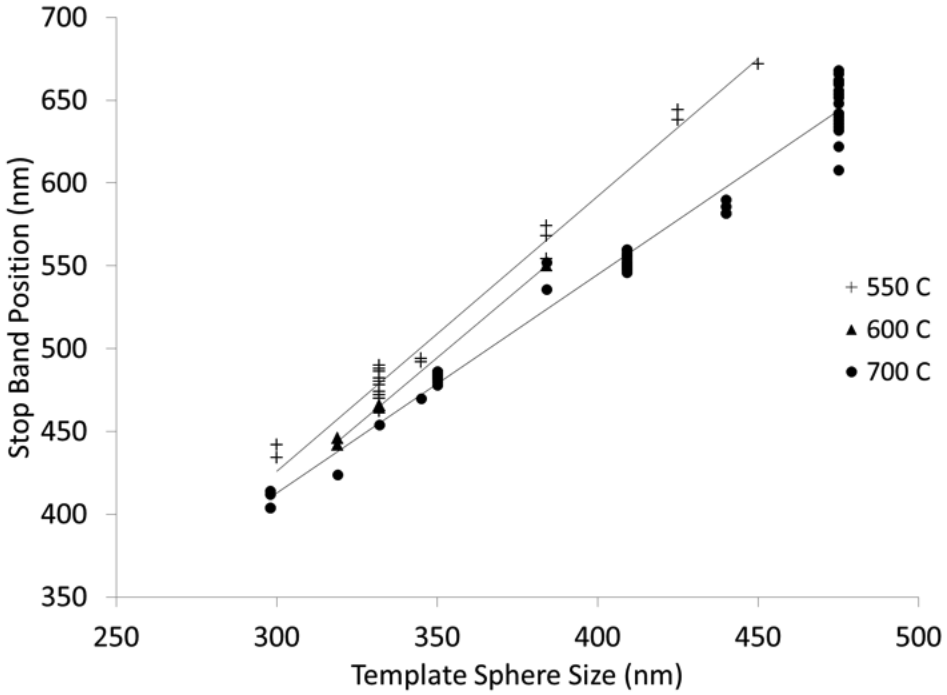

Figure 3.3. Photonic stop band positions of 3DOM SiO_2 after pyrolysis at 550 °C, 600 °C, and 700 °C using various template sphere sizes. Approximately linear relationships are observed between the diameter of the templating spheres and the final stop band position (550 °C, y = 1.659x - 71.644, R^2 = 0.983; 600°C, y = 1.6315x - 76.537, R^2 = 0.9987; 700°C, y = 1.3201x + 16.865, R^2 = 0.9784). Higher temperatures cause a blue-shift in the stop band position for a given sphere size. The magnitude of the change in stop band position increases at larger wavelengths.

The trends at the various temperatures illustrate the drastic changes in stop band position for various heating temperatures. For a given template sphere size, increases in temperature resulted in a smaller *d*-spacing between diffraction layers due to increased densification of the SiO_2 structure.[180-181] The densification of silica occurs through further condensation of silanol groups, which results in shrinkage of the silica walls. At higher temperatures, this densification was encouraged. For smaller template sizes, the densification at 700 °C was less pronounced due to the presence of thinner 3DOM walls that undergo a smaller dimensional change compared to the same degree of structural shrinkage from samples prepared with larger template sizes.

The variation in stop band position observed for materials synthesized under similar conditions was likely due to a variety of factors, including the amount of pyrolyzed material, non-uniform heating temperatures within the quartz tube during the pyrolysis step, fluctuations in house-nitrogen gas flow, and variations in the degree of infiltration of the liquid precursor during the infiltration step. Variances during any of these steps potentially changed the degree to which silica densified as it was heated. Densification also increases the average refractive index of the silica skeleton, which affects the stop band position. This densification mechanism could thus be harnessed as a tool for shifting stop band positions through the synthesis temperature without changing the template sphere size.

The ability to control silica shrinkage and band positions by the pyrolysis temperature was further demonstrated by analyzing several samples synthesized from a single infiltrated batch of 441 nm spheres but pyrolyzed at various temperatures between 550 and 865 °C at 35 °C intervals. Although there is some scatter in the data, an approximately linear stop-band shift of ca. 9 nm/100 ˚C was achieved in this temperature range (Figure 3.4).

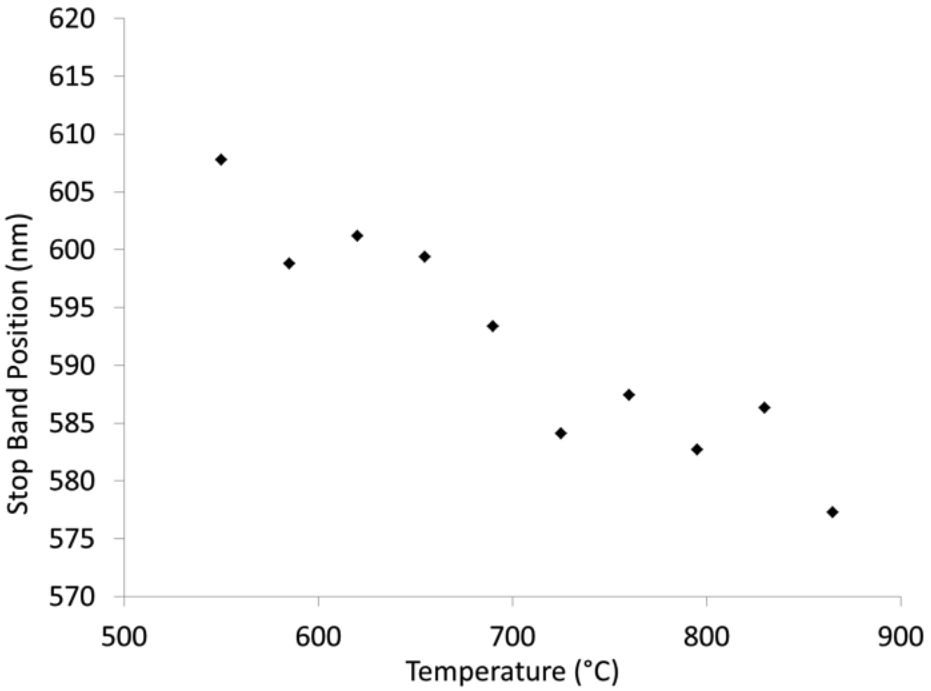

Figure 3.4. Graph showing the shift to shorter wavelength with increasing pyrolysis temperature for a series of ten samples of 3DOM SiO_2 synthesized using a 441 nm diameter colloidal crystal template and heated at intervals of 35 °C starting at 550 °C. A nearly linear change is observed in the stop band position with exposure to higher temperatures ($y = -0.0865x + 653.07$, $R^2 = 0.8847$).

In addition to stop band position shifts, stop band intensities and background reflectance values were affected by changes in the pyrolysis temperature, influencing the perceived color intensity or chroma. It was also observed that, for a fixed sphere size (384 nm in this case), the increased heating of 3DOM SiO_2 resulted in a decreased stop band intensity as well as a lowering of background reflectance (Figure 3.5). The decrease in stop band reflectance and the decrease in background reflectance are most likely related to the same mechanism. It has been shown that the extent of conversion of sp^3 carbon to sp^2 carbon increases with higher processing temperature[182] and that this change increases both the refractive index of carbon and its absorption coefficient.[183-184] Similar effects are expected for these 3DOM SiO_2 systems as carbonaceous components were

produced during pyrolysis. As a result, the samples pyrolyzed at higher temperature were less reflective across the full spectrum and appeared darker.

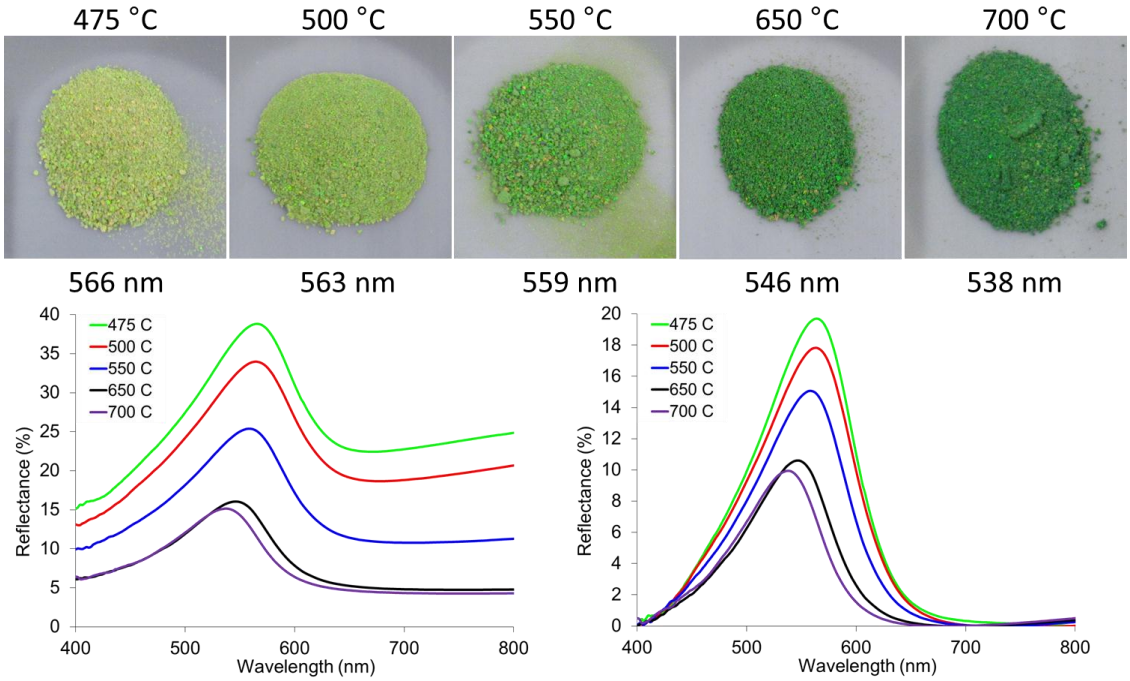

Figure 3.5. (Top) Images of 3DOM SiO_2 synthesized using 384 nm diameter templating spheres at various temperatures. The wavelengths of the corresponding (111) stop band peaks are also listed. (Bottom-left) UV-vis spectra of 3DOM SiO_2 synthesized at various temperatures. As the synthesis temperature is increased, background reflectance, stop band reflectance, as well as stop band position decrease in value. (Bottom-right) UV-vis spectra from the bottom-left graph with the background reflectance subtracted. This emphasizes the change in reflectance of the stop band peak with increasing temperature.

An additional example illustrating how both templating sphere size and pyrolysis temperature can be used to fine-tune the color of the structural pigments is shown in Figure 3.6. Spectra with the same stop band position were obtained from two different sphere sizes by using a high pyrolysis temperature for the larger template spheres. At the higher temperature, the greater amount of shrinkage compensates for the larger sphere diameters. Consistent with the results above, the sample prepared at the higher temperature is less reflective but appears darker and thus more intensely colored to the

eye (see Figure 3.7), likely due to the decrease in reflectance intensity from wavelengths surrounding the central stop band position.

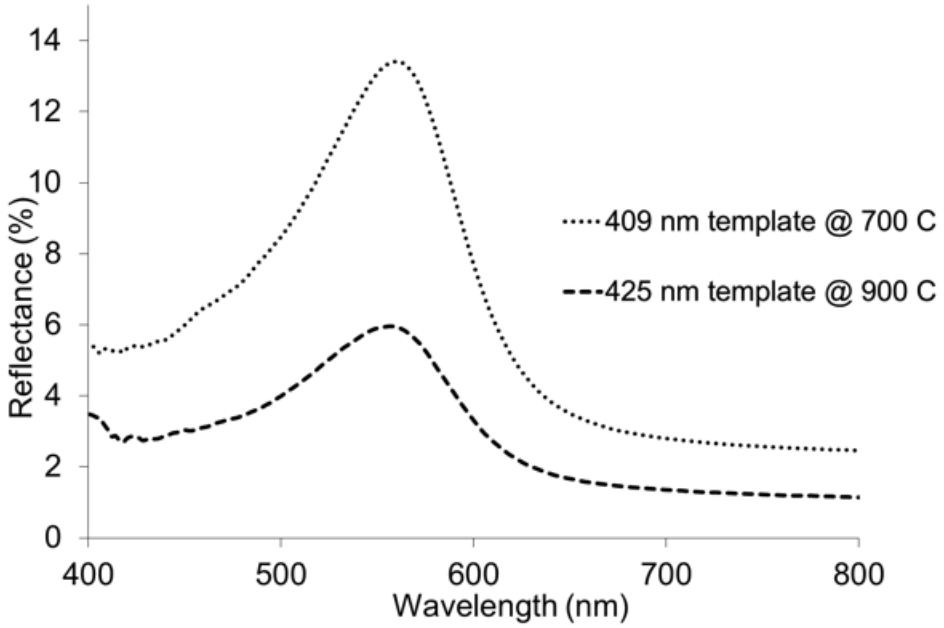

Figure 3.6. UV-vis spectra of 3DOM SiO_2 synthesized using different sphere diameters (409 nm, 425 nm) and heating temperatures (700 °C, 900 °C) in order to create identical stop band positions.

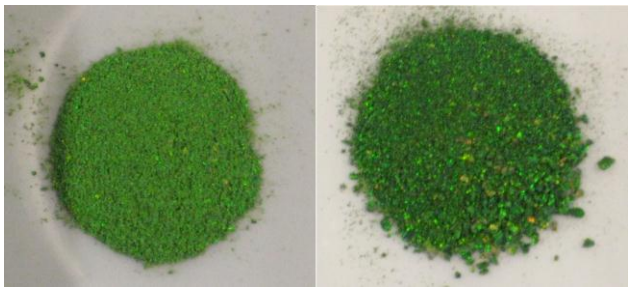

Figure 3.7. Images of 3DOM SiO_2 synthesized using PMMA colloidal crystals with different sphere diameters (left: 409 nm, right: 425 nm) and heating temperatures (left: 700 °C, right: 900 °C) in order to achieve identical stop band positions.

3.3.4. Synthesis of 3DOM SiO_2 Pigments with Primary Colors

In principle, any spectral color can be obtained by choosing an appropriate template sphere size and fine-tuning the stop band position via the synthesis conditions. However, a color like yellow is difficult to isolate due to the small portion of the spectrum that is observed as yellow (570–580 nm). The typical width of stop bands in 3DOM materials far exceeds this range, so that surrounding wavelengths (green and orange), contribute to the coloration. Also, on an industrial level, it would be preferred to produce multiple colors using only a small set of synthesis parameters and template sphere sizes. One possible solution we considered to address both of these issues was to prepare 3DOM SiO_2 pigments in three primary colors and mix these to obtain other colors.

During the investigation of mixing 3DOM powders, it became apparent that these pigments do not follow the standard color mixing mechanism of conventional pigment materials. Almost all commercially available pigments and dyes rely on a subtractive color mechanism in which specific portions of the visible spectrum are absorbed while the remaining portion of the spectrum is reflected. 3DOM materials, however, follow an additive color mechanism in which most wavelengths are absorbed or transmitted except for the wavelengths that fall within the stop band of the material. This narrow band of reflected wavelengths is visually perceived similar to emitted light, analogous to colors produced by multiple light-emitting diodes and pixels on a television screen. Because 3DOM materials follow this additive color mechanism, the three primary colors are red, green, and blue (RGB) rather than cyan, magenta, and yellow (CMY), the typical primary colors found in pigment systems and the basis for all print media.

Monochromatic RGB primaries are defined by the Commission Internationale de l'Eclairage (CIE) color space to correspond to wavelengths of 435.8, 546.1, and 700.0 nm for blue, green, and red.[185] However, other shades of these colors with alternate wavelengths can be used to create numerous spectral colors within the RGB color space. For the purpose of this study, primary colors were selected on the basis of perceived color intensity. Even though visual appearance is subjective to the observer, it was effective in identifying the target materials. To create the RGB primary colors, template arrays of 350 nm, 409 nm, and 475 nm PMMA spheres were chosen from a large array of synthesis conditions (Table 3.2) that yielded intense blue, green, and red coloration, respectively. The stop bands for the resulting powders peaked at 480 nm (blue), 554 nm (green), and 626 nm (red), respectively. Photographs of these powders and the corresponding UV-vis reflectance spectra are shown in Figure 3.8. Using measurements of *d*-spacings from SEM images (Figure 3.9), assuming a fixed refractive index value for silica (1.455), and using Equation 3.3, it was possible to relate the stop band positions to the templating sphere size and evaluate the fill fraction of solid material and pore shrinkage (Table 3.3).

Table 3.3. Table of structural and optical parameters for blue, green, and red 3DOM SiO_2. Values shown are the template sphere diameter (D_{sphere}), the pore diameter measured using SEM images (D_{pore}), pore shrinkage (ΔD), the spacing of diffraction layers calculated using D_{pore} (d_{hkl}), fill fraction of 3DOM walls (φ), and stop band position (λ).

Color	D_{sphere} (nm)	D_{pore} (nm)	ΔD (%)	d_{hkl} (nm)	φ (%)	λ (nm)
Blue	350	288	17.7	235	4.5	480
Green	409	336	17.8	274	2.1	554
Red	475	360	24.2	294	12.0	626

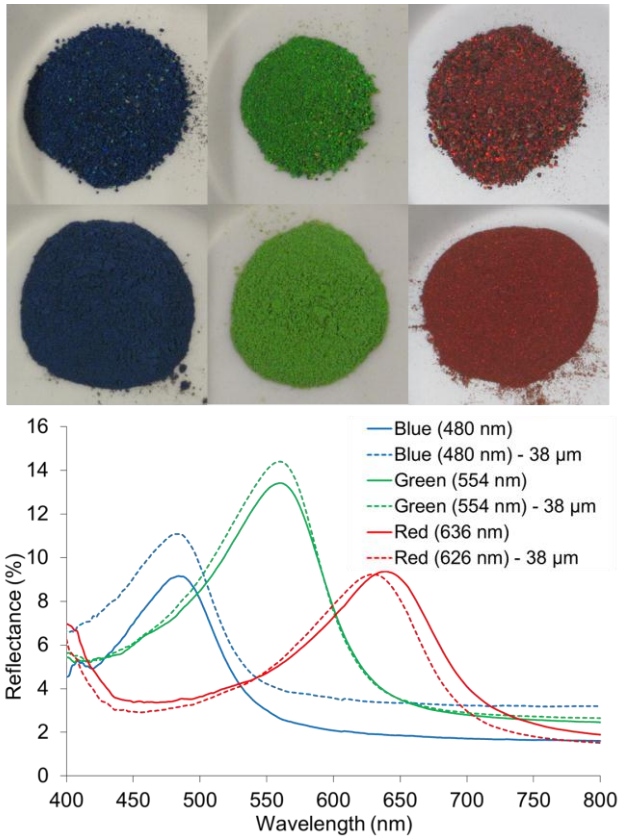

Figure 3.8. Photographs and UV-vis spectra of 3DOM SiO_2 primary-color pigments before (top, solid lines) and after (bottom, dashed lines) grinding through a 38-µm sieve.

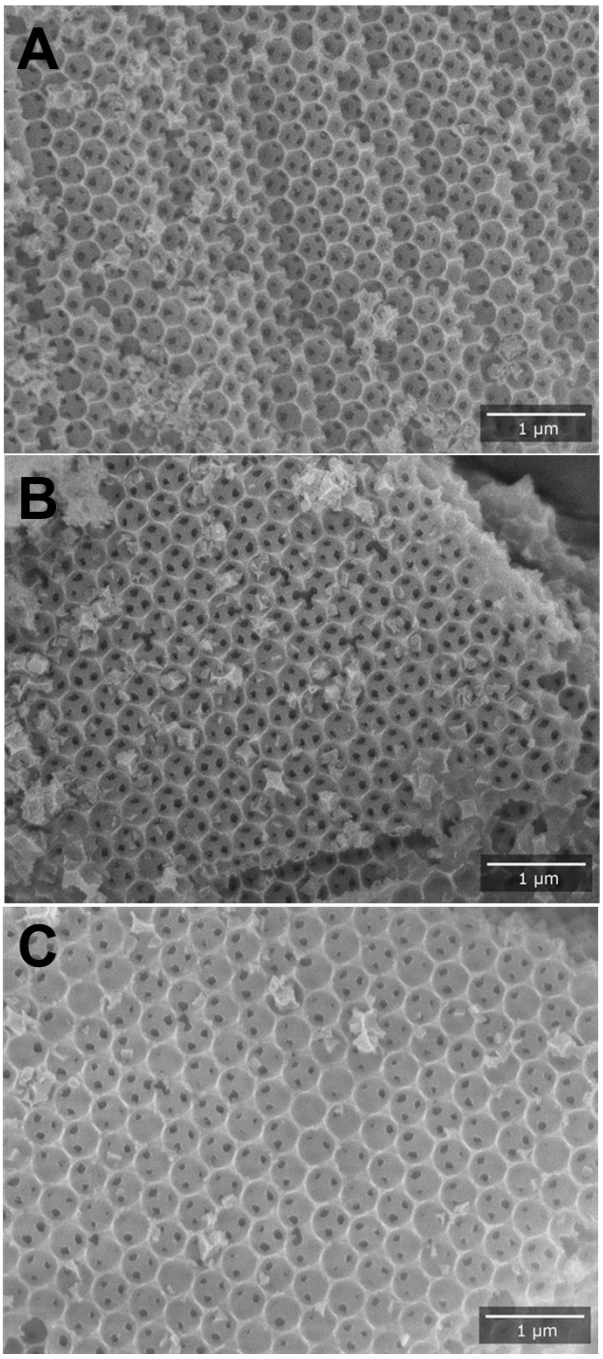

Figure 3.9. SEM images of (A) blue, (B) green, and (C) red 3DOM SiO_2 samples.

Before mixing 3DOM SiO_2 primary pigments, the powders were finely ground and sieved to achieve a more uniform appearance, both as single colors and as mixed colors in later steps. SEM images of 3DOM SiO_2 particles passed through a sieve with a mesh size of 38 μm show a wide range of particle sizes with an average size of 13.4±6.5 μm, i.e., much smaller than the mesh size (Figures 3.10 and 3.11). This size reduction was likely due to mechanical breakage of powder particles as they were forced through the sieve. Nonetheless, the resulting powders retained their intense coloration. Small changes in their UV-vis spectra (Figure 3.8) were likely due to the washing of carbonaceous absorber species from the surface of the 3DOM SiO_2 and due to less influence from large particles that can cause preferred orientation effects in the UV-vis spectra of unground samples.

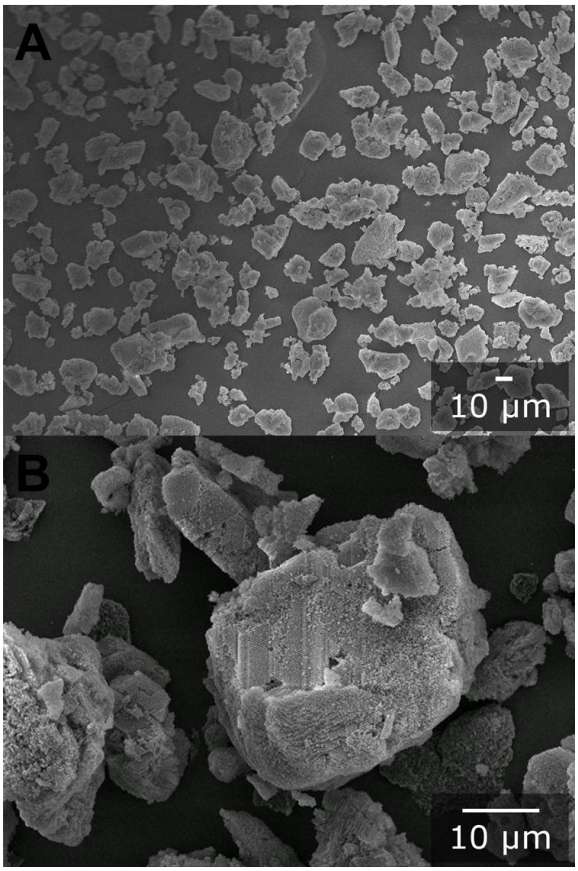

Figure 3.10. SEM images of 3DOM SiO_2 passed through a 38-µm sieve. The average particle size is 13.4±6.5 µm.

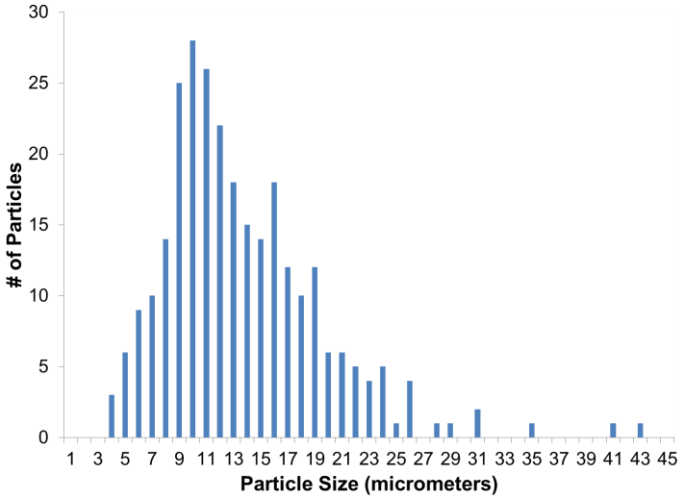

Figure 3.11. Histogram of the maximum measured particles dimensions from the SEM images in Figure 10.

The 3DOM SiO_2 primary colors were then mixed in identical mass amounts in order to study their color-mixing properties. Photographs of the mixed powders, the primary colors, and a color reference for RGB primaries can be found in Figure 3.12. Each combination of primary colors exhibited the expected mixed coloration with the blue/red, blue/green, and green/red combinations resulting in shades of magenta, cyan, and yellow. When all three primaries were mixed, a light grey coloration was achieved, which is an expected result when mixing primaries with low brightness. The grey tone was attributed to absorption by carbon residues in the pigments. The success of the two-color mixing is an important step in the implementation of 3DOM SiO_2 materials as specialty pigments.

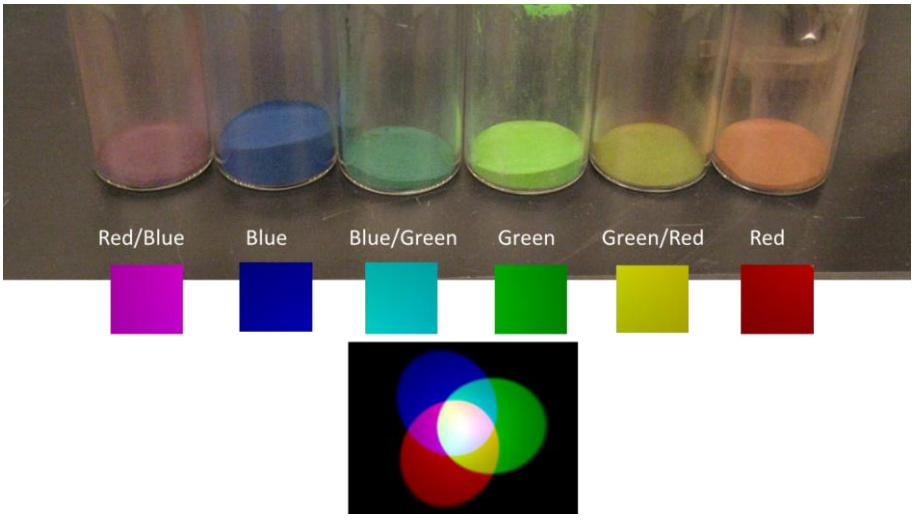

Figure 3.12. Image of mixed 3DOM SiO_2 primaries with a mixed RGB primary reference image. Color squares located below each sample are taken from the RGB primary reference and placed near each corresponding mixed sample.

3.4. Conclusions

We have demonstrated that control over the synthesis conditions of 3DOM SiO_2 materials provides a powerful approach to prepare pigments with structural color. 3DOM SiO_2 pigments could be prepared in numerous colors and color intensities through variations in template sphere size, as well as processing temperatures. The 3DOM SiO_2 materials exhibited structural densification at high temperatures following an approximately linear response within the temperature range studied, providing a potential tool for predictive color tuning. These 3DOM SiO_2 pigments retained their color properties even after grinding to particle sizes of ~10 μm. The final perceived color intensity (chroma) of the 3DOM materials was not solely a factor of stop band height, but rather a combination of several factors, including background absorption by residual carbon and structural densification.

An important observation from this study was the unique color mixing mechanism displayed by 3DOM SiO_2 pigments, which followed additive mixing rules, rather than the more conventional subtractive mixing for pigment particles. Based on this observation, blue, green, and red 3DOM SiO_2 pigment primaries were synthesized and ground to <38 μm to produce uniformly colored powders. By mixing these primary colors, it was possible to achieve new colors that corresponded to those predicted by an additive color mechanism.

The approach of controlling morphology and composition of silica described in this work provides opportunities to produce particles with tunable color properties that resist

photobleaching and are non-toxic and environmentally safe. With suitable scale-up, these materials can become interesting for specialty pigmentation and other color applications.

Chapter 4

The Synthesis and Characterization of 3DOM TiO_2/SiO_2 Composites as Photonic Materials with Stop Bands in the UV

4.1. Introduction

3DOM materials that possess color based on their structure have found applications as optical sensors[96, 144-145] and optical switches.[142-143] However, to date, photonic crystal materials have not been investigated for use in UV-blocking applications. Current UV-blocking technologies for cosmetic or material applications rely on either organic molecules that absorb UVA (320– 400 nm) or UVB (290–320 nm) radiation in a narrow band of the spectrum, or physical UV blockers such TiO_2 or ZnO, which have much broader coverage of both UVA and UVB radiation.[186-190] The organic blockers are typically molecules with conjugated carbonyl groups that absorb UV radiation and re-emit at lower-energy wavelengths. However, these molecules undergo photodegradation over time, even with the addition of certain molecular stabilizers. Another blocking mechanism is operative in the case of physical blockers such as TiO_2 and ZnO, both of which are semiconductors that absorb UV radiation based on their electronic band gaps. These physical blockers are not photobleached or discolored under UV radiation and can be made relatively transparent to visible light through modulation of particle size, shape, and distribution.[191-192]

Of all commercial UV blockers, TiO_2 provides the most uniform coverage throughout the UV range. However, its coverage between 350 nm and 400 nm (long-wave UVA) is considered insufficient and is often supplemented with organic absorbers or ZnO, which has adequate long-wave UVA coverage but low UVB coverage.[193] In this chapter, the use of 3DOM photonic materials, namely several TiO_2/SiO_2 compositions, is investigated in order to improve the coverage in the long-wave UVA range. Building on the absorbtion

properties of a physical UV blocker such as TiO_2 and extending its blocking effects using photonic stop bands has the potential to increase the already-significant UV coverage of TiO_2. Optical and structural properties of several compositions were investigated, and important considerations for the viability of these materials for UV blocking are discussed herein.

In addition, strategies to control or prevent solvent infiltration, which results in stop band shifts, in 3DOM materials were investigated. For certain applications that involve the use of 3DOM materials within liquid matrices, the prevention of liquid infiltration into the 3DOM structure may be important in order to maintain the desired stop band position and intensity. To prevent a solvent-induced stop band shift in 3DOM materials, several approaches are presented herein that incorporate template spheres or space fillers in the final structure. One strategy involved the use of SiO_2 sphere templates infiltrated with a high refractive index material (ZrO_2), conceptually resulting in a structure that would still contain regions of periodically-ordered refractive index contrast but could also be heated to high temperatures for processing.

A separate strategy to reduce solvent infiltration is also discussed that avoids thermal processing at high temperatures. A liquid precursor for silica, containing tetraethyl orthosilicate (TEOS), was infiltrated into a polymer sphere template to form a cross-linked gel at temperatures below the glass transition temperature of the polymer. The liquid precursor was then allowed to slowly dry and harden with the template spheres still present. This material was then impervious to solvent-induced stop band shifts.

Other parallel efforts are also presented herein which seek to employ such color shifts purposefully. In particular, UV 3DOM materials that are normally colorless when dry were investigated as solvent-shifted pigment materials using a dye as a contrast agent. These materials are of interest because of their UV blocking properties with added color effects. The dye was chosen on the basis of its low absorbance at the solvent-shifted stop band position. The increased reflectance at the position of the shifted stop band, along with the low absorbance in that region from the dye, produced a material that maintained intense coloration after the solvent-induced stop band shift.

4.2. Experimental

4.2.1. Materials

Reagents were obtained from the following sources: ammonia, tetraethyl orthosilicate, methyl methacrylate (99%), and zirconium acetate (in acetic acid) from Aldrich; HCl, isopropanol, potassium persulfate, and titanium tetraisopropoxide (TTIP) from Fisher; McCormick® Food dye (a mixture of FD&C Yellow 5 and FD&C Blue 1) obtained from a commercial source; air was obtained from an in-house system; water was distilled and deionized to achieve a resistivity of 18.3 MΩ·cm.

4.2.2. Poly(methyl methacrylate) PMMA Sphere Synthesis

A 4-neck, 3-liter flask was fitted with a Teflon-blade stirrer, a condenser, an NMR tube containing a thermocouple, and a glass pipette nitrogen bubbler. All attachments were affixed to the flask with rubber stoppers where necessary. The flask was placed in a heating mantle, and the thermocouple was connected to a temperature controller.

For the 270–280 nm spheres used in this study, 200 mL of methyl methacrylate (99%) (MMA) and 1900 mL of water was added to the flask, and the mixture was mechanically stirred at 350 RPM. While stirring, nitrogen was slowly bubbled into the solution and the flask was heated to 80 °C. After a stable temperature was reached, 2,2'-azobis(2-methylpropionamidine) dihydrochloride (97%) initiator was dissolved in 18 mL of water and added to the MMA/water mixture. The nitrogen bubbler was then removed and replaced with a glass stopper, and the polymerization mixture was left to react for ~3 h. The sphere suspension was then cooled and filtered through glass wool to remove any large polymer agglomerates that may have formed. The sphere synthesis typically yielded ~2.1 L of a 16 wt% suspension of PMMA spheres. For the synthesis of ~470 nm spheres, 1.6 L MMA, 0.4 L water and 1 g potassium persulfate was used and was heated to 70 °C with a stir rate of 350 RPM.

4.2.3. Colloidal Crystal Formation

The suspension was centrifuged at 1300 RPM for 3 days for the 270 nm spheres and at 1000 RPM for the 470 nm spheres. After centrifugation, water above the settled spheres was carefully removed by pipette without disturbing the ordered spheres. The remaining solid portion was left to dry for ~3 days. After drying, the template was easily broken apart by hand. Portions of the template that were difficult to break indicated incomplete drying and were left to dry further.

4.2.4. Synthesis of TiO_2/SiO_2 Liquid Precursor

A liquid precursor was synthesized containing various ratios of TiO_2 to SiO_2. A typical recipe for a liquid precursor containing 25 mol% TiO_2 and 75% SiO_2 (25:75) consisted of 2.41 g of TEOS (11.6 mmol) added to 2 g of isopropanol and 1 g of HCl. The mixture was then stirred using a magnetic stir bar for 1 min. After 1 min, 1.09 g of titanium tetraisopropoxide (TTIP) (3.8 mmol) was added dropwise with continued stirring. The solution became dark yellow in color and was stirred for ~5 min, resulting in a light yellow coloration. Other compositions ranging from 100 mol% SiO_2 to 100 mol% TiO_2 were synthesized according to the same procedure with variations only in the amounts of TEOS and TTIP used.

4.2.5. Synthesis of 3DOM TiO_2/SiO_2

The dried template was separated into 18 mL glass scintillation vials with ~1–2 g of template in each vial. The broken PMMA template pieces were placed at the bottom of a scintillation vial, and the precursor was pipetted onto the bottom of the vial using a 3:4 mass ratio of precursor:template. The materials were left to infiltrate for 24 h. After infiltration, any liquid remaining outside of the template was removed by pipette, the vial was opened to the air, and the template was allowed to dry for 24 h.

The dried precursor/template composite was then placed in a 20-mL alumina boat and heated inside a quartz tube within a Lindberg/Blue M 800W tube furnace. The synthesis was performed under 0.6 L/min of flowing air in order to remove carbon from the samples to increase transmittance in the visible range. The materials were heated at 5

°C/min to 550 °C and allowed to dwell at that temperature for 2 h before cooling to ambient temperature. Changes to sample amounts and bed thickness produced no variations in sample quality.

4.2.6. Incorporation of Dye into 3DOM Materials

A green commercial food dye consisting of FD&C Yellow 5 and FD&C Blue 1 was diluted with water to ~1% by volume. 3DOM materials with stop bands in the UV were then wetted with the diluted dye and dried. This process was repeated until a strong green coloration was observed upon wetting. The dyed 3DOM material was ground using a mortar and pestle.

4.2.7. Synthesis of SiO_2 Sphere Template

SiO_2 spheres were synthesized using a modified Stöber method.[194] Masses of 57.7 g ethanol, 18.5 g ammonia, and 5.8 g TEOS were placed in a flask and stirred for 24 h while covered. The resulting spheres had average diameters of 448±23 nm, estimated from SEM images. The sphere suspension was left to sediment in a crystallization dish for 4 days and allowed to dry. The resulting template pieces were opalescent.

4.2.8. Synthesis of 3DO SiO_2/ZrO_2

A mixture of 0.5 g zirconium acetate was diluted with 0.5 g methanol. The solution was then stirred for 5 min. An amount of 0.15 g of dried 448±23 nm SiO_2 sphere template was placed in a scintillation vial and 0.12 g of the liquid precursor was placed near the bottom of the template to be infiltrated by capillary action. The vial was sealed and allowed to infiltrate for 1 day. The composite was then allowed to dry and placed in a

quartz tube within a tube furnace and heated to 550 °C at 2 °C and held there for 2 h. Heating took place under either air or nitrogen.

4.2.9. Synthesis of SiO_2 Precursor for 3DO PMMA/SiO_2

A liquid SiO_2 precursor was prepared by mixing 1.5 g TEOS, 1 g methanol, 0.75 g water, and 0.25 g HCl. The mixture was stirred for 5 s and another 1.5 g TEOS was added in order to increase the SiO_2 density in the final product. An amount of 0.9 g of a dried PMMA template composed of 470 nm spheres was then placed in a scintillation vial. 0.68 g of the liquid SiO_2 precursor was placed near the bottom of the template to be infiltrated by capillary action. The vial was sealed and placed in an oven at 70 °C for 4 days.

4.2.10. Hydrophobic Coating of 3DOM SiO_2

3DOM SiO_2 was placed in a glass scintillation vial. Ca. 10 mL of "Liquid Wrench" silicone spray was sprayed into a glass beaker and left to de-foam. The silicone spray was then added dropwise to the 3DOM SiO_2 until the powder was wetted. Excess liquid was removed by pipette. The wetted sample was placed in an alumina boat and inserted into a quartz tube. The quartz tube was capped with rubber stoppers fitted with glass pipettes and nitrogen was flowed through the tube at 0.6 L/min. The furnace was heated at 20 °C/min to 500 °C and then allowed to cool.

4.2.11. Grinding of 3DOM Powders

3DOM powders were placed on a 38–µm stainless steel mesh sieve. The 3DOM powder and mesh were wetted with ethanol. The 3DOM powder was then gently rubbed

into the mesh using a gloved finger with frequent washings of the mesh with ethanol into a collection pan. This was done until no powder remained. The ethanol/3DOM suspension was then poured into a 0.75 L polyethylene bottle and allowed to sediment for 24 h. After this time, the ethanol was carefully removed by pipette until ~10 mL of ethanol and the sedimented 3DOM powder were left. This mixture was then washed out of the bottle with ~10 mL ethanol into a 20 mL scintillation vial. The suspension was again allowed to sediment for 24 h, after which time the ethanol was removed by pipette. The remaining wet powder was placed in an oven at 100 °C until dry.

4.2.12. Characterization

Diffuse reflectance UV-vis spectra were obtained using a Fisher Scientific Evolution 220 UV-vis spectrometer with an Evo 200 Integrating Sphere reflectance spectroscopy attachment. Select spectra were smoothed using an exponential smoothing algorithm. Scanning electron microscopy (SEM) images were obtained using a JEOL 6700 scanning electron microscope operating at 5 keV. Samples were prepared for the SEM by lightly dusting them onto adhesive carbon and affixing them to aluminum mounts. All samples were then coated with 50 Å of platinum. SEM measurements were performed using ImageJ software. XRD was performed on a Panalytical X'pert Pro diffractometer with a cobalt source (Kα, λ = 1.789 Å) operated at 45 kV, 40 mA.

For thin-film UV-vis measurements, the synthesized 3DOM powders were crushed between two quartz slides or discs in the presence of ethanol. The powders were crushed until no large particles were visible. Figure 4.1 shows a typical film with a thickness of <100 μm. The average particle size after crushing was estimated to be <50 μm by optical

microscopy. The films were allowed to dry and maintained adhesion to the quartz substrate.

Figure 4.6. 3DOM TiO_2/SiO_2 film after being dropped onto a quartz disc, together with a standard US quarter.

4.3. Results and Discussion

4.3.1. 3DOM Materials with UV Stop Bands

The use of 3DOM TiO_2/SiO_2 materials for UV applications requires a photonic stop band below 400 nm in order to diffract wavelengths in the UV and maintain a colorless appearance. The location of the stop band is approximated by a combination of Bragg's and Snell's laws presented in Chapter 1, Equation 1.2, where d_{hkl} is defined by Equation 1.3 for the face-centered cubic structure.

For this study, it was found that, for the materials involved, a template sphere size between 270 and 280 nm was ideal to place the stop band just below 400 nm. A stop band at this position resulted in materials that were not colored, but possessed a stop band that could influence the reflectance of UV light.

Intensely colored 3DOM SiO_2 with stop bands in the visible spectrum has been previously synthesized (Chapter 3). The use of SiO_2 for color applications is favorable due to its low toxicity, environmental abundance, and its ability to form well-ordered and homogeneous 3DOM materials. The structural advantages come from the SiO_2 precursor's ability to crosslink over an extended network. However, for UV applications, the stop bands in 3DOM SiO_2 are not intense enough to make an appreciable difference in UV coverage when compared to other non-nanostructured materials that are currently used for UV blocking such as TiO_2 or ZnO.

3DOM TiO_2 has also been previously synthesized for color applications (Ben Wilson, unpublished work). However, the materials did not exhibit intense stop bands due to reduced structural homogeneity and high residual carbon content. In order to create UV reflective materials that also possessed high absorbance in the UV, a composite material of SiO_2 and TiO_2 was synthesized. The SiO_2 portion of the material was present to provide structural regularity while the TiO_2 portion provided high UV absorbance as well as an increased contrast in index of refraction. The material was heated in air to remove absorbing carbon species and improve transparency in the visible region.

4.3.2. Incorporation of TiO_2 into 3DOM SiO_2

TiO_2 was initially added as 25 mol% in 75 mol% SiO_2 (3DOM TiO_2/SiO_2 25:75) in order to observe the effects of incorporated TiO_2. Figure 4.2 shows the differences in the reflectance spectra of pure 3DOM SiO_2 vs. 3DOM TiO_2/SiO_2 25:75. The UV-vis spectra shown in Figure 4.2 correspond to bulk powders with a thickness <2 mm. The most apparent difference between the two spectra is the presence of the TiO_2 band edge

beginning at ~390 nm. In the 3DOM SiO_2 sample, no band edge is present in this region due to the lack of TiO_2. The stop band itself is much more pronounced in the spectrum for 3DOM SiO_2. This is due to the absence of any light absorption by the material at or around the location of the stop band. For the 3DOM TiO_2/SiO_2 25:75, light absorption by the solid skeleton diminishes the extent of light propagation through the photonic crystal structure and hence the observable effect of the stop band at wavelengths where absorption occurs. Ideally, the stop band should be placed outside of any regions of high absorbance to facilitate diffraction events that are vital for photonic reflection.

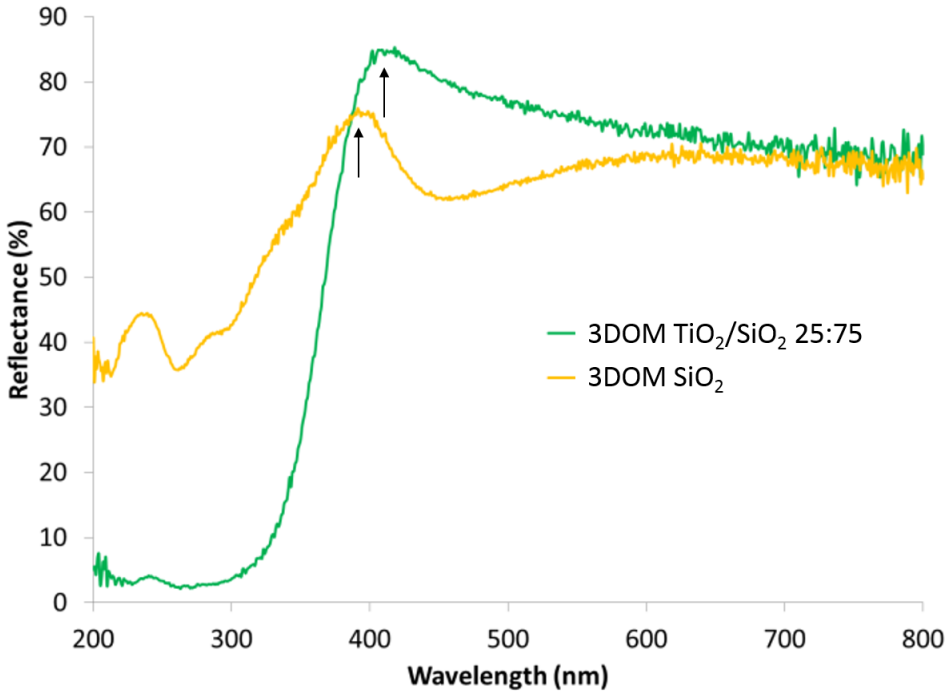

Figure 4.27. UV-vis reflectance spectra of 3DOM TiO_2/SiO_2 25:75 compared to 3DOM SiO_2. Relevant features include the TiO_2 band edge (region of low reflectance <400 nm) as well as the photonic stop bands for both materials (marked with arrows).

To investigate the effects of the 3DOM nanostructure on the UV-vis spectrum of 3DOM TiO_2/SiO_2 25:75, the spectrum was compared to that of a bulk material with the same composition (Figure 4.3). The purpose of incorporating nanostructure into these materials was to improve the coverage in the UVA range. It is, therefore, important to investigate other potential optical changes that arise due to nanostructuring. The untemplated material was synthesized using the same liquid precursor but without the templating step involving PMMA spheres. One important difference between the UV-vis reflectance spectra of the untemplated and 3DOM TiO_2/SiO_2 25:75 samples is the position of the band edge, which was determined to be 390 and 379 nm, respectively, by extrapolation of the slope of the band edge through the inflection point of the band edge curve to the x-axis. For the determination of the band edge in the untemplated sample, a Kubelka-Munk transformation was used to correct the spectrum due to the sample's isospectral scattering. For 3DOM materials, several assumptions of the Kubelka-Munk function, such as isospectral scattering and zero transmittance, break down.[195-196] Therefore, uncorrected absorbance data were used for band-edge determination in all 3DOM samples. Similar uncorrected measurements have also been performed on films of TiO_2 nanoparticles with consistent and verifiable results.[197] Values obtained using these methods in 3DOM materials were also confirmed through crystallographic data, discussed later in this chapter. The shifting of the band edge is likely due to quantum size effects resulting from regions of TiO_2 dispersed within larger regions of SiO_2. These effects are discussed in more detail later in this document. The UV-vis spectra in Figure 4.3 also reveal an increase in incoherent scattering properties in the templated material. This increase in scattering is due to the multiple material surfaces created through the

templating process. The increased incoherent scattering along with any stop band reflectance at wavelengths longer than 400 nm will potentially limit the transparency of these materials in the visible range.

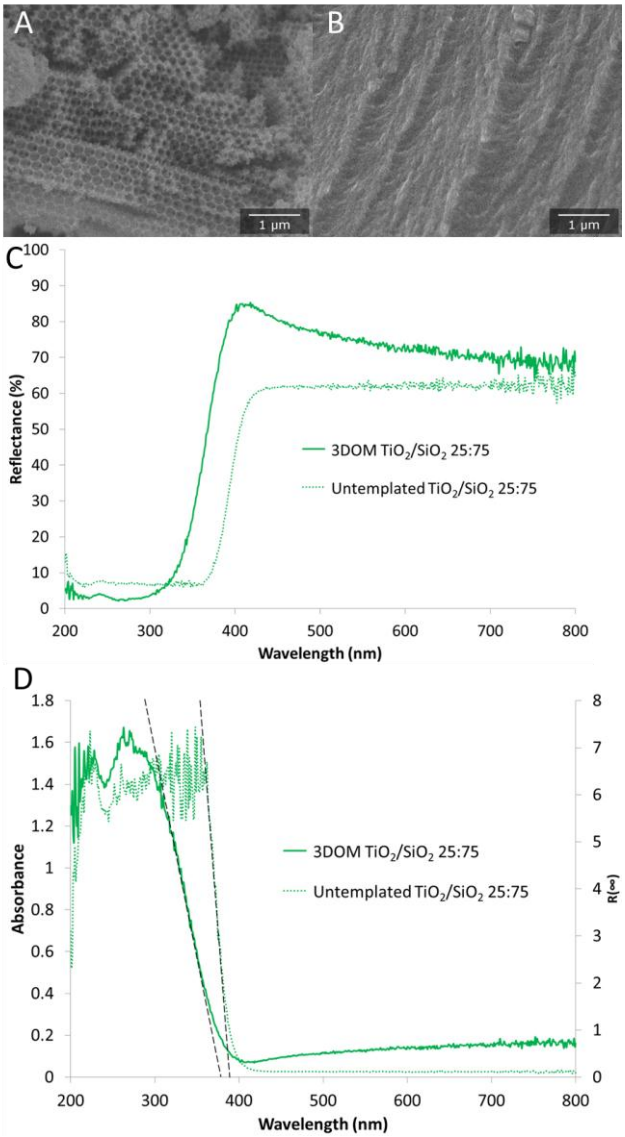

Figure 4.3. SEM images of (A) 3DOM TiO_2/SiO_2 25:75 and (B) untemplated TiO_2/SiO_2 25:75, showing the presence (A) or absence (B) of templated nanostructure within the materials. (C) UV-vis reflectance spectra of 3DOM TiO_2/SiO_2 25:75 and untemplated TiO_2/SiO_2 25:75, illustrating differences in band edge position and scattering effects. (D) UV-vis absorbance spectra of 3DOM TiO_2/SiO_2 25:75 (left axis, absorbance) and untemplated TiO_2/SiO_2 25:75 (right axis, R(∞), Kubelka-Munk) used to determine band-edge positions by extrapolation of the slope through the inflection point of the band-edge curve to the x-axis, shown as a black dotted line.

4.3.3. Optical and Structural Properties of Various Compositions of 3DOM TiO_2/SiO_2

3DOM TiO_2/SiO_2 samples containing 5, 25, 50, and 75 mol% TiO_2 in SiO_2, as well as 100% 3DOM TiO_2 and 100% 3DOM SiO_2 were synthesized in order to compare the optical properties of various compositions of 3DOM TiO_2/SiO_2. Figure 4.4 shows the UV-vis reflectance spectra of ground powders of these samples with a bed thickness of ca. 1–2 mm. Starting with pure 3DOM SiO_2, as the TiO_2 content was increased, the TiO_2 band edge became increasingly more prominent up to 25 mol% TiO_2. The band edge then shifted to longer wavelengths for samples with higher TiO_2 concentration, confirming that size effects are the likely cause of the shifting band edge. The values for the band-edge positions were determined through the extrapolation of the band edge slope as it passes through the inflection point of the curve. These values were then used to estimate TiO_2 domain size according to established procedures.[197] Values for the band edge position, TiO_2 size, as well as other structural and spectral information can be found in Table 4.1.

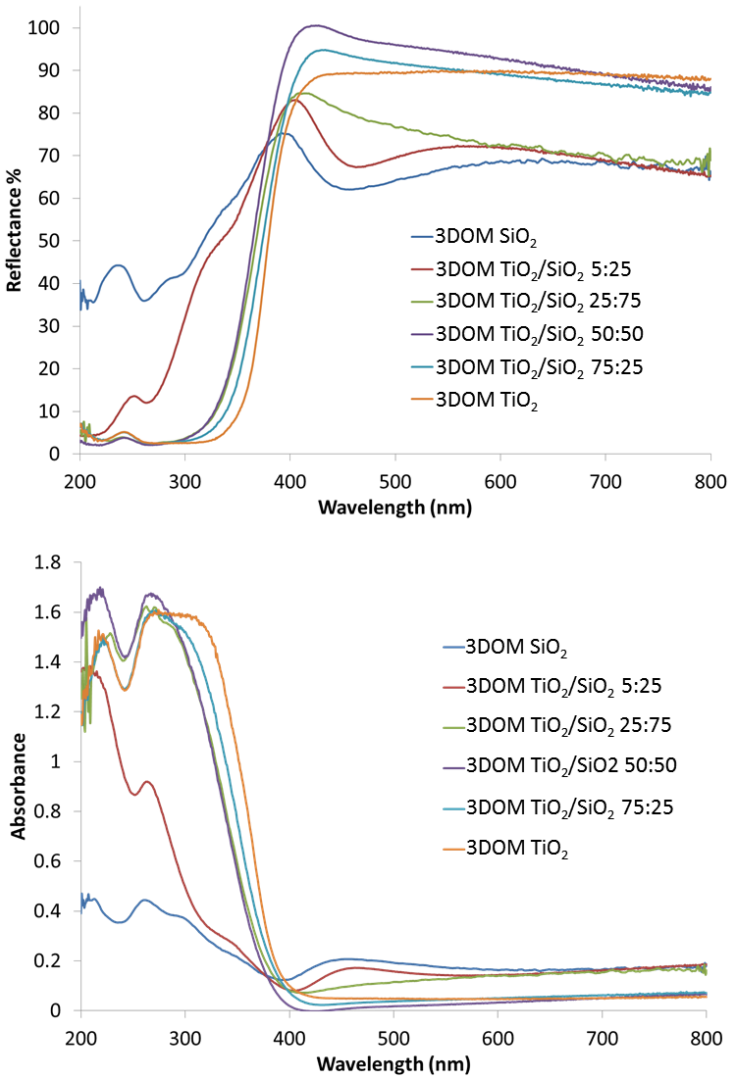

Figure 4.4. UV-vis spectra of various compositions of 3DOM TiO_2/SiO_2. Reflectance spectra (top) show a shifting band edge with increased TiO_2 content as well as the diminishing stop bands at ~400 nm. Absorbance spectra (bottom) were used to estimate TiO_2 particle size.

Table 4.1. Selection of measured and calculated values for various 3DOM material compositions of TiO_2 in SiO_2 as well as pure SiO_2 and TiO_2.

% TiO_2 in SiO_2	n_{wall}[a]	n_{avg}[b]	Fill fraction[c]	Stop band[d] (nm)	Pore size[e] (nm)	Band edge[f] (Abs) (nm)	TiO_2 size (Abs)[g] (Å)	Crystallite size[h] (Å)	Band edge[i] (XRD) (nm)
0	1.46	1.06	0.14	395	228 ± 3	N/A	N/A	N/A	N/A
5	1.51	1.07	0.18	405	227 ± 5	N/A	N/A	N/A	N/A
25	1.71	1.10	0.14	410	229 ± 3	379	27.87	30	379
50	1.97	1.14	0.14*	414†	223 ± 9	378	26.86	30	379
75	2.23	1.17	0.14*	400†	209 ± 2	385	36.5	41	385
100	2.49	1.21	0.14*	412†	213 ± 4	389	53.24	142	391

[a] n_{wall} calculated using standard refractive indices for TiO_2 (2.488) and SiO_2 (1.455) adjusted using mol% values as vol%. Actual material refractive indices may deviate from this value.
[b] n_{avg} calculated using standard refractive indices for TiO_2 (2.488), SiO_2 (1.455), and air (1) and assuming a solid fill fraction of 0.14. Actual material refractive indices may deviate from this value.
[c] Determined using stop band position (UV-vis) and pore size (SEM) data.
[d] Determined by UV-vis reflectance spectra.
[e] Measured using SEM images.
[f] Extrapolated using the slope of the absorbance curve through the inflection point of the band edge.
[g] Calculated using band edge position.[197]
[h] Calculated from XRD line broadening data using the Scherrer equation.
[i] Calculated using TiO_2 crystallite size determined by XRD.
*Approximated value based on fill fractions determined for 3DOM SiO_2, TiO_2/SiO_2 5:25, and TiO_2/SiO_2 25:75.
†Calculated value based on 0.14 solid fill fraction, calculated n_{avg}, and measured pore spacing.

Two prominent spectral differences between samples in Figure 4.4 were the stop band positions and the band edge positions. The relative position of the stop bands changed as TiO_2 concentration was increased. With increased TiO_2 content, a red-shift in peak position was observed for materials that possessed similar pore sizes according to Table 4.1. The stop band position for 3DOM SiO_2, 3DOM TiO_2/SiO_2 5:95, and 3DOM TiO_2/SiO_2 25:75 red-shifted with increasing TiO_2, consistent with the increase in average index of refraction of the material. However, for TiO_2 concentrations greater than 25 mol%, the stop band intensity diminished as greater amounts of TiO_2 were incorporated.

A shift in stop band position between materials that are synthesized from the same template spheres can typically be caused by a number of factors, including changes in overall refractive index and pore size changes due to different shrinkage properties of various components during calcination. With the addition of TiO_2 into the 3DOM structure, a rise in average refractive index of the wall material is expected due to the high refractive index of anatase TiO_2 (2.488) relative to SiO_2 (1.455). However, this red-shift is mitigated to a certain degree by the shrinkage characteristics of the different materials at high calcination temperatures. Higher TiO_2 content should increase the shrinkage (typically ~20% for pure TiO_2 vs. ~15% for pure SiO_2)[64] of the structure after calcination due to increased densification as crystalline TiO_2 is formed. These competing factors make the prediction of stop band location difficult based on refractive index alone. In addition to these factors, the observed position of the stop band maxima after these properties are considered may not correspond to the actual stop band position. This is due to the high absorbance at the onset of the TiO_2 band edge, which causes a part of the reflectance peak to be truncated. This results in a reflectance peak that appears to be located at slightly higher wavelengths than the band edge when, in reality, it may be extending into it. Table 4.1 shows values for the measureable stop band positions for 3DOM SiO_2, 3DOM TiO_2/SiO_2 5:95, and 3DOM TiO_2/SiO_2 25:75. The fill fraction was calculated using Equation 1.4 in Chapter 1 with n_{avg} broken down into fill fraction and refractive index of each component, with peak positions measured by UV-vis spectroscopy and pore sizes measured by SEM. The stop band positions for 3DOM TiO_2/SiO_2 50:50, 3DOM TiO_2/SiO_2 75:25, and 3DOM TiO_2 were then calculated using a fill fraction of 0.14 along with measured pore sizes and the expected n_{avg} of each

composition. The stop band positions were calculated to be at 414 nm, 400 nm, and 412, nm respectively. Each of these values lies within a region of the spectrum that has increased absorbance due to the TiO_2 band edge, confirming the likelihood that the stop band peaks were obscured.

This was confirmed by infiltrating the higher TiO_2 samples with ethanol in order to red-shift the stop band into the visible region where it could be observed (Figure 4.5). Expected stop band positions for ethanol-infiltrated 3DOM TiO_2/SiO_2 75:25 and 3DOM TiO_2 were calculated using the same parameters used above with the refractive index of air substituted with the refractive index of ethanol. Values of 506 nm and 518 nm were obtained for the stop band positions of these infiltrated materials. The UV-vis spectra in Figure 4.5 confirm the expected stop band shift and show that stop bands are present in the dry material but are obscured by the absorbing band edge of TiO_2. The agreement between calculated and experimental values for stop band positions in the ethanol-infiltrated samples also confirmed that the previously calculated values for the stop band position of the dry samples were valid. It was also observed that the reflectance intensity of the stop band for the pure 3DOM TiO_2 is much smaller and broader than that of 3DOM TiO_2/SiO_2 75:25. SEM analysis of all of the materials gives some insight into the diminished photonic properties observed for these samples.

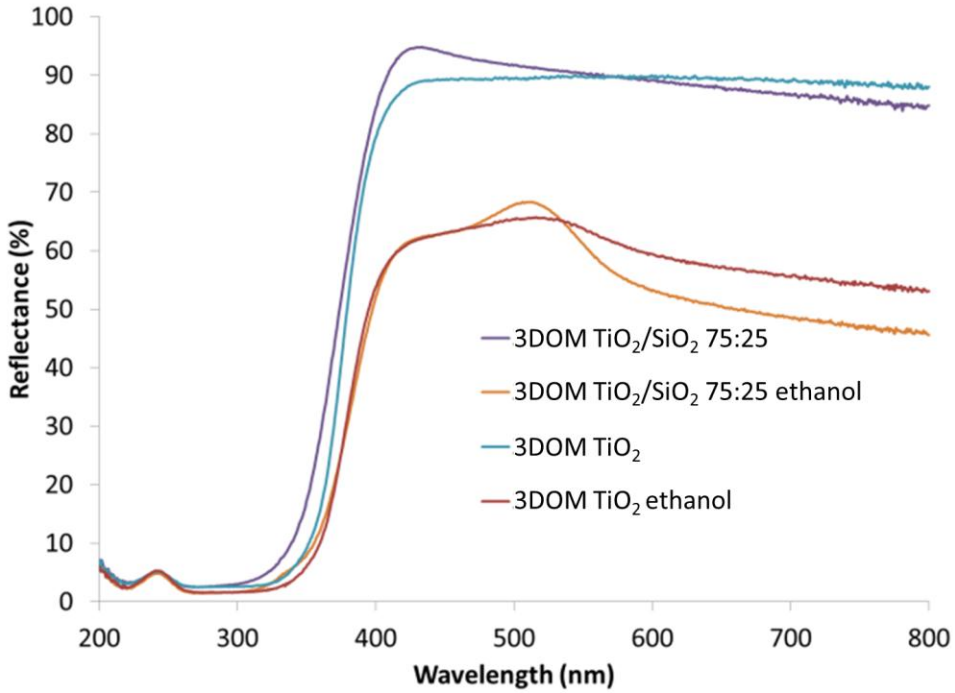

Figure 4.5. UV-vis spectra of high-TiO_2 content 3DOM TiO_2/SiO_2 with and without infiltrated ethanol. The infiltrated 3DOM exhibited red-shifted stop bands that were no longer influenced by the TiO_2 band edge to facilitate observation.

SEM images of 3DOM SiO_2, all 3DOM TiO_2/SiO_2 samples, as well as 3DOM TiO_2 can be found in Figure 4.6. The 3DOM SiO_2, 3DOM TiO_2/SiO_2 5:95, and 3DOM TiO_2/SiO_2 25:75 samples (Figure 4.6, A, B, C) exhibited the greatest degree of structural order with large domains of well-ordered pores. However, as the TiO_2 content was increased relative to SiO_2 content, the long-range structural order began to break down, as observed in Figure 4.6 D, E, F. This breakdown of long-range order was a likely culprit for the diminished stop band in the 3DOM TiO_2 sample synthesized using the methods herein.

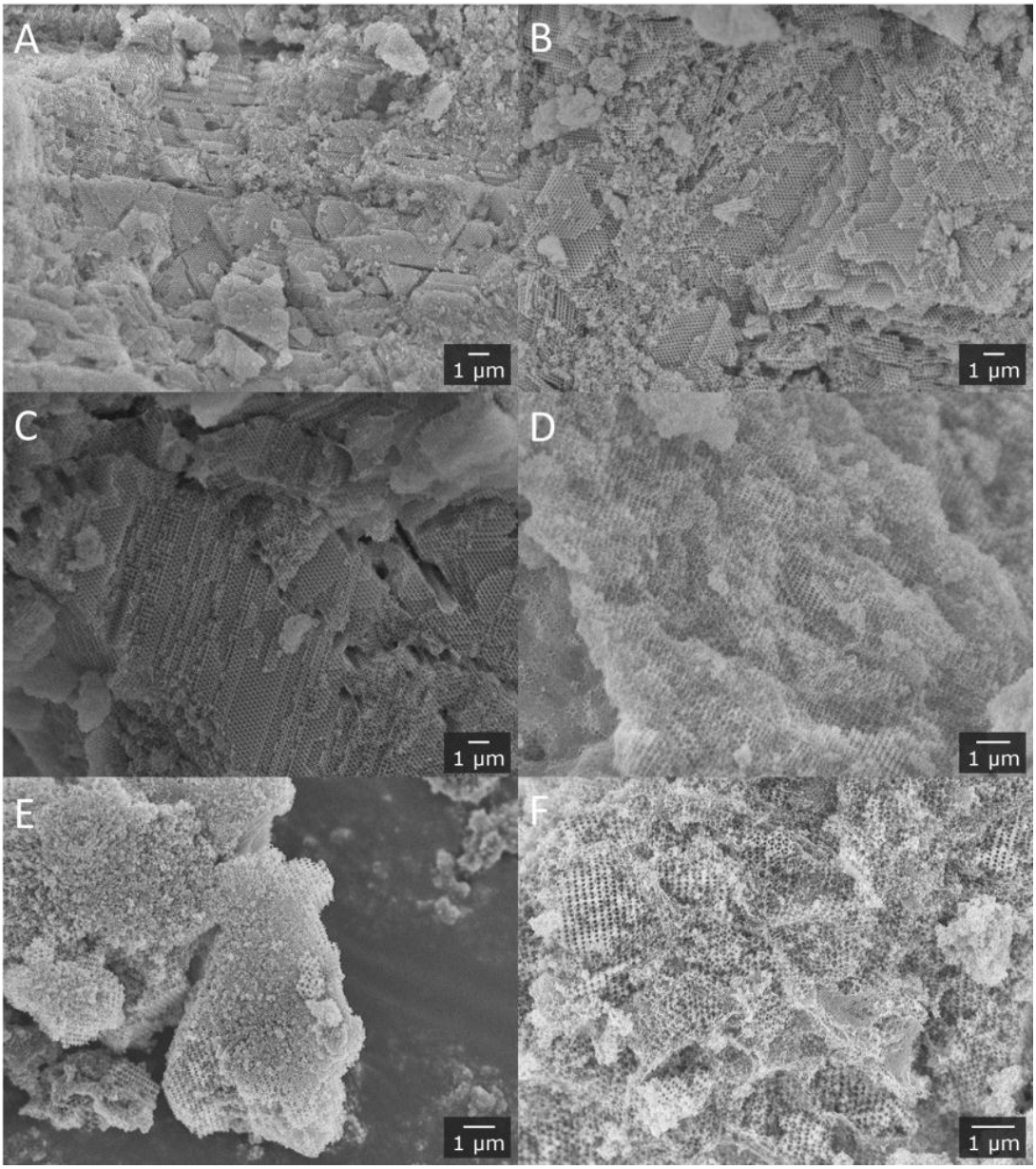

Figure 4.6. SEM images of various compositions of 3DOM SiO_2, 3DOM TiO_2/SiO_2, and 3DOM TiO_2. (A) 0:100 (B) 5:95, (C) 25:75, (D) 50:50, (E) 75:25, (F) 100:0. The structures are observed to become more irregular over large areas at higher TiO_2 concentrations.

X-ray diffraction (XRD) patterns were obtained for each sample containing TiO_2 in order to estimate TiO_2 domain size and phase (Figure 4.7). The XRD patterns show that increased TiO_2 concentration produces larger TiO_2 crystallites, as expected from band

edge positions. All TiO_2 domains that could be analyzed consisted of the low-temperature anatase phase. 3DOM TiO_2/SiO_2 25:75 and 50:50 produced similar patterns, which supports their similar band edge positions. TiO_2 domain size data extracted by analyzing peak line broading in the XRD patterns by the Scherrer equation suggested similar domain sizes as estimates from the observed band edge positions.

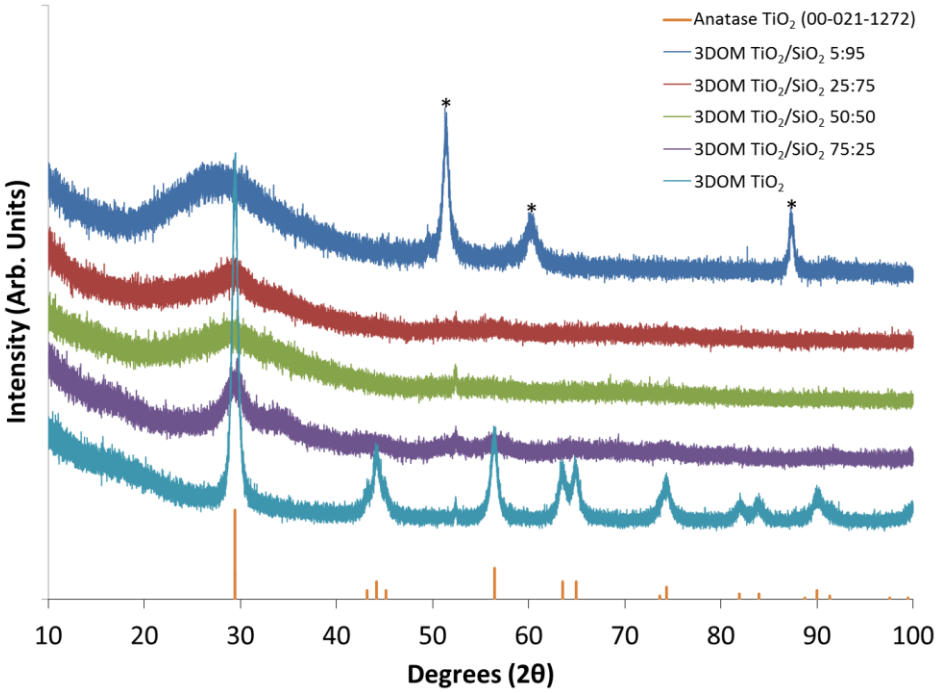

Figure 4.7. XRD patterns of all 3DOM TiO_2/SiO_2 compositions as well as 3DOM TiO_2. Patterns show increased peak broadening with low TiO_2 concentrations. Peaks from the sample holder are starred.

4.3.4. Optical Properties of Thin-film 3DOM TiO_2/SiO_2

In order to determine the effectiveness of these materials as UV-blocking structures on skin, their performance as thin films was determined. The following characterization experiments were performed by dropping a slurry of ground 3DOM particles mixed with ethanol onto a quartz disc and allowing it to dry. The maximum 3DOM particle size was

estimated to be <40 μm. However, the thickness of each film was difficult to determine as the act of measuring thickness altered the thickness of the film. It is important to note that changes in film thickness can account for differences in transmittance, scattering, and absorbance between each of the samples analyzed. Exact values for transmittance and reflectance differed greatly with changing film thicknesses.

Figure 4.8 shows reflectance and transmittance spectra for each thin film prepared using 3DOM TiO_2/SiO_2 with different TiO_2 concentrations. Reflectance and transmittance measurements for each sample were performed on the same thin film using different apertures in the UV-vis spectrometer. Each sample exhibited a sloping baseline from 400 nm to 800 nm that corresponded to the incoherent scattering of photons from the structural surfaces. The stop band was observed in the transmittance spectra as a truncation of that curve at ~400 nm. The corresponding position in the reflectance spectra showed the same stop band peak followed by increased absorbance due to the TiO_2 band edge. Also noticeable in the transmittance spectra were the TiO_2 band edge positions for each different material, which shifted to higher wavelengths as the TiO_2 concentration was increased.

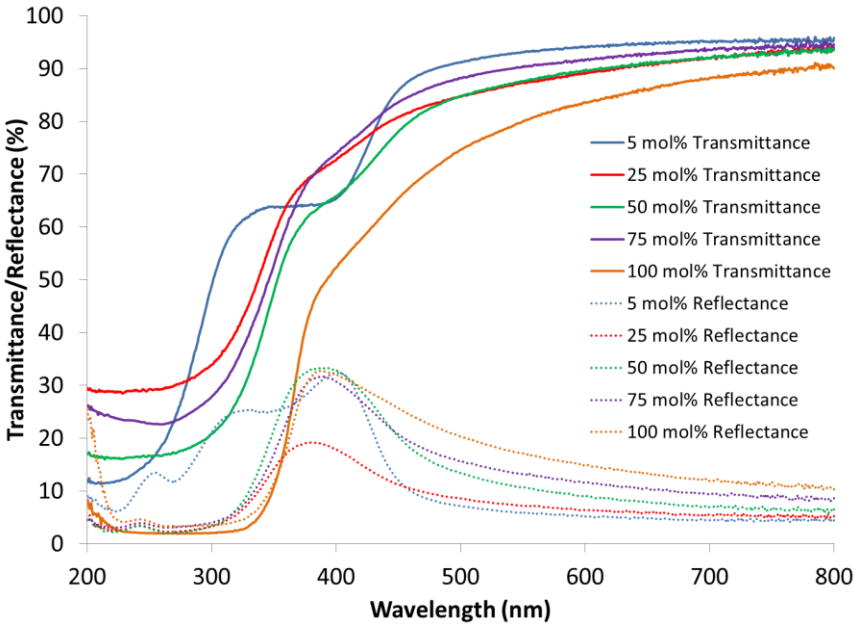

Figure 4.8. UV-vis reflectance and transmittance spectra for various compositions of 3DOM TiO_2/SiO_2.

The effect of 3DOM film thickness on transmittance and reflectance properties was further analyzed by performing UV-vis transmittance measurements on a 3DOM thin film as its thickness was increased with successive drops of 3DOM particle/ethanol slurry. Figure 4.9 illustrates the effects of film thickness on the transmittance properties of a 3DOM TiO_2/SiO_2 25:75 film. The spectra indicated that as the film thickness was increased from ~30 μm to ~100 μm, the incoherent scattering of light also increased, resulting in a decrease in transmittance at lower visible wavelengths above the band edge. The influence of the stop band also increased with larger film thickness due to the presence of more 3DOM particles causing coherent diffraction. In order to determine an ideal thickness for films of these materials, it will be necessary to balance the advantage of a larger stop band with the disadvantage of lower transmittance in the visible range.

Band edge positions for each film thickness also varied with changes in thickness. Band edge shifts observed in Figure 4.9 with increasing thickness are not true band shifts and are instead a result of increased scattering affecting the transmittance properties as thickness is increased. The true effect of the stop band on the extension of the UV coverage of these materials is difficult to determine due to the heavy influence of scattering at approximately the same region as the stop band position. Materials used in current UV blocking technologies have been optimized through size and shape manipulation to control this scattering.[191-192] While this incoherent light-scattering assists in the blocking of UV transmission in these materials, it gives the films a white appearance that is undesirable in personal UV protection products.

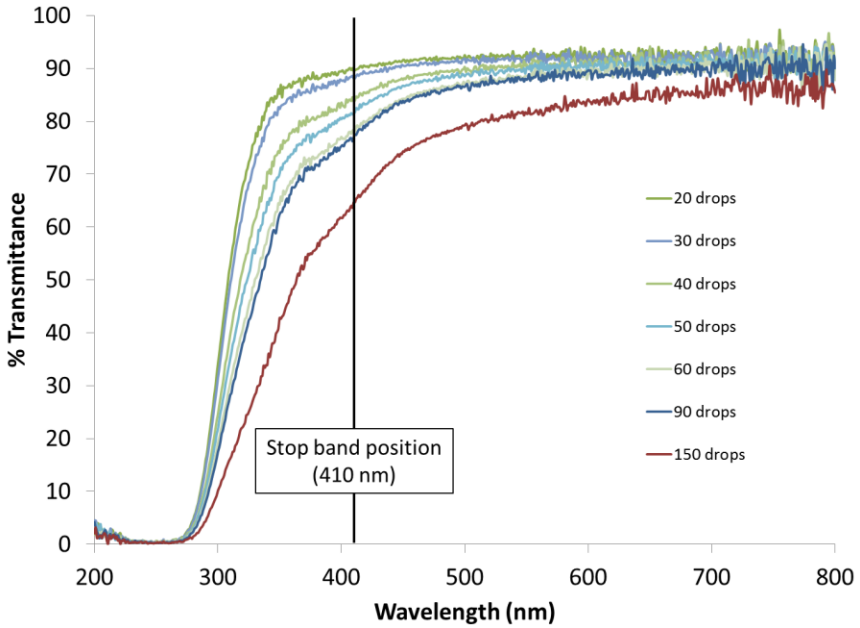

Figure 4.9. UV-vis spectra of thin films of 3DOM TiO_2/SiO_2 25:75 with increasing thicknesses. Maximum thickness was estimated to be ca. 100 µm for 150 drops of the slurry.

4.3.5. Solvent-Shifted 3DOM TiO_2/SiO_2 for Color Pigments

After observing the solvent-induced stop band shifts found in Figure 4.5, it was hypothesized that UV 3DOM materials could become colored after infiltration with specific solvents. However, due to the absence of carbon within the structure, as discussed in Chapter 2, the materials were still mostly white with only slight coloration. The role of carbon in intensely-colored 3DOM materials is to reduce the overall reflectance of the material across the visible spectrum so that the influence of the stop band can be perceived visually. Rather than re-introduce carbon into the structure using established procedures,[166] a more selective absorbing species was utilized that did not absorb across the entire visible spectrum.

3DOM TiO_2/SiO_2 5:95 was infiltrated with a diluted commercial food dye (FD&C Yellow 5 and FD&C Blue 1) and dried in order to incorporate a contrast agent into the structure. Rather than absorb across the entire visible spectrum like carbon, the dye was chosen in order to selectively absorb at wavelengths other than the position of the solvent-shifted stop band of 3DOM TiO_2/SiO_2 5:95. The UV-vis spectra of the dye as well as the 3DOM materials before and after the dye incorporation can be found in Figure 4.10 along with a final UV-vis spectra of the dyed and solvent-infiltrated 3DOM TiO_2/SiO_2 5:95. The absorbance spectrum of the green dye (right axis) shows a low absorbance between 500 nm and 550 nm and higher absorbance at the wavelengths surrounding that range. The low-absorbance range of wavelengths also corresponds to the position of the stop band in the ethanol-infiltrated 3DOM TiO_2/SiO_2 5:95. This created a situation where the solvent-shifted stop band lies in a low-absorbing range of

wavelengths of the contrasting agent. The combination of increased reflectance from the stop band in that region along with decreased reflectance at surrounding wavelengths due to the presence of the green dye contrast agent created a vibrant green color that was only observed upon solvent-shifting of the stop band position (Figure 4.11). After the solvent was allowed to dry, the color intensity decreased again due to the blue-shifting of the stop band position back into the UV range. These findings open up the way for future photonic color pigments that are amenable to infiltration without the drastic reduction in coloration that usually occurs due to a combination of index-matching and material absorbance.

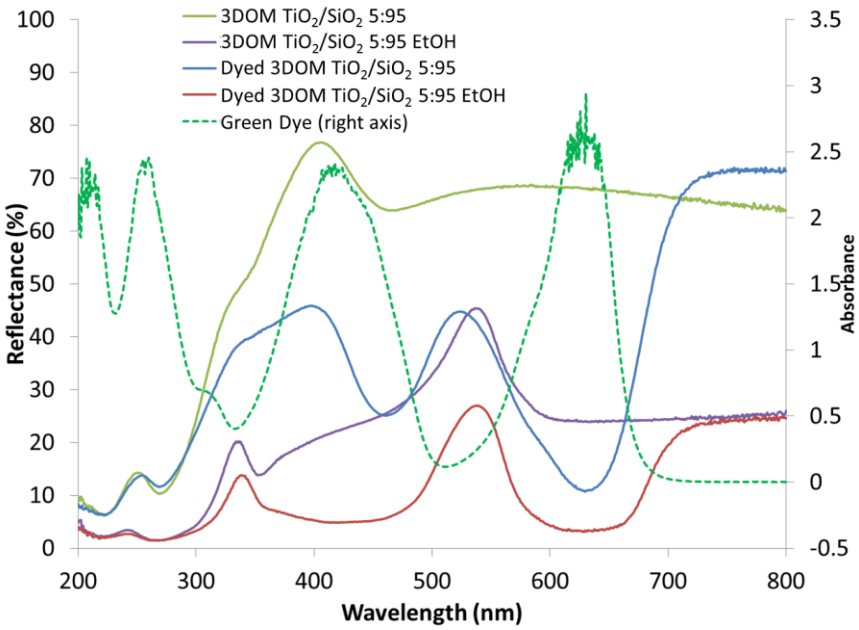

Figure 4.10. UV-vis spectra of white and dyed 3DOM TiO_2/SiO_2 5:95 with and without ethanol infiltration as well as the absorbance spectrum of the green dye. The stop band position of 3DOM TiO_2/SiO_2 5:95 was observed to line up with the low-absorbance range of the green dye.

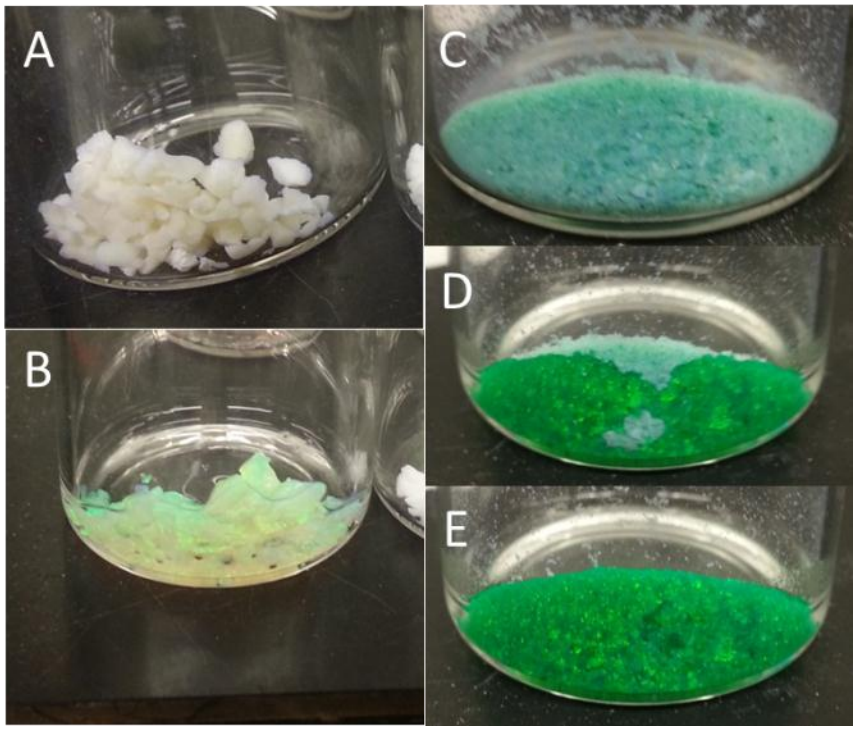

Figure 4.11. Images of dyed 3DOM TiO_2/SiO_2 25:75. (A) 3DOM TiO_2/SiO_2 25:75. (B) Ethanol-infiltrated 3DOM TiO_2/SiO_2 25:75. (C) 3DOM TiO_2/SiO_2 25:75 after dye infiltration and drying. (D) Dyed 3DOM TiO_2/SiO_2 25:75 partially wetted with ethanol. (E) Dyed 3DOM TiO_2/SiO_2 25:75 after ethanol infiltration.

4.3.6. Prevention of Solvent Infiltration in 3DOM Materials

For future applications in both UV blocking products and color pigment systems, 3DOM materials may be used inside various liquid matrices, depending on the intended function. Liquid infiltration, however, shifts the stop band location of the materials. In order to avoid this infiltration, several strategies can be employed. One such strategy involved coating 3DOM particles with a hydrophobic silicone layer. This method was viable for preventing water infiltration but was not appropriate for low-contact angle polar solvents or non-polar solvents. Due to this, other strategies were devised to prevent liquid infiltration by eliminating pore space entirely.

4.3.6.1. Hydrophobic Coating for 3DOM Materials

One strategy to prevent the infiltration of liquids into the pores of 3DOM SiO_2 was to coat the surface of the 3DOM walls with a material that would repel water and make infiltration by water unfavorable. To achieve this, already-made 3DOM SiO_2 particles were wetted with a commercial silicone spray (Liquid Wrench™) consisting of PDMS in a hydrocarbon solvent. The wetted powder was then heated at 10 °C/min to 500 °C under 0.6 L/min flowing N_2 and allowed to cool. The heating process removed the volatile hydrocarbons and deposited a hydrophobic coating on the 3DOM SiO_2 powder.

After heating, the powder became impervious to infiltration by water (Figure 4.12) while experiencing a slight improvement in reflectance% according to UV-vis data (Figure 4.13). The hydrophobic coating also repelled other polar solvents with high surface energies such as ethylene glycol. The powder was still susceptible to infiltration by low surface tension liquids such as ethanol, methanol, and isopropanol. The increase in reflectance was possibly due to a smoothing of the pore walls after coating. These powders retained their hydrophobic properties for at least 1.5 years after initial coating.

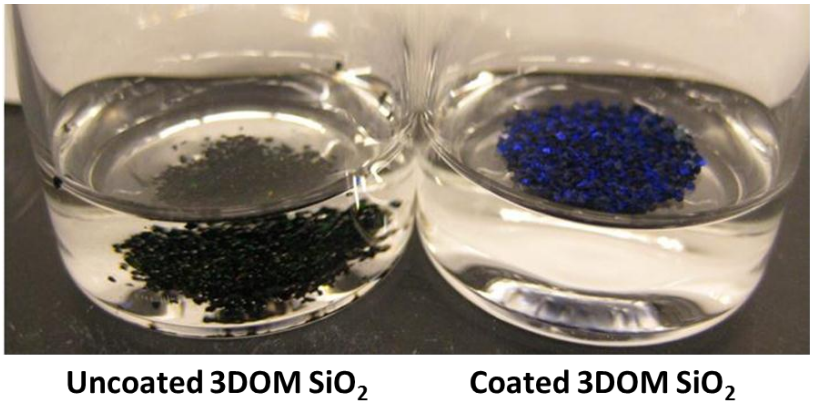

Figure 4.12. Photo showing the difference in water infiltration between uncoated 3DOM SiO_2 and coated 3DOM SiO_2. The coated 3DOM stays on top of the water and retains its purple color while the uncoated 3DOM is infiltrated by the water and sinks as a consequence.

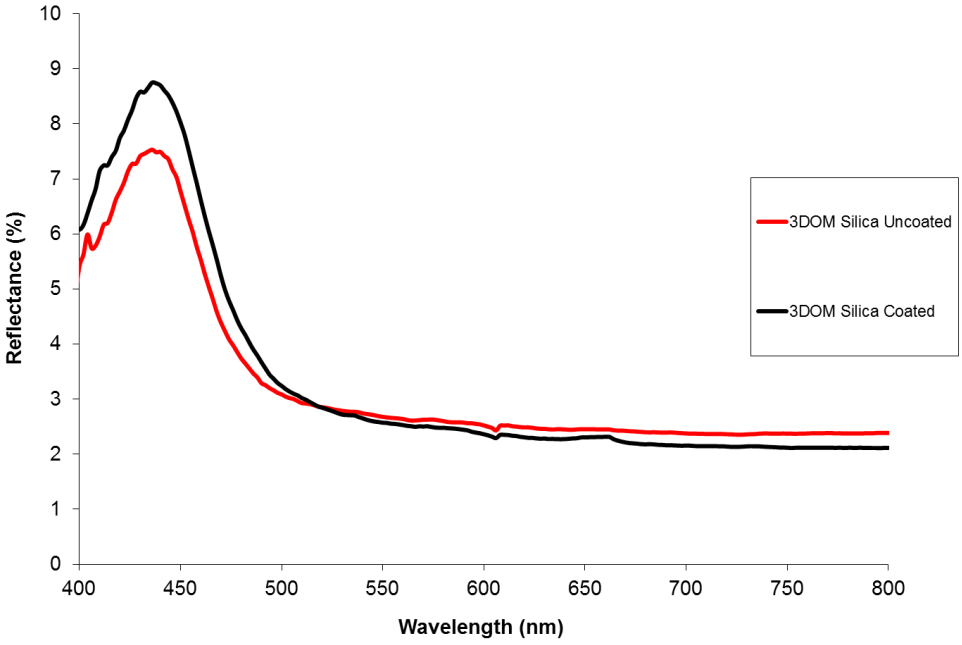

Figure 4.13. UV-Vis spectra of 3DOM SiO_2 before and after the application of a hydrophobic coating.

4.3.6.2. Three-dimensionally Ordered SiO_2 Sphere Array with ZrO_2 Filling Material

Another strategy to reduce liquid infiltration involved the use of a template made of SiO_2 spheres in order to preserve the presence of the template array after thermal processing. Theoretically, this would prevent the formation of open macropores which

allow solvent infiltration, but would still possess a photonic stop band due to the refractive index contrast of the filling material and the SiO_2 spheres.

To create the SiO_2 sphere array, SiO_2 spheres were synthesized using a modified Stöber method. SEM analysis of the self-assembled template showed small crystalline domain sizes caused by the fast, 4-day sedimentation compared to the long 3–4 week sedimentation times of less-dense PMMA spheres (Figure 4.14). The resulting spheres were measured by SEM imaging to have average diameters of 448±23 nm.

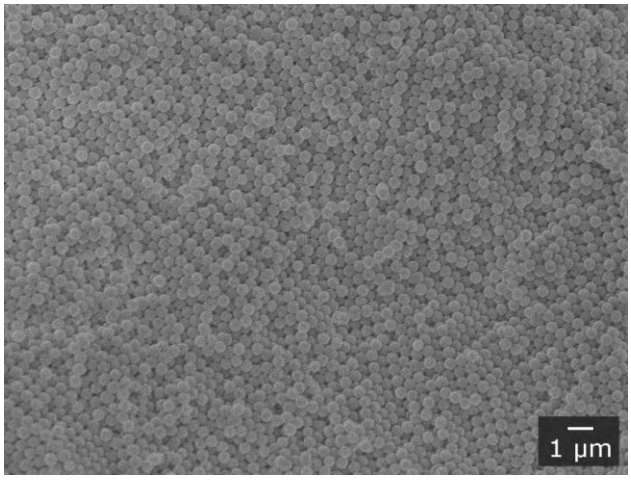

Figure 4.14. SEM image of self-assembled SiO_2 spheres.

The SiO_2 template was then infiltrated with a ZrO_2 liquid precursor and thermally processed at 550 °C to produce a three-dimensionally ordered SiO_2 array with ZrO_2 filling material (3DO SiO_2/ZrO_2). UV-vis spectra of the sphere template as well as 3DO SiO_2/ZrO_2 processed under both N_2 and air can be found in Figure 4.15. Despite the major (111) diffraction peak being outside of the visible range (~1198 nm), weak 2nd order Bragg peaks were observed at calculated positions (0.26 fill fraction, 448 nm sphere diameter).

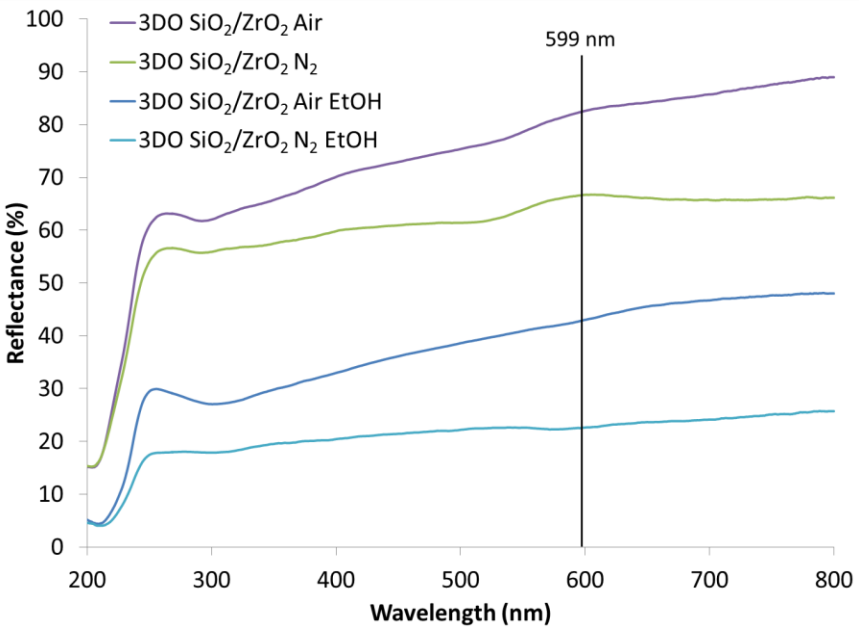

Figure 4.15. UV-vis spectra of 3DO SiO_2/ZrO_2 (processed in air or N_2) before and after infiltration with ethanol. A calculated 2nd-order diffraction peak position is shown at 599 nm (0.26 fill fraction, 448 nm sphere diameter). After infiltration, the photonic peaks at ~600 nm are no longer observed, indicating a high degree of infiltration.

Despite the absence of intense stop bands in the UV-vis spectra, the materials were still tested for resistance to solvent infiltration. Both 3DO SiO_2/ZrO_2 samples were exposed to ethanol, and both structures were readily infiltrated upon contact with the liquid. Figure 4.15 shows the UV-vis spectra of the infiltrated materials. The reflectance spectra of the infiltrated 3DO SiO_2/ZrO_2 indicated that the weak stop band peaks previously located at ~600 nm were no longer visible, as a result of solvent-induced shifting along with a reduction in intensity.

SEM images of the 3DO SiO_2/ZrO_2 samples can be found in Figure 4.16. It was observed that the ZrO_2 formed an incomplete filling of the interstitial spaces between the template spheres after calcination. Large areas of both samples contained no appreciable ZrO_2 infiltration. In most observed areas of the samples, the appearance differed little

from the original SiO_2 template. Only small domains of infiltrated material were observed (Figure 4.16 B), while other regions contained fragments of possible ZrO_2 on the surface. Several factors may have caused this incomplete infiltration. Surface incompatibility between the liquid precursor and the SiO_2 template may have caused insufficient infiltration during the liquid-infiltration phase of the synthesis. However, no regions of untemplated ZrO_2 were observed outside of the SiO_2 template.

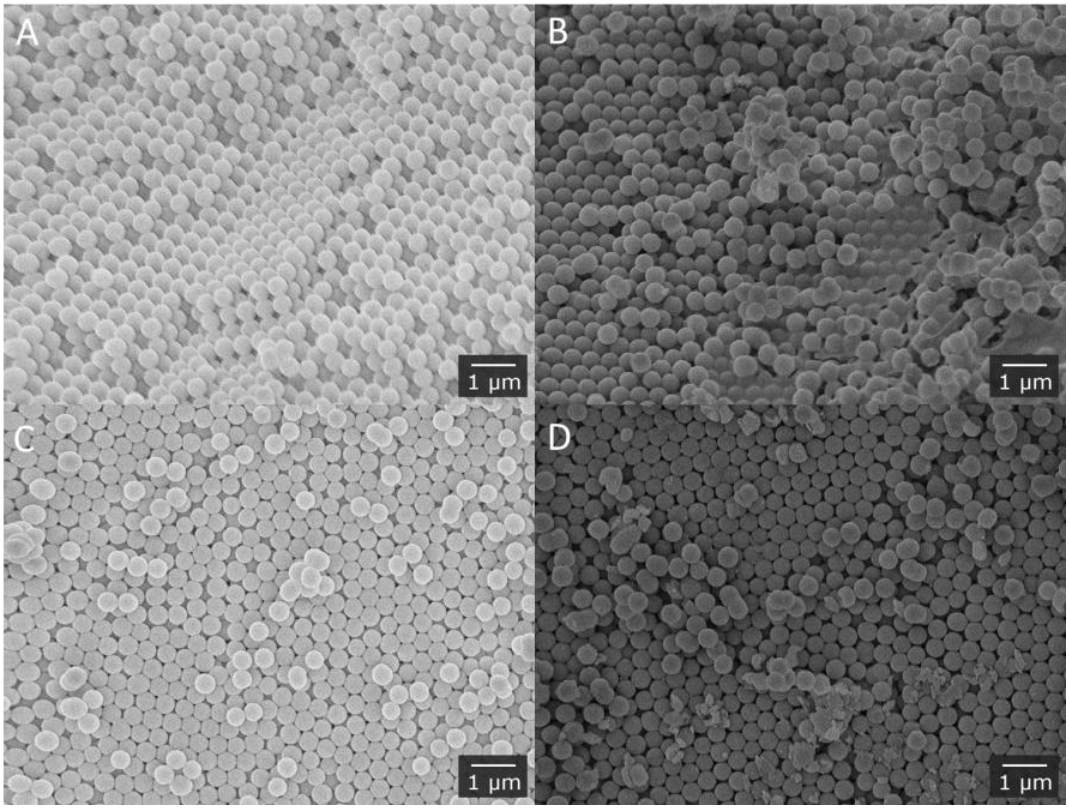

Figure 4.16. SEM images of 3DO SiO_2/ZrO_2. (A, B) 3DO SiO_2/ZrO_2 processed in N_2. (C,D) 3DO SiO_2/ZrO_2 processed in air. Images show incomplete filling of the interstitial spaces.

In order to achieve a higher degree of infiltration of ZrO_2 into the SiO_2 template, 3DO SiO_2/ZrO_2 was re-infiltrated and dried an additional 5 times before performing another calcination using conditions identical to those described above. SEM analysis of the 3DO

SiO_2/ZrO_2 that was infiltrated multiple times showed a SiO_2 sphere array infiltrated with ZrO_2 filling material (Figure 4.17). However, this sample revealed a potential pitfall in the use of these types of material composites. For materials of more than one composition undergoing thermal treatment, differences in shrinkage during processing must be taken into account. ZrO_2 undergoes ~33% shrinkage, as reported by Schroden *et al.*,[64] whereas the SiO_2 spheres do not undergo any measurable shrinkage according to measurements from SEM images before and after thermal treatment. The disparity in shrinkage properties results in a structure that still contains void spaces even after a complete initial infiltration. These void spaces arise from the area left after the filling material densified and cannot cause the shrinkage of the entire structure due to the presence of rigid SiO_2 spheres.

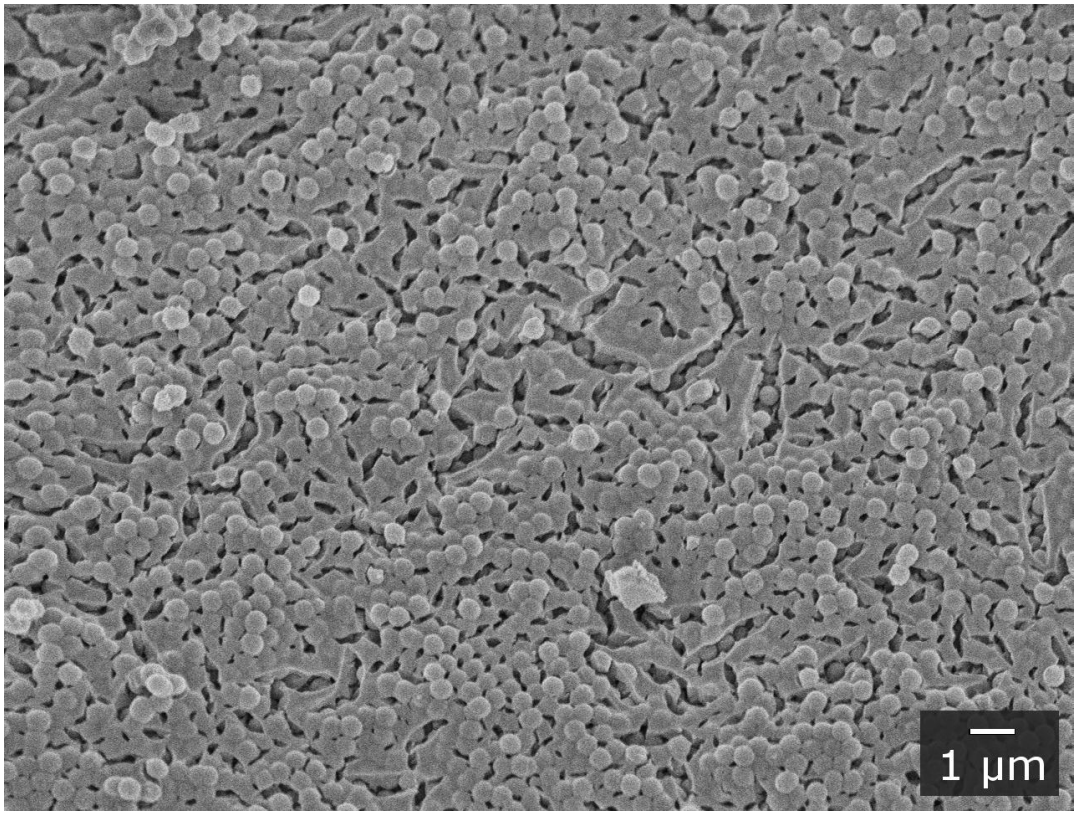

Figure 4.17. SEM image of 3DO SiO_2/ZrO_2 infiltrated five additional times before being calcined a second time. Inhomogeneous shrinkage between ZrO_2 filling material and SiO_2 spheres causes large void spaces to appear throughout the structure.

4.3.6.2 Three-dimensionally Ordered PMMA/SiO_2 with Low Temperature Thermal Treatment

In order to avoid the problem of inconsistent shrinkage between the template and filling material, a synthesis that does not require high calcination temperatures might be necessary. To test the viability of this strategy and to verify the imperviousness of the resulting material to infiltration, a synthesis involving polymer spheres and SiO_2 was attempted as a proof of concept. SiO_2 forms an extended gel network upon infiltration and drying that increases in hardness and refractive index as the network is cross-linked. High-temperature thermal processing has been used in the past to hasten cross-linking in

3DOM SiO_2, but this process removes the template spheres, which were needed to fill to pore spaces in this case.

A liquid SiO_2 precursor was infiltrated into a colloidal crystal of 470 nm PMMA spheres and placed in an oven at 70 °C for 4 days to create 3DO PMMA/SiO_2. After hardening, the infiltrated material exhibited opalescence, indicating a refractive index contrast large enough to create stop bands in the visible region. Upon addition of ethanol, a slow infiltration was observed. However, a visible color shift was not observed during this infiltration. The material before and after infiltration still possessed the same color of opalescent reflection (Figure 4.18). The infiltrated 3DO PMMA/SiO_2 also appeared to possess less structural scattering due to its wetting, becoming more transparent.

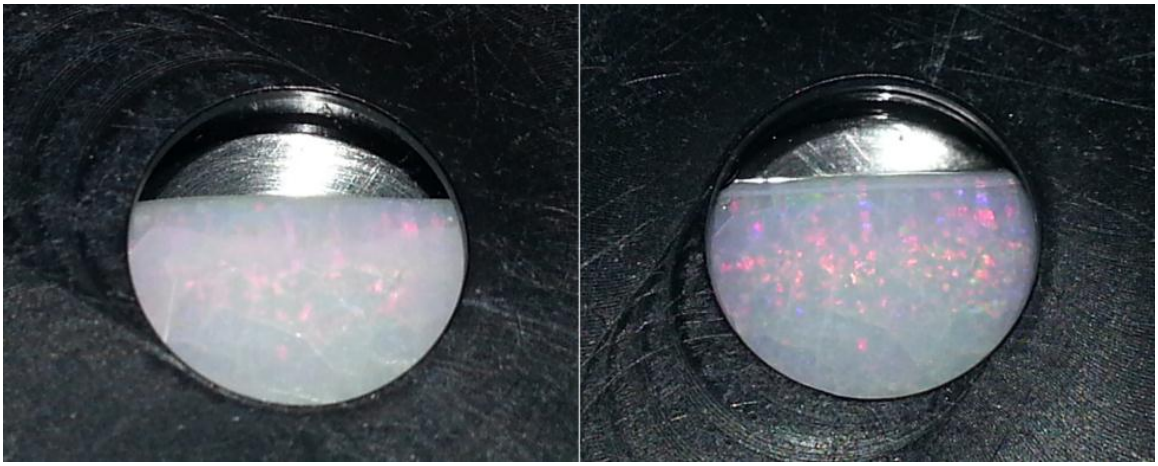

Figure 4.18. Images of 3DO PMMA/SiO_2 before (left) and after (right) infiltration with ethanol. No apparent color shift was observed, although a reduction in structural scattering produced a more transparent structure after infiltration.

UV-vis reflectance spectra of 3DO PMMA/SiO_2, before and after infiltration, were obtained (Figure 4.19). The spectra showed that, upon infiltration, a very minimal red-shift occurred. This indicated that, despite observed infiltration with ethanol, very little

void space was available and, subsequently, only a very small change in n_{avg} was experienced. SEM images of 3DO PMMA SiO_2 confirm this observation (Figure 4.20). The images show a structurally robust material with PMMA spheres filling most observable pores. The pore spacing of the material was measured to be ~410 nm, a shrinkage of ~13% from the original 470 nm sphere size. Using the measured pore spacing of ~410 nm, the peak positions observed at ~600 nm were calculated to correspond to the (220) diffraction peak of the photonic crystal lattice (0.26 fill fraction, refractive index of 1.46 for SiO_2 and 1.49 for PMMA). Upon shrinking, the SiO_2 material served to compress the pore-filling spheres, resulting in a structure with little void space available for solvent infiltration. Interestingly, the ethanol (refractive index of 1.36) that does infiltrate the structure does not affect the average index of refraction of the material in a significant manner due to the minimal amount of void space filled. The result was a structure that resisted solvent-induced stop band shifts.

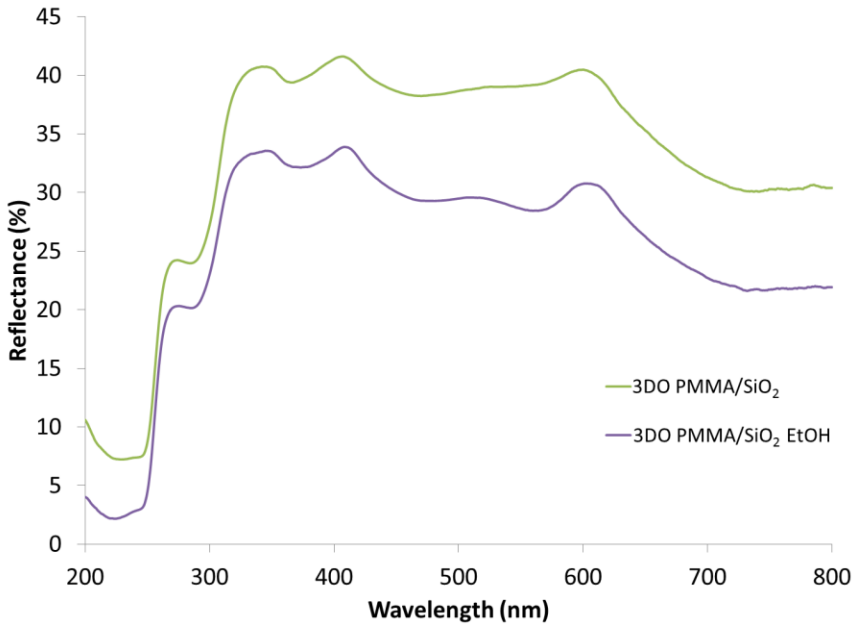

Figure 4.19. UV-vis spectra of 3DO PMMA/SiO_2 before and after infiltration. A minimal stop band shift is observed upon infiltration with ethanol due to the limited void space available within the structure.

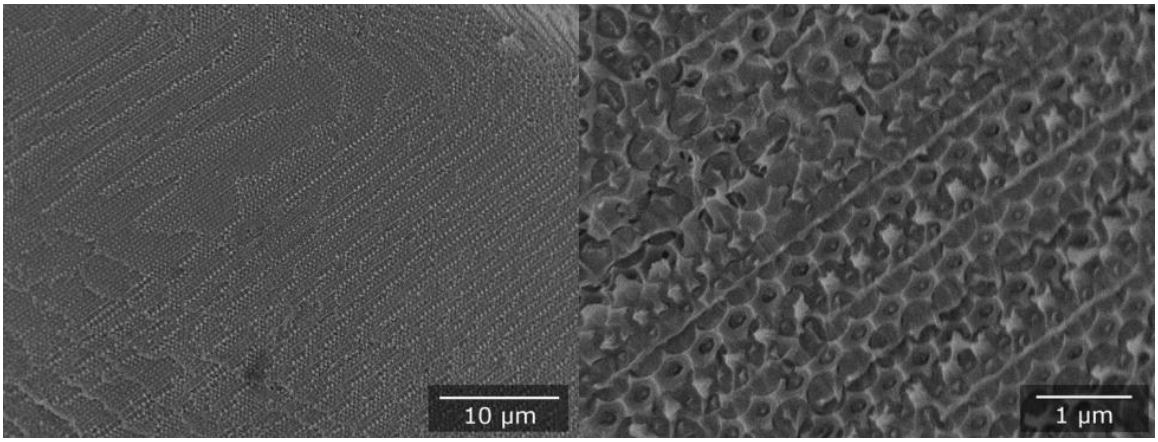

Figure 4.20. SEM images of 3DO PMMA/SiO_2. A high degree of structural order is maintained, and the combined PMMA and SiO_2 phases eliminate most of the pore space.

4.4 Conclusions

3DOM materials of various compositions were synthesized for use in UV blocking applications. Due to the limited light absorption in the UVA region by bulk TiO_2, photonic stop bands were placed in this region through colloidal crystal templating in order to extend the UV coverage of the materials. Various amounts of TiO_2 were incorporated into SiO_2 in order to observe band edge effects, stop band positions, and other optical characteristics. SiO_2 provided a regular structural component that ensured periodicity over large domains with little disassembly, while TiO_2 provided high absorbance in the UV through its electronic band edge.

Due to the isolation of TiO_2 domains within the SiO_2 matrix, quantum size effects were observed as a blue-shift in the TiO_2 band edge at low TiO_2 content. As the TiO_2 content was increased, the band edge shifted closer to the bulk value. However, with higher TiO_2 content, the structural component of the material became less regular. It was also found that the presence of a stop band below 400 nm was obscured by the high absorbance of the TiO_2 band edge. The band edge served to absorb a majority of incident photons, reducing coherent scattering from diffraction and resulting in stop bands that were either poorly-developed or absent. This effect greatly diminishes the potential of using photonic crystal stop bands to extend the UVA coverage of TiO_2.

The use of 3DOM materials as UV blockers will also be limited in the future by the high degree of incoherent scattering within the structures as well as the band edge shifts associated with the nanostructure of the materials. The issue of strong scattering has long been a known problem for physical UV blockers such as TiO_2 and ZnO. This has been

addressed in current physical UV blockers my modifying shape, size, and distribution of nanoparticles of these compositions. The modification of these parameters is more complex in 3DOM materials as the factors that affect incoherent scattering are determined by the 3DOM walls, whose dimensions are constrained by the interstitial template spaces and liquid precursor formulations. Properties such as 3DOM wall thickness have been modified in the past using etching or changes to precursor concentration. While this process could possible increase the transparency of the materials by opening up the structure, the decrease in TiO_2 domain size within those walls would cause an undesirable band edge shift further into the UV.

Thin film UV-vis transmittance spectra were obtained in order to observe the UV-blocking effects of 3DOM TiO_2/SiO_2 25:75. The stop band became more pronounced with increased film thickness. However, increased incoherent scattering was also observed as thickness was increased, limiting the transparency of the films in the visible region.

3DOM materials with stop bands in the UV were found to be effective solvent-shifted, dye-contrasted pigments. By matching regions of low absorbance in a select dye with the location of a solvent-shifted photonic peak, intense coloration was achieved. This method may open the door to the synthesis of new 3DOM materials that have anticipated stop band shifts after infiltration with select liquid media.

A separate study on the prevention of solvent infiltration on photonic materials was carried out. It was hypothesized that by eliminating the void space within the 3DOM macropores, the unwanted solvent-induced stop band shifts that occur in 3DOM materials

would be mitigated. It was found that the combination of shrinkage during thermal processing and the rigidity of a SiO_2 template prevented the elimination of void space to-date. 3DO SiO_2/ZrO_2 treated at 550 °C contained little interstitial space-filling materials and was readily infiltrated. Void spaces were mostly eliminated in a 3DO PMMA/SiO_2 composite that was not thermally treated at high temperatures. These materials showed very little stop band shift when exposed to ethanol infiltration and did not experience a major color change as a result.

Chapter 5
Synthesis of 3DOM Materials for Enhanced Thermal Emission Devices

Parts of this chapter are reproduced with permission from ref.[198]

All experimentation and characterization described in this chapter involving, specifically, the coating of refractory metals on thin films of carbon and their subsequent thermal treatment was performed by Dr. Prashant Nagpal and is included in this document as vital complementary material.

5.1. Introduction

In order to meet the energy demands of a growing world, significant advances in energy production must be realized in order to decrease our dependence on fossil fuels and utilize renewable resources. The reduction of waste heat in already-utilized energy conversion pathways is also of great importance. In order to meet these energy demands, new technologies that employ new materials are needed.

The most abundant source of renewable energy for the Earth is sunlight. However, the challenge lies in harvesting this energy. Current technologies have an incomplete conversion of these energies due to the finite bandgaps of semiconductor photocells.[199-200] One way in which the efficiencies of solar cells can be increased, while at the same time harvesting waste heat from existing sources, is through the use of thermophotovoltaics.[199]

Thermophotovoltaic cells possess a thermal-to-electric pathway to energy conversion that can be paired with specific semiconductor materials in order to increase conversion efficiency.[199, 201] These devices work by absorbing energy from the sun or waste heat sources and re-emitting photons whose wavelengths depends on the emitter type and temperature. These emitted photons can then be absorbed by a semiconductor material

chosen to pair with the emitted wavelengths, increasing efficiency. However, this approach has been limited by the choice of emitter materials.

Recently, metallic photonic crystals have been studied as possible thermophotovoltaic emitters due to their low emissivity in the infrared and their unique emission properties near the photonic band edge.[154, 164, 202-204] By patterning a metallic photonic crystal with a specific periodic spacing between structural features, it may be possible to tailor the emission properties of the emitter material. With tailored emission properties, these materials can then be precisely paired with a semiconductor photodiode to take advantage of the increased emission at certain wavelengths.

Several techniques such as lithography, holography, direct laser writing, and layering have been previously used to synthesize metallic photonic crystals.[116, 164, 202, 205-213] However, in order to create inexpensive devices for a mass market, techniques that require specialized equipment may not be economically viable. Due to this, one of the most promising avenues in regards to cost and ease of synthesis lies in colloidal crystal templating of metallic photonic crystals.[73-79, 214] More information on the colloidal crystal templating process can be found in Chapter 1.

In this chapter, the synthesis of a metallic photonic thermophotovoltaic emitter material is investigated. Several issues in the synthesis of this material are addressed. First, challenges related to the creation of colloidal crystals for the templating of photonic materials with stop bands in the IR are addressed. Then, the synthesis of metallic photonic crystals with refractory metal coatings is discussed. The thermal stability of these metallic photonic crystals at high temperatures is then investigated.

5.2. Experimental

5.2.1. Materials

Reagents were obtained from the following sources: ammonium hydroxide, methyl methacrylate (99%), tungsten hexacarbonyl (97%), molybdenum hexacarbonyl (98%), tantalum pentachloride (99.8%), tetrakis(ethylmethylamino)hafnium(IV), resorcinol (99%) and formaldehyde (37 wt% in water) from Sigma-Aldrich; potassium persulfate from Fisher Scientific; sodium carbonate (anhydrous) from J.T. Baker; hydrogen peroxide (30%) from Mallinckrodt. Nitrogen and deionized water were obtained from in-house systems.

5.2.2. Synthesis of Poly(methyl methacrylate) (PMMA) Spheres

PMMA nanospheres were synthesized using an established literature method.[64] A 5-neck, 3-liter flask was fitted with a Teflon stir blade, a condenser, an NMR tube containing a thermocouple, a glass pipette nitrogen bubbler, and a glass stopper. All attachments were affixed to the flask with rubber stoppers where necessary. The flask was then placed in a heating mantle and the thermocouple was connected to a temperature controller. 500 mL of water was added to the 5-neck flask followed by 400 mL of methyl methacrylate and another 980 mL of water. 1 g of potassium persulfate was then dissolved in a separate vial in 20 mL of water. The monomer mixture was then stirred at 350 rpm and nitrogen was bubbled through the solution at ~0.1 L/min to purge dissolved oxygen as the mixture was heated to 70 °C and left to stabilize. When the desired temperature was reached, the potassium persulfate (KPS) solution was added to

the water/monomer mixture and the nitrogen bubbler was stopped. After 3 or more hours, the polymer suspension was allowed to cool to 50 °C. It was then filtered by glass wool to separate out any large pieces of PMMA and placed into a large plastic container for storage. A portion of this colloidal suspension was placed in a glass crystallization dish and sedimented over several weeks to form dried colloidal crystal template with centimeter dimensions. The remaining liquid suspension was used for capillary flow cell experiments.

5.2.3. Synthesis of Poly(styrene) (PS) Spheres

Due to the challenge of obtaining monodisperse PMMA spheres in the micrometer size range, a PS dispersion polymerization from literature sources was used with the goal of synthesizing large spheres for 3DOM IR stop bands.[72, 215] A 250 mL 3-neck round bottom flask was fitted with a mechanical overhead stirrer connected to a glass stir rod with a Teflon stir blade, a nitrogen bubbler attached to a glass pipette, and a water condenser. Styrene monomer (25 mL) was washed with a molar equivalent of 1 M sodium hydroxide solution in a separatory funnel to remove the polymerization inhibitor. This washing process was repeated three times. The styrene was then added to the flask, along with 200 mL of ethanol. The flask was heated to 60 °C in an oil bath. Nitrogen was bubbled into the solution until the time just before the initiator was added and continued to flow above the liquid surface after the initiation. When the mixture reached the desired temperature, 0.4 g of 2,2-azobisisobutyronitrile (AIBN) initiator and 0.6 g polyvinylpyrrolidone (PVP) stabilizer were dissolved in 20 mL ethanol and added to the monomer solution. The reaction was carried out under nitrogen for 24 h and then cooled

to room temperature and filtered through glass wool. The PS suspension was then centrifuged for 15 min at 1,000 rpm and decanted multiple times after the addition of more water in order to remove small spheres that were a byproduct of the reaction and to remove unreacted monomer and PVP. In order to increase the size of PS particles, a second PS sphere synthesis was performed using 50 mL of ethanol instead of 200 mL. By lowering solvent levels, more chain combination events take place during polymerization due to the increased concentration of monomer, resulting in an increase in average diameter.[23] However, this synthesis resulted in polydisperse spheres that were used for infiltration experiments described later in this chapter.

5.2.4. Assembly of Colloidal Crystal Films

Two 1”×3” glass or quartz slides were cleaned in a solution of 10 mL hydrogen peroxide and 10 mL of ammonium hydroxide for 30 min. The slides were then removed, rinsed with deionized water, and dried under a nitrogen flow. Two 1’’×1’’ silica glass microscope slip covers with a thickness of 120 µm were used as spacers between the two slides and were placed on the far ends. Two binder clips were attached to the ends of the slides in order to secure the slides and the spacers in place. This arrangement created a capillary plane in between the two slides. The plane was fixed to the middle of a 3’’×3’’ polyethylene stage. The assembly was placed at a 5° angle lengthwise to aid in sphere deposition.

A 1.5 mm hole was drilled into the side of a 30-mL polyethylene bottle to coincide with the height of the prepared capillary plane. A 4 cm long capillary tube measuring 1.5 mm in diameter was bent at a 90° angle 1 cm from the end of the tube using a Bunsen

burner flame. The tube was inserted into the hole in the polycarbonate bottle so that one end rested inside the bottle and the other end pointed outward. The outward end of the capillary tube was then joined to the capillary plane on the upward end of the tilted plane and the entire apparatus was secured with masking tape so that contact between the capillary tube and the capillary plane was not interrupted. A photo of the apparatus can be seen in Figure 5.3.

This apparatus was used to make both small-sphere PMMA and large-sphere PS films. The PMMA template was made using a 10 wt% suspension of 440±7 nm PMMA spheres in water. The PS films used a 20 wt% suspension of either 2.78±0.14 μm or 4.13±0.48 μm PS spheres. The suspensions were then pipetted into the polycarbonate bottles until the liquid level was near the level of the hole. The larger PS spheres were mechanically agitated in the polycarbonate bottle using a magnetic stir bar to prevent sedimentation.

5.2.5. Synthesis of Resorcinol/Formaldehyde (RF) Carbon Precursor

Resorcinol/formaldehyde (RF) precursor was synthesized using an existing literature synthesis.[102] 6.4 g of resorcinol was placed in a scintillation vial. A mass of 0.12 g of sodium carbonate catalyst was added. This solid mixture was then added to 9.74 g of 37% formaldehyde. The resorcinol-formaldehyde mixture was capped and stirred for 20 min. on a magnetic stir plate. The resulting product was a yellow solution that slowly polymerized and became more viscous with time. After several hours, the liquid became a hard solid.

5.2.6. Synthesis of Tungsten/Molybdenum Precursor

A 95/5 wt% tungsten/molybdenum precursor was synthesized using a synthesis adapted from the literature.[216] Molybdenum was added in order to control the grain growth of the final structure at high temperatures.[114] Volumes of 60 mL of glacial acetic acid and 60 mL of hydrogen peroxide were placed in a 350 mL round bottom flask. A stir bar was added and the flask was then placed into a magnetically stirred ice bath. Masses of 0.25 g of molybdenum powder and 4.75 g of tungsten powder were weighed inside of a glove box and placed in separate containers. The molybdenum was added to the stirring solvent mixture first. The tungsten powder was then divided into thirds, and each third was successively added every 5 min to control the exothermic dissolution of tungsten metal. The solution was capped and stirred for 1 day. A water condenser was then added to the top of the flask and the solution was then refluxed at 55 °C overnight, creating acetylated peroxotungstic acid (APTA). After reflux, the solution was placed in an oil bath at 40 °C and attached to a rotary evaporation apparatus. After all solvent had evaporated, the remaining yellow solid was re-dissolved in ethanol and evaporated again using the same rotary evaporation method in an oil bath at 40 °C to remove any remaining acetic acid. The remaining solid was then placed in a glass vial and stored under nitrogen atmosphere.

5.2.7. Synthesis of 3DOM Carbon Films

Colloidal crystal thin films of either 440 nm PMMA or 2.78 μm PS spheres were used to fabricate carbon films. Three 1.5 mm diameter capillary tubes were each bent at 90° angles at the center using a Bunsen burner flame. The enclosed film was then placed

on a 3’’×3’’ polyethylene stage. The tubes were placed perpendicularly against the colloidal crystal thin film with the opposite end of the tube arranged vertically. Two of the tubes were evenly spaced on one side, while the other was placed on the opposite side directly across from one of the other tubes. This allowed for a small open space on one side of the film so that air could escape from the enclosed film during infiltration. All of the tubes were then secured to the stage using masking tape. RF precursor was carefully pipetted into the upturned capillary tubes. The tubes were checked for air bubbles that would halt the flow of precursor into the film. If air bubbles were present, the tube was emptied and new precursor was pipetted in. After all three tubes were filled with precursor, the enclosed film was returned to its position in between the three capillary tubes and infiltration was initiated. Due to the increasingly viscous nature of the precursor, these steps were done as quickly as possible. The film was then left to infiltrate overnight, or until the precursor solution became too viscous to flow. The infiltrated RF film remained between the silica slides and was then placed in an oven at 85 °C for 3 days. The film was then removed from the slides and placed in an alumina combustion boat and heated to 900 °C with a ramp rate of 5 °C/min for 1 h under 0.6 L/min flowing N_2.

5.2.8. Synthesis of 3DOM Tungsten/Molybdenum Films

A colloidal crystal thin film of ~4 μm PS spheres, formed using a procedure identical to the one described previously for ~2.78 μm spheres, was used for the fabrication of tungsten/molybdenum films in order to analyze precursor infiltration without sacrificing a well-ordered template. A 3 M solution of 95/5 wt% tungsten-molybdenum precursor with

either an 80/20 or 50/50 ratio of water/methanol was made. The colloidal crystal film was enclosed by the quartz slides, which were placed on a 3'×3' polyethylene stage and secured with masking tape. A 1.5 mm hole was drilled into the side of a 35 mL polyethylene bottle to coincide with the level of the colloidal crystal film opening. The film was then infiltrated using the same procedure described in section 5.2.7. The film was left to infiltrate for 2 days with a subsequent drying time of 1 day. The cell was placed in a tube furnace after the removal of the silica glass spacers. The furnace was set at 800 °C at a ramp rate of 5 °C/min and the film was reduced for 1 h under a hydrogen atmosphere with a flow rate of 0.5 L/min. After reduction, the cell was removed from the furnace and the quartz substrate slides were separated.

5.2.9. Synthesis of 3DOM Carbon Monoliths

A suspension of 440 nm PMMA spheres was allowed to sediment in a large crystallization dish to form face-centered cubic colloidal crystal templates with mm dimensions. The colloidal crystal arrays were infiltrated with a resorcinol/formaldehyde (RF) precursor according to reported methods.[102] The RF composites were then placed in a tube furnace and heated at 5 °C min^{-1} to 900 °C and held for 2 h under N_2. The resulting 3DOM carbon monoliths were sanded with 600-grit sandpaper to remove any untemplated surface carbon and sonicated in water for 15 min and rinsed to remove any loose material.

5.2.10. Chemical Vapor Deposition of Refractory Metals on 3DOM Carbon Films

The 3DOM carbon thin films were coated with the desired refractory metal using chemical vapor deposition (CVD). A simple batch-CVD setup was used in which the carbon sample and the desired metal precursor were loaded into a glass flask, which was then evacuated. The CVD chamber was backfilled with nitrogen and evacuated three more times to remove any oxygen or water vapor. The chamber was pumped down to the desired pressure (typically 20 mtorr) and heated to the desired temperature. The precursor vapor pressure rose, and the precursor vapor decomposed on the hot carbon substrate, coating it with the metal layer. The precursors used for tungsten, molybdenum, and tantalum were tungsten hexacarbonyl, molybdenum hexacarbonyl, and tantalum(V) chloride, respectively. The temperature used for the metal depositions was in the range from 350–400 °C for tungsten and molybdenum and 450–500 °C for tantalum CVD . This resulted in a thermally stable metallic photonic crystal, which extended over cm^2-areas with defect-free regions ranging over hundreds of micrometers. Excess metal in the case of thick coatings was removed using SF_6 reactive ion etching (20 mtorr, 50 W platen power).

5.2.11. Chemical Vapor Deposition of Tungsten on Monolithic 3DOM Carbon

The 3DOM carbon monoliths were coated with refractory metals using a bench-top CVD apparatus that consisted of a one-neck vacuum flask containing a metal mesh stage. Pieces of 3DOM carbon weighing ~50 mg with approximate dimensions of 5 mm × 5 mm × 2 mm were used as substrates. A sample of 3DOM carbon was positioned on the stage and metal precursor was placed underneath (typically 0.6 g $W(CO)_6$ for tungsten

deposition). The system was then evacuated and flushed with nitrogen three times. The evacuated flask (~20 mtorr) was lowered into a sand bath at 400 °C for 20 min. After cooling, the flask was opened to the atmosphere and the sample was recovered and weighed. Samples were prepared with differing amounts of $W(CO)_6$ per CVD run. CVD of tungsten on 3DOM carbon monoliths was performed using two different deposition schedules. Sample 3DOM C/W1 was prepared with a total of 0.6 g $W(CO)_6$ spread out over six different depositions of 0.1 g each. Sample 3DOM C/W2 was also synthesized using 0.6 g $W(CO)_6$, but over two runs of 0.3 g $W(CO)_6$ each. The mass of sample 3DOM C/W1 increased from 48.2 to 55.2 mg after deposition and that of sample 3DOM C/W2 from 48.7 to 55.4 mg.

5.2.12. Deposition of Hafnia Interlayer

To improve the adhesion of metal coatings on the carbon scaffolds, these were coated with hafnium oxide (melting point 2758 °C) using atomic layer deposition (ALD). The ALD coatings were prepared using a Savannah ALD system from Cambridge Nanotech, employing alternate cycles of tetrakis(ethylmethylamino)hafnium(IV) and water at 150 °C (15 cycles, 1 min/cycle).

5.2.13. Thermal Stability Test of 3DOM Materials

To evaluate the thermal stability of the tungsten composite samples, they were heated using a sealed heating stage attached to a turbo-pump. The stage was first evacuated to a pressure of ~10^{-6} torr and then heated at 5 °C min^{-1} to 1000 °C. The samples were held at 1000 °C for 1 h, then allowed to cool to room temperature. The thermal stability was then

analyzed by imaging the samples using scanning electron microscopy and by X-ray diffraction measurements to characterize grain growth. One monolithic sample, 3DOM C coated with a hafnia interlayer and a tungsten layer (3DOM C/W2H), was heated at 1000 °C for another 5 h after sample characterization following the first 1 h heat treatment.

5.2.14. Characterization

Scanning electron microscope images were obtained using a JEOL field emission gun SEM. Samples were mounted onto sample stubs with conductive carbon tape. Lower accelerating voltages were used on polymer samples in order to prevent charging. The polymer samples were also coated with a 50 Å thick layer of platinum to improve its conductivity and further prevent charging. Feature sizes were obtained using SEM images in ImageJ software.

5.3. Results and Discussion

5.3.1. Synthesis of Poly(styrene) (PS) Colloidal Crystals

Two PS sphere suspensions were synthesized and then analyzed by SEM for size and dispersity. One synthesis was performed using 200 mL of ethanol while the other used only 50 mL. For the synthesis using 200 mL of ethanol, the sphere size was measured by optical microscopy as 2.78±0.14 μm. Aliquots of this suspension dropped onto optical microscope slides exhibited good self-assembly characteristics (Figure 5.1). There was no observable aggregation and spheres were observed to quickly flow and self-assemble upon drying.

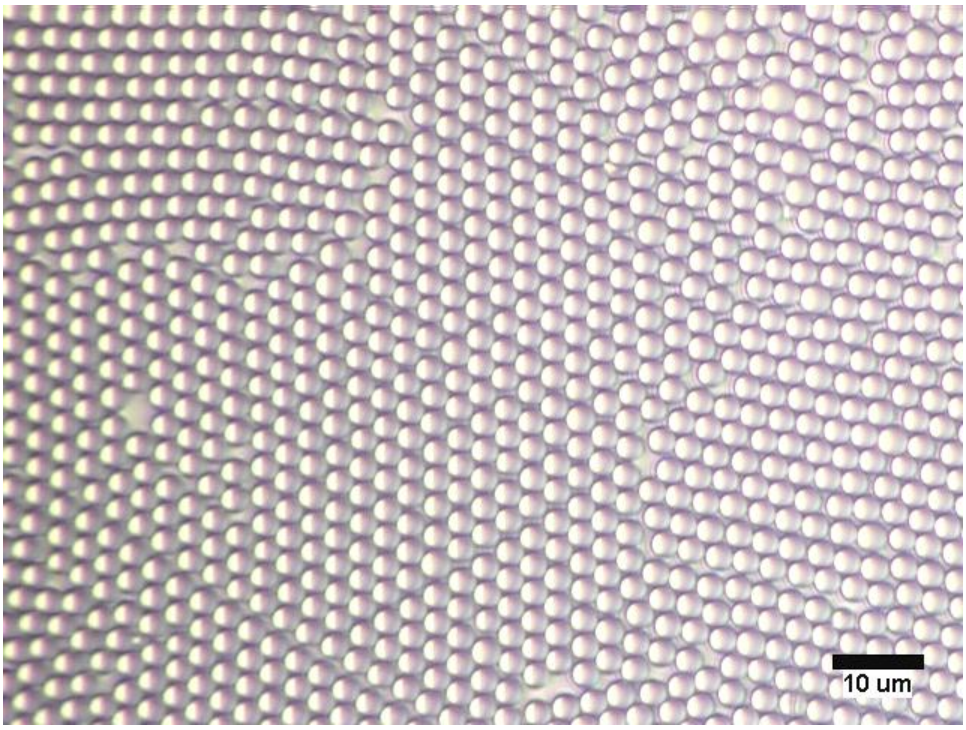

Figure 5.1. Optical microscope image of 2.78 um PS spheres after self-assembly.

While the sphere synthesis using 200 mL of ethanol resulted in relatively monodisperse sizes, it was thought that larger sphere may be needed for future experiments that would require a stop band position farther into the IR region. A separate synthesis using only 50 mL of ethanol was performed in order to increase particle size. This synthesis resulted in a polydisperse size range of 4.13±0.48 μm (Figure 5.2). While these spheres were not useful for fabricating metallic photonic crystals with good photonic properties, they were utilized for the testing of colloidal crystal thin film growth and precursor infiltration techniques described throughout this chapter.

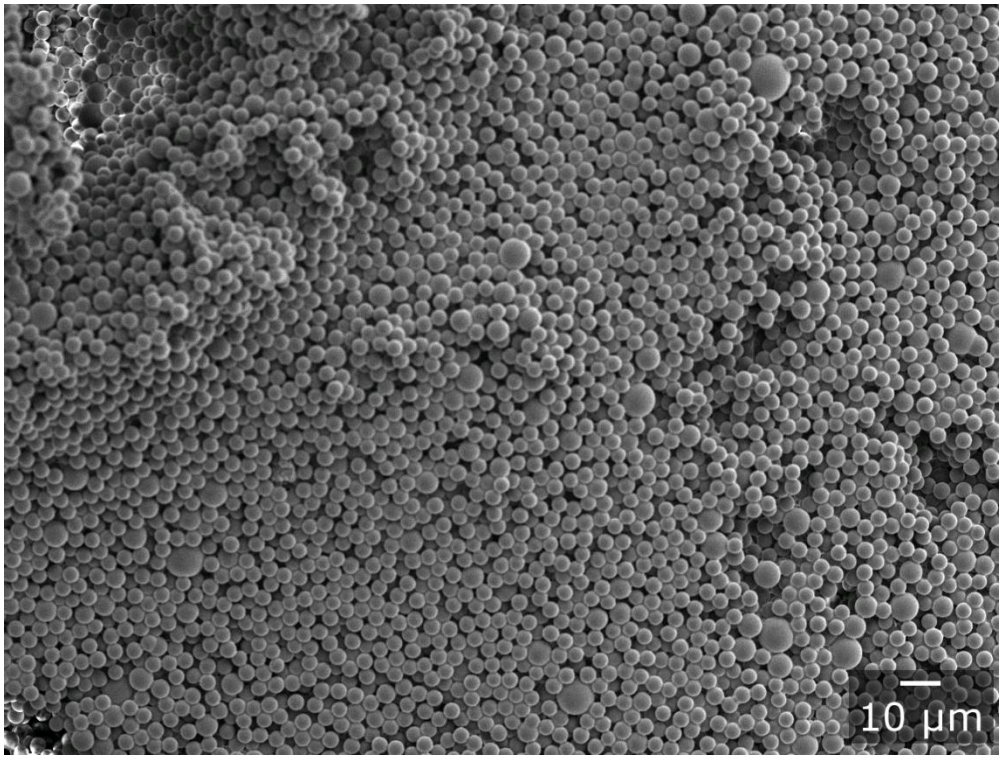

Figure 5.2. SEM image of 4.13±0.48 µm PS.

5.3.2. Self-Assembly of Large Colloidal Spheres

In order to obtain high-quality photonic crystals, it is necessary to create large crystalline domains of periodic features in order to maximize coherent scattering from the photonic crystal surfaces. In order for a 3DOM material to contain well-ordered domains, the template used for its synthesis must be well ordered. The ability of colloidal spheres to self-assemble into fcc crystals with large domains is dictated by several factors such as charge, size dispersity, and diameter.

The charge of the colloidal spheres involved in this chapter originates from the AIBN or KPS initiator groups on the polymer spheres. These electrostatic charges must be

sufficiently large in order to produce long-range repulsions between individual spheres to prevent aggregation but small enough to allow for self-assembly upon volume restriction.

The dispersity of sphere size also plays a large role in the quality of the template. In order to form a perfect fcc array, all spheres must be relatively monodisperse. When spheres that deviate from ideal size are present in the array, structural defects arise that reduce the crystallinity of the material.[217] In order to form colloidal crystals with a high degree of order, it is necessary for the dispersity in sphere sizes within a given suspension to be as low as possible.[218]

The greatest hurdle toward the self-assembly of colloidal spheres in this study is sphere size. The effects of sphere size on the sedimentation time and, consequently, the self-assembly of large spheres in the micrometer size range can be observed by considering the equation for the sedimentation velocity of colloidal spheres in Chapter 1 (Equation 1.1). If this equation is used to approximate the sedimentation velocity of two particles of different size, it provides a useful insight into how size can affect self-assembly. Performing a calculation for a PMMA sphere of 450 nm and a PS sphere of 4 μm results in values of 0.28 mm/h and 7.01 mm/h, respectively, for sedimentation velocity. In order for colloidal spheres to properly self-assembly, sufficient time must be given in order for the particles to travel and find the lowest-energy conformation. In the case of large colloidal spheres, sedimentation occurs faster than the time it takes to properly crystallize.

5.3.3. Assembly of Colloidal Crystal Films

One technique that can produce colloidal crystal films while also assisting the ordering of large spheres is the capillary cell technique described in this study (Figure 5.3). The cell was based on a design from Li *et al*.[219]

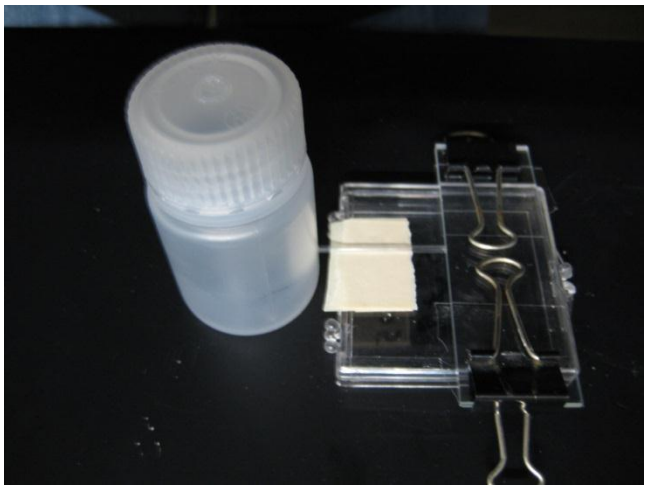

Figure 5.3. Photo of the thin film apparatus used in this study. The capillary tube carries a colloidal suspension from the reservoir bottle and into the capillary plane created by two microscope slides.

In this setup, the colloidal spheres preferentially deposit onto the downward sloping end of the cell as well as at the open sides of the capillary plane where evaporation occurs. This method of deposition relies less on the force of gravity because solvent flow brings free spheres to the edge of the plane where they are forced to assemble into ordered array, rather than rely on the spheres to self-assemble. Norris *et al*. proposed that these forces assist in the self-assembly of colloidal spheres in vertical deposition techniques and are also likely to be important in other cases where solvent flow through a colloidal crystal is present.[42] According to this theory, as the solvent flows outward due

to constant evaporation, the colloidal spheres within the thin-film flow cell devised here self-assemble at the solvent/air interface similar to colloidal spheres during vertical deposition processes described by Norris *et al*. As spheres start to partially block the open sides, the solvent is forced to flow through the open niches surrounding the spheres. The solvent carries free spheres with it into to these open niches and deposits them directly into the open spaces. As long as solvent continues to flow in the outward direction, monodisperse spheres should continue to assemble into fcc arrays (Figure 5.4).

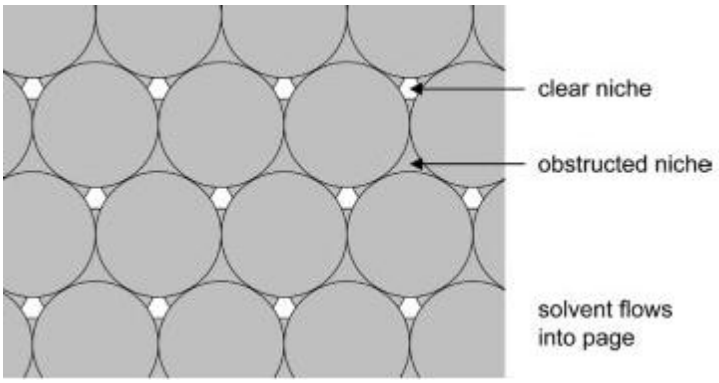

Figure 5.4. Figure depicting the location of niches that allow solvent to flow through and facilitate ordered deposition of colloidal spheres. Reproduced from Norris *et al.*[42]

In order to test the horizontal flow-cell device, smaller 450 nm spheres were initially used in order to gauge the effectiveness of this technique on the ordering of spheres that would otherwise naturally self-assemble through sedimentation. As free spheres entered the capillary plane from the reservoir, they preferentially deposited around the edges of the plane (Figure 5.5). Over time, the region of deposited spheres spread toward the center of the film and eventually formed a completed film over the course of ~72 h.

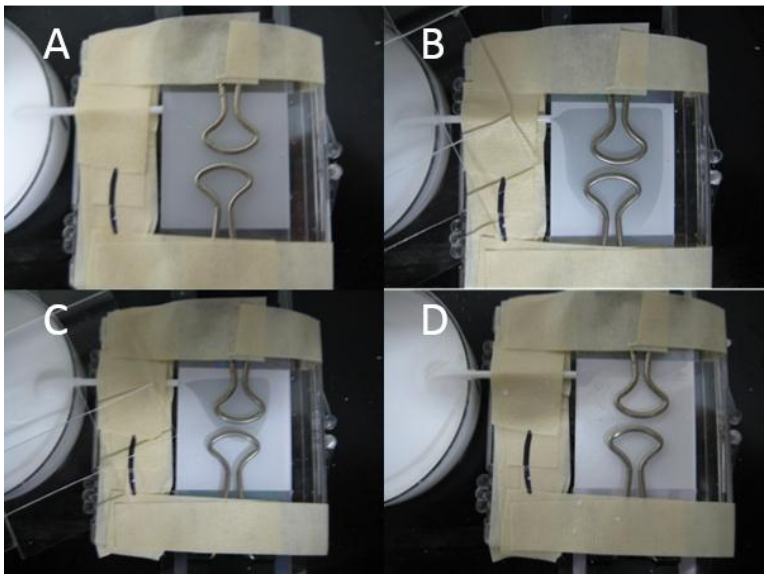

Figure 5.5. Timed photos of sphere filling of capillary cells after (A) 0 h, (B) 24 h, (C) 48 h, and (D) 72 h. In the top-right the film is noticeably darker due to a low concentration of spheres inside the cell. As time is elapsed, the film becomes more and more infiltrated with spheres and takes on a lighter color where the spheres are depositing.

The 450 nm colloidal crystal film formed during this process was highly opalescent (Figure 5.6). This indicated that there was a high degree of structural order within the template. Attempted removal of the film resulted in the breakup of the film into sub-millimeter flakes. Subsequent SEM images of the flakes confirmed the crystalline order of the PMMA template. The film exhibited large crystalline domains with dimensions in the tens of micrometers (Figure 5.7). The successful synthesis of a well-ordered colloidal crystal template using this technique indicated that a similarly well-ordered template may be possible using larger colloidal spheres.

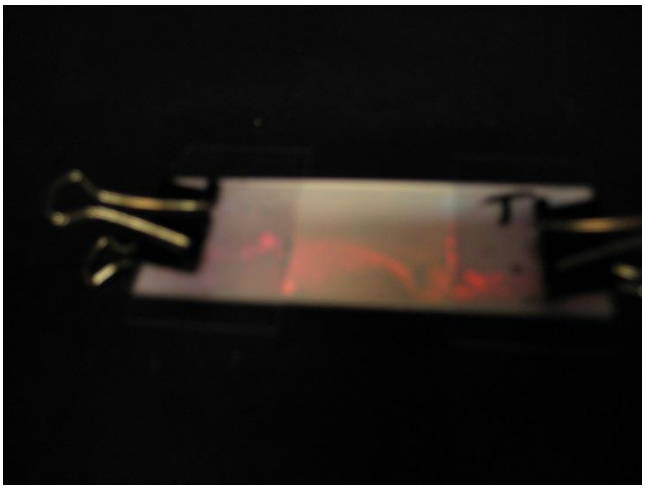

Figure 5.6. Photo of a PMMA colloidal crystal thin film showing opalescence. The opalescence of the film indicates a high degree of order in the structure.

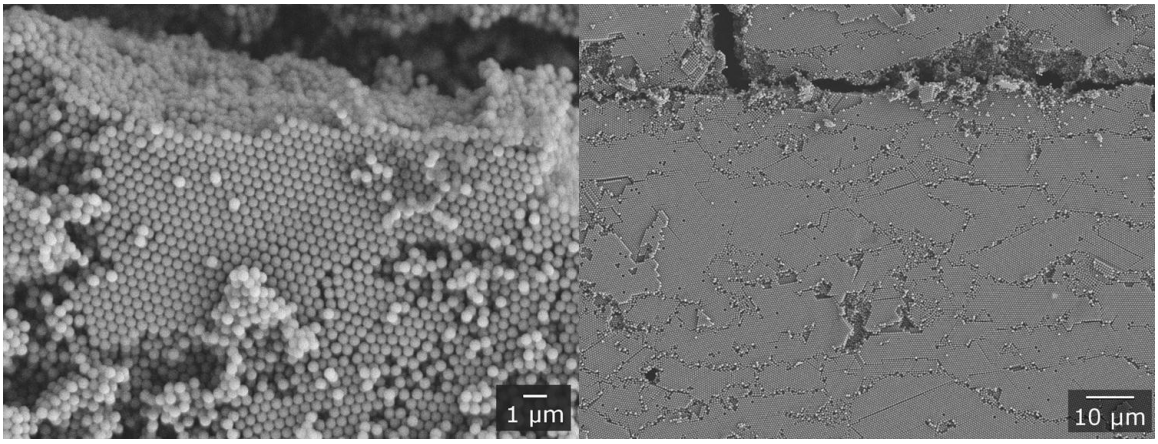

Figure 5.7. SEM images of a PMMA colloidal crystal thin film. Large crystalline domains can be observed in the image on the right.

A colloidal crystal film of 2.78 µm spheres was then synthesized using the same procedure described above. The growth of the film proceeded identically to the growth observed with smaller PMMA spheres. After drying, the film exhibited no colorful opalescence, possibly due to the primary stop band lying outside of the visible range.

When separated from the substrate, the film adhered to the glass and was not easily removed without damaging the template. SEM images of the PS film scraped from the substrate showed a random array of spheres with no obvious order (Figure 5.8). It was not believed that this was typical of the order of the large-sphere PS films because analysis of the spheres with optical microscopy showed that the spheres have a propensity to self-assemble in an evaporating confined drop (Figure 5.1), similar to conditions that were believed to be present during capillary flow cell self-assembly.

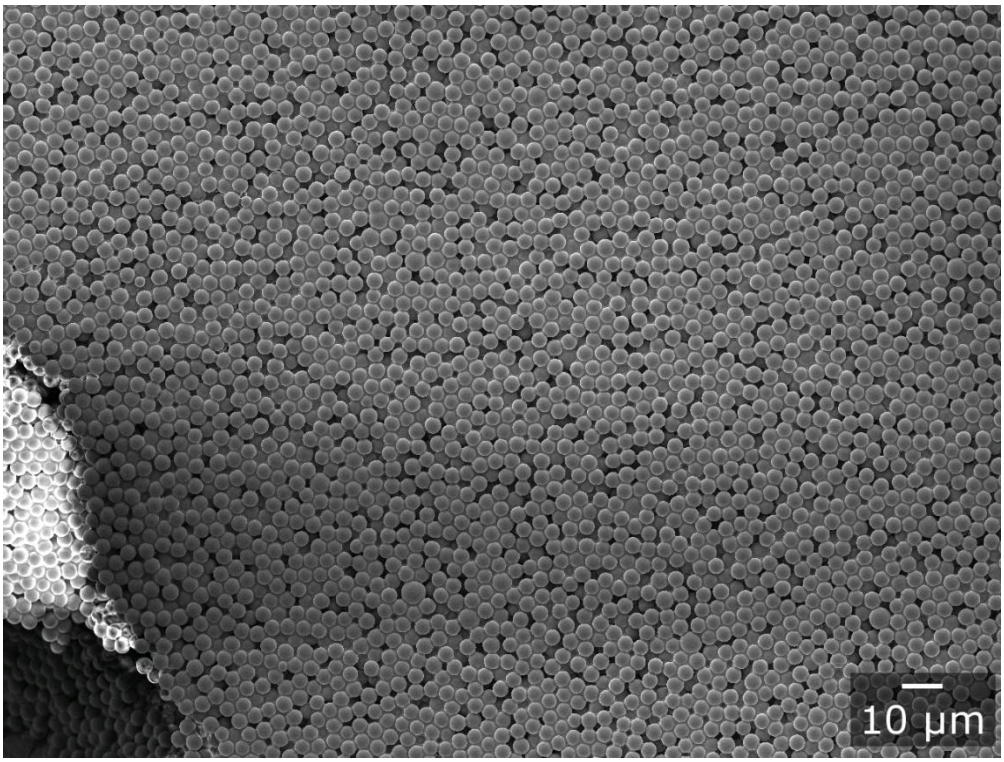

Figure 5.8. SEM image of 2.78 µm spheres PS spheres after flow-cell assembly.

5.3.4. Synthesis of 3DOM Carbon Films

In order to confirm that the large PS spheres underwent ordered self-assembly using the capillary flow cell technique, both the PMMA and PS templates were infiltrated with a resorcinol/formaldehyde (RF) precursor to 3DOM carbon while remaining confined within the capillary cell. The creation of an inverse opal film would aid in the observation of the template order by locking in the template structure in inverse form. These films were infiltrated using loaded capillary tubes that were abutted to the template film and allowed to dispense their precursor contents into the film by capillary action.

After infiltration with RF precursor, the colloidal crystal templates appeared yellow in color, indicating that the precursor had been fully absorbed by the template. After 3 days in an oven at 85°C, the color became brownish red due to extensive cross-linking of the RF polymer network between the template spheres. When the substrate slides were removed, a solid film of RF-infiltrated template was obtained for the large-sphere PS template while several smaller pieces were obtained for the small-sphere PMMA template (Figure 5.9). The films were semi-transparent and flexible. After pyrolysis, the small-sphere carbon films broke into numerous small pieces of ~1 mm dimension. The large-sphere templated 3DOM carbon appeared black with an undulating surface caused by uneven shrinkage during pyrolysis as well as the softening of the RF polymer film at high temperatures before carbonization (Figure 5.9b). This 3DOM film did not exhibit opalescence as its projected stop band would not fall within the visible range and subsequent diffraction peaks from other crystal planes would be too weak to be observed above the high absorbance of the material.

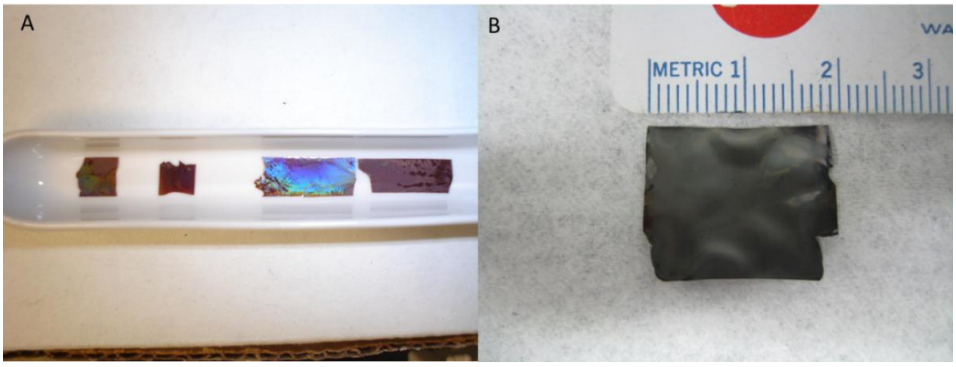

Figure 5.9. (A) RF infiltrated templates of 440 nm PMMA spheres. Opalescence was observed on the film surface. (B) Thermally processed 3DOM carbon film synthesized from a 2.78 µm sphere template. This film exhibited no opalescence.

The bottom surfaces of both films appeared smooth and unbroken while the top surfaces of the films contained areas of roughness that were visible to the eye. The PS templated film was measured to be 140 µm thick. It was mechanically stable and could be handled gently without breaking. Both carbon surfaces of the PS film exhibited a peculiar visual effect that is akin to the "oil slick effect" of hydrocarbon layers on water (Figure 5.10). This feature is likely caused by an untemplated surface layer of carbon creating an interference effect similar to a layer of oil on water.

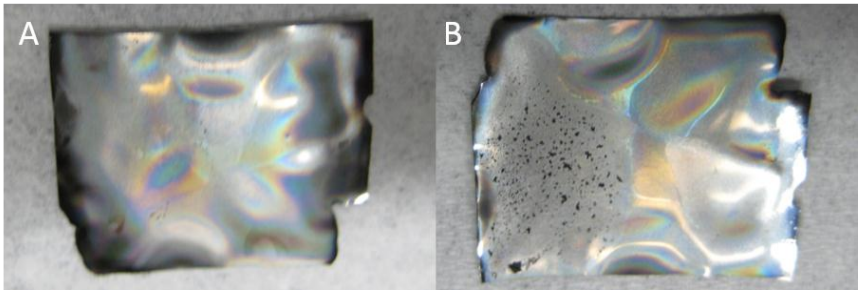

Figure 5.10. Photo of a 3DOM carbon thin film templated using large PS spheres. (A) Bottom side of the film showing a smooth surface. (B) Top of 3DOM film showing a rough surface on a portion of the film. Both sides were observed to exhibit an "oil-slick" coloration effect.

SEM images of both 3DOM carbon thin films were obtained. The PMMA-templated film, as expected due to its vivid opalescence, appeared to have large crystalline domains, confirming the previously observed crystallinity of the template (Figure 5.11). The SEM analysis (not shown) also revealed a surface layer on the film that arises due to extra void space between the substrate and the template spheres during infiltration. SEM images of the PS-templated film show that the bottom of the film has a surface layer of untemplated carbon similar to that observed on the PMMA-templated 3DOM carbon. The PS-templated 3DOM carbon film appears well ordered on both the top and bottom surface, indicating that the PS template was similarly well-ordered. The film also included rounded features observed on the top of the film in Figure 5.12b and c. These features are most likely due to pockets of air trapped during infiltration of the precursor into the colloidal template. The precursor was then templated around these features. An SEM image was also obtained showing a cross-section of the 3DOM film (Figure 5.12c). This image shows evidence of order throughout the center of the film. Subsequent 3DOM carbon thin films made using this same method were also found to be well ordered with the same surface features.

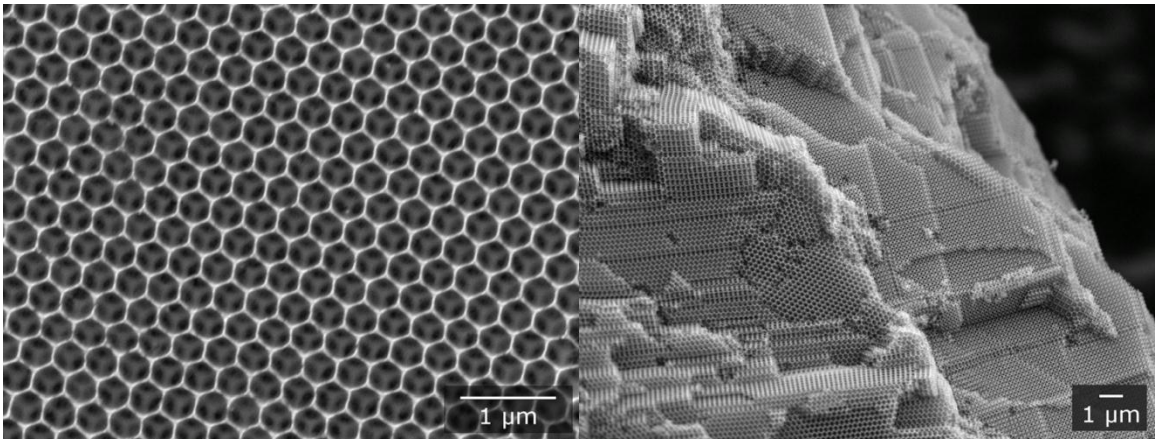

Figure 5.11. SEM images of 3DOM carbon films synthesized using a template of 440 nm PMMA spheres. Excellent pore order is observed for these 3DOM films.

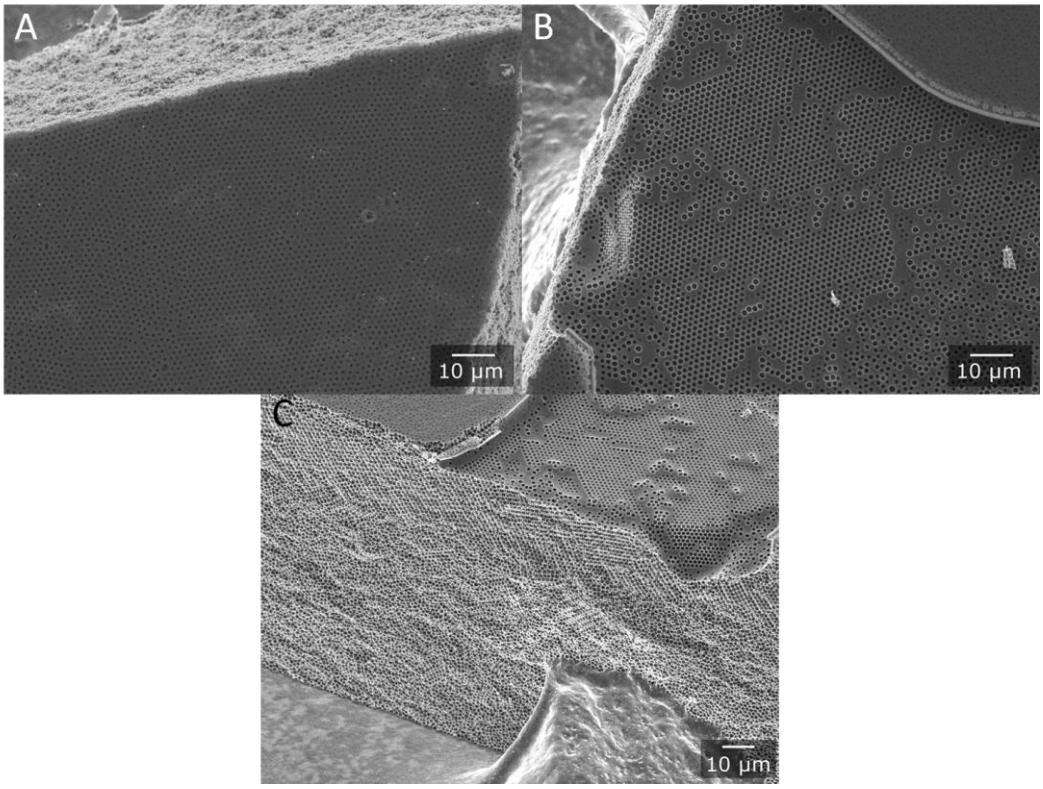

Figure 5.12. SEM images of (A) the bottom and (B) top surfaces of a 3DOM carbon thin film synthesized using a 2.78 µm sphere template. Both surfaces exhibit a layer of untemplated carbon. Air pockets are visible on the top surface, which were formed during the precursor infiltration step. (C) A cross-section of the film.

5.3.5. Synthesis of 3DOM Tungsten/Molybdenum Films

In order to create thermally stable 3DOM metallic photonic crystals with good structural order, it is necessary to consider more than simply the order of the sacrificial template. A highly regular structure is also dependent on the quality of precursor infiltration. The precursor must be able to infiltrate the template material well, fully-filling the interstitial spaces before thermal processing. Inconsistencies in infiltration lead to disassembly of structural features as well as differences in 3DOM wall thickness. These inconsistencies result in diminished photonic characteristics due to the absence of regular periodic features.

Different precursor materials often have different interactions with sphere surfaces during infiltration. For example, liquid infiltration commonly creates a volume-templated material. Volume templating occurs when the interactions between the precursor constituents are stronger than the interactions between the precursor and the sphere walls. This leads to the precursor material favoring the interstitial spaces and not the sphere surfaces. It results in larger openings between adjacent pores in the 3DOM structure at the points where template spheres touch.[75]

Vapor phase infiltration of tungsten into a 3DOM structure has also been accomplished in previous studies.[114, 220] However, vapor-phase infiltration commonly results in a different infiltration pattern due to its deposition and growth occurring at a substrate surface. This is referred to as surface-templating. Surface-templated materials undergo a more complete coating on the template sphere surface due to stronger interactions with the template material. This high degree of coating produces a more

"closed off" structure with smaller windows.[75] A comparison of surface and volume templated structures can be found in Figure 5.13.

Figure 5.13. Complete 3DOM structures made from a surface-templating precursor (left) and a volume-templating precursor (right). The window sizes are affected due to different surface interactions. Figure reproduced from Stein *et al.*[40]

For photonic crystal modified thermal emission devices, it is beneficial to have an open structure that permits photons to interact with multiple diffraction layers.[77] Therefore, vapor deposition of refractory metals is not ideal in this case. Instead, a liquid tungsten/molybdenum precursor was synthesized and infiltrated into a template film consisting of polydisperse ~4 μm spheres. Polydisperse, large sphere templates were used in early experiments in order to observe how the infiltration of these large-sphere films proceeded without sacrificing well-ordered templates, which were time-intensive to grow.

Two separate infiltrations were performed using the APTA precursor dissolved in different ratios of solvent, either 80/20 wt% or 50/50 wt% water/methanol. A greater amount of methanol was used in the latter mixture in order to increase the rate of

evaporation and to potentially lower the surface energy of the infiltrating liquid and facilitate easier filling of the interstitial spaces around the sphere template.

The films were infiltrated with APTA and thermally processed within the quartz slides that containing the template film. After pyrolysis under H_2, the final products appeared grey in color but consisted of a fine powder with no large pieces of 3DOM film present. SEM analysis (Figure 5.14) of the 80/20 film showed no significant structural order and evidence of varying degrees of initial infiltration, as evidenced by structural disassembly of the 3DOM material (Figure 5.14b).

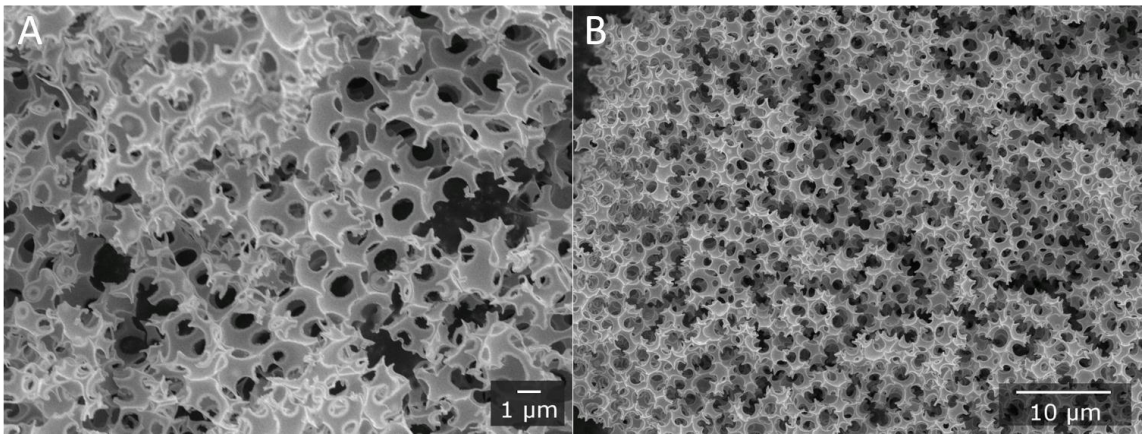

Figure 5.14. SEM images of two different domains of the 80/20 3DOM tungsten-molybdenum film. Images show evidence of (A) incomplete filling and (B) structural disassembly of the 3DOM material.

The second film, infiltrated with APTA dissolved in 50/50 wt% water/methanol, exhibited a much greater degree of infiltration as observed by SEM analysis (Figure 5.15). Ordered, templated areas were visible in certain domains of the film (Figure 5.15a). Other areas showed inconsistent infiltration but still maintained a continuous

structure (Figure 5.15b). For this film, evidence of a surface layer similar to the surface layers observed for 3DOM carbon films could also be seen.

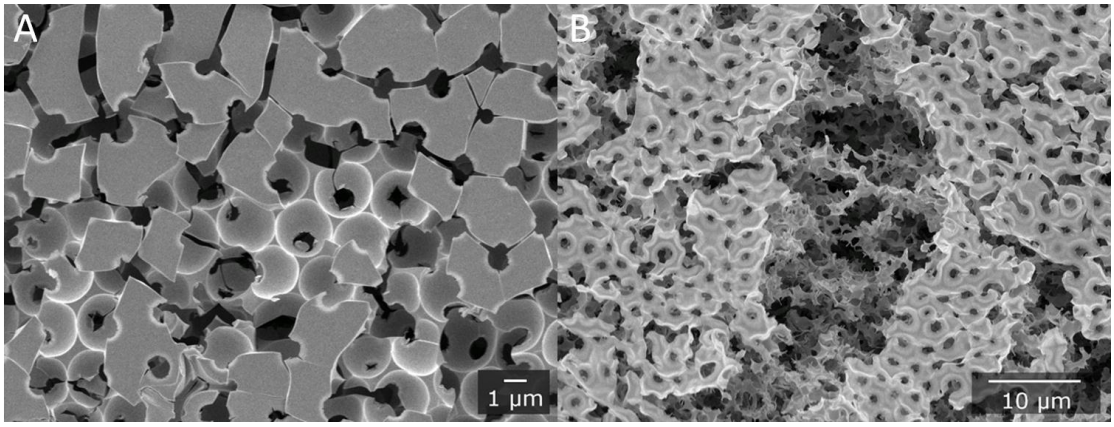

Figure 5.15. SEM images of thin film 3DOM W/Mo. Images show regions of (A) well-ordered pores and separate regions that exhibited (B) incomplete structural filling.

It was believed that with many more subsequent infiltrations of precursor material or by fine-tuning of precursor solvents, a complete film could be obtained. However, parallel studies began to show that the films would likely not be thermally stable after heating to high temperatures.[114] Based on those results, a new pathway was investigated involving more thermally stable 3DOM structures.

5.3.6. Chemical Vapor Deposition of Refractory Metals on 3DOM Carbon Films

While difficulties were previously encountered in forming complete structures using liquid precursors, vapor-phase methods were equally as undesirable due to their tendency to surface-template. Additionally, structures made solely of metallic constituents were found to be sensitive to thermal degradation of the photonic structure even after doping.[114] Therefore, a more thermally stable material was needed in order to achieve

functional structures with long thermal lifetimes. Previous studies on 3DOM carbon found that the structure was stable up to at least 2200 °C in argon.[104] In order to achieve a thermally stable structure that also possesses regular periodic features, a metallic photonic crystal was created using a thermally stable 3DOM carbon scaffold as a substrate for the vapor-phase deposition of tungsten and other refractory metals.

To synthesize the 3DOM carbon scaffolds, self-assembled opal thin films were prepared using two different synthesis techniques. One of the techniques involved convective self-assembly of polymer opals[28] on glass or silicon substrates, followed by infiltration with a resorcinol-formaldehyde (RF) carbon precursor. The patterned precursor, along with the opal layer, was then peeled off the substrate and heated in nitrogen to convert it into glassy carbon.[102] One side of the carbon inverse opal, which was in contact with the substrate possessed a thin surface layer described previously, but could be easily modified by treatment in oxygen plasma to achieve the desired top surface. This method produced periodically ordered carbon structures with open windows connecting neighboring macropores, as shown in Figure 5.16a. The modified side (after coating the metal) (Figure 5.16b) would be used to couple the modified thermal emission into far field radiation, which can be subsequently converted into electricity using an infrared photocell.

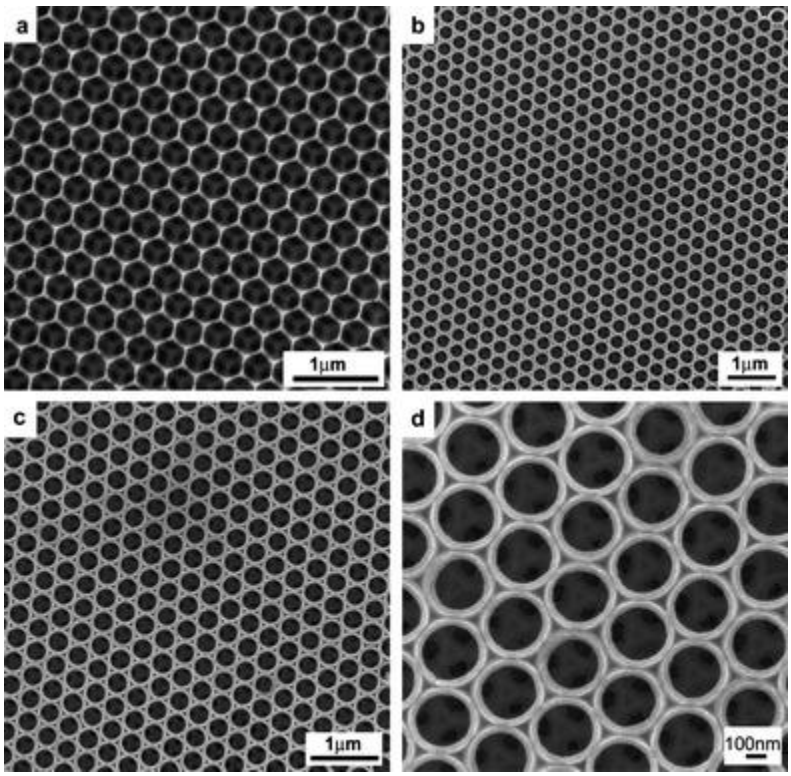

Figure 5.16. (A) 3DOM carbon substrate prepared using monodisperse PMMA spheres as a template, followed by oxygen plasma to tailor the surface termination and fill fraction. (B) Top side of a self-assembled, tungsten-coated metallic photonic crystal fabricated using convective self-assembly on glass. (C) Top side of a self-assembled, tungsten-coated metallic photonic crystal fabricated using self-assembly in confinement between two parallel glass slides. (d) High-resolution image of the bottom side of the same sample.

To achieve a uniform, stable metal coating, the thin film carbon scaffolds were first conformally coated with hafnia (melting point 2758 °C) using atomic layer deposition (ALD). As demonstrated below, this adhesion-promoting layer prevents delamination of metal coatings from the carbon scaffold upon heat treatment. CVD with $W(CO)_6$ produced ca. 50–100 nm thick tungsten coatings, which were sufficiently thick to exceed the skin depth for light penetration into tungsten[203] while maintaining an open structure (Figure 5.16b). Thus, these composite structures are expected to absorb/emit light like pure tungsten inverse opals. An XRD pattern of the composite film (Figure 5.17) showed

only peaks for face-centered cubic (fcc) tungsten, the expected phase at the deposition temperature used here, and a broad peak from the glassy carbon scaffold.[203] Because the hafnia interlayers were much thinner (estimated to be ca. 1–1.5 nm based on the number of deposition cycles[221-222] than the tungsten coatings, no hafnia peaks were observed in the XRD pattern.

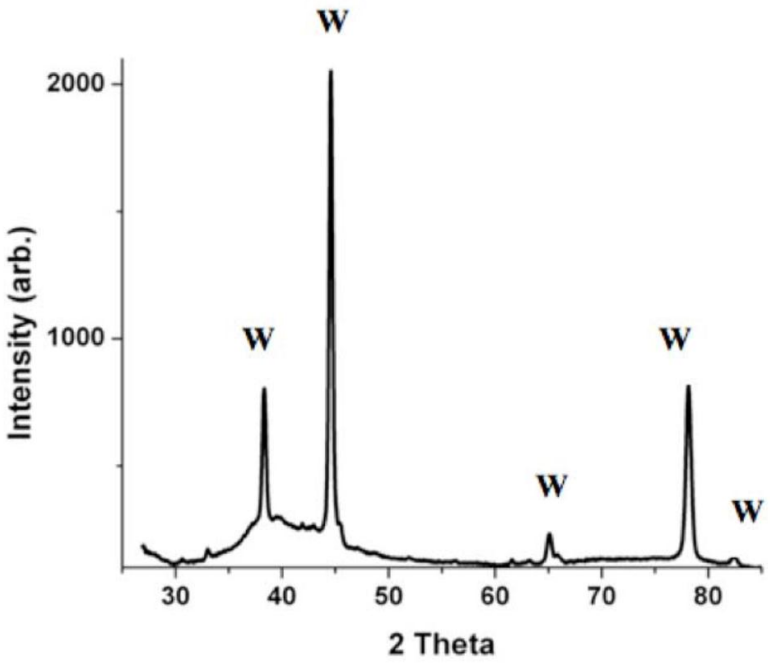

Figure 5.17. XRD pattern of a tungsten-coated 3DOM carbon film. Peaks originating from fcc tungsten are labeled. The broad peak around 40º 2θ originated from the carbon scaffold.

The second synthesis route for obtaining thin film samples involved growing opal templates in confinement between two parallel glass slides (as discussed in previous sections) followed by identical 3DOM carbon fabrication, oxygen plasma treatment, and metal coating steps. In these inverse opal sheets, both surfaces could be precisely tailored by oxygen plasma treatment as would be necessary for optimal coupling to radiation in

the far field (Figure 5.16c,d).[154] These procedures produced metallic photonic crytstals that extended over large areas (a few cm^2) and were relatively defect-free over regions extending at least a few hundred micrometres (Figure 5.18).

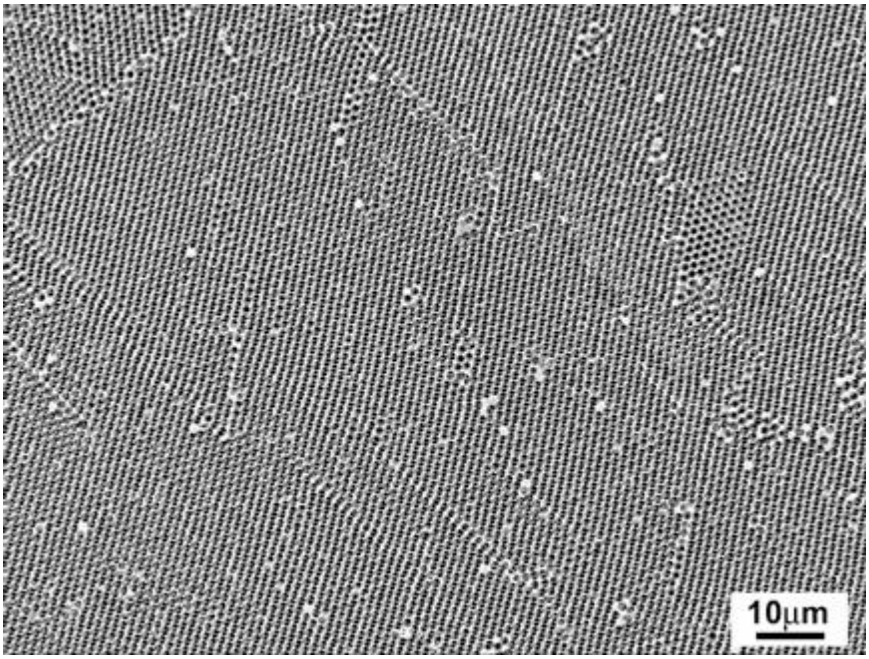

Figure 5.18. Large-area, relatively defect-free metallic photonic crystal film consisting of tungsten-coated 3DOM carbon using template formed between parallel plates.

An important consideration for tailoring the thermal emission from nanostructured metals is the choice of metal. The thermal stability of these metallic photonic crystals is limited mainly by the adhesion of the metal coating on carbon. In addition to tungsten (Figure 5.16, 5.19c), we coated 3DOM carbon films with the refractory metals molybdenum (Figure. 5.19a, b) and tantalum (Figure 5.19d). In all of these cases, hafnia interlayers were applied to improve the adhesion of the metal layer on the carbon support and, in the case of tantalum, to prevent the tantalum pentachloride precursor from etching

the carbon scaffold. As shown in the SEM images in Figure 5.19a-d, open pore structures with smooth surfaces were maintained in all cases.

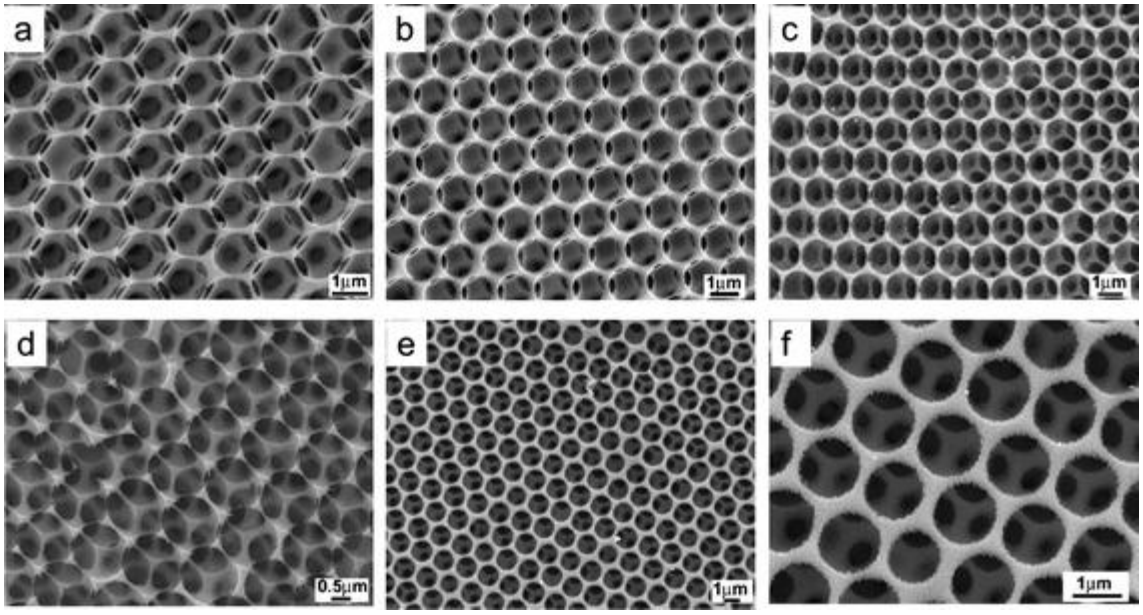

Figure 5.19. SEM images of 3DOM carbon coated with (a) a thin layer of molybdenum, (b) a thicker molybdenum layer, (c) tungsten, and (d) tantalum. (e) The composite tungsten nanostructure was heated in high vacuum (10−6 torr) at 1000 °C without any visible degradation of the metallic photonic crystal. (f) High-resolution scan of the same sample showing excellent 3D fidelity after heat treatment. Although the grain sizes of the deposited metal films increase, the thermally stable carbon scaffold maintains the overall 3D nanostructure.

5.3.7. Chemical Vapor Deposition of Tungsten on 3DOM Carbon

To test the limits of refractory metal penetration within porous carbon supports by CVD methods, monolithic 3DOM carbon substrates with external dimensions of several mm in each direction were also evaluated. In this case, multiple CVD steps were needed to penetrate deeper into the 3DOM carbon monolith. The monoliths used for the penetration depth-probing experiments were not coated with a hafnia interlayer in order to maintain a consistent substrate surface, because hafnia was found to penetrate only to a

depth of ca. 8–9 μm into these samples when applied by ALD (Figure 5.20), using the same conditions as for the 3DOM thin films. After CVD was complete, the samples retained the opalescence that was seen in the original 3DOM carbon scaffold.

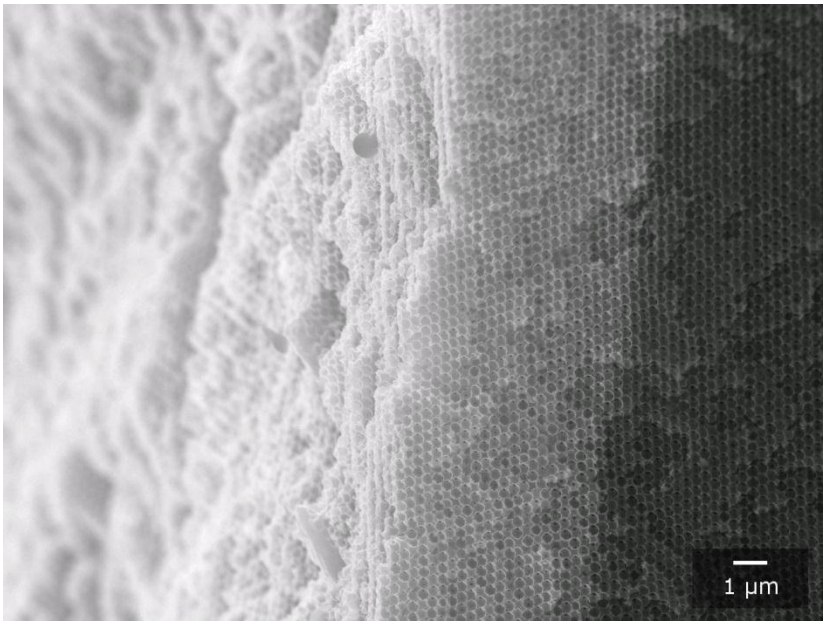

Figure 5.20. SEM cross-section of a 3DOM carbon monolith with a coating of hafnium oxide. The oxide can be seen as a bright layer against the darker carbon background.

In contrast to the uniform coatings of refractory metals observed for the thin film nanocomposite metallic photonic crystals, 3DOM carbon monoliths showed significant variation in tungsten thickness with depth. In an attempt to improve the extent of tungsten penetration and homogeneity throughout the 3DOM carbon monolith, samples were prepared with different amounts of $W(CO)_6$ precursor material per CVD run, but with a fixed total amount of $W(CO)_6$ over all runs. Sample 3DOM C/W1 was prepared with a total of 0.6 g $W(CO)_6$ spread out over six different depositions of 0.1 g each, sample 3DOM C/W2 with two runs of 0.3 g $W(CO)_6$ each. These conditions were chosen based

on the premise that using smaller amounts of precursor over multiple runs would prevent tungsten from building up near the surface of the material and blocking the pores. The mass increase was nearly identical for both deposition procedures (ca. 14 wt%).

SEM imaging combined with EDS analysis of a tungsten-coated 3DOM carbon monolith revealed the extent to which tungsten was deposited on the 3DOM carbon scaffold (Figure 5.21). While EDS signals corresponding to tungsten are numerous, the signals are not uniform throughout the monolith. The EDS map of a cross-section of the monolith shows the greatest signal intensity for tungsten near the edges of the monolith with near-zero signal in the middle, while the inverse is true for the carbon signal. The relatively low oxygen signal in tungsten-rich areas indicates a low amount of undesirable WO_3. The X-ray diffraction pattern of the tungsten-coated 3DOM carbon monoliths (Figure 5.22) shows relatively weak, broad peaks corresponding to the expected low-temperature tungsten phase with fcc structure, as well as a peak for amorphous carbon. The low signal intensity is consistent with a relatively low tungsten content in the composite sample (ca. 14 wt%).

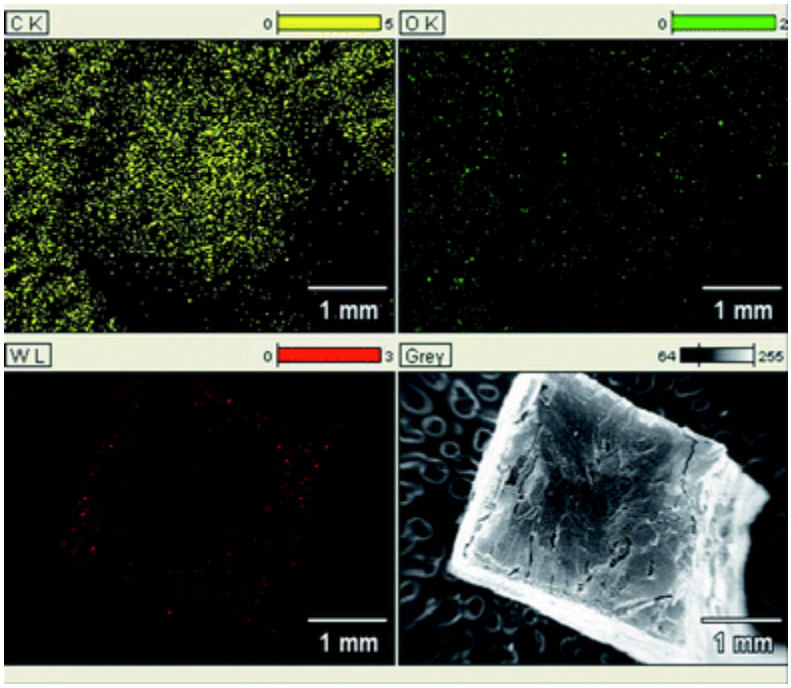

Figure 5.21. EDS maps of a cross-section of 3DOM carbon after CVD of tungsten. The maps include signals for carbon (top left), oxygen (top right), tungsten (bottom left), and a gray-scale image (bottom right). The tungsten signal shows preferential deposition near the surface of the monolith.

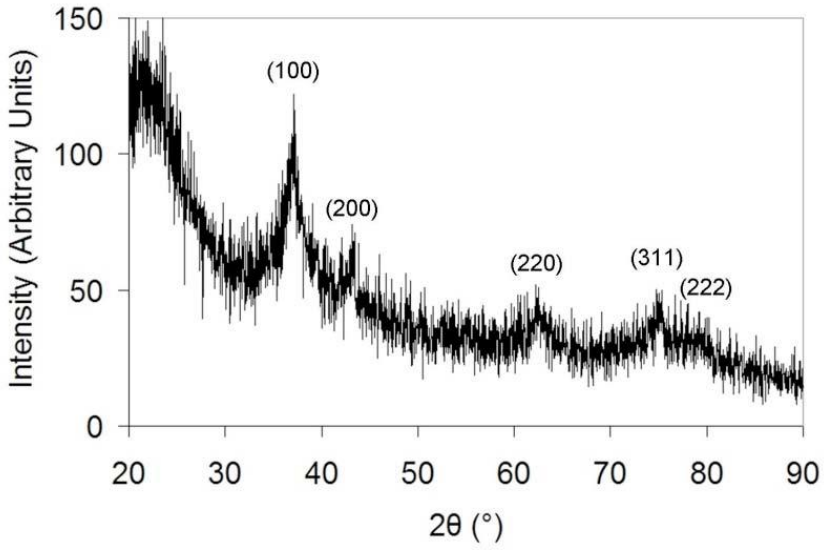

Figure 5.22. XRD pattern of fcc tungsten coated onto 3DOM carbon monolith

SEM analysis of a cross-section of both 3DOM C/W1 (Figure 5.23) and C/W2 (Figure 5.24) confirmed the presence of a gradient in deposition thickness. The tungsten layer was observed as a grainy surface on smooth 3DOM carbon. The thickness of the deposited tungsten was greatest near the surface of the monolith, gradually diminishing until the presence of tungsten became indistinguishable from the surrounding carbon though SEM analysis. The thickness of the deposit can also be estimated from the size of the windows that connect adjacent macropores. As shown in Table 5.1, window sizes consistently increased with increasing sample depth, corresponding to thinner surface coatings. After a depth of ca. 20 μm, the window sizes remained constant for both samples.

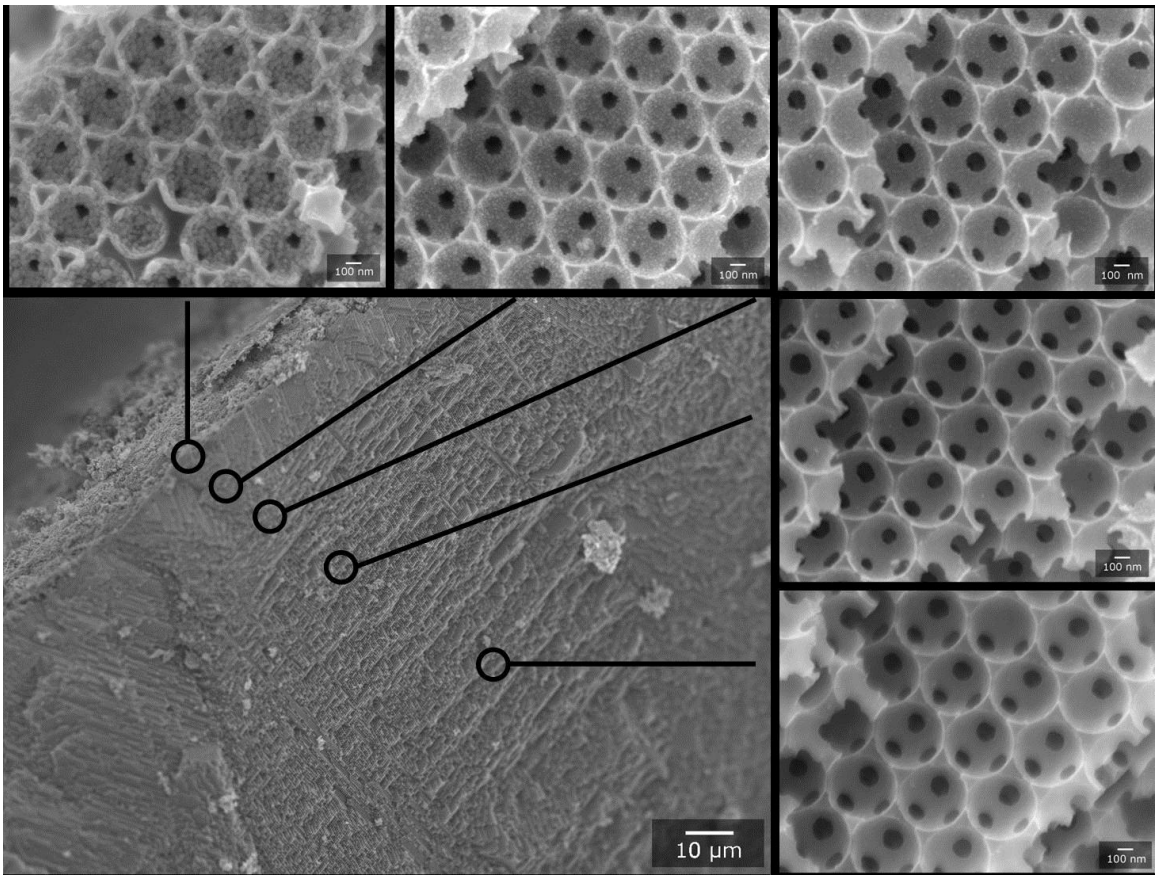

Figure 5.23. SEM images of the cross-section of sample 3DOM C/W1 (no hafnia interlayer). Clockwise from top left: images at depths of 1 µm, 9 µm, 20 µm, 40 µm, and 83 µm. The bottom left image is an overview showing the respective position of the other images with the surface

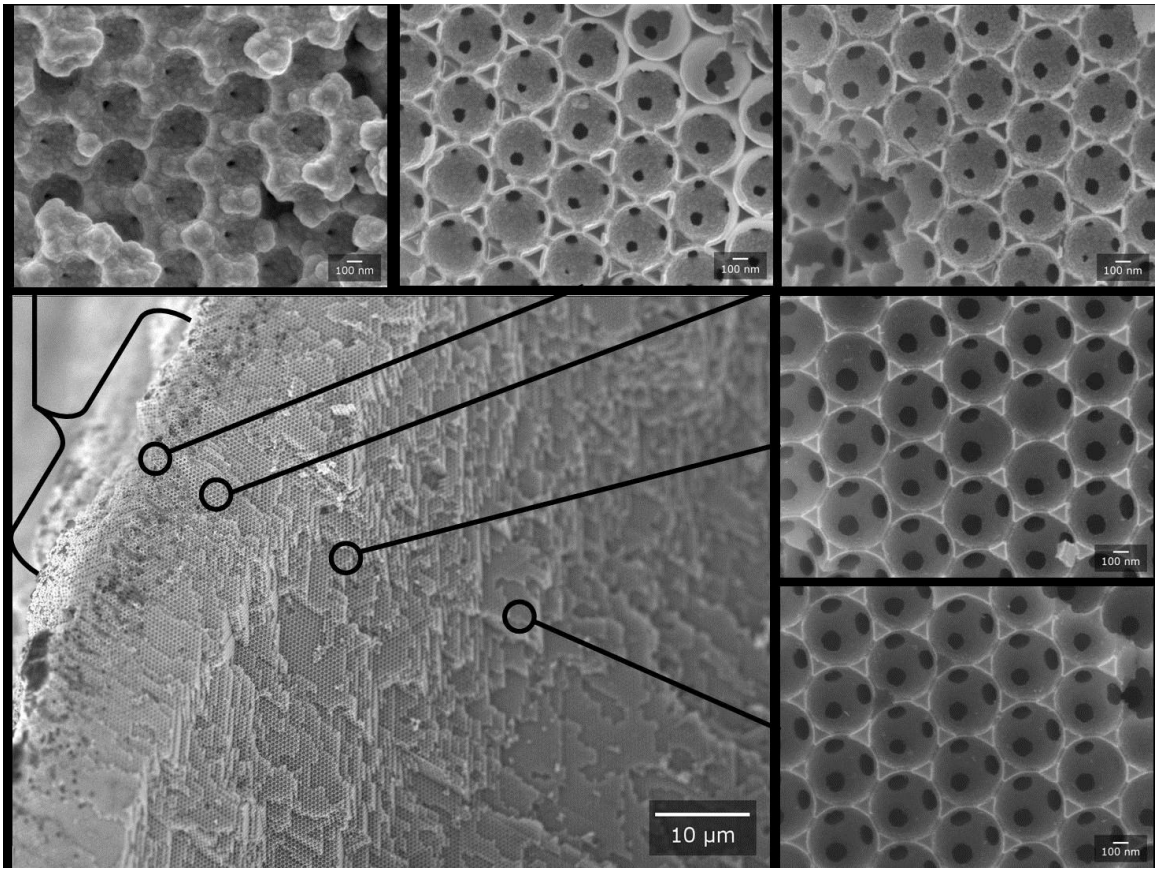

Figure 5.24. SEM images of the cross section of sample 3DOM C/W2 (without a hafnia interlayer). Clockwise from top-left: images at depths of 0 µm, 1 µm, 8 µm, 43 µm, and 97 µm. The bottom-left image is an overview showing the respective position of the other images with the surface of the material appearing in the top-left of the image.

Table 5.1. Window sizes of samples 3DOM C/W1 and 3DOM C/W2 as functions of depth in the 3DOM C monolith. Window size measurements are based on the SEM images in Figure 5.23 and Figure 5.24.

Sample 3DOM C/W1		**Sample 3DOM C/W2**	
Depth (μm)	Window Size (nm)	Depth (μm)	Window Size (nm)
1	67 ± 11	0	30 ± 9
9	99 ± 11	1	84 ± 13
20	119 ± 10	8	110 ± 11
40	119 ± 10	43	130 ± 15
83	126 ± 10	97	128 ± 11

For the 3DOM C/W2 sample, a difference in the texture of the deposit was noted. Sample 3DOM C/W1 exhibited a larger amount of coarse tungsten near the surface with coarseness diminishing with depth, whereas sample 3DOM C/W2 showed a much smoother profile throughout. This different behavior suggests that increasing the number of deposition steps increases the surface roughness throughout the structure as already-deposited tungsten grains undergo multiple growth steps with each successive run. Under the conditions tested in this study, tungsten penetration remained limited to a few tens of micrometers. Since this depth includes several tens of pore layers, this would, in principle, be sufficient for photonic effects.

5.3.8. Investigation of Thermal Degradation in 3DOM Materials

All of the refractory metals employed in this study have extremely low vapor pressures and low surface diffusivities at the temperatures of interest for TPV and lighting applications. Therefore these metallic photonic crystals should demonstrate

higher thermal stability than pure metallic nanostructures. Indeed, on heating the 3DOM carbon/tungsten film structure (with a hafnia interlayer) in Figure 5.19c at 1000 °C for 30 min, no change in structure of the sample was observed (Figure 5.19e). A high-resolution SEM image also revealed no significant change in the fidelity of the nanostructure or the coating stability (Figure 5. 19f). Similar thermal treatment of 3DOM tungsten without a 3DOM carbon scaffold showed significant grain coarsening under these conditions, which was detrimental to the 3D nanostructures unless they were stabilized by alloy formation.[114, 223] Therefore, it was concluded that these composite carbon–metal modified inverse opal structures have better thermal stability than similar reported metallic photonic crystals.[154]

However, the hafnia interlayer is critical to maintain this thermal stability, as the following experiments illustrate. Monoliths of 3DOM C/W1 and 3DOM C/W2 without a hafnia interlayer were heated under high vacuum (10^{-6} torr) at 5 °C min^{-1} to 1000 °C and held at that temperature for 1 h to assess their thermal stability. After heating, both samples retained their macropore structure and still exhibited a high degree of opalescence. However, SEM images of cross-sections of the heated samples showed extensive coalescence of the deposited tungsten into larger, droplet-like grains (Figures 5.25 and 5.26). In addition, the sizes of windows between adjacent pores were larger than before heating, being nearly constant with sample depth after tungsten had coalesced at positions away from the window edges (Table 5.2). Overall, the quality of the tungsten coating deteriorated after heat treatment in samples lacking a hafnia interlayer.

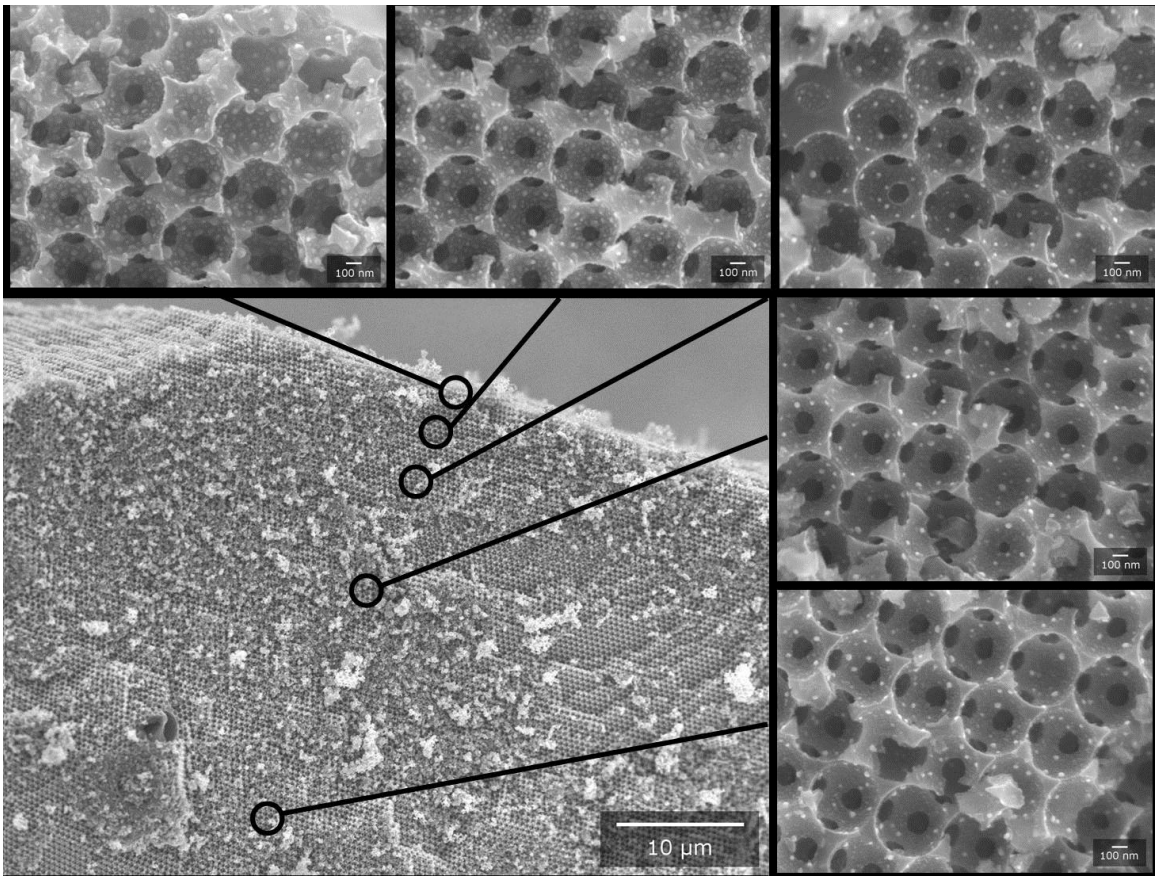

Figure 5.25. SEM images of sample 3DOM C/W1 (without a hafnia interlayer) after vacuum-thermal treatment at 1000 °C for 1 h. Clockwise from top left: images at depths of 1 µm, 8.5 µm, 20 µm, 40 µm, and 83 µm. The bottom-left image is an overview showing the respective position of the other images with the surface of the material appearing in the top-right of the image.

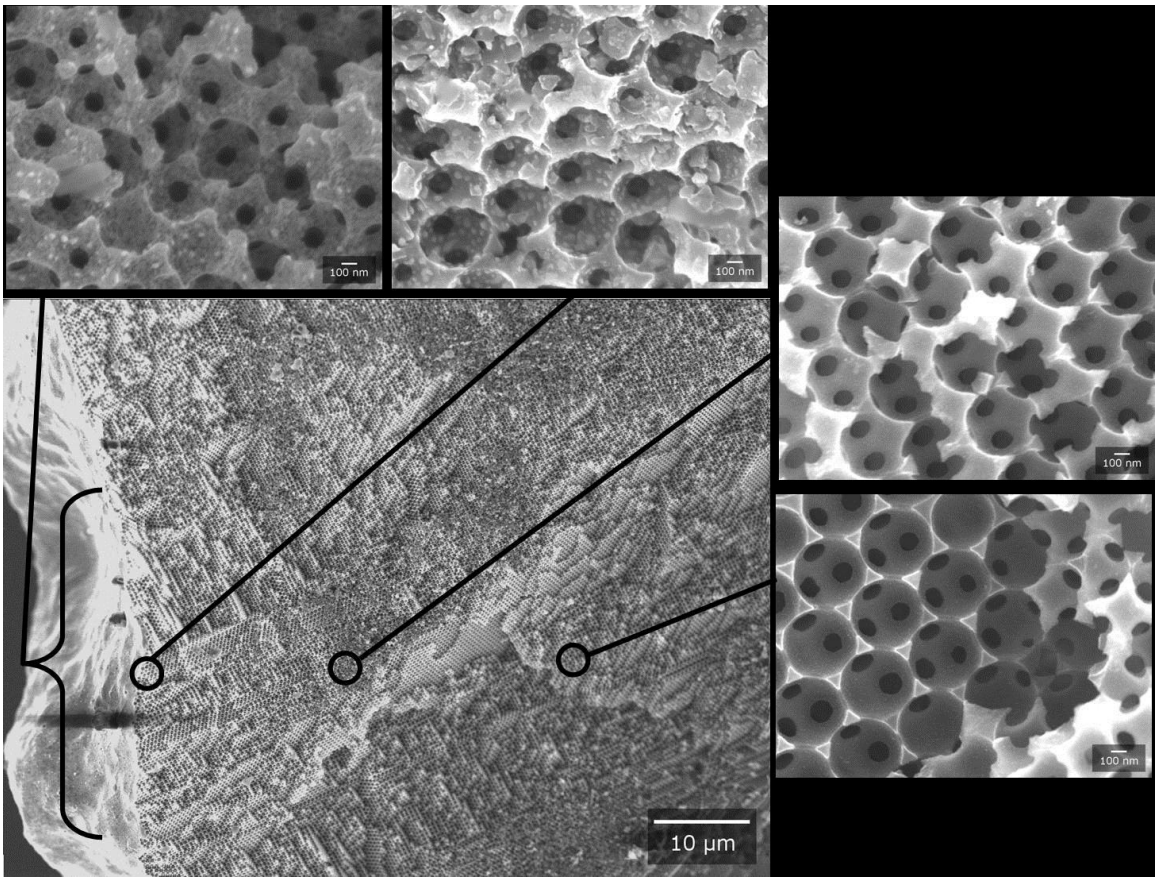

Figure 5.26. SEM images of sample 3DOM C/W2 (without a hafnia interlayer) after thermal treatment. Clockwise from top left: images at depths of 0 µm, 1 µm, 23 µm, and 46 µm. The bottom left is an overview showing the respective position of the other images with the surface of the material appearing on the left of the image. The images at depths of 23 and 46 µm (right corner) show no penetration of tungsten CVD layer (smooth 3DOM C scaffold). This indicates while using more metal precursor per deposition results in smoother metal coating, it leads to blocking of scaffold windows with metal deposition, and hence thinner metal deposition deeper into the sample.

Table 5.2. Variation in window sizes of samples 3DOM C/W1 and 3DOM C/W2, without a hafnia interlayer, after thermal treatment as a function of depth in the 3DOM C structure.

Sample 3DOM C/W1		**Sample 3DOM C/W2**	
Depth (μm)	Window	Depth (μm)	Window
1	142 ± 10	0	129 ± 8
9	140 ± 14	1	142 ± 13
20	133 ± 13	23	136 ± 15
40	138 ± 10	46	135 ± 11
83	141 ± 11		

When 3DOM C monoliths were coated with hafnia by ALD (3DOM C/W2H) using the same deposition conditions as for the thin film 3DOM C substrates, the hafnia layer penetrated the monoliths only to a depth of ca. 8–9 μm (Figure 5.20) As discussed above, tungsten coatings penetrated a little further into the monolith. As a result, the partial coating with hafnia provided an opportunity to observe the effect of hafnia on tungsten layer stability within the same sample. Figure 5.27 shows SEM images of a sample heated under vacuum at 1000 °C for 1 h, focusing on a region without a hafnia interlayer (Figure 5.27a), the interlayer border (Figure 5.27b), and a region with the hafnia interlayer (Figure 5.27c). Whereas the hafnia-free region shows the same pattern of tungsten agglomeration as described above, tungsten on the hafnia coating remained stable after heat treatment. The border region shows the transition from a smooth tungsten coating to agglomerates.

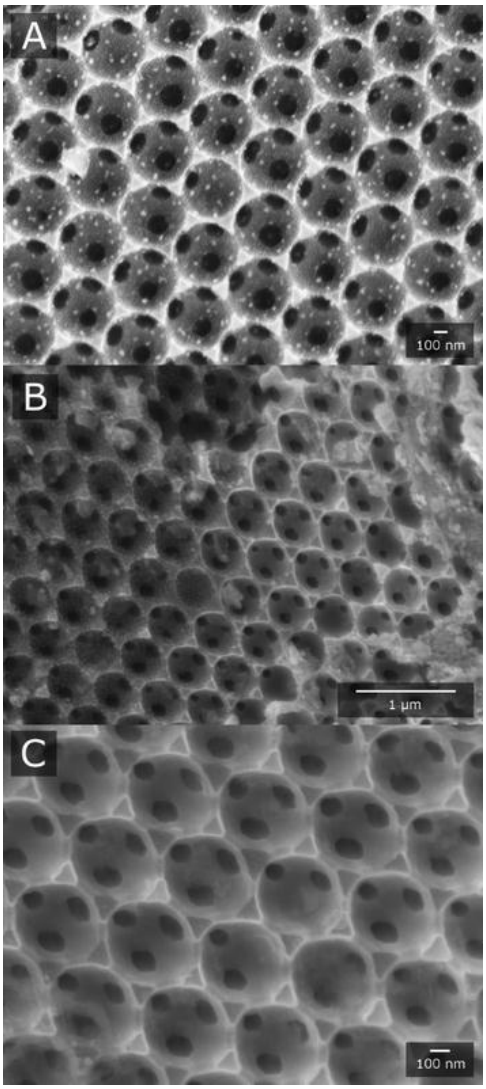

Figure 5.27 SEM images of a cross-section of a 3DOM C/W2H monolith with a partial hafnia interlayer after vacuum thermal treatment at 1000 °C for 1 h. (A) A region deeper in the monolith and not coated with hafnia. The white spots correspond to tungsten agglomerates. (B) A region showing the border for hafnia deposition. The area on the right was closer to the external surface of the monolith and had a hafnia coating. A smooth tungsten layer was maintained in this region after heat treatment. The hafnia coating did not extend to the region on the left. As a result, tungsten agglomerated in this region during thermal treatment. (C) A region closer to the external surface of the monolith which had been coated with hafnia and with tungsten. A smooth tungsten coating was maintained after thermal treatment.

Thus, the hafnia interlayer indeed served as a good adhesion promoter and prevented metal agglomeration successfully in thin films and in areas of 3DOM monoliths that could be covered by this layer. Similar observations were made after the 3DOM C/W2H

monolith was heated to 1000 °C for an additional 5 h: the monolith remained intact on the bulk scale and maintained a relatively smooth tungsten coating in regions coated with a hafnia interlayer (Figure 5.28), but not in regions lacking the hafnia interlayer. Although the observed penetration depth in the 3DOM carbon monoliths was not sufficient for forming a conformal hafnia adhesion layer throughout entire monoliths, thin films were well coated using this method. Moreover, several ALD processing parameters, like partial pressures of the gases, the evacuation time, and the final vapor pressure between sequential runs, can be optimized to increase the depth of penetration. But since light penetration in the nanocomposite metal structures is less than the coating depth, no further optimization was carried out. Therefore, the thermal stability of these nanocomposite materials is mainly limited by the adhesion of metal on the carbon scaffold, which is improved here by the use of a thermally stable hafnia interlayer.

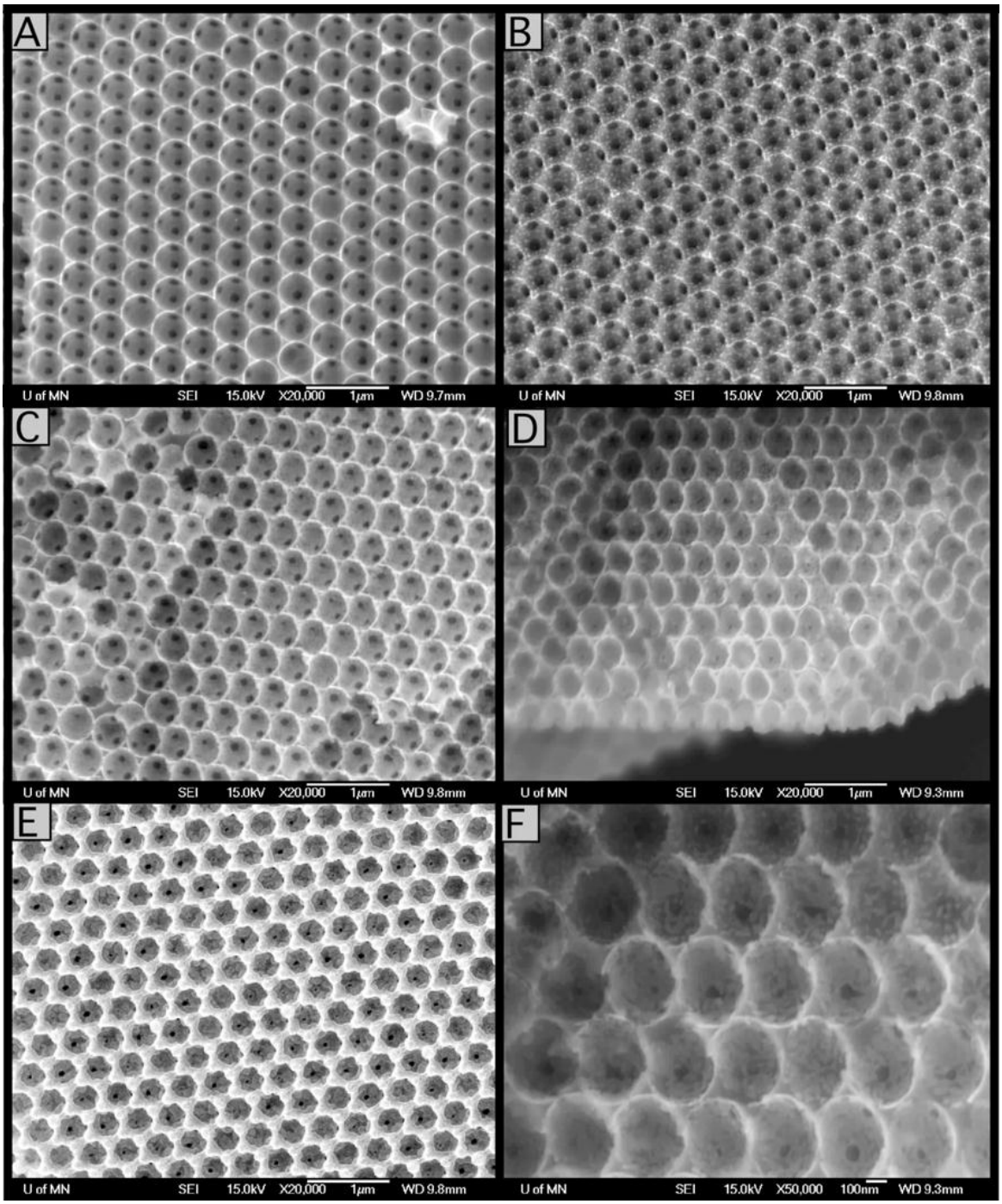

Figure 5.28. SEM images showing the texture gradient across the 3DOM C/W2H monolith which had been heated in vacuum at 1000 °C for 1 h and later for an additional 5 h. (A) Region near the center of the monolith, which had not been coated with hafnia or tungsten. (B-E) Regions with increasing amounts of tungsten. No hafnia interlayer was present in (B) and little in (C). Image (D) shows a region where the boundary for hafnia penetration becomes apparent from differences in brightness (increased charging where the hafnia layer insulates tungsten from carbon). Image (E) shows a surface layer. (F) Expanded view near the hafnia boundary in (D).

5.4. Conclusions

Photonic crystal materials with photonic band gaps in the IR range are of interest as thermophotovoltaics emitters. In order to achieve a materials with a band gap in this region, periodic features with micrometer spacing are needed. Towards this end, a method of improving the self-assembly of microspheres through a convection process between parallel plates was devised. This assembly method permitted the formation of colloidal crystal films with large, ordered regions. These films could then be infiltrated with various liquid precursors in order to form 3DOM structures with large pore diameters.

The fabrication of thermally stable metallic photonic crystals by CVD of refractory metals like tungsten, molybdenum, and tantalum on porous carbon scaffolds with a photonic crystal structure was demonstrated. These metallic photonic crystals were patterned in a modified inverse opal geometry that has been deemed suitable to tailor the thermal emission at different wavelengths. The thermal stability of the structures was enhanced by using the 3DOM carbon scaffold in combination with a thin hafnia interlayer as an adhesion promoter. The nanocomposites were mechanically much more robust than single-phase three-dimensionally patterned tungsten materials and could therefore be easily handled. The deposition procedure permits the formation of uniform refractory metal coatings throughout thin 3DOM carbon films over cm^2 areas and throughout the external regions in monolithic 3DOM carbon pieces, deep enough into the structure to expect modification of thermal emission. The smoothness of the surface layer

depends on the CVD schedule, more deposition steps leading to an increase in the visible surface roughness of the material.

The methods outlined here permit the design of three-dimensionally patterned metal nanostructures with a carbon core that enhances thermal and mechanical stability of the nanostructured metal, and a metallic surface that is thicker than the skin depth for light penetration into the metal (>50 nm) so that it should block direct light interaction with the scaffold.[203] With the goal of developing efficient thermal emitters for TPV modules across different wavelength ranges and perhaps for lighting applications,[224] the methods enable us to obtain the desired three-dimensional metal architecture and surface geometry with a choice of refractory metal. This approach may also be extended to nanostructured carbon scaffolds with different geometries for fabrication of other thermally stable, functional nanocomposite materials.

Chapter 6
Review and Future Outlook

6.1 Colored 3DOM Materials for Pigmentation

The investigations into colored 3DOM materials and their properties that were presented in this dissertation were largely fruitful. 3DOM pigments were created in almost every spectral color through various synthetic pathways that served to tune the color, chroma, and brightness of these materials. The use of 3DOM materials in pigment applications has a bright future. These structurally-colored materials have many advantages over most traditional organic or metal complex pigments in that they are resistant to photodegradation and can be synthesized in numerous spectral colors while being composed of only one material. These pigments also manifest a unique color mixing mechanism that is not currently seen in commercially available pigmentation. However, certain limitations must be addressed in order for these colored materials to fully realize their potential.

One such issue is the goniochromaticity that these materials exhibit. The coloration in 3DOM pigments is governed by a combination of Bragg's and Snell's laws described in Chapter 1. Under diffuse lighting, the observed color of 3DOM pigments, which depends on the angle of incident light, appears as the average of all incident angles and is approximated to be normal to the plane of diffraction. However, under directional light sources, the color can blue-shift with increasing changes in angle of incidence. This is manifested as a shift in coloration upon positional change of either the light source or the material. The effect is not readily observed in 3DOM samples with stop bands in the short-wave portion of the visible spectrum. This is due to the angle-dependent stop band blue-shifting into the UV range where it is not perceived as a color change, but rather a

reduction in color intensity. However, for 3DOM pigments with colors near the red portion of the spectrum, the color shift is pronounced, shifting from red to all other spectral colors as the angle of incidence is increased. Currently, this effect forces 3DOM materials into the category of specialty pigments so that they cannot be used for applications were a specific coloration is desired. In order to expand the range of applications of these pigments, solutions for this effect are needed. Currently, angle-dependent coloration is an inevitable side effect of the 3DOM structure. Any work towards the mitigation of this effect will have to involve novel structures or changes to the inverse opal structure itself in order to achieve this.

The elimination of solvent infiltration into 3DOM materials is also of great importance for future applications where 3DOM powders will be incorporated into various liquid matrices (i.e. paints, cosmetics). While the work outlined in Chapter 4 addresses this topic, further studies are needed in order to create a structure that is impervious to infiltration but also exhibits intense stop bands. Currently, for 3DO materials that resist infiltration, SiO_2 has been the most successful filling material for a PMMA template due to the extended gel network formed by the liquid precursor through crosslinking. This gelation mechanism serves to maintain a high fill fraction and ensures structural regularity with minimal void space and does not necessitate a thermal treatment step at high temperatures. However, SiO_2 has a low index of refraction (1.455) compared to the PMMA spheres it surrounds (1.49), resulting in low stop band intensity. Higher index of refraction filling materials such as TiO_2 (2.45), or ZrO_2 (2.15) could increase the refractive index contrast of these structures and improve stop band intensity. Both materials form cross-linked sol-gel networks under certain conditions[225-226] and could

potentially form regular structures which need not undergo thermal treatment at high temperatures, preserving the inclusion of the PMMA template which prevents infiltration into the pores.

The use of SiO_2 template spheres in structures that resist infiltration resulted in incomplete filling of void spaces within the 3DO structure discussed in Chapter 4. This was due to a mismatch in degree of shrinkage between the ZrO_2 filling material and the sphere material. Choosing a filling material that closely matches the shrinkage properties of the SiO_2 template could serve to reduce the amount of void space in the resulting structure. Additionally, several rounds of infiltration followed by thermal treatment could be used to fill void spaces.

Additionally, one important aspect for any colored photonic structure is the presence of a contrast agent within the material, as shown in Chapter 2. For both 3DOM ZrO_2 and 3DOM SiO_2, carbon was formed within the structure during pyrolysis and served as the contrast agent. For materials not undergoing thermal treatment at high temperatures, a contrast agent must be introduced another way. As described in Chapter 4, this was accomplished through the addition of a commercial dye into an as-synthesized 3DOM structure. However, for non-porous materials such as 3DO PMMA/SiO_2, also discussed in Chapter 4, other methods must be devised in order to increase the coloration of these structures. One potential route could be the addition of staining agents into the PMMA synthesis itself, or the application of the agents after synthesis. The PMMA spheres would then perform the dual role of template and contrast agent. For the targeting of specific wavelengths, specialized colored dyes could be used in order to layer the

photonic stop band of the material with a region of low absorbance of the dye, increasing a specific coloration through both photonic and molecular pathways.

One aspect of the inclusion of carbon as a contrast agent that remains to be studied is the long-term photo-stability of the carbon species that are created during the pyrolysis of 3DOM materials. The molecular structure of these species of carbon is currently unknown and the materials could potentially experience photo-bleaching over time. While the 3DOM structure itself is resistant to photobleaching due to the structural nature of the color mechanism, a reduction in contrast agent would effectively reduce the coloration of the 3DOM pigments. Long-term studies involving UV exposure of these pigments should be initiated in order to address this potential pitfall.

As research progresses in this area, care must be taken along the way to ensure that the processes involved in the production of colored photonic materials remain economically feasible. A major drawback in the current large-scale production of photonic materials is the intensive templating, infiltration, and thermal treatment of these materials. Therefore, efforts to combine or eliminate production steps in the synthesis of these materials are vital to their success in commercial applications.

6.2 3DOM UV Stop Band Materials

3DOM TiO_2/SiO_2 UV stop band materials were synthesized in order to partner the absorbance of the band edge of TiO_2 with the reflectance from a photonic stop band located near the band edge. Theoretically, this would partially extend the band edge to cover more of the UV range than would be possible with bulk TiO_2 alone. However,

multiple drawbacks in the nanostructuring of band edge materials were observed throughout the course of the study. The most prominent issue was that with low concentrations of TiO_2, extensive band edge shifts due to quantum size effects were detected. The shifting of the band edge greatly reduced the UV coverage of the material, contrary to the intended goal. When high amounts of TiO_2 were used in order to prevent these size effects, the 3DOM structure exhibited less long-range order, reducing the effects of the stop band. It was also found that, for materials with good structural order, the influence from the photonic stop band was minimal when compared to the influence of the TiO_2 band edge. The photonic stop band above the band edge only accounted for a reduction in transmittance of ca. <10%. In addition to these drawbacks, the high porosity of the 3DOM UV materials causes a high degree of incoherent scattering within the structure due to the multitude of surfaces with the material, causing a white appearance even when very thin films were observed. This white appearance is not desirable if these materials are to be used as commercial UV protectants.

In order to address these issues, several synthetic modifications will be required. Of primary importance is the elimination of the band edge shift in order to maximize the UV coverage. Alterations to the liquid precursor composition must be studied in order to achieve 3DOM materials with long-range structural order and high TiO_2 content. This would increase the influence of the stop band while maximizing the band edge influence. Various recipes for sol-gel TiO_2 precursors exist in the literature[227-229] and should be systematically analyzed for their resulting structural order and scattering properties.

Additionally, 3DOM composites of TiO_2/ZnO are of interest in order to combine the band-edge absorbances of both of these materials. TiO_2 is an effective absorber at short-wave UVB wavelengths while ZnO is more effective as a long-wave UVA blocker. The combination of the absorbance of these two materials along with strategic placement of the photonic stop band could be advantageous as long as care was taken to avoid quantum size effects and control incoherent scattering.

6.3 3DOM Metallic Photonic Crystals For Thermophotovoltaics

The use of 3DOM metallic photonic crystals for high temperature applications has previously been limited by the grain growth experienced by the 3DOM nanostructure. Changes to the periodic spacing of the materials through grain coarsening reduced the periodicity and reduced the functionality of the materials. In the work described in Chapter 5, a solution to this issue was found that involved using amorphous structures that do not experience grain growth at high temperatures and coating them with refractory metals that were pinned to the structure using a hafnia interlayer. These materials were found to be stable at 1000 °C for several hours. While the material aspects of the structure were addressed in that study, a functional thermophotovoltaic emitter using those materials was not synthesized. Similar work has since been published by Arpin *et al.*[230] that involved tungsten inverse opal structures formed through an atomic layer deposition process. This process resulted in a tungsten structure that resisted grain growth up to 1400 °C after coating with a refractory hafnia layer.

Future work within this field will likely consist of the modification of structural components in order to improve long-term thermal stability without loss of periodic

structure. However, the viability of these structures within thermophotovoltaic cells will ultimately depend on production costs. With solar energy pathways currently being utilized through solar cell technology that becomes more and more efficient and inexpensive every year, the production of photonic thermophotovoltaic cells will have to be similarly inexpensive. With current synthetic methods employing expensive atomic layer deposition and chemical vapor deposition techniques, scale-up of these materials will remain a challenge unless more facile synthetic pathways are found.

References

1. Li, F.; Josephson, D. P.; Stein, A. Colloidal Assembly: The Road from Particles to Colloidal Molecules and Crystals. *Angew. Chem. Int. Ed.* **2011,** *50*, 360-388.
2. Josephson, D.; Stein, A., Chapter 4: Tuning Color and Chroma of Opal and Inverse Opal Structures. In *Responsive Photonic Nanostructures: Smart Nanoscale Optical Materials*, Yin, Y., Ed. The Royal Society of Chemistry: **2013**; pp 63-90.
3. Luckiesh, M., *Color and Its Applications*. D. Van Nostrand Company: **1915**.
4. Brill, R. H. In *The Scientific Investigation of Ancient Glasses*, Proceedings of the Eighth International Congress on Glass, Scheffield, Eng., Society of Glass Technology: Scheffield, Eng., **1968**; pp 47-68.
5. Land, E. H., *The Retinex Theory of Color Vision*. Scientific America.: **1977**.
6. Kurucz, R. L.; Furenlid, I.; Brault, J.; Testerman, L., *Solar Flux Atlas from 296 to 1300 Nm*. **1984**.
7. Nassau, K., *The Physics and Chemistry of Color: The Fifteen Causes of Color, 2nd Ed.* John Wiley & Sons Inc.: New York, **2001**.
8. Yablonovitch, E. Inhibited Spontaneous Emission in Solid-State Physics and Electronics. *Phys. Rev. Lett.* **1987,** *58*, 2059-2062.
9. John, S. Strong Localization of Photons in Certain Disordered Dielectric Superlattices. *Phys. Rev. Lett.* **1987,** *58*, 2486-2489.
10. Kinoshita, S.; Yoshioka, S.; Kawagoe, K. Mechanisms of Structural Colour in the Morpho Butterfly: Cooperation of Regularity and Irregularity in an Iridescent Scale. *Proc. R. Soc. London, Ser. B* **2002,** *269*, 1417-1421.
11. Parker, A. R.; McPhedran, R. C.; McKenzie, D. R.; Botten, L. C.; Nicorovici, N. A. Photonic Engineering. Aphrodite's Iridescence. *Nature* **2001,** *409*, 36-7.
12. Lee, D. W. Ultrastructural Basis and Function of Iridescent Blue Colour of Fruits Inelaeocarpus. *Nature* **1991,** *349*, 260-262.
13. Bolton, H. C.; Bursill, L. A.; McLaren, A. C.; Turner, R. G. On the Origin of the Colour of Labradorite. *Phys. Status Solidi B* **1966,** *18*, 221-230.
14. Sanders, J. Diffraction of Light by Opals. *Acta Crystallogr., Sect. A: Found. Crystallogr.* **1968,** *24*, 427-434.
15. Sanders, J. V. Colour of Precious Opal. *Nature* **1964,** *204*, 1151-1153.
16. Lin, S. Y.; Fleming, J. G.; Hetherington, D. L.; Smith, B. K.; Biswas, R.; Ho, K. M.; Sigalas, M. M.; Zubrzycki, W.; Kurtz, S. R.; Bur, J. A Three-Dimensional Photonic Crystal Operating at Infrared Wavelengths. *Nature* **1998,** *394*, 251-253.
17. Noda, S.; Tomoda, K.; Yamamoto, N.; Chutinan, A. Full Three-Dimensional Photonic Bandgap Crystals at near-Infrared Wavelengths. *Science* **2000,** *289*, 604-606.
18. Shoji, S.; Kawata, S. Photofabrication of Three-Dimensional Photonic Crystals by Multibeam Laser Interference into a Photopolymerizable Resin. *Appl. Phys. Lett.* **2000,** *76*, 2668-2670.
19. Campbell, M.; Sharp, D. N.; Harrison, M. T.; Denning, R. G.; Turberfield, A. J. Fabrication of Photonic Crystals for the Visible Spectrum by Holographic Lithography. *Nature* **2000,** *404*, 53-56.
20. Wanke, M. C.; Lehmann, O.; Müller, K.; Wen, Q.; Stuke, M. Laser Rapid Prototyping of Photonic Band-Gap Microstructures. *Science* **1997,** *275*, 1284-1286.

21. Lee, J.-H.; Singer, J. P.; Thomas, E. L. Micro-/Nanostructured Mechanical Metamaterials. *Adv. Mater.* **2012,** *24*, 4782-4810.
22. Pusey, P. N.; van Megen, W.; Bartlett, P.; Ackerson, B. J.; Rarity, J. G.; Underwood, S. M. Structure of Crystals of Hard Colloidal Spheres. *Phys. Rev. Lett.* **1989,** *63*, 2753-2756.
23. Xia, Y.; Gates, B.; Yin, Y.; Lu, Y. Monodispersed Colloidal Spheres: Old Materials with New Applications. *Adv. Mater.* **2000,** *12*, 693-713.
24. Koh, Y. K.; Yip, C. H.; Chiang, Y.-M.; Wong, C. C. Kinetic Stages of Single-Component Colloidal Crystallization. *Langmuir* **2008,** *24*, 5245-5248.
25. Kaplan, P. D.; Rouke, J. L.; Yodh, A. G.; Pine, D. J. Entropically Driven Surface Phase Separation in Binary Colloidal Mixtures. *Phys. Rev. Lett.* **1994,** *72*, 582-585.
26. Dhont, J. K. G.; Smits, C.; Lekkerkerker, H. N. W. A Time Resolved Static Light Scattering Study on Nucleation and Crystallization in a Colloidal System. *J. Colloid Interface Sci.* **1992,** *152*, 386-401.
27. Woodcock, L. V. Entropy Difference between the Face-Centred Cubic and Hexagonal Close-Packed Crystal Structures. *Nature* **1997,** *385*, 141-143.
28. Jiang, P.; Bertone, J. F.; Hwang, K. S.; Colvin, V. L. Single-Crystal Colloidal Multilayers of Controlled Thickness. *Chem. Mater.* **1999,** *11*, 2132-2140.
29. Denkov, N. D.; Velev, O. D.; Kralchevsky, P. A.; Ivanov, I. B.; Yoshimura, H.; Nagayama, K. Two-Dimensional Crystallization. *Nature* **1993,** *361*, 26-26.
30. Cong, H.; Cao, W. Colloidal Crystallization Induced by Capillary Force. *Langmuir* **2003,** *19*, 8177-8181.
31. Im, S. H.; Lim, Y. T.; Suh, D. J.; Park, O. O. Three-Dimensional Self-Assembly of Colloids at a Water–Air Interface: A Novel Technique for the Fabrication of Photonic Bandgap Crystals. *Adv. Mater.* **2002,** *14*, 1367-1369.
32. Míguez, H.; Meseguer, F.; López, C.; Blanco, Á.; Moya, J. S.; Requena, J.; Mifsud, A.; Fornés, V. Control of the Photonic Crystal Properties of Fcc-Packed Submicrometer Sio_2 Spheres by Sintering. *Adv. Mater.* **1998,** *10*, 480-483.
33. Velev, O. D.; Jede, T. A.; Lobo, R. F.; Lenhoff, A. M. Porous Silica Via Colloidal Crystallization. *Nature* **1997,** *389*, 447-448.
34. Trau, M.; Saville, D. A.; Aksay, I. A. Assembly of Colloidal Crystals at Electrode Interfaces. *Langmuir* **1997,** *13*, 6375-6381.
35. Holland, B. T.; Blanford, C. F.; Stein, A. Synthesis of Macroporous Minerals with Highly Ordered Three-Dimensional Arrays of Spheroidal Voids. *Science* **1998,** *281*, 538-540.
36. Cai, Z.; Teng, J.; Yan, Q.; Zhao, X. S. Solvent Effect on the Self-Assembly of Colloidal Microspheres Via a Horizontal Deposition Method. *Colloids Surf., A* **2012,** *402*, 37-44.
37. Kanai, T.; Sawada, T. New Route to Produce Dry Colloidal Crystals without Cracks. *Langmuir* **2009,** *25*, 13315-13317.
38. Wang, L.; Zhao, X. S. Fabrication of Crack-Free Colloidal Crystals Using a Modified Vertical Deposition Method. *J. Phys. Chem. C* **2007,** *111*, 8538-8542.
39. Zhang, Z.; Shen, W.; Ye, C.; Luo, Y.; Li, S.; Li, M.; Xu, C.; Song, Y. Large-Area, Crack-Free Polysilazane-Based Photonic Crystals. *J. Mater. Chem.* **2012,** *22*, 5300-5303.

40. Stein, A.; Li, F.; Denny, N. R. Morphological Control in Colloidal Crystal Templating of Inverse Opals, Hierarchical Structures, and Shaped Particles. *Chem. Mater.* **2008,** *20*, 649-666.
41. Hiemenz, P. C.; Rajagopalan, R., *Principles of Colloid and Surface Chemistry*. Third ed.; CRC Press: Boca Raton, **1997**.
42. Norris, D. J.; Arlinghaus, E. G.; Meng, L.; Heiny, R.; Scriven, L. E. Opaline Photonic Crystals: How Does Self-Assembly Work? *Adv. Mater.* **2004,** *16*, 1393-1399.
43. Sanders, J. V.; Murray, M. J. Ordered Arrangements of Spheres of Two Different Sizes in Opal. *Nature* **1978,** *275*, 201-203.
44. Hachisu, S.; Yoshimura, S. Optical Demonstration of Crystalline Superstructures in Binary Mixtures of Latex Globules. *Nature* **1980,** *283*, 188-189.
45. Bartlett, P.; Ottewill, R. H.; Pusey, P. N. Superlattice Formation in Binary Mixtures of Hard-Sphere Colloids. *Phys. Rev. Lett.* **1992,** *68*, 3801-3804.
46. Hunt, N.; Jardine, R.; Bartlett, P. Superlattice Formation in Mixtures of Hard-Sphere Colloids. *Phys. Rev. E* **2000,** *62*, 900-913.
47. Kitaev, V.; Ozin, G. A. Self-Assembled Surface Patterns of Binary Colloidal Crystals. *Adv. Mater.* **2003,** *15*, 75-78.
48. Cong, H.; Cao, W. Array Patterns of Binary Colloidal Crystals. *J. Phys. Chem. B* **2005,** *109*, 1695-1698.
49. Wang, L.; Wan, Y.; Li, Y.; Cai, Z.; Li, H.-L.; Zhao, X. S.; Li, Q. Binary Colloidal Crystals Fabricated with a Horizontal Deposition Method. *Langmuir* **2009,** *25*, 6753-6759.
50. Zhou, Z.; Yan, Q.; Li, Q.; Zhao, X. S. Fabrication of Binary Colloidal Crystals and Non-Close-Packed Structures by a Sequential Self-Assembly Method. *Langmuir* **2006,** *23*, 1473-1477.
51. Rugge, A.; Tolbert, S. H. Effect of Electrostatic Interactions on Crystallization in Binary Colloidal Films. *Langmuir* **2002,** *18*, 7057-7065.
52. Leunissen, M. E.; Christova, C. G.; Hynninen, A.-P.; Royall, C. P.; Campbell, A. I.; Imhof, A.; Dijkstra, M.; van Roij, R.; van Blaaderen, A. Ionic Colloidal Crystals of Oppositely Charged Particles. *Nature* **2005,** *437*, 235-240.
53. Vermolen, E. C. M.; Kuijk, A.; Filion, L. C.; Hermes, M.; Thijssen, J. H. J.; Dijkstra, M.; van Blaaderen, A. Fabrication of Large Binary Colloidal Crystals with a Nacl Structure. *Proc. Natl. Acad. Sci. U.S.A.* **2009,** *106*, 16063-16067.
54. Bartlett, P.; Campbell, A. I. Three-Dimensional Binary Superlattices of Oppositely Charged Colloids. *Phys. Rev. Lett.* **2005,** *95*, 128302.
55. Kalsin, A. M.; Fialkowski, M.; Paszewski, M.; Smoukov, S. K.; Bishop, K. J. M.; Grzybowski, B. A. Electrostatic Self-Assembly of Binary Nanoparticle Crystals with a Diamond-Like Lattice. *Science* **2006,** *312*, 420-424.
56. Shevchenko, E. V.; Talapin, D. V.; Kotov, N. A.; O'Brien, S.; Murray, C. B. Structural Diversity in Binary Nanoparticle Superlattices. *Nature* **2006,** *439*, 55-59.
57. Shevchenko, E. V.; Talapin, D. V.; Murray, C. B.; O'Brien, S. Structural Characterization of Self-Assembled Multifunctional Binary Nanoparticle Superlattices. *J. Am. Chem. Soc.* **2006,** *128*, 3620-3637.

58. Ming, T.; Kou, X.; Chen, H.; Wang, T.; Tam, H.-L.; Cheah, K.-W.; Chen, J.-Y.; Wang, J. Ordered Gold Nanostructure Assemblies Formed by Droplet Evaporation. *Angew. Chem. Int. Edit.* **2008,** *47*, 9685-9690.
59. Pietrobon, B.; McEachran, M.; Kitaev, V. Synthesis of Size-Controlled Faceted Pentagonal Silver Nanorods with Tunable Plasmonic Properties and Self-Assembly of These Nanorods. *ACS Nano* **2008,** *3*, 21-26.
60. Li, F.; Wang, Z.; Stein, A. Shaping Mesoporous Silica Nanoparticles by Disassembly of Hierarchically Porous Structures. *Angew. Chem. Int. Edit.* **2007,** *46*, 1885-1888.
61. Li, F.; Delo, S. A.; Stein, A. Disassembly and Self-Reassembly in Periodic Nanostructures: A Face-Centered-to-Simple-Cubic Transformation. *Angew. Chem. Int. Edit.* **2007,** *46*, 6666-6669.
62. Lewandowski, E. P.; Bernate, J. A.; Tseng, A.; Searson, P. C.; Stebe, K. J. Oriented Assembly of Anisotropic Particles by Capillary Interactions. *Soft Matter* **2009,** *5*, 886-890.
63. Li, F.; Qian, Y.; Stein, A. Template-Directed Synthesis and Organization of Shaped Oxide/Phosphate Nanoparticles. *Chem. Mater.* **2010,** *22*, 3226-3235.
64. Schroden, R. C.; Al-Daous, M.; Blanford, C. F.; Stein, A. Optical Properties of Inverse Opal Photonic Crystals. *Chem. Mater.* **2002,** *14*, 3305-3315.
65. Wijnhoven, J. E. G. J.; Vos, W. L. Preparation of Photonic Crystals Made of Air Spheres in Titania. *Science* **1998,** *281*, 802-804.
66. Yan, H.; Blanford, C. F.; Holland, B. T.; Smyrl, W. H.; Stein, A. General Synthesis of Periodic Macroporous Solids by Templated Salt Precipitation and Chemical Conversion. *Chem. Mater.* **2000,** *12*, 1134-1141.
67. Waterhouse, G. I. N.; Metson, J. B.; Idriss, H.; Sun-Waterhouse, D. Physical and Optical Properties of Inverse Opal CeO_2 Photonic Crystals. *Chem. Mater.* **2008,** *20*, 1183-1190.
68. Stein, A.; Wilson, B. E.; Rudisill, S. G. Design and Functionality of Colloidal-Crystal-Templated Materials-Chemical Applications of Inverse Opals. *Chem. Soc. Rev.* **2013**.
69. Velev, O. D.; Jede, T. A.; Lobo, R. F.; Lenhoff, A. M. Microstructured Porous Silica Obtained Via Colloidal Crystal Templates. *Chem. Mater.* **1998,** *10*, 3597-3602.
70. Yang, P.; Deng, T.; Zhao, D.; Feng, P.; Pine, D.; Chmelka, B. F.; Whitesides, G. M.; Stucky, G. D. Hierarchically Ordered Oxides. *Science* **1998,** *282*, 2244-2246.
71. Holland, B. T.; Abrams, L.; Stein, A. Dual Templating of Macroporous Silicates with Zeolitic Microporous Frameworks. *J. Am. Chem. Soc.* **1999,** *121*, 4308-4309.
72. Holland, B. T.; Blanford, C. F.; Do, T.; Stein, A. Synthesis of Highly Ordered, Three-Dimensional, Macroporous Structures of Amorphous or Crystalline Inorganic Oxides, Phosphates, and Hybrid Composites. *Chem. Mater.* **1999,** *11*, 795-805.
73. Velev, O. D.; Tessier, P. M.; Lenhoff, A. M.; Kaler, E. W. Materials: A Class of Porous Metallic Nanostructures. *Nature* **1999,** *401*, 548-548.
74. Yan, H.; Blanford, C. F.; Holland, B. T.; Parent, M.; Smyrl, W. H.; Stein, A. A Chemical Synthesis of Periodic Macroporous Nio and Metallic Ni. *Adv. Mater.* **1999,** *11*, 1003-1006.

75. Denny, N. R.; Han, S.; Turgeon, R. T.; Lytle, J. C.; Norris, D. J.; Stein, A. In *Synthetic Approaches toward Tungsten Photonic Crystals for Thermal Emission*, Henry, H. D., Ed. SPIE: **2005**; p 600505.
76. Jiang, P.; Cizeron, J.; Bertone, J. F.; Colvin, V. L. Preparation of Macroporous Metal Films from Colloidal Crystals. *J. Am. Chem. Soc.* **1999,** *121*, 7957-7958.
77. von Freymann, G.; John, S.; Schulz-Dobrick, M.; Vekris, E.; Tetreault, N.; Wong, S.; Kitaev, V.; Ozin, G. A. Tungsten Inverse Opals: The Influence of Absorption on the Photonic Band Structure in the Visible Spectral Region. *Appl. Phys. Lett.* **2004,** *84*, 224-226.
78. Wijnhoven, J. E. G. J.; Zevenhuizen, S. J. M.; Hendriks, M. A.; Vanmaekelbergh, D.; Kelly, J. J.; Vos, W. L. Electrochemical Assembly of Ordered Macropores in Gold. *Adv. Mater.* **2000,** *12*, 888-890.
79. Yan, H.; Blanford, C. F.; Smyrl, W. H.; Stein, A. Preparation and Structure of 3D Ordered Macroporous Alloys by Pmma Colloidal Crystal Templating. *Chem. Commun.* **2000**, 1477-1478.
80. Park, S. H.; Xia, Y. Macroporous Membranes with Highly Ordered and Three-Dimensionally Interconnected Spherical Pores. *Adv. Mater.* **1998,** *10*, 1045-1048.
81. Park, S. H.; Xia, Y. Fabrication of Three-Dimensional Macroporous Membranes with Assemblies of Microspheres as Templates. *Chem. Mater.* **1998,** *10*, 1745-1747.
82. Jiang, P.; Hwang, K. S.; Mittleman, D. M.; Bertone, J. F.; Colvin, V. L. Template-Directed Preparation of Macroporous Polymers with Oriented and Crystalline Arrays of Voids. *J. Am. Chem. Soc.* **1999,** *121*, 11630-11637.
83. Johnson, S. A.; Ollivier, P. J.; Mallouk, T. E. Ordered Mesoporous Polymers of Tunable Pore Size from Colloidal Silica Templates. *Science* **1999,** *283*, 963-965.
84. Lee, Y. J.; Braun, P. V. Tunable Inverse Opal Hydrogel Ph Sensors. *Adv. Mater.* **2003,** *15*, 563-566.
85. Takeoka, Y.; Watanabe, M. Polymer Gels That Memorize Structures of Mesoscopically Sized Templates. Dynamic and Optical Nature of Periodic Ordered Mesoporous Chemical Gels. *Langmuir* **2002,** *18*, 5977-5980.
86. Wei, Y.; Liu, J.; Zhao, Z.; Duan, A.; Jiang, G. The Catalysts of Three-Dimensionally Ordered Macroporous $Ce_{1-X}Zr_xO_2$-Supported Gold Nanoparticles for Soot Combustion: The Metal–Support Interaction. *J. Catal.* **2012,** *287*, 13-29.
87. Wu, Q.; Liao, J.; Yin, Q.; Li, Y. Synthesis, Characterization and Catalytic Activity of Ordered Macroporous Silicas Functionalized with Organosulfur Groups. *Mater. Res. Bull.* **2008,** *43*, 1209-1217.
88. Han, D.; Li, X.; Zhang, L.; Wang, Y.; Yan, Z.; Liu, S. Hierarchically Ordered Meso/Macroporous Γ-Alumina for Enhanced Hydrodesulfurization Performance. *Microporous Mesoporous Mater.* **2012,** *158*, 1-6.
89. Chen, J. I. L.; von Freymann, G.; Choi, S. Y.; Kitaev, V.; Ozin, G. A. Amplified Photochemistry with Slow Photons. *Adv. Mater.* **2006,** *18*, 1915-1919.
90. Lin, Y.-G.; Hsu, Y.-K.; Chen, S.-Y.; Chen, L.-C.; Chen, K.-H. O2 Plasma-Activated Cuo-Zno Inverse Opals as High-Performance Methanol Microreformer. *J. Mater. Chem.* **2010,** *20*, 10611-10614.

91. Cheng, C.; Karuturi, S. K.; Liu, L.; Liu, J.; Li, H.; Su, L. T.; Tok, A. I. Y.; Fan, H. J. Quantum-Dot-Sensitized Tio2 Inverse Opals for Photoelectrochemical Hydrogen Generation. *Small (Weinheim an der Bergstrasse, Germany)* **2012,** *8*, 37-42.
92. Zhang, L.; Baumanis, C.; Robben, L.; Kandiel, T.; Bahnemann, D. Bi2wo6 Inverse Opals: Facile Fabrication and Efficient Visible-Light-Driven Photocatalytic and Photoelectrochemical Water-Splitting Activity. *Small (Weinheim an der Bergstrasse, Germany)* **2011,** *7*, 2714-2720.
93. Petkovich, N. D.; Rudisill, S. G.; Venstrom, L. J.; Boman, D. B.; Davidson, J. H.; Stein, A. Control of Heterogeneity in Nanostructured $Ce_{1-X}Zr_xO_2$ Binary Oxides for Enhanced Thermal Stability and Water Splitting Activity. *J. Phys. Chem. C* **2011,** *115*, 21022-21033.
94. Lim, M. H.; Blanford, C. F.; Stein, A. Synthesis of Ordered Microporous Silicates with Organosulfur Surface Groups and Their Applications as Solid Acid Catalysts. *Chem. Mater.* **1998,** *10*, 467-470.
95. Li, J.; Zheng, T. A Comparison of Chemical Sensors Based on the Different Ordered Inverse Opal Films. *Sens. Act. B Chem.* **2008,** *131*, 190-195.
96. Nishijima, Y.; Ueno, K.; Juodkazis, S.; Mizeikis, V.; Misawa, H.; Tanimura, T.; Maeda, K. Inverse Silica Opal Photonic Crystals for Optical Sensing Applications. *Opt. Express* **2007,** *15*, 12979-12988.
97. Liu, Z.; Xie, Z.; Zhao, X.; Gu, Z.-Z. Stretched Photonic Suspension Array for Label-Free High-Throughput Assay. *J. Mater. Chem.* **2008,** *18*, 3309-3312.
98. Pan, Z.; Ma, J.; Yan, J.; Zhou, M.; Gao, J. Response of Inverse-Opal Hydrogels to Alcohols. *J. Mater. Chem.* **2012,** *22*, 2018-2025.
99. Lai, C.-Z.; Fierke, M. A.; Stein, A.; Buhlmann, P. Ion-Selective Electrodes with Three-Dimensionally Ordered Macroporous Carbon as the Solid Contact. *Anal. Chem.* **2007,** *79*, 4621-4626.
100. Ergang, N. S.; Fierke, M. A.; Wang, Z.; Smyrl, W. H.; Stein, A. Fabrication of a Fully Infiltrated 3-Dimensional Solid-State Interpenetrating Electrochemical Cell. *J. Electrochem. Soc.* **2007,** *154*, A1135-A1139.
101. Ergang, N. S.; Lytle, J. C.; Lee, K. T.; Oh, S. M.; Smyrl, W. H.; Stein, A. Photonic Crystal Structures as a Basis for a Three-Dimensionally Interpenetrating Electrochemical-Cell System. *Adv. Mater.* **2006,** *18*, 1750-1753.
102. Lee, K. T.; Lytle, J. C.; Ergang, N. S.; Oh, S. M.; Stein, A. Synthesis and Rate Performance of Monolithic Macroporous Carbon Electrodes for Lithium-Ion Secondary Batteries. *Adv. Funct. Mater.* **2005,** *15*, 547-556.
103. Vu, A.; Stein, A. Multiconstituent Synthesis of $LiFePO_4$/C Composites with Hierarchical Porosity as Cathode Materials for Lithium Ion Batteries. *Chem. Mater.* **2011,** *23*, 3237-3245.
104. Wang, Z. Design, Fabrication, and Testing of Nanostructured Carbons and Composites. Ph.D. Thesis, University of Minnesota, Minneapolis, MN, **2008**.
105. Zhou, D.-D.; Liu, H.-J.; Wang, Y.-G.; Wang, C.-X.; Xia, Y.-Y. Ordered Mesoporous/Microporous Carbon Sphere Arrays Derived from Chlorination of Mesoporous Tic/C Composite and Their Application for Supercapacitors. *J. Mater. Chem.* **2012,** *22*, 1937-1943.

106. Blanco, A.; Chomski, E.; Grabtchak, S. I., M.; John, S.; Leonard, S. W.; Lopez, C.; Meseguer, F.; Miguez, H.; Mondia, J. P.; Ozin, G. A.; Toader, O.; van Driel, H. M. Large-Scale Synthesis of a Silicon Photonic Crystal with a Complete Three-Dimensional Bandgap near 1.5 Micrometres. *Nature* **2000,** *405*, 437-440.
107. Blanford, C. F.; Yan, H.; Schroden, R. C.; Al-Daous, M.; Stein, A. Gems of Chemistry and Physics: Macroporous Metal Oxides with 3d Order. *Adv. Mater.* **2001,** *13*, 401-407.
108. Blanford, C. F.; Schroden, R. C.; Al-Daous, M.; Stein, A. Tuning Solvent-Dependent Color Changes of Three-Dimensionally Ordered Macroporous (3DOM) Materials through Compositional and Geometric Modifications. *Adv. Mater.* **2001,** *13*, 26-29.
109. Schroden, R. C.; Blanford, C. F.; Melde, B. J.; Johnson, B. J. S.; Stein, A. Direct Synthesis of Ordered Macroporous Silica Materials Functionalized with Polyoxometalate Clusters. *Chem. Mater.* **2001,** *13*, 1074-1081.
110. Yan, H.; Zhang, K.; Blanford, C. F.; Francis, L. F.; Stein, A. In Vitro Hydroxycarbonate Apatite Mineralization of CaO-SiO_2 Sol-Gel Glasses with a Three-Dimensionally Ordered Macroporous Structure. *Chem. Mater.* **2001,** *13*, 1374-1382.
111. Wang, Z.; Ergang, N. S.; Al-Daous, M. A.; Stein, A. Synthesis and Characterization of Three-Dimensionally Ordered Macroporous Carbon/Titania Nanoparticle Composites. *Chem. Mater.* **2005,** *17*, 6805-6813.
112. Wang, Z.; Li, F.; Ergang, N. S.; Stein, A. Effects of Hierarchical Architecture on Electronic and Mechanical Properties of Nanocast Monolithic Porous Carbons and Carbon-Carbon Nanocomposites. *Chem. Mater.* **2006,** *18*, 5543-5553.
113. Stein, A.; Wang, Z.; Fierke, M. A. Functionalization of Porous Carbon Materials with Designed Pore Architecture. *Adv. Mater.* **2009,** *21*, 265-293.
114. Denny, N. R.; Han, S. E.; Norris, D. J.; Stein, A. Effects of Thermal Processes on the Structure of Monolithic Tungsten and Tungsten Alloy Photonic Crystals. *Chem. Mater.* **2007,** *19*, 4563-4569.
115. Han, S. E.; Stein, A.; Norris, D. J. Tailoring Self-Assembled Metallic Photonic Crystals for Modified Thermal Emission. *Phys. Rev. Lett.* **2007,** *99*, 053906/1-4.
116. Lin, S. Y.; Moreno, J.; Fleming, J. G. Three-Dimensional Photonic-Crystal Emitter for Thermal Photovoltaic Power Generation. *Appl. Phys. Lett.* **2003,** *83*, 380-382.
117. Rundquist, P. A.; Photinos, P.; Jagannathan, S.; Asher, S. A. Dynamical Bragg Diffraction from Crystalline Colloidal Arrays. *J. Chem. Phys.* **1989,** *91*, 4932-4941.
118. Monovoukas, Y.; Gast, A. P. A Study of Colloidal Crystal Morphology and Orientation Via Polarizing Microscopy. *Langmuir* **1991,** *7*, 460-468.
119. Liu, L.; Li, P.; Asher, S. A. Fortuitously Superimposed Lattice Plane Secondary Diffraction from Crystalline Colloidal Arrays. *J. Am. Chem. Soc.* **1997,** *119*, 2729-2732.
120. Johnson, S. G.; Joannopoulos, J. D. Designing Synthetic Optical Media: Photonic Crystals. *Acta. Mater.* **2003,** *51*, 5823-5835.
121. Kanai, T.; Sawada, T.; Toyotama, A.; Yamanaka, J.; Kitamura, K. Tuning the Effective Width of the Optical Stop Band in Colloidal Photonic Crystals. *Langmuir* **2007,** *23*, 3503-3505.

122. Bonifacio, L. D.; Lotsch, B. V.; Puzzo, D. P.; Scotognella, F.; Ozin, G. A. Stacking the Nanochemistry Deck: Structural and Compositional Diversity in One-Dimensional Photonic Crystals. *Adv. Mater.* **2009,** *21*, 1641-1646.
123. Lotsch, B. V.; Ozin, G. A. All-Clay Photonic Crystals. *J. Am. Chem. Soc.* **2008,** *130*, 15252-15253.
124. Caruso, R. A.; Susha, A.; Caruso, F. Multilayered Titania, Silica, and Laponite Nanoparticle Coatings on Polystyrene Colloidal Templates and Resulting Inorganic Hollow Spheres. *Chem. Mater.* **2001,** *13*, 400-409.
125. Asher, S. A.; Holtz, J.; Liu, L.; Wu, Z. Self-Assembly Motif for Creating Submicron Periodic Materials. Polymerized Crystalline Colloidal Arrays. *J. Am. Chem. Soc.* **1994,** *116*, 4997-4998.
126. Iwayama, Y.; Yamanaka, J.; Takiguchi, Y.; Takasaka, M.; Ito, K.; Shinohara, T.; Sawada, T.; Yonese, M. Optically Tunable Gelled Photonic Crystal Covering Almost the Entire Visible Light Wavelength Region. *Langmuir* **2003,** *19*, 977-980.
127. Debord, J. D.; Lyon, L. A. Thermoresponsive Photonic Crystals. *J. Phys. Chem. B* **2000,** *104*, 6327-6331.
128. Sharma, A. C.; Jana, T.; Kesavamoorthy, R.; Shi, L.; Virji, M. A.; Finegold, D. N.; Asher, S. A. A General Photonic Crystal Sensing Motif: Creatinine in Bodily Fluids. *J. Am. Chem. Soc.* **2004,** *126*, 2971-2977.
129. Lee, K.; Asher, S. A. Photonic Crystal Chemical Sensors: Ph and Ionic Strength. *J. Am. Chem. Soc.* **2000,** *122*, 9534-9537.
130. Nakayama, D.; Takeoka, Y.; Watanabe, M.; Kataoka, K. Simple and Precise Preparation of a Porous Gel for a Colorimetric Glucose Sensor by a Templating Technique. *Angew. Chem. Int. Ed.* **2003,** *42*, 4197-4200.
131. Wang, J. Y.; Cao, Y.; Feng, Y.; Yin, F.; Gao, J. P. Multiresponsive Inverse-Opal Hydrogels. *Adv. Mater.* **2007,** *19*, 3865-3871.
132. Lee, Y.-J.; Pruzinsky, S. A.; Braun, P. V. Glucose-Sensitive Inverse Opal Hydrogels: Analysis of Optical Diffraction Response. *Langmuir* **2004,** *20*, 3096-3106.
133. Honda, M.; Kataoka, K.; Seki, T.; Takeoka, Y. Confined Stimuli-Responsive Polymer Gel in Inverse Opal Polymer Membrane for Colorimetric Glucose Sensor. *Langmuir* **2009,** *25*, 8349-8356.
134. Arsenault, A. C.; Clark, T. J.; von Freymann, G.; Cademartiri, L.; Sapienza, R.; Bertolotti, J.; Vekris, E.; Wong, S.; Kitaev, V.; Manners, I.; Wang, R. Z.; John, S.; Wiersma, D.; Ozin, G. A. From Colour Fingerprinting to the Control of Photoluminescence in Elastic Photonic Crystals. *Nat. Mater.* **2006,** *5*, 179-184.
135. Li, J.; Wu, Y.; Fu, J.; Cong, Y.; Peng, J.; Han, Y. Reversibly Strain-Tunable Elastomeric Photonic Crystals. *Chem. Phys. Lett.* **2004,** *390*, 285-289.
136. Wang, J.; Han, Y. Tunable Multicolor Pattern and Stop-Band Shift Based on Inverse Opal Hydrogel Heterostructure. *J. Colloid Interface Sci.* **2011,** *357*, 139-146.
137. Wang, J.; Han, Y. Tuning the Stop Bands of Inverse Opal Hydrogels with Double Network Structure by Controlling the Solvent and Ph. *J. Colloid Interface Sci.* **2011,** *353*, 498-505.
138. Yuan, Y.; Li, Z.; Liu, Y.; Gao, J.; Pan, Z.; Liu, Y. Hydrogel Photonic Sensor for the Detection of 3-Pyridinecarboxamide. *Chem. Eur. J.* **2012,** *18*, 303-309.

139. Wang, L.-Q.; Lin, F.-Y.; Yu, L.-P. A Molecularly Imprinted Photonic Polymer Sensor with High Selectivity for Tetracyclines Analysis in Food. *Analyst* **2012,** *137*, 3502-3509.
140. Bogomolov, V. N.; Gaponenko, S. V.; Germanenko, I. N.; Kapitonov, A. M.; Petrov, E. P.; Gaponenko, N. V.; Prokofiev, A. V.; Ponyavina, A. N.; Silvanovich, N. I.; Samoilovich, S. M. Photonic Band Gap Phenomenon and Optical Properties of Artificial Opals. *Phys. Rev. E: Stat. Nonlinear Soft Matter Phys.* **1997,** *55*, 7619-7625.
141. Bogomolov, V. N.; Gaponenko, S. V.; Kapitonov, A. M.; Prokofiev, A. V.; Ponyavina, A. N.; Silvanovich, N. I.; Samoilovich, S. M. Photonic Band Gap in the Visible Range in a Three-Dimensional Solid State Lattice. *Appl. Phys. A-Mater.* **1996,** *63*, 613-616.
142. Burgess, I. B.; Mishchenko, L.; Hatton, B. D.; Kolle, M.; Lončar, M.; Aizenberg, J. Encoding Complex Wettability Patterns in Chemically Functionalized 3d Photonic Crystals. *J. Am. Chem. Soc.* **2011,** *133*, 12430-12432.
143. Burgess, I. B.; Koay, N.; Raymond, K. P.; Kolle, M.; Lončar, M.; Aizenberg, J. Wetting in Color: Colorimetric Differentiation of Organic Liquids with High Selectivity. *ACS Nano* **2011,** *6*, 1427-1437.
144. Kamp, U.; Kitaev, V.; von Freymann, G.; Ozin, G. A.; Mabury, S. A. Colloidal Crystal Capillary Columns—Towards Optical Chromatography. *Adv. Mater.* **2005,** *17*, 438-443.
145. Li, H.; Chang, L.; Wang, J.; Yang, L.; Song, Y. A Colorful Oil-Sensitive Carbon Inverse Opal. *J. Mater. Chem.* **2008,** *18*, 5098-5103.
146. Li, H.; Wang, J.; Yang, L.; Song, Y. Superoleophilic and Superhydrophobic Inverse Opals for Oil Sensors. *Adv. Funct. Mater.* **2008,** *18*, 3258-3264.
147. Zhao, Y.; Zhao, X.; Hu, J.; Xu, M.; Zhao, W.; Sun, L.; Zhu, C.; Xu, H.; Gu, Z. Encoded Porous Beads for Label-Free Multiplex Detection of Tumor Markers. *Adv. Mater.* **2009,** *21*, 569-572.
148. Busch, K.; John, S. Liquid-Crystal Photonic-Band-Gap Materials: The Tunable Electromagnetic Vacuum. *Phys. Rev. Lett.* **1999,** *83*, 967-970.
149. Kubo, S.; Gu, Z.-Z.; Takahashi, K.; Ohko, Y.; Sato, O.; Fujishima, A. Control of the Optical Band Structure of Liquid Crystal Infiltrated Inverse Opal by a Photoinduced Nematic−Isotropic Phase Transition. *J. Am. Chem. Soc.* **2002,** *124*, 10950-10951.
150. Busch, K.; John, S. Photonic Band Gap Formation in Certain Self-Organizing Systems. *Phys. Rev. E: Stat. Nonlinear Soft Matter Phys.* **1998,** *58*, 3896-3908.
151. Rugge, A.; Park, J.-S.; Gordon, R. G.; Tolbert, S. H. Tantalum(V) Nitride Inverse Opals as Photonic Structures for Visible Wavelengths. *J. Phys. Chem. B* **2004,** *109*, 3764-3771.
152. Vlasov, Y. A.; Bo, X.-Z.; Sturm, J. C.; Norris, D. J. On-Chip Natural Assembly of Silicon Photonic Bandgap Crystals. *Nature* **2001,** *414*, 289-293.
153. Meseguer, F.; Blanco, A.; Míguez, H.; García-Santamaría, F.; Ibisate, M.; López, C. Synthesis of Inverse Opals. *Colloids Surf., A* **2002,** *202*, 281-290.
154. Yu, X.; Lee, Y. J.; Furstenberg, R.; White, J. O.; Braun, P. V. Filling Fraction Dependent Properties of Inverse Opal Metallic Photonic Crystals. *Adv. Mater.* **2007,** *19*, 1689-1692.

155. Aguirre, C. I.; Reguera, E.; Stein, A. Colloidal Photonic Crystal Pigments with Low Angle Dependence. *ACS Appl. Mater. Interfaces* **2010,** *2*, 3257-3262.
156. Shen, Z.; Shi, L.; You, B.; Wu, L.; Zhao, D. Large-Scale Fabrication of Three-Dimensional Ordered Polymer Films with Strong Structure Colors and Robust Mechanical Properties. *J. Mater. Chem.* **2012,** *22*, 8069-8075.
157. Pursiainen, O. L.; Baumberg, J. J.; Winkler, H.; Viel, B.; Spahn, P.; Ruhl, T. Nanoparticle-Tuned Structural Color from Polymer Opals. *Opt. Express* **2007,** *15*, 9553-9561.
158. Finlayson, C. E.; Spahn, P.; Snoswell, D. R. E.; Yates, G.; Kontogeorgos, A.; Haines, A. I.; Hellmann, G. P.; Baumberg, J. J. 3d Bulk Ordering in Macroscopic Solid Opaline Films by Edge-Induced Rotational Shearing. *Adv. Mater.* **2011,** *23*, 1540-1544.
159. Snoswell, D. R. E.; Kontogeorgos, A.; Baumberg, J. J.; Lord, T. D.; Mackley, M. R.; Spahn, P.; Hellmann, G. P. Shear Ordering in Polymer Photonic Crystals. *Phys. Rev. E: Stat. Nonlinear Soft Matter Phys.* **2010,** *81*, 020401.
160. Pursiainen, O. L. J.; Baumberg, J. J.; Winkler, H.; Viel, B.; Spahn, P.; Ruhl, T. Shear-Induced Organization in Flexible Polymer Opals. *Adv. Mater.* **2008,** *20*, 1484-1487.
161. Baumberg, J. J.; Pursiainen, O. L.; Spahn, P. Resonant Optical Scattering in Nanoparticle-Doped Polymer Photonic Crystals. *Phys. Rev. B: Condens. Matter* **2009,** *80*, 201103.
162. He, L.; Wang, M.; Ge, J.; Yin, Y. Magnetic Assembly Route to Colloidal Responsive Photonic Nanostructures. *Acc. Chem. Res.* **2012,** *45*, 1431-1440.
163. Sigalas, M. M.; Chan, C. T.; Ho, K. M.; Soukoulis, C. M. Metallic Photonic Band-Gap Materials. *Phys. Rev. B* **1995,** *52*, 11744.
164. Fleming, J. G.; Lin, S. Y.; El-Kady, I.; Biswas, R.; Ho, K. M. All-Metallic Three-Dimensional Photonic Crystals with a Large Infrared Bandgap. *Nature* **2002,** *417*, 52-55.
165. Lin, S.-Y.; Fleming, J. G.; El-Kady, I. Experimental Observation of Photonic-Crystal Emission near a Photonic Band Edge. *Appl. Phys. Lett.* **2003,** *83*, 593-595.
166. Josephson, D. P.; Popczun, E. J.; Stein, A. Effects of Integrated Carbon as a Light Absorber on the Coloration of Photonic Crystal-Based Pigments. *J. Phys. Chem. C* **2013,** *117*, 13585-13592.
167. Pfaff, G.; Reynders, P. Angle-Dependent Optical Effects Deriving from Submicron Structures of Films and Pigments. *Chem. Rev.* **1999,** *99*, 1963-1982.
168. Wang, Z.; Al-Daous, M. A.; Kiesel, E. R.; Li, F.; Stein, A. Design and Synthesis of 3D Ordered Macroporous ZrO_2/Zeolite Nanocomposites. *Microporous Mesoporous Mater.* **2009,** *120*, 351-358.
169. Pursiainen, O. L. J.; Baumberg, J. J.; Ryan, K.; Bauer, J.; Winkler, H.; Viel, B.; Ruhl, T. Compact Strain-Sensitive Flexible Photonic Crystals for Sensors. *Appl. Phys. Lett.* **2005,** *87*, 101902-3.
170. Goodwin, J. W.; Ottewill, R. H.; Pelton, R.; Vianello, G.; Yates, D. E. Control of Particle Size in the Formation of Polymer Latices. *Br. Polym. J.* **1978,** *10*, 173-180.
171. Zou, D.; Ma, S.; Guan, R.; Park, M.; Sun, L.; Aklonis, J. J.; Salovey, R. Model Filled Polymers. V. Synthesis of Crosslinked Monodisperse Polymethacrylate Beads. *J. Polym. Sci., Part A: Polym. Chem.* **1992,** *30*, 137-144.

172. Pitcher, M. W.; Ushakov, S. V.; Navrotsky, A.; Woodfield, B. F.; Li, G.; Boerio-Goates, J.; Tissue, B. M. Energy Crossovers in Nanocrystalline Zirconia. *J. Am. Ceram. Soc.* **2005,** *88*, 160-167.
173. Li, B.; Gonzalez, R. D. Sol−Gel Synthesis and Catalytic Properties of Sulfated Zirconia Catalysts. *Ind. Eng. Chem. Res.* **1996,** *35*, 3141-3148.
174. Jun, S.; Joo, S. H.; Ryoo, R.; Kruk, M.; Jaroniec, M.; Liu, Z.; Ohsuna, T.; Terasaki, O. Synthesis of New, Nanoporous Carbon with Hexagonally Ordered Mesostructure. *J. Am. Chem. Soc.* **2000,** *122*, 10712-10713.
175. Gajan, D.; Coperet, C. Silica-Supported Single-Site Catalysts: To Be or Not to Be? A Conjecture on Silica Surfaces. *New J. Chem.* **2011,** *35*, 2403-2408.
176. Ali, I.; Al-Othman, Z. A.; Nagae, N.; Gaitonde, V. D.; Dutta, K. K. Recent Trends in Ultra-Fast Hplc: New Generation Superficially Porous Silica Columns. *J. Sep. Sci.* **2012,** *35*, 3235-3249.
177. Ciriminna, R.; Fidalgo, A.; Pandarus, V.; Béland, F.; Ilharco, L. M.; Pagliaro, M. The Sol–Gel Route to Advanced Silica-Based Materials and Recent Applications. *Chem. Rev.* **2013,** *113*, 6592-6620.
178. Giraldo, L. F.; López, B. L.; Pérez, L.; Urrego, S.; Sierra, L.; Mesa, M. Mesoporous Silica Applications. *Macromol. Symp.* **2007,** *258*, 129-141.
179. Tanrisever, T.; Okay, O.; Sönmezoğlu, I. Ç. Kinetics of Emulsifier–Free Emulsion Polymerization of Methyl Methacrylate. *J. Appl. Polym. Sci.* **1996,** *61*, 485-493.
180. Klein, L. C.; Gallo, T. A.; Garvey, G. J. Densification of Monolithic Silica Gels Below 1000°C. *J. Non-Cryst. Solids* **1984,** *63*, 23-33.
181. Nogami, M.; Moriya, Y. Glass Formation through Hydrolysis of $Si(OC_2H_5)_4$ with Nh4oh and Hcl Solution. *J. Non-Cryst. Solids* **1980,** *37*, 191-201.
182. Robertson, J. Amorphous Carbon. *Adv. Phys.* **1986,** *35*, 317-374.
183. Dischler, B.; Bubenzer, A.; Koidl, P. Hard Carbon Coatings with Low Optical Absorption. *Appl. Phys. Lett.* **1983,** *42*, 636-638.
184. Grill, A. Electrical and Optical Properties of Diamond-Like Carbon. *Thin Solid Films* **1999,** *355–356*, 189-193.
185. Smith, T.; Guild, J. The C.I.E. Colorimetric Standards and Their Use. *Trans. Opt. Soc.* **1931,** *33*, 73.
186. Herzog, B.; Hüglin, D.; Borsos, E.; Stehlin, A.; Luther, H. New Uv Absorbers for Cosmetic Sunscreens - a Breakthrough for the Photoprotection of Human Skin. *Chimia* **2004,** *58*, 554-559.
187. Tsatsaroni, E. G.; Eleftheriadis, I. C. Uv-Absorbers in the Dyeing of Polyester with Disperse Dyes. *Dyes Pigm.* **2004,** *61*, 141-147.
188. Lee, J. J.; Lee, H. H.; Eom, S. I.; Kim, J. P. Uv Absorber Aftertreatment to Improve Lightfastness of Natural Dyes on Protein Fibres. *Color. Technol.* **2001,** *117*, 134-138.
189. Lapidot, N.; Gans, O.; Biagini, F.; Sosonkin, L.; Rottman, C. Advanced Sunscreens: UV Absorbers Encapsulated in Sol-Gel Glass Microcapsules. *J. Sol-Gel Sci. Technol.* **2003,** *26*, 67-72.

190. Osterwalder, U.; Herzog, B. The Long Way Towards the Ideal Sunscreen-Where We Stand and What Still Needs to Be Done. *Photochem. Photobiol. Sci.* **2010,** *9*, 470-481.
191. Dransfield, G. P. Inorganic Sunscreens. *Radiat. Prot. Dosim.* **2000,** *91*, 271-273.
192. Lewicka, Z.; Benedetto, A.; Benoit, D.; Yu, W.; Fortner, J.; Colvin, V. The Structure, Composition, and Dimensions of Tio2 and Zno Nanomaterials in Commercial Sunscreens. *J. Nanopart. Res.* **2011,** *13*, 3607-3617.
193. Mahltig, B.; Böttcher, H.; Rauch, K.; Dieckmann, U.; Nitsche, R.; Fritz, T. Optimized Uv Protecting Coatings by Combination of Organic and Inorganic UV Absorbers. *Thin Solid Films* **2005,** *485*, 108-114.
194. Stöber, W.; Fink, A.; Bohn, E. Controlled Growth of Monodisperse Silica Spheres in the Micron Size Range. *J. Colloid Interface Sci.* **1968,** *26*, 62-69.
195. Tolvaj, L.; Mitsui, K.; Varga, D. Validity Limits of Kubelka–Munk Theory for Drift Spectra of Photodegraded Solid Wood. *Wood Sci. Technol.* **2011,** *45*, 135-146.
196. Olmsted, R., Chapter 4: Advanced Color Formulation Technology. In *Coloring of Plastics: Fundamentals. Second Edition*, Charvat, R. A., Ed. John Wiley & Sons, Inc.: Hoboken, New Jersey, pp 50-52.
197. Kormann, C.; Bahnemann, D. W.; Hoffmann, M. R. Preparation and Characterization of Quantum-Size Titanium Dioxide. *J. Phys. Chem.* **1988,** *92*, 5196-5201.
198. Nagpal, P.; Josephson, D. P.; Denny, N. R.; DeWilde, J.; Norris, D. J.; Stein, A. Fabrication of Carbon/Refractory Metal Nanocomposites as Thermally Stable Metallic Photonic Crystals. *J. Mater. Chem.* **2011,** *21*, 10836-10843.
199. Green, M. A., *Third Generation Photovoltaics*. Springer: Berlin, 2006.
200. Luque, A.; Marti, A., Non-Conventional Photovoltaic Technology: A Need to Reach Goals. In *Next Generation Photovoltaics: High Efficiency through Full Spectrum Utilization*

Institute of Physics Publishing Ltd.: 2004; pp 1-18.
201. Coutts, T. J.; Fitzgerald, M. C., Thermophotovoltaics. *Sci. Am.* 1998, pp 90-95.
202. Lin, S.-Y.; Fleming, J. G.; El-Kady, I. Three-Dimensional Photonic-Crystal Emission through Thermal Excitation. *Opt. Lett.* **2003,** *28*, 1909-1911.
203. Nagpal, P.; Han, S. E.; Stein, A.; Norris, D. J. Efficient Low-Temperature Thermophotovoltaic Emitters from Metallic Photonic Crystals. *Nano. Lett.* **2008,** *8*, 3238-3243.
204. Lee, J. H.; Kim, Y. S.; Constant, K.; Ho, K. M. Woodpile Metallic Photonic Crystals Fabricated by Using Soft Lithography for Tailored Thermal Emission. *Adv. Mater.* **2007,** *19*, 791-794.
205. Luo, C.; Johnson, S.; Joannopoulos, J.; Pendry, J. Negative Refraction without Negative Index in Metallic Photonic Crystals. *Opt. Express* **2003,** *11*, 746-754.
206. Ho, K. M.; Chan, C. T.; Soukoulis, C. M.; Biswas, R.; Sigalas, M. Photonic Band Gaps in Three Dimensions: New Layer-by-Layer Periodic Structures. *Solid State Commun.* **1994,** *89*, 413-416.
207. Cao, Y. Y.; Takeyasu, N.; Tanaka, T.; Duan, X. M.; Kawata, S. 3d Metallic Nanostructure Fabrication by Surfactant-Assisted Multiphoton-Induced Reduction. *Small (Weinheim an der Bergstrasse, Germany)* **2009,** *5*, 1144-8.

208. Sun, H.-B.; Matsuo, S.; Misawa, H. Three-Dimensional Photonic Crystal Structures Achieved with Two-Photon-Absorption Photopolymerization of Resin. *Appl. Phys. Lett.* **1999,** *74*, 786-788.
209. Berger, V.; Gauthier-Lafaye, O.; Costard, E. Photonic Band Gaps and Holography. *J. Appl. Phys.* **1997,** *82*, 60-64.
210. De La Rue, R. Photonic Crystals: Microassembly in 3d. *Nat. Mater.* **2003,** *2*, 74-76.
211. Saravanamuttu, K.; Blanford, C. F.; Sharp, D. N.; Dedman, E. R.; Turberfield, A. J.; Denning, R. G. Sol-Gel Organic-Inorganic Composites for 3-D Holographic Lithography of Photonic Crystals with Submicron Periodicity. *Chem. Mater.* **2003,** *15*, 2301-2304.
212. Sell, C.; Christensen, C.; Muehlmeier, J.; Tuttle, G. Waveguide Networks in Three-Dimensional Layer-by-Layer Photonic Crystals. *Appl. Phys. Lett.* **2004,** *84*, 4605.
213. Deubel, M.; von Freymann, G.; Wegener, M.; Pereira, S.; Busch, K.; Soukoulis, C. M. Direct Laser Writing of Three-Dimensional Photonic-Crystal Templates for Telecommunications. *Nat. Mater.* **2004,** *3*, 444-447.
214. Akimov, A. V.; Meluchev, A. A.; Kurdyukov, D. A.; Scherbakov, A. V.; Holst, A.; Golubev, V. G. Plasmonic Effects and Visible Light Diffraction in Three-Dimensional Opal-Metal Photonic Crystals. *Appl. Phys. Lett.* **2007,** *90*, 171108-3.
215. Wen-Chien, L.; Chang-Hung, L.; Ruoh-Chyu, R.; Keh-Ying, H. High-Performance Affinity Chromatography of Proteins on Non-Porous Polystyrene Beads. *J. Chromatogr.* **1995,** *704*, 307-314.
216. Sharma, N.; Deepa, M.; Varshney, P.; Agnihotry, S. A. Ftir and Absorption Edge Studies on Tungsten Oxide Based Precursor Materials Synthesized by Sol-Gel Technique. *J. Non-cryst. Solids* **2002,** *306*, 129-137.
217. Pronk, S.; Frenkel, D. Large Effect of Polydispersity on Defect Concentrations in Colloidal Crystals. *J. Chem. Phys.* **2004,** *120*, 6764-6768.
218. Pusey, P. N.; Zaccarelli, E.; Valeriani, C.; Sanz, E.; Poon, W. C. K.; Cates, M. E. Hard Spheres: Crystallization and Glass Formation. *Philos. Trans. R. Soc. London, Ser. A* **2009,** *367*, 4993-5011.
219. Li, H.-L.; Dong, W.; Bongard, H.-J.; Marlow, F. Improved Controllability of Opal Film Growth Using Capillaries for the Deposition Process. *J. Phys. Chem. B* **2005,** *109*, 9939-9945.
220. Zakhidov, A. A.; Baughman, R. H.; Iqbal, Z.; Cui, C.; Khayrullin; I.; Dantas, S. O.; Marti, J.; Ralchenko, V. G. Carbon Structures with Three-Dimensional Periodicity at Optical Wavelengths. *Science* **1998,** *282*, 897-901.
221. Kukli, K.; Ritala, M.; Sajavaara, T.; Keinonen, J.; Leskelä, M. Atomic Layer Deposition of Hafnium Dioxide Films from Hafnium Tetrakis(Ethylmethylamide) and Water. *Chem. Vap. Deposition* **2002,** *8*, 199-204.
222. Liu, X.; Ramanathan, S.; Longdergan, A.; Srivastava, A.; Lee, E.; Seidel, T. E.; Barton, J. T.; Pang, D.; Gordon, R. G. Ald of Hafnium Oxide Thin Films from Tetrakis(Ethylmethylamino)Hafnium and Ozone. *J. Electrochem. Soc.* **2005,** *152*, G213-G219.

223. Denny, N. R.; Li, F.; Norris, D. J.; Stein, A. In Situ High Temperature Tem Analysis of Sintering in Nanostructured Tungsten and Tungsten-Molybdenum Alloy Photonic Crystals. *J. Mater. Chem.* **2010,** *20*, 1538-1545.
224. Chang, A. S.; Kim, Y. S.; Chen, M.; Yang, Z. P.; Bur, J. A.; Lin, S. Y.; Ho, K. M. Visible Three-Dimensional Metallic Photonic Crystal with Non-Localized Propagating Modes Beyond Waveguide Cutoff. *Optics express* **2007,** *15*, 8428-37.
225. Courtin, E.; Boy, P.; Rouhet, C.; Bianchi, L.; Bruneton, E.; Poirot, N.; Laberty-Robert, C.; Sanchez, C. Optimized Sol–Gel Routes to Synthesize Yttria-Stabilized Zirconia Thin Films as Solid Electrolytes for Solid Oxide Fuel Cells. *Chem. Mater.* **2012,** *24*, 4540-4548.
226. Yoldas, B. E.; O?Keeffe, T. W. Antireflective Coatings Applied from Metal-Organic Derived Liquid Precursors. *Appl. Opt.* **1979,** *18*, 3133-3138.
227. Terabe, K.; Kato, K.; Miyazaki, H.; Yamaguchi, S.; Imai, A.; Iguchi, Y. Microstructure and Crystallization Behaviour of TiO_2 Precursor Prepared by the Sol-Gel Method Using Metal Alkoxide. *J. Mater. Sci.* **1994,** *29*, 1617-1622.
228. Yoshida, M.; Prasad, P. N. Sol−Gel-Processed SiO_2/TiO_2/Poly(Vinylpyrrolidone) Composite Materials for Optical Waveguides. *Chem. Mater.* **1996,** *8*, 235-241.
229. Zhu, Y.; Zhang, L.; Gao, C.; Cao, L. The Synthesis of Nanosized TiO_2 Powder Using a Sol-Gel Method with $TiCl_4$ as a Precursor. *J. Mater. Sci.* **2000,** *35*, 4049-4054.
230. Arpin, K. A.; Losego, M. D.; Cloud, A. N.; Ning, H.; Mallek, J.; Sergeant, N. P.; Zhu, L.; Yu, Z.; Kalanyan, B.; Parsons, G. N.; Girolami, G. S.; Abelson, J. R.; Fan, S.; Braun, P. V. Three-Dimensional Self-Assembled Photonic Crystals with High Temperature Stability for Thermal Emission Modification. *Nat. Commun.* **2013,** *4*, doi:10.1038/ncomms3630.